UAB
Universitat Autònoma de Barcelona

FIRST- PRINCIP LES THEORY OF SPATIAL DISPERSION

Asier ZABALO

ADVERTIMENT. L'accés als continguts d'aquesta tesi queda condicionat a l'acceptació de les condicions d'ús establertes per la següent llicència Creative Commons: https://creativecommons.org/licenses/?lang=ca

ADVERTENCIA. El acceso a los contenidos de esta tesis queda condicionado a la aceptación de las condiciones de uso establecidas por la siguiente licencia Creative Commons: https://creativecommons.org/licenses/?lang=es

WARNING. The access to the contents of this doctoral thesis it is limited to the acceptance of the use conditions set by the following Creative Commons license: https://creativecommons.org/licenses/?lang=en

UAB
Universitat Autònoma
de Barcelona

PhD THESIS

DOCTORAL PROGRAM IN PHYSICS

FIRST-PRINCIPLES THEORY OF SPATIAL DISPERSION

Author:
Asier ZABALO

Supervisor:
Dr. Massimiliano STENGEL

Tutor:
Dr. Aitor LOPEANDIA

A thesis submitted in fulfillment of the requirements
of the PhD in Physics program of the UAB

in the

Institut de Ciència de Materials de Barcelona

Academic Year 2024/2025

Ya para entonces me había dado cuenta de que buscar
era mi signo, emblema de los que salen de noche sin propósito fijo,
razón de los matadores de brújulas.

Julio Cortázar – Rayuela

CONTENTS

APPENDIX

LIST OF FIGURES

LIST OF TABLES

ACKNOWLEDGMENTS

First of all, I want to express my deep gratitude to my supervisor, Massimiliano Stengel. Being able to work with him during these years has been an absolute honor and privilege for me. His knowledge and passion for the subject, combined with the patience he has shown me and the sense of freedom I have felt in my work during this PhD journey, have made this experience exceptional and unforgettable for me. I have profound admiration and respect for him, both as a scientist and, most importantly, as a person. All I can say is a big thank you.

I would like to express my gratitude to Cyrus E. Dreyer, with whom I had the opportunity to work during my three-month stay in New York. Without a doubt, he played a crucial role in making my visit to the "Big City" truly memorable, both professionally and personally.

I would also like to thank all the people I have met during these years: Miquel, Matteo, Kostya, Madhura, Vladimir, Alex, Emanuele, Jean Paul, and Giulio. While science (and life) may take us in different directions, I am hopeful we will keep in touch and meet again in the near future.

I cannot conclude my acknowledgments here, since there are many people whose support and presence over these years have meant so much to me.

I will start expressing my gratitude to Dani. Thank you for making the stay in New York far more enjoyable than it would have been otherwise. I will never forget that never-ending walk on Long Island in search of the beach. An epic and eternal journey that we endured without complaints: this is probably an accurate metaphor for the thesis, and also a good story for "La Ruina" (I will miss those nights watching this show...). I would also like to thank the members of *Invent Park*: Aitor Duñabeitia, Markel Astorkia and Iratz Fernández. I will always remember Markel Astorkia's deep, passionate and technical analysis of the movie "Mystic River", Aitor Duñabeitia's life lessons about the importance of eye contact to truly connect with other human beings at that Cuban pub in Gràcia, and the house filled with flour due to Iratz's spontaneous passion for baking bread. It was only during one year that we were living together, but I retain really good memories from that time. Gora Deba! Iratz, you have been present for longer than a year in Barcelona, so I guess I will start with you and then continue, without any particular order, logic or pause, with the rest of people, while always maintaining a tone of irony, sarcasm, and humor (so don't take me too seriously here...). Thank you, Iratz (*the Stoic*), for all the walks and runs together —those were sometimes only an excuse for our *therapy in motion*—, and for transmitting your knowledge about music and the stoics to me ("Sabio de Mínimo" would be really proud to see that his ancient teachings are still alive through your actions). During all this time, you were the true *maestro*. Thank you, Roberto, for showing me what "3%" means, for introducing me to some of the most amazing music I have ever heard in my life, for the athletic exhibitions and performances with *el Torito* in Portbou and for helping me explore the 80% of *la ciudad condal*. Thank you, Núria, for all the unforgettable Wednesday nights in Barcelona, for the countless messages and notes in *italics* and for showing me that sometimes, the only way to tame chaos is to embrace it with even more (this is the kind of wisdom I would expect from a genuine *life mentor*). That peaceful night in your terrace, drinking wine while listening to the Goldberg Variations, was merely an illusion amid all the pandemonium we have witnessed. Ho has intentat, però els meus intents per aprendre català van començar i van acabar amb "L'indi americà". Quina vergonya la meva... Almenys vaig poder provar, per fi, els musclos. Un petit èxit! (Special mention to the three of you, Iratz, Roberto and Núria, for those memorable trips over the past few years. That weekend we spent at *The Overlook* and its surroundings, skiing and contemplating the constellation of Orion, will be hard to forget. On that note, was that the standard initiation protocol for first-time skiers? Don't get me wrong: skiing in complete darkness at night, without any lights or experience, while praying not to fall off a cliff, was really fun. I'm just curious... Thank you, Iratz and Núria, for those days in Morocco. That night in the desert gazing at the stars, or that other night listening to the life teachings of Jean Marouis in a random terrace of Marrakesh, felt like a surreal dream. Thank you, Roberto, for that weekend in Málaga: sleeping on the beach, on the streets, or even in jail would have been more comfortable and safer than the hostel you chose.) Thank you, Jon López (*the coding wizard*), for all the crazy-late-night-chats, for sharing, even from a distance, our respective struggles with the thesis, and for adding new ideas to our never-ending list of future plans that we will probably never fulfill. To be honest, your friendship is the best thing I take away from studying physics in Leioa; everything else —learning quantum mechanics, programming or even finishing the thesis— is *just* poetic noise in the background... (By the way, what do you think about attempting the ascent of El Teide in the following weeks? This is an official proposal to finally carry out this plan.) Thank you, Maria Aizpurua, for organizing *El golpe*, for your contagious positivity and energy, and for joining efforts with me in the bathroom of that "escape room": your control of the situation, along with your calm and gentle whispers, were key to our success. Thank you, Jordi, for teaching me how to navigate life in "modo Zen" and for showing me, through your example, how to behave like an actual "mamífero superior". *Nos vemos en el aire.* Thank you, Adrià Todó, for joining me in sharing our feelings, whether it was frustration, happiness, anger, a psychotic break or something else, with screams, yelling, and roars at home (the neighbors might have another opinion, but it was really fun...) and for demonstrating your mastery of palindromes, anagrams and words in general. That night walk through Las Ramblas, shrouded in fog, was a particularly memorable experience I will not forget. Thank you, Jordi Solà (*the poet*), for sharing your life adventures with us (we are all willing to see your diary published), for all the Monday nights at "Club Cronopios" reading poetry, and for being our personal guide while exploring nature in Catalunya: that river trip was amazing. Thank you, Frans, for showing me that life is all about attitude (you demonstrated me with empirical facts that is possible to have fun even while playing Bingo, which is, honestly, truly remarkable...) and for being the greatest (and probably only) supporter of my diary (I will try to keep you updated on all the future misfortunes of my comic life). Thank you, Maria Garcia, for your contagious positivity and energy (is this a Déjà vu?) and for spreading the Basque culture throughout Cardedeu, Llinars del Vallès and Catalunya in general: the fan base of *El Konkis* is definitely increasing under your guidance. Thank you, Kimetz, for being the biggest promoter of *els dijous universitaris* and for being one of the most loyal —and, to be honest, unexpected— running partners I could have imagined: we have become familiar with every nook and cranny of Montjuïc. Thank you, Raúl, for always supporting my culinary creations: the line that separates genius from madness is really thin, yet we must take risks in the kitchen. Thank you, Claudia, for joining me on this perilous journey into the sinister caverns of the Spanish language (anacoluto, hipálage, diritámbico, justipreciarse, arregosto, sinalagmático, dodicocéfalo, animálculo... I think we have conquered them all!) and for sharing with me your extensive knowledge, undoubtedly acquired over a lifetime of study (*well...*), of the novel *Madame Bovary*. Thank you, Alex Palomar, for showing me your driving skills while I was trying to teach you Euskera. Thank you, Carme, for the sporadic and unexpected calls on Friday nights: our conversations were too profound to summarize them here in a few words. Thank you, Cian, for your calmness and quietude so representative of Ireland and Panticosa. Thank you, Sergio, for bringing true calm and wisdom when chaos reigns among us. Thank you, Bella, for preparing that sushi in Portbou the first time we met (I was literally speechless... Maria and Carme can corroborate it). Thank you, Piotr, for being our personal DJ and for filling the house with so many plants (this is becoming a botanical wonderland!). Thank you, Kat, for understanding (and even sharing!) my obsession with post-its. Niech żyje Polska i jej ludzie!

I am thankful to all my lifelong friends from Eibar. My visits to my hometown have not been very frequent in recent years, but it is always incredible to be there and experience, with all of you, *Eibarko poteoa*. Hau al da hiriko proposamenik erakargarriena? Agian bai. I am particularly grateful to Asier Castillo (*the philosopher*) for all our *pseudo-philosophical* (the "pseudo" prefix is, of course, only intended to reflect my limited knowledge...) conversations, both in person and from afar.

Last but not least, I am deeply grateful to my family for always supporting me and for being there at all times. I love you all.

RESUMEN

Esta tesis se centra en el avance de la comprensión fundamental de una amplia clase de propiedades de dispersión espacial en el campo de la física de la materia condensada. Para ello desarrollamos y aplicamos métodos novedosos, precisos y eficientes basados en primeros principios. Nos centramos en tres ejemplos representativos, respectivamente en óptica (actividad óptica natural) dinámica de redes (fuerzas de Lorentz y factores g moleculares) y electromecánica (flexoelectricidad en metales polares). Los cálculos de estructura electrónica a primeros principios se realizan en el marco de la teoría del funcional de la densidad (DFT) y de la teoría perturbacional del funcional de la densidad (DFPT), con ondas planas y pseudopotenciales. Las propiedades de dispersión espacial se estudian en el marco teórico del recién implementado "long-wave DFPT", sobre lo que desarrollamos nuestras nuevas implementaciones teóricas y computacionales.

Generalizamos el método "long-wave DFPT" a metales, logrando un nivel de precisión y eficiencia computacional comparables al alcanzado en aislantes. Aplicamos nuestro nuevo método en el contexto de fonones y gradientes de deformación, calculando los coeficients de dispersión espacial de los fonones ópticos en Γ y el tensor de fuerza-respuesta flexoeléctrico en estructuras metálicas seleccionadas.

Aprovechamos las ventajas de nuestra nueva implementación para la dispersión espacial en metales para demostrar que la flexoelectricidad puede resolver uno de los problemas persistentes de los metales polares, a saber, el cambio de dirección del parámetro de orden polar mediante un campo externo. Tomamos $\mathrm{LiOsO_3}$ como caso de prueba y demostramos que el cambio del parámetro de orden polar mediante gradientes de deformación debería ser experimentalmente factible.

Exploramos, en el contexto DFPT, la íntima conexión entre dispersión espacial y magnetismo orbital estudiando los efectos de un campo magnético sobre la dinámica de moléculas (factores g rotacionales) y sólidos (fuerzas de Lorentz generalizadas). La magnetización inducida bien por una rotación rígida de una muestra finita o por una pseudorrotación producida por fonones circularmente polarizados se describe en términos de sólo dos propiedades de respuesta lineal: un término de *carga puntual* procedente de la polarización macroscópica inducida por un desplazamiento atómico (tensor de carga efectiva de Born) y un término *dispersivo* procedente de su dispersión espacial a primer orden. Encontramos que esta última contribución, que había sido sistemáticamente ignorada en estudios anteriores, puede dominar la respuesta.

Establecemos, bajo el marco teórico "long-wave DFPT", una novedosa metodología a primeros principios para calcular la actividad óptica natural, que supera la mayoría de las limitaciones de los métodos actualmente disponibles. En particular, nuestra metodología evita sumas sobre estados vacíos, trata adecuadamente los términos de campos autoconsistentes, toma las derivadas con respecto a $\mathbf{q}$ analíticamente y es igualmente válida tanto en moléculas como en sólidos.

SUMMARY

This thesis focuses on advancing the fundamental understanding of a broad class of spatial dispersion properties within the field of condensed matter physics, by developing and applying novel, accurate, and efficient first-principles methods. We target three representative examples, respectively in optics (natural optical activity), lattice dynamics (Lorentz forces and molecular g factors), and electromechanics (flexoelectricity in polar metals). First-principles electronic structures calculations are performed within the framework of density-functional theory (DFT) and density-functional perturbation theory (DFPT), with plane waves and pseudopotentials. Spatial dispersion properties are studied under the framework of the recently implemented long-wave DFPT, on top of which we further develop our new theoretical and computational implementations.

We generalize the long-wave DFPT method to metals, achieving a level of accuracy and computational efficiency comparable to that attained in insulators. We test our implementation with phonons and strain gradients, by computing the spatial dispersion coefficients of zone-center optical phonons and the flexoelectric force-response tensor of selected metal structures.

We exploit the advantages of our new implementation for spatial dispersion in metals to demonstrate that flexoelectricity can solve one of the long-standing issues that polar metals have been facing over the last years, namely the switching of the polar order parameter via an external field. We take $LiOsO_3$ as a test case and conclude that the switching of its bulk polar order parameter mediated by strain gradients should be experimentally feasible.

We further explore, within a DFPT context, the intimate connection between spatial dispersion and orbital magnetism by studying the effects of an applied magnetic field on the lattice dynamics of molecules (rotational g factors) and solids (generalized Lorentz forces). The magnetization induced either by a rigid rotation of a finite sample or by a pseudorotation produced by circularly polarized phonons is described in terms of only two linear-response properties: a *point-charge* term coming from the macroscopic polarization induced by an atomic displacement (Born effective charge tensor) and a *dispersive* term coming from its first-order spatial dispersion. We find that the latter contribution, which had been systematically neglected in previous studies, can dominate the response.

We establish, within the framework of long-wave DFPT, a novel first-principles approach to calculate the natural optical activity, which overcomes most of the limitations of currently available methods. In particular, our methodology avoids cumbersome sums over empty states, treats self-consistent field terms appropriately, takes the derivatives with respect to $\mathbf{q}$ analytically and is equally valid both in molecules and solids.

PUBLICATIONS

The PhD candidate is co-author of the following works:

[1] A. Zabalo and M. Stengel, "Ensemble density functional perturbation theory: spatial dispersion in metals," Phys. Rev. B **109**, 245116 (2024).

[2] A. Zabalo and M. Stengel, "Natural optical activity from density-functional perturbation theory," Phys. Rev. Lett. **131**, 086902 (2023).

[3] A. Zabalo, C. E. Dreyer, and M. Stengel, "Rotational g factors and lorentz forces of molecules and solids from density functional perturbation theory," Phys. Rev. B **105**, 094305 (2022).

[4] A. Zabalo and M. Stengel, "Switching a polar metal via strain gradients," Phys. Rev. Lett. **126**, 127601 (2021).

- Ref. [1] is used in Chapter 3.
- Ref. [2] is used in Chapter 6.
- Ref. [3] is used in Chapter 5.
- Ref. [4] is used in Chapter 4.

1

INTRODUCTION

The objective of this thesis is to advance our fundamental understanding of a broad class of materials properties that relate to spatial dispersion, by developing and applying novel, accurate, and efficient first-principles methods. In short, spatial dispersion deals with properties that depend on the spatial modulation of an external perturbation, i.e., gradients in real space. Equivalently, if one works in reciprocal or Fourier space, this reduces to the dependence of the response function on the wave vector $\mathbf{q}$ that modulates the external perturbation. Spanning over several scientific disciplines, including physics, chemistry, biology, material science and engineering, manifestations of spatial dispersion can be observed in a wide range of areas. Here, we will focus our attention on the field of condensed matter physics. Representative examples thereof include optics, strain gradient mediated effects either in elasticity or flexoelectricity, and phonon or magnon spatial dispersion phenomena, among others. In particular, we target three representative examples, respectively in optics (natural optical activity), lattice dynamics (Lorentz forces and molecular g factors), and electromechanics (flexoelectricity in polar metals).

From a historical perspective, the first observation of spatial dispersion phenomena in crystals is often attributed to early research studies in optics, which concerns the interaction between an electromagnetic wave (e.g., visible light) with atoms. Amid the entire spectrum of optical spatial dispersion phenomena, natural optical activity (NOA) can be regarded as the most fundamental. Mathematically, the natural optical activity describes the first-order spatial dispersion of the macroscopic dielectric permittivity tensor. At difference with the Faraday effect [1], NOA does not require the presence of an external magnetic field ($\mathbf{B}$) to be present. Empirically, it manifests as optical rotation (OR), which is a property of certain structures to rotate the plane of the polarization of light [2] that travels through them [a schematic representation of this phenomenon is provided in Fig. 1.1 (c)]. It was first measured in quartz crystals back in 1811 by Arago, and historically, most of the studied optically active materials turned out to be chiral. In fact, chirality is a sufficient but not necessary condition for NOA to be present, as optically active achiral systems also exist [3, 4]. Since its discovery, natural optical activity has been attracting increasing research interest, and reliable experimental measurements now exist for many materials, both in molecular [5–9] and crystalline form [10–16].

Generalized Lorentz forces in solids and molecules originate from a time-reversal (TR) symmetry breaking that is caused by an external magnetic field, $\mathbf{B}$. Their main physical consequence can be regarded as the phonon counterpart of the optical Faraday effect, resulting in a frequency splitting between circularly polarized phonons or molecular rotation modes; because of this, their inclusion in the present list of spatial dispersion properties may appear surprising at first sight. As we shall explain shortly, however, an orbital $\mathbf{B}$ field enters the electronic Hamiltonian via the electromagnetic vector potential, and more specifically corresponds to the spatial gradients thereof. This observation implies that orbital magnetism is ubiquitous in the physics of spatial dispersion, and the study of Lorentz forces will help us emphasize this important fact. These are of great fundamental interest as manifestations of "geometric magnetization" [17], and enjoy an elegant formulation in terms of geometric phases [18] and Berry curvatures [19]. They are also related to the angular momentum of phonons via the "phonon Zeeman effect" [20, 21], and are a crucial ingredient in the theory of the phonon Hall effect (PHE) [19, 22]. In this context, the study of molecules has been the most prevalent up to date; in particular, in regard to the orbital magnetic moment generated by a rotation in a molecule and the associated g factor, which is commonly referred to as the "molecular g factor" or "rotational g factor". In a nutshell, the rotational g factor of a molecule is the ratio between the total molecular magnetic moment (including both ionic and electronic effects) and the angular momentum that is associated with a rigid rotation of the body. In general, the magnetic moment contains a crucial contribution from the adiabatic orbital currents, which can partially or completely screen (or even overscreen in some cases) the contribution of the bare nuclear point charges. In addition to pure rotations, a magnetic moment can also arise from *pseudorotations* where individual atoms describe closed orbits around their equilibrium positions [see Fig. 1.1 (a)]. These are generated, for example, as a result of circularly polarized phonons, to which, in close analogy to the molecular case, a phonon g factor can be attributed. In the presence of an external magnetic field, degenerate phonon modes undergo the commonly referred to as "phonon Zeeman effect" or "phonon Zeeman frequency splitting". This phenomenon is characterized by a linear dependence of the phonon frequencies on the applied $\mathbf{B}$ field, where the proportionality constant is determined by the phonon g factor [see Fig. 1.1 (b)].

Flexoelectricity describes the coupling between a strain gradient and the macroscopic polarization and can be regarded as the spatially dispersive counterpart of piezoelectricicty. Unlike the latter, it does not require any particular crystal symmetry to be present: it is a universal property of all insulators. It was first predicted back in 1964 by Kogan [23], but until quite recently it has not been given much attention, since flexoelectric effects are practically negligible in macroscopic samples. Only in the past few years flexoelectricity has become a popular topic within the material science community, owing to the impressive progress in the microscopic theoretical understanding of this phenomenon and in the experimental control of nanoscale structures, where strain gradient effects can be large. As a consequence, nowadays applications of flexoelectric materials can be found in many different fields: flexoelectric energy harvesters [24], actuators that do not depend on the crystal symmetries [25], sensors (such as curvature detectors [26]), and so on. Even if strain gradients are ubiquitous both in insulators and metals, the vast majority of studies have targeted the former class of materials. This seems reasonable, as it is universally known that the electric polarization is ill-defined in metals. As a consequence, one could naively expect flexoelectricity to be completely irrelevant to conductors. One of the goals of this thesis is to show that this is by no means the case: a strain gradient does induce polar distortions on the crystal lattice regardless of the nature of the electronic ground state [see Fig. 1.1 (d)], and this effect can be of great importance in the context of the so-called "ferroelectric" or polar metals.

These are materials in which metallicity and polarity coexist, two properties that were initially considered as mutually exclusive. They were first proposed more than a half century ago by Anderson and Blount [27] in the context of martensitic transformations. They have been attracting a lot of attention recently, particularly after the experimental observation in 2013 of $LiOsO_3$, a material which undergoes a ferroelectric-like transition at 140 K from the centrosymmetric $R\bar{3}c$ to the noncentrosymmetric and polar $R3c$ space group [28]. (Note that all crystals belonging to polar space groups are noncentrosymmetric; however, the other way around is not true.) Polar metals are not only interesting for the their potential novel applications, ranging from electronic to thermoelectric devices and detectors [29], but they are also really interesting from a fundamental physical perspective, as they offer exciting opportunities to study exotic quantum phenomena such as superconductivity in polar systems [30, 31] or spin-polarized currents [32].

Despite the remarkably rapid growth witnessed in this field over recent years [33–35], a fundamental aspect still remains unresolved, which is the ability to switch their polar order parameter through the application of an external field. Due to the presence of free carriers in the bulk, the most obvious method for switching polarity in ferroelectrics, i.e., an external electric field, is apparently ruled out. Indeed, while electrical switching of thin 2D metals [36] has been previously achieved, a general method for reversing polarity at the bulk level is still missing. In this thesis we will demonstrate that strain gradients can be a viable solution. Note that flexoelectric switching of polar domains in insulators, and in particular in the prototypical ferroelectric barium titanate [37, 38], has already been accomplished. Still, whether the same switching mechanism is even applicable in metals was an open question at the time this thesis started.

METHODS AND EXISTING CHALLENGES

In the context of condensed matter theory, quantum mechanical first-principles calculations have been demonstrated to be extremely effective, especially with the increasingly growing computational capabilities and methodological tools. Among the latter, density functional theory (DFT) has emerged as one of the most popular and reliable techniques. Its appeal rests on the perfect balance that this method exhibits between numerical accuracy and computational efficiency. The success of DFT is particularly manifest in its linear-response implementation, widely known as density functional perturbation theory (DFPT), with calculated phonon frequencies that are often [40] within 2% of the experiment. One key advantage of DFPT is that it allows the computation of response functions at any wave vector $\mathbf{q}$ just by considering the unit cell of the system, even if $\mathbf{q}$ is incommensurate with respect to the periodicity of the lattice. In other words, building supercells as is common practice with frozen phonon techniques, can be completely avoided.

General methods to treat spatial dispersion effects in crystals have been elusive until very recently. The problem has been solved with the newly implemented [41] analytical long-wavelength approach, which works within the framework of DFPT. This is a computationally efficient and powerful method that is nowadays a publicly available feature of the ABINIT [42, 43] software. Successful applications of the long-wavelength DFPT technique for the calculation of first-order spatial dispersion coefficients have been demonstrated in several contexts, including flexoelectric coefficients [41, 44] or dynamical quadrupoles [41]. In fact, flexoelectricity can be regarded as the finest illustration of the advances that the first-principles theory of spatial dispersion has undertaken over the last few years. The progress in the theory

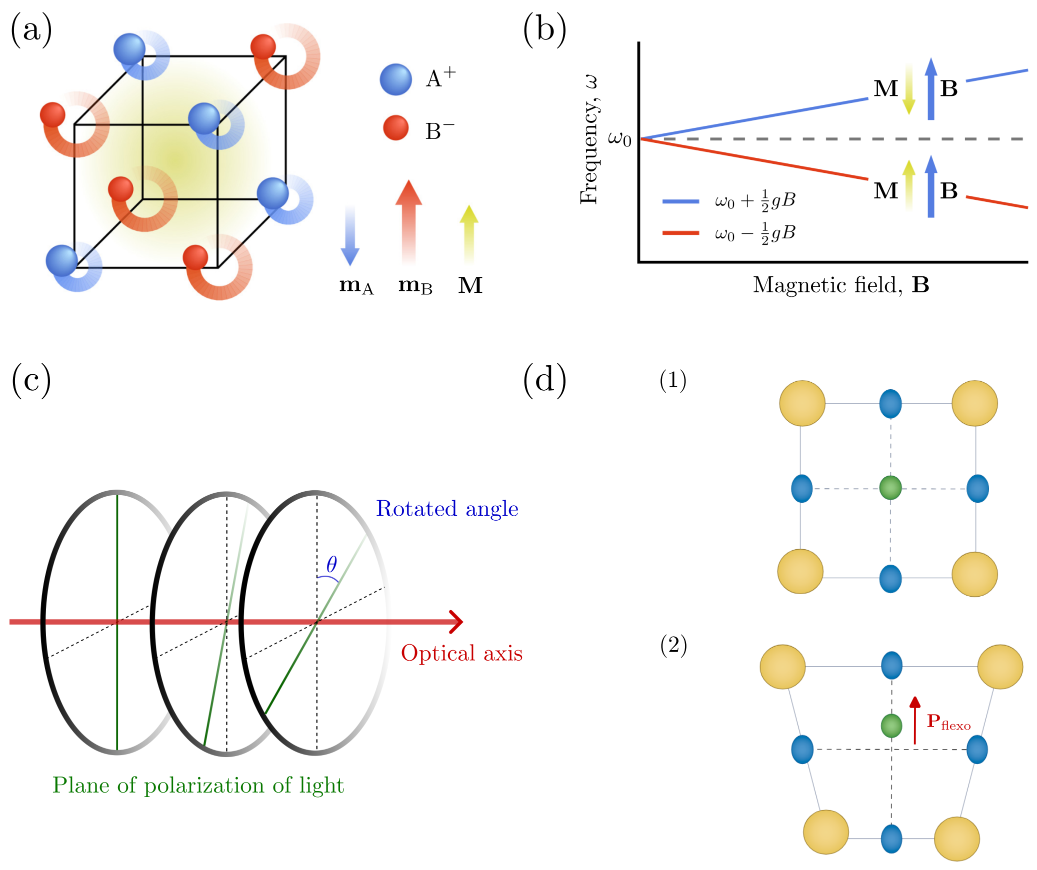

Figure 1.1: (a) Cartoon illustrating the local magnetic moments, $\mathbf{m}_A$ and $\mathbf{m}_B$, generated from ions, A^+ and B^-, describing closed orbits around their equilibrium positions. If the sum of all local magnetic moments does not cancel out, a macroscopic magnetic moment, $\mathbf{M}$, is produced. (b) Illustration of the phonon Zeeman frequency splitting, where ω_0 represent the phonon frequency in absence of the applied $\mathbf{B}$ field and g is the phonon gyromagnetic factor. (c) Cartoon illustrating the optical rotation of an optically active crystal. The incipient linearly polarized light travels along the optical axis, and the plane of the polarization of light is changed. The angle of rotation, denoted here by the symbol θ, is the quantity that is observed in experiments. (d) Flexoelectric polarization ($\mathbf{P}_{\text{flexo}}$) induced by an applied vertical strain gradient. Subfigure (1) shows the unit cell of a centrosymetric crystal at mechanical equilibrium, where $\mathbf{P}_{\text{flexo}} = 0$. Subfigure (2) shows the distorted unit cell with a polar distortion induced by flexoelectricity, $\mathbf{P}_{\text{flexo}} \neq 0$. (Figures (a) and (b) are adapted from Ref. [21]; and figure (d) is adapted from Ref. [39].)

and calculation of flexoelectricity has been especially impressive, reaching the point where it is nowadays possible to routinely compute the full flexoelectric tensor, both electronic and lattice-mediated [44] contributions, completely from first-principles. Although the majority of existing literature is about 3D bulk crystals, exciting advancements have been made in relation to 2D materials as well [45, 46].

While the aforementioned long-wavelength DFPT technique is, in principle, completely general (i.e., it can be applied in any physical context), there is still abundant work to be done both from the theoretical and computational perspectives. At the time this thesis was initiated, the contributions of orbital magnetization (**M**) to spatial dispersion were systematically neglected [41] in the available implementation of long-wave DFPT, ruling out the calculation of many outstanding physical properties where **M** plays a crucial role, including natural optical activity and Lorentz forces in solids. In addition, the implementation was restricted to insulators, meaning that metallic systems remained out of the discussion. Indeed, the problem with metallic systems seemed to be more profound, as a well-established variational perturbative formulation for metals was missing in the literature. As we shall see in the next chapters, both limitations have been lifted in the course of this thesis, thus significantly broadening the scopes of linear-response methods based on DFPT.

Regarding natural optical activity, *ab-initio* methods like Hartee-Fock (HF) [8], coupled-cluster (CC) [47] and density functional theory (DFT) [5, 6, 48] have recently become popular for the computation of gyration coefficients, which quantify the strength of natural optical activity. While most of the available literature is about small molecules, notable attempts at calculating optical activity in solids do exist. It is worth mentioning, for example, the pioneering works by Zhong, Levine, Allan and Wilkins, [49, 50] based on a numerical long-wavelength expansion of the electromagnetic vector potential response. Later, Malashevich and Souza [51] and Pozo and Souza [52] derived analytical expressions for the NOA, thus reviving the interest in the field; their formalism has been implemented very recently within an *ab initio* context [53]. The agreement between theory and experiment achieved in these works is quite good, e.g., for trigonal Se [51, 52], α-quartz [49, 50] and trigonal Te [54]. In spite of the remarkable progress, however, a systematic, quantitatively predictive, first-principles-based and computationally efficient methodology to compute the NOA both in molecules *and* solids has not been established yet. The first issue concerns the treatment of self-consistent fields (SCF). These have been accounted for, by instance, in Ref. [55] by Jönsson, Levine and Wilkins, and found to be of crucial importance, but the numerical differentiation with respect to the wave vector **q** that was used therein has limited a widespread application of their method. The existing analytical expressions [51, 52] for the NOA are, in principle, better suited to an *ab initio* implementation [53], but the SCF contributions are systematically neglected therein. Another disadvantage with the prevailing techniques lies in that they require cumbersome sums over empty states; this introduces an additional potential source of error, as the convergence with respect to the number of bands tends to be slow.

Concerning rotational g factors, first-principles electronic-structure methods have traditionally been highly successful in this regard. Reference values with chemical accuracy have been obtained long ago [56, 57] in the context of post–Hartree–Fock ab initio methods, like coupled-cluster (CC) or Møller–Plesset (MP) perturbation theory. Ceresoli and Tosatti [58, 59] later demonstrated that DFT can provide reliable values at a significantly lower computational cost. The strategy of Ceresoli and Tosatti consists in identifying the magnetization induced by a rigid rotation of the molecule with the Berry phase [60] accumulated around a closed orbit in presence of a uniform magnetic field. Additionally, their pioneering Berry-phase approach has paved the way towards the development of the "modern theory of magnetization" [61–63].

The case of extended solids has been comparatively much less explored. The reason is that previous approaches required performing calculations in the presence of a finite external magnetic field, which is a challenge to incorporate with periodic boundary conditions. Though there has been theoretical work in this direction [64, 65], so far a widespread implementation is lacking. This situation is in stark contrast with the case of isolated molecules, where finite-$\mathbf{B}$ methods are well established in existing codes [66, 67]. As a result, reference theoretical values for the coupling constants between phonons in solids and an external magnetic field are still scarce. Recent works by Spaldin and coworkers [20, 21] do report first-principles values for the phonon g factors in a broad range of crystalline insulators; however, a point-charge model for the microscopic currents associated with the ionic orbits was assumed therein. This certainly constitutes a drastic simplification from the computational perspective, as it only requires calculating standard linear-response properties (e.g., the Born effective charge tensor). Nevertheless, whether this approximation is reasonable remains to be proved.

Last but not least, regarding flexoelectricity and related effects in metals, we are unaware of previous attempts at theoretical calculations. Thus, it entails exploring hitherto uncharted territories. As we shall explain shortly, we have developed two distinct approaches for estimating strain gradient-induced polar distortions in metals. First, we have developed a method based on lattice sums of real space interatomic force-constants (IFCs). This method requires only modest coding efforts, as it builds on the standard implementation of phonons withing DFPT. At a later stage, we have generalized the long-wave DFPT to conductors, thus closing the gap between insulators and metals in regard to first-principles spatial dispersion theory. Strain gradient-induced polar distortions in metals represent only a special case of the capabilities of the method we have developed, which opens many exciting avenues for future work.

OUTLINE OF THE THESIS

The remainder of the thesis is organized as follows. Before presenting our original work (Chapters 3, 4, 5 and 6), we provide in Chapter 2 a short introduction to the electronic structure methods that are used in this thesis. In particular, we summarize the fundamentals of density-functional theory, density-functional perturbation theory and the long-wavelength DFPT [41] technique that is employed to access spatial dispersion coefficients.

In Chapter 3 we generalize the long-wavelength DFPT method of Ref. [41] to metals, thus enabling an accurate and efficient calculation of spatial dispersion coefficients in conductors. As a first step towards achieving this ambitious goal, we focus on the static regime and validate our methodology by computing the first-order spatial dispersion coefficients of zone-center optical phonons of selected metal structures. As a necessary intermediate step, we have also formally established a variational perturbative framework for metals, which was lacking in the literature.

In Chapter 4, we explore flexoelectricity as a viable means of switching the polar order parameter of the well-known polar metal LiOsO_3. Our main conclusion is that the switching of the polar order parameter in LiOsO_3 mediated by strain gradients should be experimentally attainable. More broadly, Chapter 4 represents a natural step forward of Chapter 3, as it allows to test our long-wavelength DFPT implementation of spatial dispersion in metals within the context of strain gradients in a real-world practical case. This enables us to report, for the first time, the flexoelectric force-response tensor and the flexocoupling coefficients of a metal.

In Chapter 5 we develop an efficient first-principles methodology based on DFPT to calculate, up to linear order in the applied magnetic field, rotational g factors and Lorentz forces of molecules and solids. Our method only requires the knowledge of two linear-response quantities: the macroscopic polarization induced by an atomic displacement, corresponding to the Born effective charges, and its first-order spatial dispersion. We validate our methodology in finite systems by computing the rotational g factor of several simple molecules, showing excellent agreement with experiment and previous theoretical calculations. In addition, we compute the Lorentz forces and the splitting of the low-frequency transverse-optical phonon mode of cubic SrTiO_3 in the presence of a magnetic field. We find that the *dispersive* contribution to the phonon g factor coming from the first-order spatial dispersion of the induced polarization, which had been neglected in some previous approaches, dominates the response.

In Chapter 6 we present a new strategy for the computation of the natural optical activity, which is based on the long-wave DFPT methodology of Ref. [41], and addresses most of the shortcomings of currently available approaches. We demonstrate the accuracy and efficiency of our method with representative chiral crystals and molecules. Our results corroborate that SCF contributions have a huge impact on the final result for the NOA, thus bringing us to the conclusion that neglecting SCF terms, as is common practice with some established methods, is not justified. Last but not least, we have found out that the analytical expression for the gyration coefficients in crystals is not unique, which can be traced back to the electromagnetic gauge freedom.

We conclude this thesis in Chapter 7 with the conclusions.

2

METHODOLOGICAL FRAMEWORK

The main objective of this chapter is to summarize the required first-principles theoretical techniques that we will use throughout this thesis. In particular, our work will be carried out within the context of density-functional theory (DFT) and density-functional perturbation theory (DFPT). Excellent reviews on these topics are available in the literature [68–71], and it is a matter of personal preference to choose one over the other.

This chapter is organized as follows. First, we shall explain the foundations of DFT as formulated by Hohenberg and Kohn [72] in 1964, where the density becomes the central quantity of the theory. Next, we shall discuss the Kohn and Sham *ansatz* [73], which asserts that the many-body problem of interacting electrons can be completely described through an auxiliary system of non-interacting particles, where all the many-body effects are reabsorbed into an exchange-correlation functional. In Sec. 2.3, the necessary linear-response techniques to access second and higher order energy derivatives are described. The main references here are the works by Xavier Gonze and coworkers [74–77]. The last section will be devoted to discuss the analytical long-wavelength expansion of the second-order energy functional, which allows the computation of first-order spatial dispersion coefficients with essentially the same computational cost as standard linear-response quantities. This methodology, developed by Royo and Stengel [41] in 2019, constitutes the current state-of-the-art first-principles theory of spatial dispersion on top of which we further develop our new theoretical and computational implementations.

2.1 THE SCHRÖDINGER EQUATION

A *first-principles* or an *ab-initio* approach in our context means describing our many-body system of interacting electrons and nuclei without relying on empirical data; i.e., using only the fundamental quantum-mechanical laws. Except for the simplest textbook systems (hydrogen atom) this is a very complex many-body problem, generally intractable even with the most powerful computers available nowadays. Thus, for all practical applications of the first-principles approach, several approximations are required. First, it is common practice to decouple the motion of the electrons from that of the nuclei, and treat the latter as classical point particles, by means of the Born-Oppenheimer [78] (also known as the adiabatic) approximation. This approximation is founded on the premise that the nuclei move much more slowly than electrons due to their greater mass and, therefore, the electrons are able follow the motion of the nuclei adiabatically while remaining in their ground state. In other words, if we assume a Hamiltonian formulation,[1] the many-body wave function Ψ for the electrons from which we can extract all

---

[1] Not that a Hamiltonian description of the system is not strictly necessary, since a Lagrangian formulation is in some cases advantageous. In fact, we take this approach in Chapter 5.

the information can be obtained from the following time-independent Schrödinger equation,

$$\hat{H}\left|\Psi\right\rangle = E\left|\Psi\right\rangle, \tag{2.1}$$

which is solved for a given configuration of the nuclei. In Hartree atomic units,[2] the Hamiltonian of Eq. (2.1) is given by

$$\hat{H} = -\frac{1}{2}\sum_i \boldsymbol{\nabla}_i^2 - \sum_i\sum_I \frac{Z_I}{|\mathbf{R}_I - \mathbf{r}_i|} + \frac{1}{2}\sum_{i\neq j}\frac{1}{|\mathbf{r}_i - \mathbf{r}_j|}. \tag{2.2}$$

The first term in Eq. (2.2) is the kinetic energy of the electrons, where $\boldsymbol{\nabla}_i = \boldsymbol{\nabla}_{\mathbf{r}_i}$ and $\mathbf{r}_i$ represents the position of the i-th electron. The second term accounts for the electron-nucleus interaction, where $\mathbf{R}_I$ are the (fixed) nuclear positions and Z_I their atomic number. This term will be referred to as $V_{\text{ext}}(\mathbf{r})$ hereafter, and the dependence on the nuclear coordinates will be kept implicit. The last term describes the electron-electron interaction. Notice that in the Born-Oppenheimer approximation the nucleus-nucleus interaction term becomes a constant and has not been included in Eq. (2.2). Nevertheless, for a correct treatment of the Coulomb electrostatics in solids, it is crucial to incorporate this contribution in the final energy expression of the system.

Of course, finding a solution for the electronic system described by Eq. (2.1) is still beyond reach, as the equations that need to be solved depend on $3N$ degrees of freedom, where N is the number of electrons in the system. Already in the 1920s a parading shift occurred when Thomas and Fermi [79] formulated a theory for a many-body system of interacting electrons in terms of the electron density, which depends only on 3 variables. This is sometimes considered as the first *density-functional theory* (DFT), though it was not until 1964 when Hohenberg and Kohn [72] formulated their renowned theorems and Kohn and Sham (1965) [73] introduced their auxiliary *non-interacting* system that DFT became a useful theory for studying real physical problems. In the next section we shall recap the main ideas of DFT as formulated by Hohenberg and Kohn and we will briefly discuss the limitations of the theory, emphasizing the required approximations that need to be made in view of a practical implementation.

2.2 DENSITY-FUNCTIONAL THEORY

Density-functional theory is nowadays the most widely used electronic structure method for describing many-body effects through independent particle equations. The basic idea of DFT rests on the fact that all the information of the system can be extracted merely from the knowledge of the ground-state electron density. Mathematically, this principle is expressed by stating that any property of the interacting electron system can be described as a *functional* of the ground-state electron density, denoted as $n(\mathbf{r})$, which is a function of the three dimensional real-space vector, $\mathbf{r}$. In practice, one could naively think that some fundamental information is necessarily lost when going from $3N$ degrees of freedom to just 3.

---

[2] $\hbar = e = 4\pi\epsilon_0 = 1$, where $\hbar = h/2\pi$ is the reduced Planck constant, $-e$ is the electron charge and ϵ_0 is the vacuum permittivity. Notice that, in those units, the speed of light is $c \sim 137$.

Yet, this approach is justified with the iconic Hohengerg-Kohn theorems, whose formulation and prove is remarkably simple, despite their profound significance.

2.2.1 THE HOHENBERG-KOHN THEOREMS

In 1964, in their seminar paper "*Inhomogeneous Electron Gas*" [72] Hohenberg and Kohn stated that the energy of the many-body interacting electron system can be expressed as a functional of the electron density,

$$E[n(\mathbf{r})] = F[n(\mathbf{r})] + \int V_{\text{ext}}(\mathbf{r})n(\mathbf{r})\, d^3r, \tag{2.3}$$

where $F[n]$ is a universal functional, independent of the external potential, given by

$$F[n(\mathbf{r})] = T_{\text{e}}[n(\mathbf{r})] + V_{\text{e–e}}[n(\mathbf{r})]. \tag{2.4}$$

Here, T_{e} is the kinetic energy and $V_{\text{e–e}}$ stands for the electron-electron interaction. It can be proven that:

1. For a system of interacting electrons in an external potential $V_{\text{ext}}(\mathbf{r})$, the potential $V_{\text{ext}}(\mathbf{r})$ is a unique functional of the ground-state electron density $n(\mathbf{r})$, apart from an additive constant. In other words, there is a one-to-one correspondence between the external potential and the ground-state electron density.

2. The energy functional $E[n(\mathbf{r})]$ given by Eq. (2.3) can be defined for any external potential, $V_{\text{ext}}(\mathbf{r})$. For a particular external potential, the ground-state energy of the system is the global minimum of $E[n(\mathbf{r})]$, and the density that minimizes that functional is the exact ground-state electron density of the system.

The major achievement of the Hohenberg-Kohn theorems resides in the demonstration that finding the ground state of a system of N interacting electrons boils down to minimizing the energy functional $E[n(\mathbf{r})] = F[n(\mathbf{r})] + \int V_{\text{ext}}(\mathbf{r})n(\mathbf{r})\, d^3r$ with respect to the electron density, which depends only on three spacial coordinates. Mathematically,

$$\frac{\delta}{\delta n(\mathbf{r})}\left[F[n(\mathbf{r})] + \int V_{\text{ext}}(\mathbf{r})n(\mathbf{r})\, d^3r - \mu\left(\int n(\mathbf{r})\, d^3r - N\right)\right] = 0, \tag{2.5}$$

where the Lagrange multiplier μ ensures that the density integrates to N. The Euler-Lagrange equation associated to Eq. (2.5) is given by

$$\frac{\delta F[n(\mathbf{r})]}{\delta n(\mathbf{r})} + V_{\text{ext}}(\mathbf{r}) = \mu. \tag{2.6}$$

The main obstacle resides in finding an expression for the universal functional $F[n(\mathbf{r})]$, and the Hohenberg-Kohn theorems offer no guidance whatsoever on how to construct it. As a preliminary step, one could extract from $F[n(\mathbf{r})]$ the classical Coulomb interaction, denoted here as the Hartree (H) term, and write

$$F[n(\mathbf{r})] = E_{\text{H}}[n(\mathbf{r})] + G[(\mathbf{r})]. \tag{2.7}$$

While the functional form of $E_{\mathrm{H}}[n(\mathbf{r})]$ is well-established,

$$E_{\mathrm{H}}[n(\mathbf{r})] = \frac{1}{2}\int \frac{n(\mathbf{r})n(\mathbf{r}')}{|\mathbf{r}-\mathbf{r}'|}\, d^3r\, d^3r', \tag{2.8}$$

$G[n(\mathbf{r})]$ still is, unfortunately, an unknown universal functional, just like $F[n(\mathbf{r})]$.

2.2.2 THE KOHN-SHAM AUXILIARY SYSTEM

From the Hohenberg-Kohn theorems we know that the ground-state density of a many-body interacting electrons under an external potential can be found by solving Eq. (2.5), the *only* problem being that the universal functional $F[n(\mathbf{r})]$ is unknown. In 1965 Kohn and Sham (KS) [73] asserted that it is possible to find an auxiliary system of *non-interacting* particles, which are subject to an effective potential, $V_{\mathrm{KS}}(\mathbf{r})$, whose ground-state density is the one that enters the Hohenberg-Kohn functional, $F[n(\mathbf{r})]$. Starting from Hohenberg and Kohn energy functional,

$$E[n(\mathbf{r})] = G[n(\mathbf{r})] + E_{\mathrm{H}}[n(\mathbf{r})] + \int V_{\mathrm{ext}}(\mathbf{r})n(\mathbf{r})\, d^3r, \tag{2.9}$$

Kohn and Sham then proceed to express the universal functional as follows,

$$G[n(\mathbf{r})] = T_{\mathrm{s}}[n(\mathbf{r})] + E_{\mathrm{xc}}[n(\mathbf{r})], \tag{2.10}$$

where $T_{\mathrm{s}}[n(\mathbf{r})]$ is the kinetic energy functional of a system of *non-intercating* electrons with density $n(\mathbf{r})$ and $E_{\mathrm{xc}}[n(\mathbf{r})]$ is the *exchange and correlation* (XC) energy functional of an *interacting* system with density $n(\mathbf{r})$. This term encapsulates the non-classical electrostatic contributions of the electron-electron interaction and the difference between the real kinetic energy of the interacting system and $T_{\mathrm{s}}[n(\mathbf{r})]$. Minimizing the functional given by Eq. (2.9),

$$\frac{\delta}{\delta n(\mathbf{r})}\left[T_{\mathrm{s}}[n(\mathbf{r})] + E_{\mathrm{H}}[n(\mathbf{r})] + E_{\mathrm{xc}}[n(\mathbf{r})] + \int V_{\mathrm{ext}}(\mathbf{r})n(\mathbf{r})\, d^3r\right] = 0, \tag{2.11}$$

under the constraint that $\int n(\mathbf{r})\, d^3r = N$, is equivalent to solving the following independent-particle Schrödinger equation,

$$\left(-\frac{1}{2}\nabla^2 + \hat{V}_{\mathrm{KS}}\right)|\psi_i\rangle = \epsilon_i\,|\psi_i\rangle\,, \tag{2.12}$$

under the constraint that the KS wave functions are orthonormal, $\langle\psi_i|\psi_j\rangle = \delta_{ij}$. In Eq. (2.12), $-\frac{1}{2}\nabla^2$ is the kinetic energy operator, ϵ_i denotes the energy eigenvalue and the KS effective potential is given by

$$\hat{V}_{\mathrm{KS}} = \hat{V}_{\mathrm{H}} + \hat{V}_{\mathrm{xc}} + \hat{V}_{\mathrm{ext}}, \tag{2.13}$$

with

$$\begin{aligned} V_{\mathrm{H}}(\mathbf{r}) &= \frac{\delta E_{\mathrm{H}}[n(\mathbf{r})]}{\delta n(\mathbf{r})} = \int \frac{n(\mathbf{r})}{|\mathbf{r}-\mathbf{r}'|}\, d^3r', \\ V_{\mathrm{xc}}(\mathbf{r}) &= \frac{\delta V_{\mathrm{xc}}[n(\mathbf{r})]}{\delta n(\mathbf{r})}. \end{aligned} \tag{2.14}$$

In the Kohn-Sham approach, the electron density is expressed as a function of the one-particle wave functions,

$$n(\mathbf{r}) = \sum_i f_i \langle \psi_i | \mathbf{r} \rangle \langle \mathbf{r} | \psi_i \rangle , \tag{2.15}$$

where f_i is the occupation factor of the i-th state. Likewise, even though $T_\mathrm{s}[n(\mathbf{r})]$ still remains an unknown functional of the density, it can be now expressed in terms of the KS orbitals,

$$T_\mathrm{s}[n(\mathbf{r})] = -\frac{1}{2} \sum_i f_i \langle \psi_i | \nabla^2 | \psi_i \rangle . \tag{2.16}$$

If the exchange-correlation functional $E_\mathrm{xc}[n(\mathbf{r})]$ was known, one could determine the ground-state of the many-body electron problem by solving the associated Kohn-Sham equations. These are a set of independent-particle equations that need to be solved self-consistently until convergence is reached. A schematic approach to tackle them involves the following steps. First, one starts from a trial electron density $n(\mathbf{r})$ and builds the Hartree and exchange-correlation potentials as described in Eq. (2.14). Second, the Schrödinger equation for the non-interacting particle system given by Eq. (2.12) is solved, obtaining the corresponding KS wave functions, and a new density is constructed by means of Eq. (2.15). The energy of the system is then given by

$$E = \sum_i f_i \langle \psi_i | \hat{H} | \psi_i \rangle + E_\mathrm{H}[n(\mathbf{r})] + E_\mathrm{xc}[n(\mathbf{r})] + E_\mathrm{n\text{–}n}, \tag{2.17}$$

where we have added the nucleus-nucleus constant term, $E_\mathrm{n\text{–}n}$, and the Hamiltonian is given by $\hat{H} = -\frac{1}{2}\nabla^2 + \hat{V}_\mathrm{ext}$. The process is repeated with the updated density until convergence is achieved. Notice that in Eq. (2.17) the self-consistent field (SCF) contributions are encompassed in the Hartree and exchange-correlation (Hxc) terms. In the following, whenever we want to highlight the SCF nature of the Hamiltonian, we shall use a *calligraphic* symbol, such that

$$\hat{\mathcal{H}} = \hat{H} + \hat{V}_\mathrm{SCF}, \tag{2.18}$$

where $\hat{V}_\mathrm{SCF} = \hat{V}_\mathrm{H} + \hat{V}_\mathrm{xc}$.

2.2.3 THE EXCHANGE AND CORRELATION FUNCTIONAL

It should be noted that without an expression for the exchange and correlation functional, the density-functional theory formalism described in the previous section has no real practical utility. Already in 1964 Kohn and Sham [73] introduced an approximation for $E_\mathrm{xc}[n(\mathbf{r})]$, which is suitable for systems where $n(\mathbf{r})$ is *sufficiently slowly varying*. This is nowadays known as the local density approximation (LDA), and despite its apparent simplicity, it stands as one of the most widely utilized approximations for the exchange-correlation functional. It is formulated as

$$E_\mathrm{xc}^\mathrm{LDA}[n(\mathbf{r})] = \int n(\mathbf{r}) \epsilon_\mathrm{xc}^\mathrm{LDA}[n(\mathbf{r})] \, d^3r, \tag{2.19}$$

where $\epsilon_{\text{xc}}[n(\mathbf{r})]$ is the exchange and correlation energy per electron of a uniform electron gas with density $n(\mathbf{r})$. Within this approximation, the potential $\hat{V}_{\text{xc}}^{\text{LDA}}$ entering the KS equations is given by

$$V_{\text{xc}}^{\text{LDA}}(\mathbf{r}) = \frac{\delta E_{\text{xc}}^{\text{LDA}}[n(\mathbf{r})]}{\delta n(\mathbf{r})} = \epsilon_{\text{xc}}^{\text{LDA}}[n(\mathbf{r})] + \frac{\partial \epsilon_{\text{xc}}^{\text{LDA}}[n(\mathbf{r})]}{\partial n(\mathbf{r})} n(\mathbf{r}). \tag{2.20}$$

Diverse parametrizations for $\epsilon_{\text{xc}}^{\text{LDA}}[n(\mathbf{r})]$ exist and the parametrized coefficients are usually extracted via quantum Monte Carlo simulations [80] or other semi-empirical methods. Throughout this work, we shall use the Perdew-Wang [81] parametrization for $\epsilon_{\text{xc}}^{\text{LDA}}[n(\mathbf{r})]$.

However, the LDA is by no means the end of the story, and nowadays a plethora of different approaches are employed for approximating the exchange and correlation functional. Indeed, we shall also make use of the Perdew-Burke-Ernzerhof (PBE) [82] parametrization of the generalized gradient approximation (GGA). This will serve us as a test of the robustness of our results with respect to different XC schemes. Without going into details, the GGA aims to improve the accuracy of LDA by incorporating gradient information,

$$E_{\text{xc}}^{\text{GGA}}[n(\mathbf{r})] = \int n(\mathbf{r}) \epsilon_{\text{xc}}^{\text{GGA}}[n(\mathbf{r}), \boldsymbol{\nabla} n(\mathbf{r})]\, d^3 r. \tag{2.21}$$

2.2.4 THE PLANE WAVE BASIS SET

The systems we shall consider in this thesis are solids composed by electrons and nuclei, which are repeated periodically in space. We shall assume Born-von Karman periodic boundary conditions (PBC) and we shall focus exclusively on bulk properties of perfect solids.[3] The crystal structure is entirely determined by the position of the atoms within the unit cell and the Bravais lattice, which is described by the vectors

$$\mathbf{R}^l = l_1 \mathbf{a}_1 + l_2 \mathbf{a}_2 + l_3 \mathbf{a}_3, \tag{2.22}$$

where $\mathbf{a}_i$ are the real space primitive lattice vectors and $l \equiv \{l_1, l_2, l_3\}$ determines the position of the unit cell (l_1, l_2 and l_3 are integer numbers). The periodicity of the solid manifests itself through the periodicity of the external potential, $V_{\text{ext}}(\mathbf{r})$, which in turn, imposes that the wave functions must respect the translational symmetries. By invoking the Bloch's theorem, each wave function can be written as a product of a phase factor times a cell-periodic function,

$$\psi_{m\mathbf{k}}(\mathbf{r}) = e^{i\mathbf{k}\cdot\mathbf{r}} u_{m\mathbf{k}}(\mathbf{r}), \quad \text{with} \quad u_{m\mathbf{k}}(\mathbf{r} + \mathbf{R}^l) = u_{m\mathbf{k}}(\mathbf{r}). \tag{2.23}$$

Here, m is a band index and $\mathbf{k}$ a reciprocal-space vector, which is restricted to the first Brillouin Zone (BZ), spanned by the primitive reciprocal space lattice vectors, $\mathbf{b}_i$, fulfilling the following relationship,

$$\mathbf{b}_i \cdot \mathbf{a}_j = 2\pi \delta_{ij}. \tag{2.24}$$

---

[3] We will also study isolated molecules in Chapters 5 and 6. These can be described with the same techniques employed for periodic solids by considering a molecule surrounded by empty space in a large "unit cell" that is repeated periodically in space. If sufficient empty space is added, the interaction among repeated images is negligible, allowing us to describe an isolated molecule.

A plane wave basis set is one of the most commonly used options for representing Bloch functions in solid-state calculations,

$$u_{m\mathbf{k}}(\mathbf{r}) = \sum_{\mathbf{G}} e^{i\mathbf{G}\cdot\mathbf{r}} u_{m\mathbf{k}}(\mathbf{G}), \tag{2.25}$$

where $\mathbf{G}$ are reciprocal-space lattice vectors,

$$\mathbf{G}(m_1, m_2, m_3) = m_1\mathbf{b}_1 + m_2\mathbf{b}_2 + m_3\mathbf{b}_3, \tag{2.26}$$

where m_1, m_2 and m_3 are integer numbers. In Eq. (2.25), $u_{m\mathbf{k}}(\mathbf{G})$ are the Fourier transform coefficients of $u_{m\mathbf{k}}(\mathbf{r})$, defined as

$$u_{m\mathbf{k}}(\mathbf{G}) = \frac{1}{\Omega}\int_{\Omega} e^{-i\mathbf{G}\cdot\mathbf{r}} u_{m\mathbf{k}}(\mathbf{r})\, d^3r, \tag{2.27}$$

where Ω represents the volume of the unit cell. By means of the fast Fourier transform (FFT) one can efficiently shift from real to reciprocal space representations, and vice versa. The orthonormalization condition translates to

$$\langle u_{m\mathbf{k}} | u_{n\mathbf{k}} \rangle = \frac{1}{\Omega}\int_{\Omega} u^*_{m\mathbf{k}}(\mathbf{r}) u_{n\mathbf{k}}(\mathbf{r})\, d^3r = \sum_{\mathbf{G}} u_{m\mathbf{k}}(\mathbf{G}) u_{n\mathbf{k}}(\mathbf{G}) = \delta_{nm}. \tag{2.28}$$

The electron density given by Eq. (2.15) can be expressed more conveniently in terms of the Bloch periodic functions as

$$n(\mathbf{r}) = \int_{\mathrm{BZ}} [d^3k] \sum_m f_{m\mathbf{k}} \langle u_{m\mathbf{k}} | \mathbf{r} \rangle \, \langle \mathbf{r} | u_{m\mathbf{k}} \rangle \,, \tag{2.29}$$

where $f_{m\mathbf{k}}$ is the occupation factor and we have used the following shorthand notation for the BZ integration,

$$\int_{\mathrm{BZ}} [d^3k] = \frac{\Omega}{(2\pi)^3} \int_{\mathrm{BZ}} d^3k. \tag{2.30}$$

The KS energy, Eq. (2.17), can be equivalently expressed in terms of the cell-periodic Bloch functions as

$$E = \int_{\mathrm{BZ}} [d^3k] \sum_m f_{m\mathbf{k}} \langle u_{m\mathbf{k}} | \left(\hat{T}_{\mathbf{k}} + \hat{V}_{\mathrm{ext},\mathbf{k}} \right) | u_{m\mathbf{k}} \rangle + E_{\mathrm{H}}[n(\mathbf{r})] + E_{\mathrm{xc}}[n(\mathbf{r})] + E_{\mathrm{n\text{-}n}}, \tag{2.31}$$

where the kinetic and the external potential operators are represented in momentum space. For a generic operator $\hat{O}$, we define

$$\hat{O}_{\mathbf{k}} = e^{-i\mathbf{k}\cdot\mathbf{r}} \hat{O} e^{i\mathbf{k}\cdot\mathbf{r}'}, \tag{2.32}$$

such that the corresponding matrix elements on two plane waves are given by

$$O_{\mathbf{k}}(\mathbf{G}, \mathbf{G}') = \langle \mathbf{G} + \mathbf{k} | \, \hat{O} \, | \mathbf{G}' + \mathbf{k} \rangle \,. \tag{2.33}$$

For example, the kinetic energy operator acquires a diagonal representation in reciprocal space,

$$T_{\mathbf{k}}(\mathbf{G}, \mathbf{G}') = \frac{1}{2} \delta_{\mathbf{G}\mathbf{G}'} |\mathbf{k} + \mathbf{G}|^2, \tag{2.34}$$

and the Hartree potential is given by

$$V_{\mathrm{H}}(\mathbf{G}) = \begin{cases} \frac{4\pi n(\mathbf{G})}{|\mathbf{G}|^2}, & \mathbf{G} \neq \mathbf{0} \\ 0, & \mathbf{G} = \mathbf{0}, \end{cases} \tag{2.35}$$

where $n(\mathbf{G})$ is the Fourier transform of the electron density and we have excluded the divergent [74] $\mathbf{G} = \mathbf{0}$ term in Eq. (2.35).

Before concluding with our summary of DFT and related practical computational methods for its implementation, we should address two important points that have been overlooked, which are covered in the following two subsections. The first topic is related to Brillouin Zone integration, whereas the second one deals with the pseudopotential method.

2.2.5 BRILLOUIN ZONE INTEGRATION

The integrals in $\mathbf{k}$ space as defined by Eq. (2.30) need to be evaluated as discrete sums for a finite number of $\mathbf{k}$ points,

$$\int_{\mathrm{BZ}} [d^3k] g(\mathbf{k}) \simeq \sum_{\mathbf{k}} w_{\mathbf{k}} g(\mathbf{k}), \tag{2.36}$$

where $g(\mathbf{k})$ is a generic function and $w_{\mathbf{k}}$ is the weight associated to each $\mathbf{k}$ point. Current integration methods, such as the tetrahedron method, allow for the evaluation of BZ integrals with high accuracy. Additionally, thanks to the use of crystal symmetries, the number of $\mathbf{k}$ points considered in the calculation can be substantially reduced. Nonetheless, special care is required with metals in order to accurately describe Fermi surface discontinuities, originated from abrupt changes in the Fermi-Dirac (FD) occupation distribution at zero temperature ($T = 0$), which might lead to considerable errors in the evaluation of the integrals in $\mathbf{k}$ space. The most effective and widely used strategy to deal with this issue at the ground-state level is the smearing technique [83]. In the latter approach, the sharp Fermi-Dirac distribution at $T = 0$, represented by the Heaviside step function, is approximated by a smoother function that is a broadened approximation of the former,

$$f_{m\mathbf{k}} = s \int_{-\infty}^{\frac{\mu - \epsilon_{m\mathbf{k}}}{\sigma}} \tilde{\delta}(t)\, dt, \tag{2.37}$$

where $s = 2$ is the spin multiplicity, μ is the Fermi level (also known as the chemical potential) and $\tilde{\delta}(x)$ is a (normalized) broadening function. If the equilibrium distribution of the occupancies is chosen to follow the Fermi-Dirac (FD) statistics, σ plays the role of a finite (electronic) temperature, $\sigma = K_{\mathrm{B}} T$, where K_{B} is the Boltzmann's constant. In practice, using a smeared distribution function is primarily aimed at accelerating the convergence with $\mathbf{k}$-mesh density. As a consequence, non-FD forms are often preferred [83, 84]. In this thesis, we will only consider the Gaussian smearing, which provides a smooth and differentiable representation of the Fermi-Dirac distribution via the following broadening function,

$$\tilde{\delta}(x) = \frac{1}{\sqrt{\pi}} e^{-x^2}. \tag{2.38}$$

2.2.6 THE PSEUDOPOTENTIAL METHOD

It is essential to point out that in practical calculations only a finite set of plane waves is taken into account, with their kinetic energy confined to a specified cutoff, such that $\frac{1}{2}|\mathbf{k}+\mathbf{G}|^2 < E_{\mathrm{cut}}$. However, accurately representing the rapid oscillating features of core electron orbitals near the nuclei would require considering numerous plane wave coefficients in the calculation. Given that most of the chemical and physical properties of real crystals can be characterized by considering only valence electrons, one could try to remove the problematic core orbitals from the simulation by replacing the original Coulomb potential with a smoother *effective potential* that captures the essential features of the former. This is precisely the idea behind the pseudopotential method [85], which is based on the following points:

- The core electrons, which are chemically inert, are dropped from the calculation altogether, as they do not directly participate in chemical bonding.
- The all-electron wave functions, ψ_{ae}, which have many radial nodes inside the core region (r_c), and thus, would require high Fourier components for their description, are replaced with smoother *pseudo* wave functions, ψ_{ps}, that have no radial nodes for $r < r_c$. This is done in practice by replacing the nuclear point-charge potential with a pseudopotential.
- Outside a selected core region delimited by r_c, the *pseudo* wave functions coincide with the all-electron wave functions.
- The energy eigenvalues that are extracted using the pseudopotential coincide with the energy eigenvalues one would obtain with the real potential.
- A "good" pseudopotential should be able to reproduce the scattering properties of the actual potential and one should be able to use it in different atomic environments without losing accuracy. The latter is commonly referred to as *transferability*.

Another important property that is often enforced is norm-conservation [86]. In short, norm-conservation requires that the probability density of both the all-electron and the *pseudo* wave functions is the same inside the selected core region delimited by r_c,

$$\int_0^{r_c} r^2 |\psi_{\mathrm{ae}}(r)|^2 \, dr = \int_0^{r_c} r^2 |\psi_{\mathrm{ps}}(r)|^2 \, dr. \tag{2.39}$$

While the pseudopotential method enables to accurately describe the physical properties of crystals while keeping the number of plane wave sufficiently low, the price one needs to pay is that, in general, locality is not preserved, i.e., most modern DFT calculations are performed with non-local pseudopotentials. In practice, this means that the pseudopotential is expressed as sum of a local (loc) plus a non-local separable (sep) term,

$$V^{\mathrm{psp}}(\mathbf{r},\mathbf{r}') = V^{\mathrm{loc}}(\mathbf{r})\delta(\mathbf{r}-\mathbf{r}') + V^{\mathrm{sep}}(\mathbf{r},\mathbf{r}'), \tag{2.40}$$

which, in turn, can be written as a sum of individual sublattice contributions,[4]

$$V^{\text{loc}}(\mathbf{r}) = \sum_{l,\kappa} v_\kappa^{\text{loc}}(\mathbf{r} - \mathbf{R}_\kappa^l), \tag{2.42}$$

$$V^{\text{sep}}(\mathbf{r}, \mathbf{r}') = \sum_{l,\kappa} v_\kappa^{\text{sep}}(\mathbf{r} - \mathbf{R}_\kappa^l, \mathbf{r}' - \mathbf{R}_\kappa^l). \tag{2.43}$$

In the latter equations, $\mathbf{R}_\kappa^l = \mathbf{R}^l + \boldsymbol{\tau}_\kappa$, where $\boldsymbol{\tau}_\kappa$ represents the position of the sublattice κ within the unit cell. A widely used class of pseudopotentials are norm-conserving pseudopotentials where the separable term is written in the Kleinman-Bylander (KB) [87] form,

$$V^{\text{sep}}(\mathbf{r}, \mathbf{r}') = \sum_{l,\kappa,\mu} e_{\mu\kappa} \zeta(\mathbf{r} - \mathbf{R}_\kappa^l) \zeta_{\mu\kappa}^*(\mathbf{r}' - \mathbf{R}_\kappa^l), \tag{2.44}$$

where the index μ takes into account both the azimuthal and magnetic quantum numbers, $\{l, m\}$, $\zeta_{\mu\kappa}(\mathbf{r})$ represents the KB projector function and $e_{\mu\kappa}$ are the expansion coefficients. It should be noted, however, that a single projector for each angular momentum channel is oftentimes insufficient to guarantee that all the aforementioned criteria are satisfied. Without entering into the very specifics, in this thesis we will make use of optimized norm-conserving Vanderbilt pseudopotentials (ONCVPSPs) as introduced by Hamann in Ref. [88], where norm-conserving *multiprojector* pseudopotentials are presented. (The interested reader is encouraged to refer to Ref. [88], where it is demonstrated through first-principles calculations that going beyond the KB form yields results for lattice constants and bulk moduli that are in better accordance with those of all-electron calculations essentially in all studied cases.)

2.3 DENSITY-FUNCTIONAL PERTURBATION THEORY

In the previous section we have briefly discussed the strategy to obtain the ground-state properties of a system of interacting electrons by means of density-functional theory and we have outlined the required approximations that need to be made for a practical implementation. In this section, we shall be interested in describing how the physical properties of the system are changed under an external perturbation. Even though different first-principles techniques are available for extracting response properties of solids, e.g., frozen phonon techniques [89], density-functional perturbation theory (DFPT) has emerged as the most favored approach. One key advantage that sets DFPT apart from alternative methods is its unique ability to handle incommensurate lattice distortions with arbitrary wave vectors $\mathbf{q}$ without

---

[4] The local part in Eq. (2.42) is spherically symmetric and diverges as $v_\kappa^{\text{loc}} \sim -Z_\kappa / r$, where Z_κ is the (pseudo) charge of sublattice κ. In reciprocal space, this divergence is associated with the $\mathbf{G} = \mathbf{0}$ component, and goes as [74]

$$v_\kappa^{\text{loc}}(q) \sim -\frac{4\pi}{q^2} Z_\kappa. \tag{2.41}$$

The latter is treated together with the Hartree divergence [see Eq. (2.35)] and, in the end, the divergences cancel out, leaving a residual contribution [68] that is typically added to the ion-ion energy.

the requirement of building supercells, i.e., one can compute the response to a perturbation at any $\mathbf{q}$ within the primitive unit cell, thus making it computationally superior.

We start by assuming a parametric dependence of the Hamiltonian on a small parameter λ, which describes the external perturbation. Taking advantage of standard time-independent perturbation theory techniques [90], the physical properties of the system are expanded in powers of λ,

$$X(\lambda) = \sum_n \frac{1}{n!}\lambda^n X^{(n)}, \tag{2.45}$$

where X can be the Hamiltonian $\hat{H}$, the electron density $n(\mathbf{r})$, the wave functions $\psi_m(\mathbf{r})$ or the energy E. The expansion coefficients are directly related to the derivatives of X with respect to λ,

$$X^{(n)} = \left.\frac{dX(\lambda)}{d\lambda^n}\right|_{\lambda=0}. \tag{2.46}$$

(Note that this convention differs from some earlier works [74, 76] by a $1/n!$ factor.) Due to the variational character of the Kohn-Sham energy functional, the application of perturbation theory results in a $2n+1$ theorem, i.e., knowledge of the n-th order wave functions are enough to describe $(2n+1)$-th order energies, and even derivatives of the energies acquire a variational character [76, 91]. At zero order, one recovers the ground-state objects defined in the previous section, whereas at first order in the perturbation, we obtain the following well-known expression for the energy,

$$E^{(1)} = \sum_{m\in\mathcal{V}} f_m \langle\psi_m^{(0)}|\,\hat{H}^{(1)}\,|\psi_m^{(0)}\rangle\,, \tag{2.47}$$

which is essentially the Hellmann-Feynman theorem [92]. Notice that in Eq. (2.47) we have explicitly indicated that the sums are carried out for states belonging to the valence ($\mathcal{V}$) manifold only, which are the occupied states in insulators; however, if m runs over all states, Eq. (2.47) is equally valid for metals as well (a more detailed treatment of DFPT in metals is deferred to Sec. 2.3.2). Pushing the expansion to second order in the perturbation, one can show that

$$E^{(2)} = \sum_{m\in\mathcal{V}} f_m \left(\langle\psi_m^{(1)}|\,\hat{H}^{(1)}\,|\psi_m^{(0)}\rangle + \langle\psi_m^{(0)}|\,\hat{H}^{(1)}\,|\psi_m^{(1)}\rangle + \langle\psi_m^{(0)}|\,\hat{H}^{(2)}\,|\psi_m^{(0)}\rangle \right), \tag{2.48}$$

where the first-order wave functions are obtained from the following Sternheimer equation [74, 93],

$$\hat{Q}(\hat{H}^{(0)} - \epsilon_m^{(0)})\hat{Q}\,|\psi_m^{(1)}\rangle = -\hat{Q}\hat{\mathcal{H}}^{(1)}\,|\psi_m^{(0)}\rangle\,. \tag{2.49}$$

Here, $\hat{Q}$ is the conduction band projector,

$$\hat{P} = \sum_{m\in\mathcal{V}} |\psi_m^{(0)}\rangle\,\langle\psi_m^{(0)}|\,, \quad \hat{Q} = \mathbb{1} - \hat{P}, \tag{2.50}$$

where $\mathbb{1}$ is the identity operator and $\hat{P}$ represents the valence band projector. The calligraphic symbol $\hat{\mathcal{H}}^{(1)}$ is the first order counterpart of Eq. (2.18), with

$$\hat{\mathcal{H}}^{(1)} = \hat{H}^{(1)} + \hat{V}^{(1)}, \tag{2.51}$$

where $\hat{V}^{(1)}$ is the first-order SCF potential, given by

$$V^{(1)}(\mathbf{r}) = \int K_{\mathrm{Hxc}}(\mathbf{r},\mathbf{r}')n^{(1)}(\mathbf{r})\, d^3r'. \tag{2.52}$$

$K_{\mathrm{Hxc}}(\mathbf{r},\mathbf{r}')$, on the other hand, is the Hartree and exchange-correlation (Hxc) kernel, which we define as

$$K_{\mathrm{Hxc}}(\mathbf{r},\mathbf{r}') = \frac{\delta V_{\mathrm{Hxc}}(\mathbf{r})}{\delta n(\mathbf{r}')} = \frac{\delta^2 E_{\mathrm{Hxc}}}{\delta n(\mathbf{r}) n(\mathbf{r}')}, \tag{2.53}$$

and the first-order electron density is given by

$$n^{(1)}(\mathbf{r}) = \sum_{m\in\mathcal{V}} f_m \langle\psi_m^{(1)}|\mathbf{r}\rangle\ \langle\mathbf{r}|\psi_m^{(0)}\rangle + \text{c.c.}, \tag{2.54}$$

where c.c. stands for complex conjugate. Equivalently, the linear-response problem can be recast as finding the variational minimum (with respect to the first-order wave functions) of the following second-order energy functional,

$$\begin{aligned} E^{(2)}_{\mathrm{con}} =& 2\sum_{m\in\mathcal{V}} f_m \langle\psi_m^{(1)}|\,(\hat{H}^{(0)} - \epsilon_m^{(0)})\,|\psi_m^{(1)}\rangle \\ &+ 2\sum_{m\in\mathcal{V}} f_m \langle\psi_m^{(1)}|\,\hat{H}^{(1)}\,|\psi_m^{(0)}\rangle + \text{c.c.} \\ &+ \int_\Omega\int K_{\mathrm{Hxc}}(\mathbf{r},\mathbf{r}')n^{(1)}(\mathbf{r})n^{(1)}(\mathbf{r}')\,d^3r\,d^3r' \\ &+ \sum_{m\in\mathcal{V}} f_m \langle\psi_m^{(0)}|\,\hat{H}^{(2)}\,|\psi_m^{(0)}\rangle\,. \end{aligned} \tag{2.55}$$

[The first three lines in Eq. (2.55) are typically referred to as the stationary (st) part, and the last line in Eq. (2.55), which is independent of the first-order wave functions, is the geometric (ge) term. It is common practice to encapsulate the latter, along with the ion-ion contributions, into the nonvariational (nv) term. In other words, $E^{(2)} = E^{(2)}_{\mathrm{st}} + E^{(2)}_{\mathrm{nv}}$, with $E^{(2)}_{\mathrm{nv}} = E^{(2)}_{\mathrm{ge}} + E^{(2)}_{\text{ion-ion}}$.] The subscript "con" in Eq. (2.55) means that the second-order energy functional is minimized subject to the constraint that the first-order wave functions are orthogonal to the valence ($\mathcal{V}$) manifold,

$$\langle\psi_m^{(0)}|\psi_n^{(1)}\rangle = 0, \quad \forall m,n\in\mathcal{V}, \tag{2.56}$$

which is also known as the parallel transport gauge [76]. Imposing the stationary condition on the first-order wave functions, $\delta E^{(2)}_{\mathrm{con}}/\delta\langle\psi_m^{(1)}| = 0$, immediately leads to the Sternheimer equation as defined in Eq. (2.49).

2.3.1 MONOCHROMATIC PERTURBATIONS

We now apply the general formalism of the previous section to the case of a monochromatic perturbation that is modulated by a wave vector $\mathbf{q}$. The response to an incommensurate perturbation can be mapped onto an equivalent problem that respects the symmetries of the lattice by performing the appropriate shifts in momentum space in operators and wave functions. We follow the well-established procedure [74] and work with the cell-periodic part of the Bloch functions. The operators are more conveniently expressed in momentum space (see Sec. 2.2.4). For example, the first-order Hamiltonian is written as a phase times a cell-periodic part, $\hat{\mathcal{H}}^{(1)}_{\mathbf{k},\mathbf{q}}$, such that

$$\hat{\mathcal{H}}^{(1)}_{\mathbf{k},\mathbf{q}} = e^{-i(\mathbf{k}+\mathbf{q})\cdot\mathbf{r}}\hat{\mathcal{H}}^{(1)}e^{i\mathbf{k}\cdot\mathbf{r}}. \tag{2.57}$$

Similarly, the first-order wave functions are given by

$$|\psi^{(1)}_{m\mathbf{k},\mathbf{q}}\rangle = e^{i(\mathbf{k}+\mathbf{q})\cdot\mathbf{r}}\,|u^{(1)}_{m\mathbf{k},\mathbf{q}}\rangle\,, \tag{2.58}$$

and the cell-periodic part of the first-order electron density, $n^{(1)}_{\mathbf{q}}(\mathbf{r}) = e^{-i\mathbf{q}\cdot\mathbf{r}}n^{(1)}(\mathbf{r})$, reads as follows

$$n^{(1)}_{\mathbf{q}}(\mathbf{r}) = 2\int_{\mathrm{BZ}}[d^3k]\sum_{m\in\mathcal{V}} f_{m\mathbf{k}}\,\langle u^{(0)}_{m\mathbf{k}}|\mathbf{r}\rangle\,\langle\mathbf{r}|u^{(1)}_{m\mathbf{k},\mathbf{q}}\rangle\,. \tag{2.59}$$

[Unless otherwise stated, we implicitly assume that the system under study is a time reversal (TR) symmetric insulator, which helps simplify some expressions.] For the sake of generality, we shall consider a mixed derivative with respect to two distinct perturbations, λ_1 and λ_2. In this context, the nonstationary expression for the second-order energy functional, analogous to Eq. (2.48), can be expressed as

$$E^{\lambda_1\lambda_2}_{\mathbf{q}} = \int_{\mathrm{BZ}}[d^3k]E^{\lambda_1\lambda_2}_{\mathbf{k},\mathbf{q}}, \tag{2.60}$$

where the quantity that needs to be integrated over the BZ is

$$\begin{aligned} E^{\lambda_1\lambda_2}_{\mathbf{k},\mathbf{q}} = &\sum_{m\in\mathcal{V}} f_{m\mathbf{k}}\left(\langle u^{(0)}_{m\mathbf{k}}|\,(\hat{H}^{\lambda_1}_{\mathbf{k},\mathbf{q}})^{\dagger}\,|u^{\lambda_2}_{m\mathbf{k},\mathbf{q}}\rangle + \langle u^{\lambda_2}_{m\mathbf{k},-\mathbf{q}}|\,\hat{H}^{\lambda_1}_{\mathbf{k},-\mathbf{q}}\,|u^{(0)}_{m\mathbf{k}}\rangle\right) \\ &+\sum_{m\in\mathcal{V}} f_{m\mathbf{k}}\,\langle u^{(0)}_{m\mathbf{k}}|\,\hat{H}^{\lambda_1\lambda_2}_{\mathbf{k},\mathbf{q}}\,|u^{(0)}_{m\mathbf{k}}\rangle\,. \end{aligned} \tag{2.61}$$

The stationary expression for the second-order energy at finite $\mathbf{q}$ will be deferred to Sec. 2.4.4, where it will be discussed in greater detail in the context of a long-wavelength expansion. In the following, we will introduce the specific perturbations that will be central to this thesis: atomic displacements, strain, and electric fields. However, before doing so, we will provide a brief overview of the application of perturbation theory to metals.

2.3.2 DFPT IN METALS

Even at the ground-state level, we have seen that due to the sharp discontinuities of the occupation function, special care is required when dealing with metals. Although perturbation theory in metals has been studied following slightly different techniques [94], we shall stick to de Gironcoli's approach [95], which is based on the application of the smearing technique to metals within the pseudopotential method. (We will try to maintain a notation that is close to that used in Ref. [95] by de Gironcoli.) This has enabled the computation of phonons in metals and, in turn, of a number of thermodynamic properties that depend on phonons and electron-phonon interactions, e.g., electrical and thermal conductivity.

As a starting point, consider the well known (nonstationary) Kubo-like sum-over-all-states expression for the second-order energy,

$$\begin{aligned} E^{\lambda_1\lambda_2}_{\mathbf{q}} = & \int_{\mathrm{BZ}} [d^3k] \sum_{m,n} \frac{\tilde{\theta}_{Fm\mathbf{k}} - \tilde{\theta}_{Fn\mathbf{k}}}{\epsilon^{(0)}_{m\mathbf{k}} - \epsilon^{(0)}_{n\mathbf{k}}} \langle u^{(0)}_{m\mathbf{k}} | (\hat{\mathcal{H}}^{\lambda_1}_{\mathbf{k},\mathbf{q}})^{\dagger} | u^{(0)}_{n\mathbf{k}+\mathbf{q}} \rangle \langle u^{(0)}_{n\mathbf{k}+\mathbf{q}} | \hat{H}^{\lambda_2}_{\mathbf{k},\mathbf{q}} | u^{(0)}_{m\mathbf{k}} \rangle \\ & + \int_{\mathrm{BZ}} [d^3k] \sum_{m} \tilde{\theta}_{Fm\mathbf{k}} \langle u^{(0)}_{m\mathbf{k}} | \hat{H}^{\lambda_1\lambda_2}_{\mathbf{k},\mathbf{q}} | u^{(0)}_{m\mathbf{k}} \rangle . \end{aligned} \tag{2.62}$$

Unless specified otherwise, the summations over m and n include all states. The first-order electron density enjoys a similar expression, with the sole difference being that the $\hat{H}^{\lambda_1}_{\mathbf{k},\mathbf{q}}$ external perturbation is replaced with the operator $|\mathbf{r}\rangle \langle \mathbf{r}|$,

$$n^{\lambda}_{\mathbf{q}}(\mathbf{r}) = \int_{\mathrm{BZ}} [d^3k] \sum_{m,n} \frac{\tilde{\theta}_{Fm\mathbf{k}} - \tilde{\theta}_{Fn\mathbf{k}}}{\epsilon^{(0)}_{m\mathbf{k}} - \epsilon^{(0)}_{n\mathbf{k}}} \langle u^{(0)}_{m\mathbf{k}} | \mathbf{r} \rangle \langle \mathbf{r} | u^{(0)}_{n\mathbf{k}+\mathbf{q}} \rangle \langle u^{(0)}_{n\mathbf{k}+\mathbf{q}} | \hat{\mathcal{H}}^{\lambda}_{\mathbf{k},\mathbf{q}} | u^{(0)}_{m\mathbf{k}} \rangle . \tag{2.63}$$

The new symbol appearing in Eqs. (2.62) and (2.63), $\tilde{\theta}_{mn\mathbf{k}}$, is the smeared occupation function defined by de Gironcoli in Ref. [95],

$$\tilde{\theta}_{mn\mathbf{k}} = s \int_{-\infty}^{\frac{\epsilon^{(0)}_{m\mathbf{k}} - \epsilon^{(0)}_{n\mathbf{k}}}{\sigma}} \tilde{\delta}(t)\, dt, \tag{2.64}$$

which is a generalization of our definition of the smeared occupation function, Eq. (2.37), where $\tilde{\delta}(t)$ is the broadening function. In Ref. [95] de Gironcoli realized that one can get rid of the double sum over all states of the previous equations; we shall focus on the electron density in the following, but analogous expressions can be obtained for the second-order energy. It is shown in Ref. [95] that Eq. (2.63) can be expressed as

$$n^{\lambda}_{\mathbf{q}}(\mathbf{r}) = 2 \int_{\mathrm{BZ}} [d^3k] \sum_{m \in \mathcal{M}} \sum_{n \in \mathcal{O}} \frac{\tilde{\theta}_{Fm\mathbf{k}} - \tilde{\theta}_{Fn\mathbf{k}}}{\epsilon^{(0)}_{m\mathbf{k}} - \epsilon^{(0)}_{n\mathbf{k}}} \tilde{\theta}_{nm\mathbf{k}} \langle u^{(0)}_{m\mathbf{k}} | \mathbf{r} \rangle \langle \mathbf{r} | u^{(0)}_{n\mathbf{k}} \rangle \langle u^{(0)}_{n\mathbf{k}} | \hat{\mathcal{H}}^{\lambda}_{\mathbf{k},\mathbf{q}} | u^{(0)}_{m\mathbf{k}} \rangle , \tag{2.65}$$

where $\mathcal{M}$ and $\mathcal{O}$ represent, respectively, the partially occupied and unoccupied set of bands.[5] Eq. (2.65) can be further simplified as

$$n^{\lambda}_{\mathbf{q}}(\mathbf{r}) = 2 \int_{\mathrm{BZ}} [d^3k] \sum_{m \in \mathcal{M}} \tilde{\theta}_{Fm\mathbf{k}} \langle u^{(0)}_{m\mathbf{k}} | \mathbf{r} \rangle \langle \mathbf{r} | \Delta u^{\lambda}_{m\mathbf{k},\mathbf{q}} \rangle , \tag{2.66}$$

where the $\Delta u^{\lambda}_{m\mathbf{k},\mathbf{q}}$ first-order wave functions are obtained from the following *modified* Sternheimer equation,

$$(\hat{H}^{(0)}_{\mathbf{k}+\mathbf{q}} + \hat{\mathcal{Q}}_{\mathbf{k}+\mathbf{q}} - \epsilon^{(0)}_{m\mathbf{k}}) | \Delta u^{\lambda}_{m\mathbf{k},\mathbf{q}} \rangle = -(\tilde{\theta}_{Fm\mathbf{k}} - \hat{\mathcal{P}}_{m\mathbf{k}+\mathbf{q}}) \hat{\mathcal{H}}^{\lambda}_{\mathbf{k},\mathbf{q}} | u^{(0)}_{m\mathbf{k},\mathbf{q}} \rangle , \tag{2.67}$$

with the following projectors

$$\hat{\mathcal{Q}}_{\mathbf{k}+\mathbf{q}} = \sum_{n \in \mathcal{M}} \alpha_n | u^{(0)}_{n\mathbf{k}+\mathbf{q}} \rangle \langle u^{(0)}_{n\mathbf{k}+\mathbf{q}} | , \qquad \hat{\mathcal{P}}_{m\mathbf{k}+\mathbf{q}} = \sum_{n \in \mathcal{M}} \beta_{mn\mathbf{k}} | u^{(0)}_{n\mathbf{k}+\mathbf{q}} \rangle \langle u^{(0)}_{n\mathbf{k}+\mathbf{q}} | , \tag{2.68}$$

---

[5] We are anticipating the notation that we will use in Chapter 3, where $\mathcal{M}$ will be referred to as the *active subspace*.

and coefficients

$$\begin{aligned}\alpha_{n\mathbf{k}} &= \max(\epsilon_{\mathrm{F}\mathbf{k}} + 3\sigma - \epsilon^{(0)}_{n\mathbf{k}}, 0),\\ \beta_{mn\mathbf{k}} &= \tilde{\theta}_{\mathrm{F}m\mathbf{k}}\tilde{\theta}_{mn\mathbf{k}} + \tilde{\theta}_{\mathrm{F}n\mathbf{k}}\tilde{\theta}_{nm\mathbf{k}} + \alpha_{n\mathbf{k}}\frac{\tilde{\theta}_{\mathrm{F}m\mathbf{k}} - \tilde{\theta}_{\mathrm{F}n\mathbf{k}}}{\epsilon^{(0)}_{m\mathbf{k}} - \epsilon^{(0)}_{n\mathbf{k}}}\tilde{\theta}_{nm\mathbf{k}}.\end{aligned} \tag{2.69}$$

It is straightforward to verify that $\beta_{mn\mathbf{k}}$ vanishes whenever one of the indices refers to an empty state; the same holds for $\alpha_{n\mathbf{k}}$. The downsides of de Gironcoli's approach are that i) because of the presence of the $\hat{\mathcal{P}}_{m\mathbf{k}+\mathbf{q}}$ projectors in Eq. (2.67), a different Sternheimer equation needs to be defined for each state m and, most importantly, ii) it lacks a straightforward variational formulation.

2.3.3 PHONON PERTURBATION

We shall characterize a phonon perturbation via the following monochromatic atomic displacements [74],

$$R^l_{\kappa\beta} \longrightarrow R^l_{\kappa\beta} + u^l_{\kappa\beta}, \quad \text{with} \quad u^l_{\kappa\beta} = \lambda^{\mathbf{q}}_{\kappa\beta} e^{i\mathbf{q}\cdot\mathbf{R}^l}, \tag{2.70}$$

where β is a Cartesian direction and $\mathbf{R}^l_\kappa = \mathbf{R}^l + \boldsymbol{\tau}_\kappa$, as introduced earlier in Sec. 2.2.6. The present perturbation is of special significance in the context of lattice dynamics. In particular, the force-constant (FC) matrix is defined as the second derivative of the total energy with respect to $\lambda^{\mathbf{q}}_{\kappa\beta}$,

$$C^{\mathbf{q}}_{\kappa\alpha,\kappa'\beta} = \frac{\partial^2 E}{\partial\lambda^{-\mathbf{q}}_{\kappa\alpha}\partial\lambda^{\mathbf{q}}_{\kappa'\beta}} = E^{\tau_{\kappa\alpha}\tau_{\kappa'\beta}}_{\mathrm{st},\mathbf{q}} + E^{\tau_{\kappa\alpha}\tau_{\kappa'\beta}}_{\mathrm{nv},\mathbf{q}}, \tag{2.71}$$

where the nonvariational contribution includes the ionic Ewald (Ew) energy, whose explicit expression can be found in Ref. [77]. Equivalently, the FC matrix can be expressed as a sum of the real-space inter-atomic forces,

$$C^{\mathbf{q}}_{\kappa\alpha,\kappa'\beta} = \sum_l C_{\kappa\alpha,\kappa'\beta}(0,l)e^{i\mathbf{q}\cdot\mathbf{R}^l}, \qquad C_{\kappa\alpha,\kappa'\beta}(0,l) = \frac{\partial^2 E}{\partial R^0_{\kappa\alpha}\partial R^l_{\kappa'\beta}}. \tag{2.72}$$

The knowledge of the full FC matrix provides the necessary information to compute phonon frequencies and modes of the crystal. Starting from the real-space equations of motion of the ions,

$$M_\kappa \ddot{u}^0_{\kappa\alpha}(t) = -\sum_{\kappa',\beta} C_{\kappa\alpha,\kappa'\beta}(0,l)u^l_{\kappa'\beta}(t), \tag{2.73}$$

one seeks a solution of the following type

$$u^l_{\kappa\alpha}(t) = U^{\mathbf{q}}_{\kappa\alpha}e^{i(\mathbf{q}\cdot\mathbf{R}^l - \omega t)}, \tag{2.74}$$

where $u^l_{\kappa\alpha}(t)$ are the ionic displacements, M_κ is the mass of the sublattice κ and ω is the phonon frequency. Substitution of Eq. (2.74) into Eq. (2.73) immediately leads to the following eigenvalue problem,

$$M_\kappa\omega^2_{\mathbf{q}}U^{\mathbf{q}}_{\kappa\alpha} = \sum_{\kappa',\beta} C^{\mathbf{q}}_{\kappa\alpha,\kappa'\beta}U^{\mathbf{q}}_{\kappa'\beta}. \tag{2.75}$$

Notice that the phonon frequencies are insensitive to the phase $e^{i\mathbf{q}\cdot\mathbf{R}^l}$ of the perturbation defined in Eq. (5.48). We will exploit this freedom to redefine the atomic displacements pattern with the phase $e^{i\mathbf{q}\cdot\mathbf{R}^l_\kappa}$, instead of the standard $e^{i\mathbf{q}\cdot\mathbf{R}^l}$, i.e.,

$$R^l_{\kappa\beta} \longrightarrow R^l_{\kappa\beta} + \lambda^{\mathbf{q}}_{\kappa\beta} e^{i\mathbf{q}\cdot\mathbf{R}^l_\kappa}. \tag{2.76}$$

The FC matrix that results from a displacement pattern defined by Eq. (2.76), which we identify with the symbol $\mathbf{\Phi}^{\mathbf{q}}$ from now on, is trivially related to the standard FC matrix given in Eq. (2.72),

$$\Phi^{\mathbf{q}}_{\kappa\alpha,\kappa'\beta} = C^{\mathbf{q}}_{\kappa\alpha,\kappa'\beta} e^{i\mathbf{q}\cdot(\tau_{\kappa'}-\tau_\kappa)}. \tag{2.77}$$

This phase choice poses great advantages in the context of spatial dispersion, as it leads to much simpler expressions in the long-wavelength limit. Of course, at $\mathbf{q}=\mathbf{0}$, we recover the standard treatment of phonons as defined in Refs. [74, 77]. In addition, the real-space IFCs remain invariant, i.e., $\Phi_{\kappa\alpha,\kappa'\beta}(0,l) = C_{\kappa\alpha,\kappa'\beta}(0,l)$.

2.3.4 ELECTRIC FIELD PERTURBATION

The electric field perturbation in crystals requires special care, as the potential associated to an external electric field is linear in space, $V(\mathbf{r}) = \boldsymbol{\mathcal{E}}\cdot\mathbf{r}$, and therefore, breaks the periodicity of the lattice. To overcome this issue, the standard treatment [74] of a homogeneous and static electric field is based on the long-wavelength response to a monochromatic scalar potential, $\varphi e^{i\mathbf{q}\cdot\mathbf{r}}$, with $\hat{\mathcal{H}}^{\varphi}_{\mathbf{q}} = -\mathbb{1} + \hat{V}^{\varphi}_{\mathbf{q}}$, where $\hat{V}^{\varphi}_{\mathbf{q}}$ is the SCF contribution [41] and the external perturbation is the unity operator at any $\mathbf{q}$ (the minus sign comes from the electron charge). The first-order wave functions are obtained from the following Sternheimer equation,

$$\hat{Q}_{\mathbf{k}+\mathbf{q}}\left(\hat{H}^{(0)}_{\mathbf{k}+\mathbf{q}} - \epsilon^{(0)}_{m\mathbf{k}}\right)\hat{Q}_{\mathbf{k}+\mathbf{q}}\,|u^{\varphi}_{m\mathbf{k},\mathbf{q}}\rangle = -\hat{Q}_{\mathbf{k}+\mathbf{q}}\left(-\mathbb{1} + \hat{V}^{\varphi}_{\mathbf{q}}\right)|u^{(0)}_{m\mathbf{k}}\rangle\,. \tag{2.78}$$

Note that the scalar potential perturbation vanishes at $\mathbf{q}=\mathbf{0}$, whereas at first order in the wave vector one obtains the first-order wave functions to an electric field perturbation,

$$|u^{\mathcal{E}_\delta}_{m\mathbf{k}}\rangle = |iu^{\varphi}_{m\mathbf{k},\delta}\rangle\,, \tag{2.79}$$

which are usually extracted from the following Sternheimer equation [74],

$$\hat{Q}_{\mathbf{k}}\left(\hat{H}^{(0)}_{\mathbf{k}} - \epsilon^{(0)}_{m\mathbf{k}}\right)\hat{Q}_{\mathbf{k}}\,|u^{\mathcal{E}_\alpha}_{m\mathbf{k}}\rangle = -\hat{Q}_{\mathbf{k}}\hat{\mathcal{H}}^{\mathcal{E}_\alpha}_{\mathbf{k}}\,|u^{(0)}_{m\mathbf{k}}\rangle\,, \tag{2.80}$$

with

$$\hat{\mathcal{H}}^{\mathcal{E}_\alpha}_{\mathbf{k}} = \sum_{m\in\mathcal{V}}\left(|i\,u^{k_\alpha}_{m\mathbf{k}}\rangle\,\langle u^{(0)}_{m\mathbf{k}}| + |u^{(0)}_{m\mathbf{k}}\rangle\,\langle i\,u^{k_\alpha}_{m\mathbf{k}}|\right) + \hat{V}^{\mathcal{E}_\alpha}, \tag{2.81}$$

where $|u^{k_\alpha}_{m\mathbf{k}}\rangle$ are the derivatives in k_α in the parallel transport gauge of the ground-state wave functions, i.e., the d/dk_α wave functions. Self-consistency is included via the SCF potential $\hat{V}^{\mathcal{E}_\alpha}$, which is independent of the wave vector $\mathbf{k}$.

The electric field perturbation allows for the calculation of various physical quantities [77], including the electronic contribution to the dielectric permittivity tensor,

$$\epsilon^{\infty}_{\alpha\beta} = \delta_{\alpha\beta} - \frac{4\pi}{\Omega}E^{\mathcal{E}_\alpha\mathcal{E}_\beta}_{\text{st}}, \tag{2.82}$$

and the so-called Born effective charges, $Z^*_{\alpha,\kappa\beta}$. These are calculated either as the first derivative of the macroscopic polarization with respect to an atomic displacement (at zero macroscopic electric field) or as the second derivative of the total energy with respect to an electric field and an atomic displacement,

$$Z^*_{\alpha,\kappa\beta} = Z_\kappa \delta_{\alpha\beta} + E_{\mathrm{st}}^{\tau_{\kappa\beta}\mathcal{E}_\alpha}, \tag{2.83}$$

where Z_κ is the (pseudo) charge of ion κ. (Note that our notation slightly differs from that of earlier references [77], where the indices in Eq. (2.83) are commonly rearranged as $Z^*_{\kappa,\alpha\beta}$.)

2.3.5 UNIFORM STRAIN PERTURBATION

Another basic type of perturbations are mechanical deformations that are applied to the crystal lattice. However, their treatment within the context of DFPT is not straightforward, even for the simplest case, i.e., a homogeneous strain. When a uniform strain (denoted from now on with the symbol $\eta_{\alpha\beta}$) is applied to a crystal lattice, the boundary conditions of the initial problem are unavoidably altered and, as a result, it becomes unclear whether one can expand the perturbed first-order wave functions in terms of the unperturbed wave functions. Therefore, the application of standard DFPT is not possible. The solution that Hamann, Wu, Rabe and Vanderbilt (HWRV) proposed [96] is to capture all the effects of the homogeneous strain within the metric tensor by working out the strain perturbation expressions in reduced coordinates. Mathematically, one expresses any real ($\mathbf{r}$) or reciprocal ($\mathbf{K} = \mathbf{k} + \mathbf{G}$) space vectors as

$$\mathbf{r} = \sum_i \mathbf{a}_i \tilde{r}_i, \qquad \mathbf{K} = \sum_i \mathbf{b}_i \tilde{K}_i, \tag{2.84}$$

where $\mathbf{a}_i$ and $\mathbf{b}_i$ are, respectively, the real and reciprocal space primitive lattice vectors [see Eq. (2.24)], and the *tilde* symbol is used to indicate reduced coordinates, which are unaffected by strain,

$$\frac{\partial \tilde{\mathbf{r}}}{\partial \eta_{\alpha\beta}} = \frac{\partial \tilde{\mathbf{K}}}{\partial \eta_{\alpha\beta}} = 0. \tag{2.85}$$

The central quantity in the HWRV approach is the metric tensor, which can be defined either in real (Ξ) or in reciprocal (Υ) space as follows,

$$\Xi_{ij} = \mathbf{a}_i \cdot \mathbf{a}_j, \qquad \Upsilon_{ij} = \mathbf{b}_i \cdot \mathbf{b}_j. \tag{2.86}$$

As noted in Ref. [96], all the terms that appear in the energy functional of the Kohn-Sham auxiliary system as defined in Eq. (2.17) depend on $\mathbf{r}$ and $\mathbf{K}$ exclusively via their scalar products. Therefore, the strain derivatives only act on the metric tensors [96],

$$\begin{aligned} \Xi_{ij}^{\eta_{\alpha\beta}} &= \frac{\partial \Xi_{ij}}{\partial \eta_{\alpha\beta}} = a_{i\alpha} a_{j\beta} + a_{i\beta} a_{j\alpha}, \\ \Upsilon_{ij}^{\eta_{\alpha\beta}} &= \frac{\partial \Upsilon_{ij}}{\partial \eta_{\alpha\beta}} = -b_{i\alpha} b_{j\beta} - b_{i\beta} b_{j\alpha}, \end{aligned} \tag{2.87}$$

where $a_{i\alpha}$ ($b_{i\alpha}$) is the α Cartesian component of the $\mathbf{a}_i$ ($\mathbf{b}_i$) lattice vector. As a consequence,

$$\frac{\partial(\mathbf{K}' \cdot \mathbf{K})}{\partial \eta_{\alpha\beta}} = \sum_{i,j} \frac{\partial \left(\tilde{K}'_i \Upsilon_{ij} \tilde{K}_j \right)}{\partial \eta_{\alpha\beta}} = \sum_{i,j} \tilde{K}'_i \Upsilon_{ij}^{\eta_{\alpha\beta}} \tilde{K}_j. \tag{2.88}$$

It is also straightforward to see that the scalar products between real and reciprocal space vectors are independent of the metric tensor,

$$\mathbf{K} \cdot \mathbf{r} = 2\pi \tilde{\mathbf{K}} \cdot \tilde{\mathbf{r}}, \tag{2.89}$$

and thus, their derivative with respect to the strain trivially vanishes. In the end, the first-order strain Hamiltonian can be written as

$$\hat{H}_{\mathbf{k},\mathbf{q}}^{\eta_{\alpha\beta}} = \frac{\partial \hat{H}_{\mathbf{k},\mathbf{q}}}{\partial \Xi_{ij}} \times \Xi_{ij}^{\eta_{\alpha\beta}} = \frac{\partial \hat{H}_{\mathbf{k},\mathbf{q}}}{\partial \Upsilon_{ij}} \times \Upsilon_{ij}^{\eta_{\alpha\beta}}. \tag{2.90}$$

The implementation of the strain perturbation as proposed by HWRV enables the calculation of the camped-ion elastic tensor,

$$\bar{\mathcal{C}}_{\alpha\beta,\gamma\delta}^{\text{HWRV}} = \frac{1}{\Omega} \frac{\partial^2 E}{\partial \eta_{\alpha\beta} \partial \eta_{\gamma\delta}} = \frac{1}{\Omega} \left(E_{\text{st}}^{\eta_{\alpha\beta}\eta_{\gamma\delta}} + E_{\text{nv}}^{\eta_{\alpha\beta}\eta_{\gamma\delta}} \right), \tag{2.91}$$

where the nonvariational term contains the second derivative of the Ewald energy with respect to the strain; explicit expressions for the latter can be found in Ref. [96]. In Eq. (2.91), the bar symbol indicates that the response is carried out at the clamped-ion (CI) level, i.e., without taking into account contributions coming from ionic relaxations. Similarly, the clamped-ion piezoelectric [97] tensor is given by

$$\bar{e}_{\alpha,\beta\gamma} = \frac{\partial P_\alpha}{\partial \eta_{\beta\gamma}} = -\frac{\partial^2 E}{\partial \mathcal{E}_\alpha \partial \eta_{\beta\gamma}} = -E_{\text{st}}^{\mathcal{E}_\alpha \eta_{\beta\gamma}}. \tag{2.92}$$

2.4 LONG-WAVE DENSITY-FUNCTIONAL PERTURBATION THEORY

Our primary interest is to describe spatial dispersion properties of crystals, which involves accessing first (or higher order) $\mathbf{q}$ derivatives of external perturbations. The phonon perturbation as described in Sec. 2.3.3 is valid at any arbitrary $\mathbf{q}$, meaning that, in principle, it is suitable as is for a long-wavelength analysis. However, it will be necessary to revisit the strain and electric field perturbations. In particular, we will explain how the HWRV approach can be generalized to account for inhomogeneous mechanical deformations, and we will discuss the finite $\mathbf{q}$ generalization of the electric field perturbation. In light of the importance of this topic, we will also dedicate a section to discussing the polarization response to an inhomogeneous perturbation, which is based on the current-density operator [98] formulation. Finally, we will return to the second-order energy functional as introduced in Sec. 2.3, and we will see that, after its reformulation as an *unconstrained* variational functional, it becomes feasible [41] to take its long-wavelength limit analytically.

2.4.1 TREATMENT OF INHOMOGENEOUS STRAIN

Although the methodology proposed by HWRV is the standard procedure that is employed in order to describe elastic and piezoelectric properties, this formulation is not suitable for a long-wavelength expansion, and therefore, turns out to be impractical for spatial dispersion. In Ref. [99], a more general theory of mechanical deformations was developed, valid at any order in the wave vector $\mathbf{q}$, by taking a monochromatic acoustic phonon as the starting point. The main idea of the metric wave approach as formulated in Ref. [99] consists in describing a mechanical deformation as an acoustic phonon perturbation in the curvilinear frame that is *comoving* with the atoms, which means that all the effects of the perturbation are reabsorbed into the first-order metric tensor, while the ions remain still in the curvilinear comoving frame.

We will loosely follow the notation of Ref. [99] and indicate the metric wave perturbation with the (β) symbol. In the laboratory frame, we describe an acoustic phonon perturbation (u_β) as a linear combination of the atomic displacements as defined in Sec. 2.3.3,

$$\hat{H}^{u_\beta}_{\mathbf{k},\mathbf{q}} = \sum_\kappa \hat{H}^{\tau_{\kappa\beta}}_{\mathbf{k},\mathbf{q}}. \tag{2.93}$$

It is shown in Ref. [99] that the following relationship hold between the metric wave and the phonon perturbations,

$$\sum_\kappa \hat{\mathcal{H}}^{\tau_{\kappa\beta}}_{\mathbf{k},\mathbf{q}} = \hat{\mathcal{H}}^{(\beta)}_{\mathbf{k},\mathbf{q}} + i\hat{H}^{(0)}_{\mathbf{k}+\mathbf{q}}\left(\hat{p}_{\mathbf{k}\beta}+\frac{q_\beta}{2}\right) - i\left(\hat{p}_{\mathbf{k}\beta}+\frac{q_\beta}{2}\right)\hat{H}^{(0)}_{\mathbf{k}}, \tag{2.94}$$

where $\hat{p}_{\mathbf{k}\beta} = -i\hat{\nabla}_\beta + k_\beta$ is the canonical momentum operator. The first term on the right hand side of Eq. (2.94) is the metric wave Hamiltonian as defined in Ref. [99]. The remaining terms describe an effective potential [100] contribution that arises as a consequence of the coordinate transformation from the laboratory frame to the curvilinear reference frame that is comoving with the crystal. (For a comprehensive analysis of this subject, see Ref. [99].) In a nutshell, the key points regarding the metric-wave perturbation that we should keep in mind for the scopes of this thesis are the following:

- At $\mathcal{O}(q^0)$ an acoustic phonon reduces to a rigid translation of the whole crystal, which cannot have any effect on the reference frame that is comoving with the crystal itself. This means that the metric-wave perturbation trivially vanishes: $\hat{H}^{(\beta)}_{\mathbf{k},\mathbf{q}} = 0$.
- At $\mathcal{O}(q^1)$ the metric tensor formulation of the uniform strain as proposed by HWRV is recovered: $\hat{\mathcal{H}}^{(\beta)}_{\mathbf{k},\delta} = i\hat{\mathcal{H}}^{\eta_{\beta\delta}}_{\mathbf{k}}$.
- At $\mathcal{O}(q^2)$ strain gradient mediated effects are described, e.g., flexoelectricity.

2.4.2 REVISITING THE ELECTRIC FIELD PERTURBATION

The drawback of the standard treatment of the electric field perturbation [74] based on the scalar potential is that it is limited to the longitudinal response, in which the homogeneous electric field and the wave vector are parallel, $\boldsymbol{\mathcal{E}} \parallel \mathbf{q}$. If the transverse components of the response functions are required, one needs to consider a vector potential, $\mathbf{A}$, instead of a scalar perturbation, φ. We shall follow the prescriptions of Ref. [41] and work in an electromagnetic gauge where the scalar potential vanishes ($\varphi = 0$) and $\boldsymbol{\mathcal{E}} = -\partial_t \mathbf{A}$. (The latter is broadly known as the "velocity gauge" as opposed to the "length gauge" discussed earlier in Sec. 2.3.4.) The response to an electric field is then computed within a time-dependent framework, using adiabatic perturbation theory. In particular, the following Sternheimer equation

$$(\hat{H}^{(0)} - \epsilon^{(0)}) |\partial_{\dot{\lambda}} n\rangle = i |\partial_{\lambda} n\rangle \tag{2.95}$$

allows the computation of the first-order adiabatic wave functions in response to $\dot{\lambda}$, $|\partial_{\dot{\lambda}} n\rangle$, once the first-order wave functions in response to the static perturbation λ are known, $|\partial_{\lambda} n\rangle$. For the present case, considering a monochromatic vector potential, $A_\beta = A^{\mathbf{q}}_\beta e^{i\mathbf{q}\cdot\mathbf{r}}$, we obtain

$$\hat{Q}_{\mathbf{k}+\mathbf{q}}(\hat{H}^{(0)}_{\mathbf{k}+\mathbf{q}} - \epsilon^{(0)}_{m\mathbf{k}})\hat{Q}_{\mathbf{k}+\mathbf{q}} |u^{\mathcal{E}_\beta}_{m\mathbf{k},\mathbf{q}}\rangle = -i |u^{A_\beta}_{m\mathbf{k},\mathbf{q}}\rangle - \hat{Q}_{\mathbf{k}+\mathbf{q}} \hat{V}^{\mathcal{E}_\beta} |u^{(0)}_{m\mathbf{k}}\rangle , \tag{2.96}$$

where the usual SCF term, $\hat{V}^{\mathcal{E}_\beta}$, has been added. Direct comparison with a conventional Sternheimer equation leads to the conclusion that the $\mathbf{A}$-field response function acts like an external perturbation [41] in the context of the electric field response,

$$\hat{Q}_{\mathbf{k}+\mathbf{q}} \hat{H}^{\mathcal{E}_\beta}_{\mathbf{k},\mathbf{q}} |u^{(0)}_{m\mathbf{k}}\rangle \longrightarrow |iu^{A_\beta}_{m\mathbf{k},\mathbf{q}}\rangle . \tag{2.97}$$

Similar to the standard treatment of the electric field perturbation as introduced in Sec. 2.3.4, where the previous knowledge of the d/dk_β wave functions was needed, the present treatment based on the vector potential requires the computation of the $|u^{A_\beta}_{m\mathbf{k},\mathbf{q}}\rangle$ wave functions. These are solutions of a Sternheimer equation, where the external perturbation is set to $\hat{H}^{A_\beta}_{\mathbf{k},\mathbf{q}} = \partial \hat{H}_{\mathbf{k},\mathbf{q}} / \partial A^{\mathbf{q}}_\beta$.

When dealing with nonlocal pseudopotentials, which is almost always the case, it is important to take special care in establishing the coupling between a generic Hamiltonian and a vector potential. In Ref. [101], Ismail-Beigi, Chang and Louie developed a rigorous and exact formalism, based on Feynman path integrals, for the coupling between a nonlocal potential to an electromagnetic vector potential $\mathbf{A}$. It can also be proven that the latter approach is equivalent to the *straight-line* formulation of Essin *et al.* [102], where the $\mathbf{A}$ dependence of the first-order Hamiltonian is exclusively included in the phase. In real-space representation,

$$H(\mathbf{r}, \mathbf{r}') = H^{(0)}(\mathbf{r}, \mathbf{r}') e^{-i \int_{\mathbf{r}'}^{\mathbf{r}} \mathbf{A} \cdot d\ell}, \tag{2.98}$$

where $H(\mathbf{r}, \mathbf{r}') = \langle \mathbf{r} | \hat{H} | \mathbf{r}' \rangle$ and the integral is taken along a straight path from $\mathbf{r}'$ to $\mathbf{r}$. Expanding Eq. (2.98) up to first order in $\mathbf{A}$,

$$H(\mathbf{r}, \mathbf{r}') \simeq H^{(0)}(\mathbf{r}, \mathbf{r}') - iH^{(0)}(\mathbf{r}, \mathbf{r}') \int_{\mathbf{r}'}^{\mathbf{r}} \mathbf{A} \cdot d\ell. \tag{2.99}$$

By carrying out the integral, one obtains the following real-space representation for the first-order Hamiltonian in response to a monochromatic vector potential,

$$H^{A_\beta}_{\mathbf{q}}(\mathbf{r}, \mathbf{r}') = -iH^{(0)}(\mathbf{r}, \mathbf{r}')(r_\beta - r'_\beta) \frac{e^{i\mathbf{q}\cdot\mathbf{r}} - e^{i\mathbf{q}\cdot\mathbf{r}'}}{i\mathbf{q} \cdot (\mathbf{r} - \mathbf{r}')}. \tag{2.100}$$

At $\mathbf{q} = \mathbf{0}$, it is easy to see that, in momentum space, Eq. (2.100) reduces to the well-known velocity operator [41],

$$\hat{H}^{A_\beta}_{\mathbf{k},\mathbf{q}=\mathbf{0}} = \frac{\partial \hat{H}^{(0)}_{\mathbf{k}}}{\partial k_\beta} = \hat{H}^{k_\beta}_{\mathbf{k}}. \tag{2.101}$$

2.4.3 TREATMENT OF INHOMOGENEOUS POLARIZATION RESPONSE

We will devote this section to describing the polarization response to a spatially varying perturbation. At the linear-response level, this can be recast as the microscopic current-density response to the time-derivative of the perturbation [103],

$$\frac{\partial P_\alpha(\mathbf{r})}{\partial \lambda^{\mathbf{q}}} = \frac{\partial J_\alpha(\mathbf{r})}{\partial \dot{\lambda}^{\mathbf{q}}}. \tag{2.102}$$

The problem here is to find a proper definition for the current-density operator that meets the following two basic criteria: i) the continuity equation must hold and ii) at $\mathbf{q} = \mathbf{0}$ the current-density operator should reduce to the (minus) velocity operator,

$$\nabla \cdot \mathbf{J}(\mathbf{r}) = -\partial_t n(\mathbf{r}), \qquad \hat{J}_{\alpha\mathbf{k},\mathbf{q}=\mathbf{0}} = -\hat{H}^{k_\alpha}_{\mathbf{k}}. \tag{2.103}$$

If the Hamiltonian is local, it can be shown that the textbook form for the current-density operator,

$$\hat{J}^{\text{loc}}_\alpha = -\frac{1}{2}\Big(|\mathbf{r}\rangle \, \langle \mathbf{r}| \, \hat{p}_\alpha + \hat{p}_\alpha \, |\mathbf{r}\rangle \, \langle \mathbf{r}| \Big) \tag{2.104}$$

nicely meets all the required physical properties, where $\hat{p}_\alpha$ is the α-th component of the momentum operator. However, in presence of nonlocal potentials, the total current-density operator acquires an additional contribution from the nonlocal (nl) terms, $\hat{J}_\alpha = \hat{J}^{\text{loc}}_\alpha + \hat{J}^{\text{nl}}_\alpha$, and Eq. (2.103) no longer holds. It was demonstrated in Ref. [98] that both conditions in Eq. (2.103) are automatically satisfied if the current-density operator is defined as the first-order Hamiltonian in response to an electromagnetic vector potential as defined in the previous section,

$$\hat{J}_{\alpha\mathbf{k},-\mathbf{q}} = -\hat{H}^{A_\alpha}_{\mathbf{k},\mathbf{q}}. \tag{2.105}$$

By employing a reciprocal-space formulation, the macroscopic polarization response at any $\mathbf{q}$ can then be defined and calculated using a primitive unit cell as [98]

$$J^{\mathbf{q}}_{\alpha,\lambda} = -2 \int_{\text{BZ}} [d^3k] \sum_{m\in\mathcal{V}} f_{m\mathbf{k}} \, \langle i u^{A_\alpha}_{m\mathbf{k},\mathbf{q}} | u^{\lambda}_{m\mathbf{k},\mathbf{q}} \rangle \,, \tag{2.106}$$

where we have defined $J^{\mathbf{q}}_{\alpha,\lambda} = \Omega \, \partial P^{\mathbf{q}}_\alpha / \partial \lambda^{\mathbf{q}}$; remember that Ω represents the volume of the unit cell.

2.4.4 ANALYTICAL LONG-WAVE EXPANSION OF THE SECOND-ORDER ENERGY

Although density-functional perturbation theory, as described in Sec. 2.3, is a really powerful tool for computing linear-response physical properties in solids, it was not until quite recently that it also became practical for computing spatially dispersive responses, i.e., computing gradients with respect to the wave vector $\mathbf{q}$. In order to understand why, consider the polarization response given in Eq. (2.106) as an illustrative example, and let's compute its first $\mathbf{q}$ gradient,

$$\left.\frac{dJ^{\mathbf{q}}_{\alpha,\lambda}}{dq_{\gamma}}\right|_{\mathbf{q}=\mathbf{0}} = -2\int_{\mathrm{BZ}}[d^3k]\sum_{m\in\mathcal{V}} f_{m\mathbf{k}}\left(\langle iu^{A_\alpha}_{m\mathbf{k},\gamma}|u^{\lambda}_{m\mathbf{k}}\rangle + \langle iu^{A_\alpha}_{m\mathbf{k}}|u^{\lambda}_{m\mathbf{k},\gamma}\rangle\right), \tag{2.107}$$

where the following notation is used,

$$|u^{\lambda}_{m\mathbf{k},\gamma}\rangle = \left.\frac{\partial\,|u^{\lambda}_{m\mathbf{k},\mathbf{q}}\rangle}{\partial q_{\gamma}}\right|_{\mathbf{q}=\mathbf{0}}, \qquad |u^{\lambda}_{m\mathbf{k}}\rangle = |u^{\lambda}_{m\mathbf{k},\mathbf{q}=\mathbf{0}}\rangle\,. \tag{2.108}$$

The principal issue here is that the $|u^{\lambda}_{m\mathbf{k},\gamma}\rangle$ wave functions are not a standard capability of publicly available DFT codes (neither are the $|u^{A_\alpha}_{m\mathbf{k},\gamma}\rangle$ wave functions, but we address this point in Appendix D). As a consequence, Eq. (2.107) seems unlikely to be useful. Is there any way of avoiding gradients of the first-order wave function responses? A simple route forward consists in repeating the desired linear-response calculation, e.g., the polarization response via Eq. (2.106), for different values of the wave vector $\mathbf{q}$ and computing the derivative via finite differences. However, the detrimental consequences of such a procedure are clear as i) it becomes computationally very demanding and ii) the final result will suffer from undesired errors coming from numerical derivatives.

To overcome these obstacles, Royo and Stengel reformulated the linear-response problem as follows. To begin with, as is customary, the second-order energy is defined as a stationary functional plus a nonvariational contribution,

$$E^{\lambda_1\lambda_2}_{\mathbf{q}} = E^{\lambda_1\lambda_2}_{\mathrm{st},\mathbf{q}} + E^{\lambda_1\lambda_2}_{\mathrm{nv},\mathbf{q}}, \tag{2.109}$$

where the form of the nonvariational term depends on the specific perturbations. The key idea of Royo and Stengel [41] is to recast the stationary contribution as finding the variational minimum of the following *unconstrained* second-order energy functional,

$$E^{\lambda_1\lambda_2}_{\mathrm{st},\mathbf{q}} = 2\int_{\mathrm{BZ}}[d^3k]E^{\lambda_1\lambda_2}_{\mathbf{k},\mathbf{q}} + \int_{\Omega}\int n^{\lambda_1 *}_{\mathbf{q}}(\mathbf{r})K_{\mathbf{q}}(\mathbf{r},\mathbf{r}')n^{\lambda_2}_{\mathbf{q}}(\mathbf{r}')\,d^3r\,d^3r', \tag{2.110}$$

where $K_{\mathbf{q}}(\mathbf{r},\mathbf{r}') = K_{\mathrm{Hxc}}(\mathbf{r},\mathbf{r}')e^{i\mathbf{q}\cdot(\mathbf{r}'-\mathbf{r})}$ is the phase-corrected Coulomb and exchange-correlation kernel. The integrand in the first term of Eq. (2.110) is given by

$$\begin{aligned} E^{\lambda_1\lambda_2}_{\mathbf{k},\mathbf{q}} = &\sum_{m\in\mathcal{V}} f_{m\mathbf{k}}\,\langle u^{\lambda_1}_{m\mathbf{k},\mathbf{q}}|\,(\hat{H}^{(0)}_{\mathbf{k}+\mathbf{q}} + a\hat{P}_{\mathbf{k}+\mathbf{q}} - \epsilon^{(0)}_{m\mathbf{k}})\,|u^{\lambda_2}_{m\mathbf{k},\mathbf{q}}\rangle \\ &+ \sum_{m\in\mathcal{V}} f_{m\mathbf{k}}\,\langle u^{\lambda_1}_{m\mathbf{k},\mathbf{q}}|\,\hat{Q}_{\mathbf{k}+\mathbf{q}}\hat{H}^{\lambda_2}_{\mathbf{k},\mathbf{q}}\,|u^{(0)}_{m\mathbf{k}}\rangle \\ &+ \sum_{m\in\mathcal{V}} f_{m\mathbf{k}}\,\langle u^{(0)}_{m\mathbf{k}}|\,(\hat{H}^{\lambda_1}_{\mathbf{k},\mathbf{q}})^{\dagger}\hat{Q}_{\mathbf{k}+\mathbf{q}}\,|u^{\lambda_2}_{m\mathbf{k},\mathbf{q}}\rangle\,. \end{aligned} \tag{2.111}$$

Notice the explicit inclusion of the conduction band projectors in the second and third lines of Eq. (2.111), which enforces orthogonality between the first-order wave functions and the valence manifold, without the need of incorporating additional constraints. These projectors are also present in the first-order electron densities,

$$n^{\lambda}_{\mathbf{q}}(\mathbf{r}) = 2\int_{\mathrm{BZ}}[d^3k]\sum_{m\in\mathcal{V}} f_{m\mathbf{k}}\,\langle u^{(0)}_{m\mathbf{k}}|\mathbf{r}\rangle\,\langle\mathbf{r}|\,\hat{Q}_{\mathbf{k}+\mathbf{q}}\,|u^{\lambda}_{m\mathbf{k},\mathbf{q}}\rangle\,. \tag{2.112}$$

The stationary condition on the first-order wave functions results in the following Sternheimer equation, as proposed by Baroni *et al.* [104],

$$(\hat{H}^{(0)}_{\mathbf{k}+\mathbf{q}} + a\hat{P}_{\mathbf{k}+\mathbf{q}} - \epsilon^{(0)}_{m\mathbf{k}})\,|u^{\lambda}_{m\mathbf{k},\mathbf{q}}\rangle = -\hat{Q}_{\mathbf{k}+\mathbf{q}}\hat{\mathcal{H}}^{\lambda}_{\mathbf{k},\mathbf{q}}\,|u^{(0)}_{m\mathbf{k}}\rangle\,, \tag{2.113}$$

where the parameter a is a constant with dimension of energy that ensures that the left-hand side of Eq. (2.113) does not become singular and that the second-order energy functional of Eq. (2.111) is stable.

It should be noted that both the constrained second-order energy functional as initially proposed by Gonze, Eq. (2.55), and the minimization of the unconstrained functional given by Eq. (2.111) are equivalent and lead to the exact same solution. However, we shall stick to Eq. (2.111) in the following, as it poses great advantages in light of performing a long-wavelength expansion. The are two key reasons for this. First, note that in the constrained variational formulation proposed by Gonze, the second-order energy functional is minimized under the constraint that the first-order wave functions are orthogonal to the valence manifold [74],

$$\langle u^{(0)}_{m\mathbf{k}+\mathbf{q}}|u^{\lambda}_{n\mathbf{k},\mathbf{q}}\rangle = 0, \quad \forall n,m\in\mathcal{V}, \tag{2.114}$$

which is the finite $\mathbf{q}$ counterpart of Eq. (2.56). Taking the $\mathbf{q}$ derivative of the constrained second-order energy functional is far from obvious, as the ground-state Bloch functions evaluated at $\mathbf{k}+\mathbf{q}$, $|u^{(0)}_{m\mathbf{k}+\mathbf{q}}\rangle$, suffer from the typical phase indeterminacy. Conversely, in the unconstrained variational formulation proposed by Royo and Stengel, the only objects that explicitly depend on the wave vector $\mathbf{q}$ are operators, which are gauge-independent mathematical objects without the inherent phase indeterminacy of the Bloch functions. Note that the dependence on $\mathbf{q}$ of the first-order wave functions, $|u^{\lambda}_{m\mathbf{k},\mathbf{q}}\rangle$, arises due to the stationary condition imposed on them, since they should be regarded as trial solutions to the variational problem. The latter implies that they depend on $\mathbf{q}$ only implicitly. Second, the wave vector $\mathbf{q}$ can be regarded as a perturbation parameter in the unconstrained second-order energy functional, meaning that it allows the application of the well-established machinery of standard perturbation theory and, in particular, the $2n+1$ theorem.

2.4.4.1 *First order in* $\mathbf{q}$

At first-order in $\mathbf{q}$, straightforward application of the $2n+1$ theorem leads to

$$E^{\lambda_1\lambda_2}_{\gamma} = \left.\frac{dE^{\lambda_1\lambda_2}_{\mathbf{q}}}{dq_{\gamma}}\right|_{\mathbf{q}=\mathbf{0}} = \left.\frac{\partial E^{\lambda_1\lambda_2}_{\mathbf{q}}}{\partial q_{\gamma}}\right|_{\mathbf{q}=\mathbf{0}}, \tag{2.115}$$

which means that the total derivative in $\mathbf{q}$ coincides with the partial derivative of the second-order energy functional, where the first-order wave functions, $|u^{\lambda}_{m\mathbf{k},\mathbf{q}}\rangle$, are excluded from differentiation. This implies that the knowledge of the wave function responses to uniform ($\mathbf{q} = \mathbf{0}$) field perturbations, $|u^{\lambda}_{m\mathbf{k}}\rangle$, is enough to access first-order spatial dispersion coefficients. We write the first $\mathbf{q}$ gradient of the second-order energy as

$$E^{\lambda_1\lambda_2}_{\gamma} = E^{\lambda_1\lambda_2}_{\mathrm{st},\gamma} + E^{\lambda_1\lambda_2}_{\mathrm{nv},\gamma}. \tag{2.116}$$

The stationary part reads as [41]

$$E^{\lambda_1\lambda_2}_{\mathrm{st},\gamma} = 2\int_{\mathrm{BZ}} [d^3k] E^{\lambda_1\lambda_2}_{\mathbf{k},\gamma} + \int_{\Omega}\int n^{\lambda_1 *}(\mathbf{r}) K_{\gamma}(\mathbf{r},\mathbf{r}') n^{\lambda_2}\, d^3r\, d^3r', \tag{2.117}$$

where

$$K_{\gamma}(\mathbf{r},\mathbf{r}') = \left.\frac{\partial K_{\mathbf{q}}(\mathbf{r},\mathbf{r}')}{\partial q_{\gamma}}\right|_{\mathbf{q}=\mathbf{0}} \tag{2.118}$$

represents the first $\mathbf{q}$ gradient of the Hxc kernel, and the quantity that needs to be integrated over the whole BZ in Eq. (2.117) is given by

$$\begin{aligned} E^{\lambda_1\lambda_2}_{\mathbf{k},\gamma} = {} & \sum_{m\in\mathcal{V}} f_{m\mathbf{k}} \langle u^{\lambda_1}_{m\mathbf{k}}| \hat{H}^{k_\gamma}_{\mathbf{k}} |u^{\lambda_2}_{m\mathbf{k}}\rangle \\ & - \sum_{m,n\in\mathcal{V}} f_{m\mathbf{k}} \Big(\langle u^{\lambda_1}_{m\mathbf{k}}|u^{k_\gamma}_{n\mathbf{k}}\rangle \langle u^{(0)}_{n\mathbf{k}}| \hat{\mathcal{H}}^{\lambda_2}_{\mathbf{k}} |u^{(0)}_{m\mathbf{k}}\rangle + \langle u^{(0)}_{m\mathbf{k}}| (\hat{\mathcal{H}}^{\lambda_1}_{\mathbf{k}})^{\dagger} |u^{(0)}_{n\mathbf{k}}\rangle \langle u^{k_\gamma}_{n\mathbf{k}}|u^{\lambda_2}_{m\mathbf{k}}\rangle \Big) \\ & + \sum_{m\in\mathcal{V}} f_{m\mathbf{k}} \Big(\langle u^{\lambda_1}_{m\mathbf{k}}| \hat{H}^{\lambda_2}_{\mathbf{k},\gamma} |u^{(0)}_{m\mathbf{k}}\rangle + \langle u^{(0)}_{m\mathbf{k}}| (\hat{H}^{\lambda_1}_{\mathbf{k},\gamma})^{\dagger} |u^{(0)}_{m\mathbf{k}}\rangle \Big). \end{aligned} \tag{2.119}$$

The new symbol appearing in the last equation is

$$\hat{H}^{\lambda}_{\mathbf{k},\gamma} = \left.\frac{\partial \hat{H}^{\lambda}_{\mathbf{k},\mathbf{q}}}{\partial q_{\gamma}}\right|_{\mathbf{q}=\mathbf{0}}. \tag{2.120}$$

The analytical long-wave methodology presented here has been successfully applied, e.g., in the context of flexoelectricity: it is now possible to compute the complete flexoelectric tensor, both the electronic [41] and lattice mediated [44] contributions, completely from first-principles. It has been also proven to be very useful for the computation of the dynamical quadrupoles [41].

We have deliberately excluded from our analysis an important aspect: for the long-wavelength expansion we have considered to be true, the second-order energy must be an analytic function of $\mathbf{q}$ around $\mathbf{q} = \mathbf{0}$. However, the Coulomb potential diverges in the $\mathbf{q} \to 0$ limit. In insulators, the latter results in a nonanalytic contribution to the response that is caused by long-range electric fields. Prior to the long-wave expansion, those macroscopic electric fields must be suppressed, which corresponds physically to imposing *short-circuit* [103] electrical boundary conditions. However, there is more than one way of doing so: this ambiguity is the cause of the well-known *potential energy reference* [105, 106] issue inherent to spatial dispersion in insulators. (More details are given in the Appendix in Sec. A.1 and Sec. B.2.)

Our original work starts in the next chapter, where we generalize the long-wavelength DFPT methodology to metals.

3

ENSEMBLE DFPT: SPATIAL DISPERSION IN METALS

In this chapter we generalize the analytical long-wavelength DFPT methodology, which was introduced at the end of the previous chapter, to metals. Through this approach, we were able to overcome some of the long-standing methodological challenges that have characterized most earlier attempts at calculating spatial dispersion in metals, namely the treatment of SCF fields and cumbersome sums over unoccupied states.

Ideally, one would want to directly apply the analytical long-wave DFPT methodology of Sec. 2.4.4 to an energy functional that describes a metallic system. However, this unavoidably requires working within a *variational* framework. As previously discussed in Sec. 2.3.2, the methodology proposed by de Gironcoli lacks a straightforward variational formulation, which prevents the application of the $2n+1$ theorem, essential for our scopes. It is therefore of the utmost importance to figure out an alternative starting point.

Here we develop a general perturbative framework for metallic systems by using the ensemble density-functional theory formalism of Marzari, Vanderbilt and Payne (MVP) [107] as a conceptual basis. The invariance of the latter with respect to unitary transformations within the *active subspace* allows us to write an unconstrained second-order energy functional at an arbitrary $\mathbf{q}$ vector, which is stationary both in the first-order wave functions and in the first-order occupation matrix. Then, mimicking the well-established procedure that is employed with insulators [41], the wave vector $\mathbf{q}$ is treated as a perturbation parameter, which provides (via the $2n+1$ theorem) an analytic long-wavelength expansion of the second-order energy functional at any desired order. Our methodology brings the first-principles calculation of spatial dispersion properties in metals to the same level of accuracy and efficiency as in insulators, i.e., only the knowledge of uniform field perturbations is required to access first-order spatial dispersion coefficients.

Before moving forward, we would like to mention Ref. [108], where Gonze *et al.* developed a variational formulation of density functional perturbation theory for metals, essentially at the same time as we did. (We became aware of their work after submission of our manuscript.) Even if they reach the same formal conclusions for the second-order energy functional at finite $\mathbf{q}$, we will see shortly that our *unconstrained* formulation proves to be essential for a long-wavelength expansion, and therefore, for spatial dispersion.

This chapter is organized as follows. First of all, we summarize the fundamentals of ensemble density-functional theory as described in Ref. [107] by Marzari, Vanderbilt and Payne. Next, we perform a perturbation expansion of the ensemble DFT energy functional of MVP, obtaining an unconstrained second-order energy functional of the first-order wave functions and occupation matrices at an arbitrary wave vector $\mathbf{q}$. In Sec. 3.3, following the guidelines of Ref. [41], we take the first-order long-wavelength expansion of the aforementioned second-order energy. In Sec. 3.4, we validate our methodology by computing the spatial dispersion coefficients of zone-center optical phonons of selected crystal structures. We conclude this chapter in Sec. 3.5, where we discuss both the strengths and limitations of the current formalism and give a brief outlook.

3.1 MVP'S FORMULATION OF ENSEMBLE DFT

Here we recap the basics of ensemble DFT as formulated by Marzari, Vanderbilt and Payne [107], which can be regarded as a generalization of Mermin's formulation of finite temperature DFT [109]. The key assumption of MVP consists in adopting a matrix representation for the occupancies (f_{mn}) via the following [107] energy functional,[1]

$$\begin{aligned} E[\{\psi_m\},\{f_{mn}\}] = &\sum_{m,n\in\mathcal{M}} f_{nm} \langle\psi_m| \,(\hat{T}+\hat{V}_{\text{ext}})\, |\psi_n\rangle + E_{\text{Hxc}}[n] - \sigma S[\{f_{mn}\}] \\ &- \sum_{m,n\in\mathcal{M}} \Lambda_{mn} \left(\langle\psi_m|\psi_n\rangle - \delta_{mn} \right) - \mu \left(\mathrm{Tr}\,(\mathbf{f}) - N \right). \end{aligned} \tag{3.1}$$

Here, $\hat{T}$ is the kinetic energy operator, $\hat{V}_{\text{ext}}$ refers to the atomic pseudopotentials and E_{Hxc} is the Hartree exchange and correlation energy, which is a functional of the electron density,

$$n(\mathbf{r}) = \sum_{m,n\in\mathcal{M}} f_{nm} \langle\psi_m|\mathbf{r}\rangle \, \langle\mathbf{r}|\psi_n\rangle \,. \tag{3.2}$$

In Eq. (3.1), σ and S are, respectively, the smearing parameter and the entropy. The Lagrange multipliers Λ_{mn} and μ enforce the orthonormality of wave functions and particle number conservation, where N is the total number of electrons. Sums are carried out for a number of states M with nonzero occupancies that belong to the *active subspace*, $\mathcal{M}$. As long that the occupancies of the highest energy states within this *active subspace* are vanishingly small, further increasing M does not produce any change in the total energy or in any other observable derived from Eq. (3.1).

If a diagonal representation for the occupation matrix $\mathbf{f}$ is enforced at all times, Eq. (3.1) reduces to the standard formulation [110–112] of Mermin's approach. As the system evolves adiabatically in parameter space, however, the numerical integration of the resulting electronic equations of motion suffers from severe ill-conditioning issues [111]. Indeed, whenever level crossings occur near the Fermi surface, the orbitals need to abruptly change in character (via a subspace rotation) along the trajectory due to the explicit imposition of the Hamiltonian gauge. (Sharp symmetry-protected crossings are the most catastrophic, as they imply a discontinuity in the adiabatic evolution of the orbitals involved.) This is obviously not an issue in insulators, where the energy is invariant with respect to arbitrary unitary transformations within the occupied manifold.

The breakthrough idea of ensemble density-functional theory consists in allowing for nonzero off-diagonal elements of the occupation matrix (f_{mn}), and to treat them together with the wave functions (ψ_m) as variational parameters. By doing so, it is

---

[1] To avoid overcomplicating the notation, we will initially avoid explicit reference to the quantum number $\mathbf{k}$.

easy to prove that Eq. (3.1) is *covariant* under any unitary rotation $\mathbf{U}$ of the following type [107],

$$\begin{aligned} \mathbf{f}' &= \mathbf{U}\mathbf{f}\mathbf{U}^\dagger, \\ |\psi_m\rangle' &= \sum_{n\in\mathcal{M}} U^\dagger_{mn} |\psi_n\rangle, \end{aligned} \tag{3.3}$$

which implies that one is no longer forced to stick to the Hamiltonian gauge. This way, the problematic [113, 114] subspace rotations can be conveniently reabsorbed into f_{mn}.

Before moving forward, it is noteworthy to observe the various forms the entropy can acquire depending on the smearing scheme that is chosen. To see this, consider the stationary conditions on the energy functional given in Eq. (3.1),

$$\begin{aligned} \frac{\delta E}{\delta f_{nm}} = 0 \quad &\longrightarrow \quad h_{mn} - \mu\delta_{nm} = \sigma\frac{\partial S}{\partial f_{nm}}, \\ \frac{\delta E}{\delta \langle\psi_m|} = 0 \quad &\longrightarrow \quad \sum_{m\in\mathcal{M}} \left(f_{nm}\hat{\mathcal{H}}|\psi_n\rangle - \Lambda_{nm}|\psi_n\rangle\right) = 0, \end{aligned} \tag{3.4}$$

where we have defined $h_{mn} = \langle\psi_m|\hat{H}|\psi_n\rangle$ and μ plays the role of the Fermi energy. The first stationary condition in Eq. (3.4) provides a formal link between the functional form of the entropy with respect to the occupation matrix and the ground-state energy eigenvalues of the Hamiltonian, h_{mn}. All the matrices appearing in Eq. (3.4) commute, and consequently, it can be solved in the diagonal gauge, where it reduces to the usual equation for the occupation numbers,

$$\epsilon_m - \mu = \sigma\frac{\partial S}{\partial f_m}, \tag{3.5}$$

with $\epsilon_m = h_{mm}$. Following the Kohn-Sham scheme, a non-interacting picture is assumed, which implies that [107] the total entropy can be written as a sum of individual contributions, $S = \sum_m S_m$. By combining Eq. (3.5) with the definition of the smeared occupation function, Eq. (2.37), the entropy can be expressed as

$$S_m = -s\int_{-\infty}^{\frac{\mu-\epsilon_m}{\sigma}} t\tilde{\delta}(t)\,dt, \tag{3.6}$$

where s is, as usual, the spin multiplicity. It can be readily observed that a Gaussian smearing [see Eq. (2.38)] generates the following Gaussian entropy,

$$S_m = \frac{1}{\sqrt{\pi}}e^{-\left(\frac{\mu-\epsilon_m}{\sigma}\right)^2}. \tag{3.7}$$

Had we stick to the Fermi-Dirac smearing, we would have obtained the well-known result for the entropy as a function of the occupation numbers, $S_m(f) = f_m\ln(f_m) + (1-f_m)\ln(1-f_m)$. The price one needs to pay for going beyond the Fermi-Dirac distribution function is that the entropy is no longer a function of the occupation numbers, but of the energy eigenvalues, ϵ_m.

3.2 PERTURBATION EXPANSION

We now assume that the Hamiltonian of the system under study depends on some adiabatic parameter λ and apply the time-independent perturbation theory as described in Sec. 2.3 to the energy functional given in Eq. (3.1). The parametric dependence of the Hamiltonian propagates to the wave functions and to the occupation matrix [see Eq. (2.45) and (2.46)],

$$f_{mn}(\lambda) = f^{(0)}_{mn} + \lambda f^{(1)}_{mn} + \dots \tag{3.8}$$

The second-order energy can be recast as a constrained variational minimum of a functional that depends on both the first-order wave functions, $|\psi^{(1)}_m\rangle$, and the first-order occupation matrix, $f^{(1)}_{mn}$. We find

$$\begin{aligned} E^{(2)}_{\text{con}} =& 2 \sum_{m,n\in\mathcal{M}} \left(f^{(0)}_{mn} \langle\psi^{(1)}_n| \hat{H}^{(0)} |\psi^{(1)}_m\rangle - \Lambda^{(0)}_{mn} \langle\psi^{(1)}_n|\psi^{(1)}_m\rangle \right) \\ &+ 2 \sum_{m,n\in\mathcal{M}} f^{(0)}_{mn} \left(\langle\psi^{(1)}_n| \hat{H}^{(1)} |\psi^{(0)}_m\rangle + \langle\psi^{(0)}_n| \hat{H}^{(1)} |\psi^{(1)}_m\rangle \right) \\ &+ 2 \sum_{m,n\in\mathcal{M}} f^{(1)}_{mn} \langle\psi^{(0)}_n| \hat{H}^{(1)} |\psi^{(0)}_m\rangle - \sigma \sum_{m,n,l,k\in\mathcal{M}} f^{(1)}_{mn} \frac{\partial^2 S}{\partial f^{(0)}_{nm} \partial f^{(0)}_{lk}} f^{(1)}_{lk} \\ &+ \int_\Omega \int n^{(1)}(\mathbf{r}) K_{\text{Hxc}}(\mathbf{r},\mathbf{r}') n^{(1)}(\mathbf{r}')\, d^3r\, d^3r' + \sum_{m,n\in\mathcal{M}} f^{(0)}_{mn} \langle\psi^{(0)}_n| \hat{H}^{(2)} |\psi^{(0)}_m\rangle\,, \end{aligned} \tag{3.9}$$

where the Lagrange multipliers $\Lambda^{(0)}_{mn}$ are related to the matrix elements of the ground-state Hamiltonian, $\Lambda^{(0)}_{mn} = f^{(0)}_{nm} \langle\psi^{(0)}_m| \hat{H}^{(0)} |\psi^{(0)}_n\rangle$, with $f^{(0)}_{nm} = f_m \delta_{nm}$. The constrained energy functional is minimized under the following condition,

$$\langle\psi^{(0)}_m|\psi^{(1)}_n\rangle = 0, \quad \forall m,n \in \mathcal{M}. \tag{3.10}$$

There is a new term appearing in the third line of Eq. (3.9), which is the second derivative of the entropy with respect to the occupation matrix. By assuming a diagonal representation for the unperturbed occupation matrix, one can show that the following relationship holds,

$$\sigma \frac{\partial^2 S}{\partial f^{(0)}_{mn} \partial f^{(0)}_{kl}} = \frac{\delta_{mk}\delta_{nl}}{\bar{f}_{mn}}, \tag{3.11}$$

where the matrix $\bar{f}_{mn} \equiv G(\epsilon_m, \epsilon_n)$ is defined as [114]

$$G(x,y) = \begin{cases} \frac{f(x)-f(y)}{x-y} & , \quad \text{if } x \neq y, \\ \frac{1}{2}\left(\frac{\partial f(x)}{\partial x} + \frac{\partial f(y)}{\partial y} \right) & , \quad \text{if } x = y. \end{cases} \tag{3.12}$$

Here, $f_m \equiv f(\epsilon_m)$ represents the occupation function. In our numerical implementation, we set a finite tolerance to test the equality of x and y, hence the need for the symmetrization in the second line of Eq. (3.12). The stationary condition on the first-order occupation matrix allows us to find a solution for $f^{(1)}_{mn}$,

$$\frac{\delta E^{(2)}}{\delta f^{(1)}_{mn}} = 0 \quad \longrightarrow \quad f^{(1)}_{mn} = \bar{f}_{mn} \langle\psi^{(0)}_m| \hat{\mathcal{H}}^{(1)} |\psi^{(0)}_n\rangle\,. \tag{3.13}$$

3.2.1 UNCONSTRAINED VARIATIONAL FORMULATION

At this stage, in complete analogy with the insulating case and with the forthcoming goal of performing an analytical long-wavelength expansion of the energy functional, we write the second-order energy as the following unconstrained variational functional,

$$
\begin{aligned}
E^{(2)} =& 2 \sum_{m\in\mathcal{M}} f_m \langle\psi_m^{(1)}| \, (\hat{H}^{(0)} + a\hat{P} - \epsilon_m^{(0)}) \, |\psi_m^{(1)}\rangle \\
&+ 2 \sum_{m\in\mathcal{M}} f_m \left(\langle\psi_m^{(1)}| \, \hat{Q}\hat{H}^{(1)} \, |\psi_m^{(0)}\rangle + \text{c.c.} \right) \\
&+ 2 \sum_{m\in\mathcal{M}} f_{mn}^{(1)} \langle\psi_n^{(0)}| \, \hat{H}^{(1)} \, |\psi_m^{(0)}\rangle - \sum_{m,n\in\mathcal{M}} f_{mn}^{(1)} \frac{\epsilon_n^{(0)} - \epsilon_m^{(0)}}{f_n - f_m} f_{nm}^{(1)} \\
&+ \int_\Omega \int n^{(1)}(\mathbf{r}) K_{\text{Hxc}}(\mathbf{r},\mathbf{r}') n^{(1)}(\mathbf{r}') \, d^3r \, d^3r' + \sum_{m\in\mathcal{M}} f_m \langle\psi_m^{(0)}| \, \hat{H}^{(2)} \, |\psi_m^{(0)}\rangle ,
\end{aligned}
\tag{3.14}
$$

where the operators

$$
\hat{P} = \sum_{m\in\mathcal{M}} |\psi_m^{(0)}\rangle \, \langle\psi_m^{(0)}| , \quad \hat{Q} = \mathbb{1} - \hat{P} \tag{3.15}
$$

are projectors onto and out of the active subspace, respectively. Note that, unlike in the insulating case, $\hat{P}$ does not correspond to the ground-state density operator. The first-order electron density is given by

$$
n^{(1)}(\mathbf{r}) = \sum_{m\in\mathcal{M}} f_m \left(\langle\psi_m^{(1)}| \, \hat{Q} \, |\mathbf{r}\rangle \, \langle\mathbf{r}|\psi_m^{(0)}\rangle + \text{c.c.} \right) + \sum_{m,n\in\mathcal{M}} f_{mn}^{(1)} \langle\psi_n^{(0)}|\mathbf{r}\rangle \, \langle\mathbf{r}|\psi_m^{(0)}\rangle . \tag{3.16}
$$

It is interesting to observe that the stationary condition on the first-order wave functions leads to a standard Sternheimer equation as defined by Baroni *et al.* [104] [see Eq. (2.113)]. This implies that, from a computational standpoint, the first-order wave functions for metals are calculated in an identical manner to those for insulators; i.e., the subroutine that solves the Sternheimer problem does not even need to know that the system is metallic or not. The formalism presented in this section therefore solves the two weaknesses of de Gironcoli's approach that were highlighted in Sec. 2.3.2: apart from the obvious advantage of having a variational formulation, the first-order wave functions are extracted from Eq. (2.113), which avoids constructing m-dependent projectors for each state, $|\psi_m^{(1)}\rangle$. A more formal link to de Gironcoli's approach will be made in subsequent subsections, once the nonstationary expressions for the present methodology have been derived.

3.2.2 NONSTATIONARY FORMULAS

Simpler nonstationary expressions for the second-order energy can be obtained by plugging the stationary conditions for $f_{mn}^{(1)}$ and $|\psi_m^{(1)}\rangle$ into Eq. (3.14),

$$
\begin{aligned}
E^{(2)} =& \sum_{m\in\mathcal{M}} f_m \left(\langle\psi_m^{(1)}| \, \hat{H}^{(1)} \, |\psi_m^{(0)}\rangle + \text{c.c.} \right) + \sum_{m,n\in\mathcal{M}} f_{mn}^{(1)} \langle\psi_n^{(0)}| \, \hat{H}^{(1)} \, |\psi_m^{(0)}\rangle \\
&+ \sum_{m\in\mathcal{M}} f_m \langle\psi_m^{(0)}| \, \hat{H}^{(2)} \, |\psi_m^{(0)}\rangle .
\end{aligned}
\tag{3.17}
$$

Interestingly, the only difference between the nonstationary expression of the second-order energy, Eq. (3.17), and the first-order electron density, Eq. (3.16), is that the first-order external perturbation, $\hat{H}^{(1)}$, appearing in the second-order energy is replaced with the operator $|\mathbf{r}\rangle\langle\mathbf{r}|$ in the first-order electron density expression. A more compact version of the latter quantities can be achieved by writing both the second-order energy and the first-order electron density as a trace,

$$\begin{aligned} E^{(2)} &= \mathrm{Tr}\left(\hat{\rho}^{(1)}\hat{H}^{(1)} + \hat{\rho}^{(0)}\hat{H}^{(2)}\right), \\ n^{(1)}(\mathbf{r}) &= \mathrm{Tr}\left(\hat{\rho}^{(1)}|\mathbf{r}\rangle\langle\mathbf{r}|\right), \end{aligned} \tag{3.18}$$

where the ground-state density operator is given by

$$\hat{\rho}^{(0)} = \sum_{m\in\mathcal{M}} |\psi_m^{(0)}\rangle f_m \langle\psi_m^{(0)}|, \tag{3.19}$$

and we have defined the *first-order density operator* as

$$\hat{\rho}^{(1)} = \sum_{m\in\mathcal{M}} \left(|\psi_m^{(0)}\rangle f_m \langle\psi_m^{(1)}| + \text{c.c.}\right) + \sum_{m,n\in\mathcal{M}} |\psi_m^{(0)}\rangle f_{mn}^{(1)} \langle\psi_n^{(0)}|. \tag{3.20}$$

3.2.3 RELATION TO DE GIRONCOLI'S APPROACH

The formalism that we have presented so far in this chapter naturally recovers de Gironcoli's approach, which was briefly summarized in Sec. 2.3.2. To see this, it is useful to introduce the following *tilded* first-order wave functions,

$$|\tilde{\psi}_m^{(1)}\rangle = |\psi_m^{(1)}\rangle + \frac{1}{2f_m}\sum_{n\in\mathcal{M}} |\psi_n^{(0)}\rangle f_{mn}^{(1)}. \tag{3.21}$$

The first-order density matrix is then given by

$$\hat{\rho}^{(1)} = \sum_{m\in\mathcal{M}} |\psi_m^{(0)}\rangle f_m \langle\tilde{\psi}_m^{(1)}| + \text{c.c.}, \tag{3.22}$$

which, in turn, exactly reduces to our Eq. (3.20). The nonstationary second-order energy and the first-order electron density can then be expressed more compactly using this notation as

$$\begin{aligned} E^{(2)} &= \sum_{m\in\mathcal{M}} f_m \left(\langle\tilde{\psi}_m^{(1)}|\hat{H}^{(1)}|\psi_m^{(0)}\rangle + \text{c.c.}\right) + \sum_{m\in\mathcal{M}} f_m \langle\psi_m^{(0)}|\hat{H}^{(2)}|\psi_m^{(0)}\rangle, \\ n^{(1)} &= \sum_{m\in\mathcal{M}} f_m \langle\tilde{\psi}_m^{(1)}|\mathbf{r}\rangle\langle\mathbf{r}|\psi_m^{(0)}\rangle + \text{c.c.} \end{aligned} \tag{3.23}$$

Those expressions for the first-order electron density and the second-order energy are equivalent to those obtained by de Gironcoli [95]. (In fact, our tilded first-order wave functions defined here are directly related to the "Δ" first-order wave functions of de Gironcoli's methodology as introduced in Sec. 2.3.2. Note that the projection of Eq. (2.67) into the space perpendicular to the *active subspace* immediately gives rise to a Sternheimer equation as that obtained by imposing the stationary condition on the first-order wave functions in our variational second-order energy functional.) Interestingly, our expressions given in Eq. (3.23) resemble the ones that are commonly employed in insulators. Here, however, the *tilded* first-order wave functions take into account the subspace unitary rotations in the active subspace, via the second term on the right-hand side of Eq. (3.21); this term is absent in insulators.

3.2.4 PARAMETRIC DERIVATIVE OF OPERATORS

The first-order electron density operator given by Eq. (3.20) is special case of a more general rule for differentiating operators along adiabatic paths in parameter space. We establish this rule in the following, since it is key to the long-wavelength expansion of the second-order energy functional that we aim to perform in the next section. Consider an operator of the following form,

$$\hat{O} = \sum_{m\in\mathcal{M}} |\psi_m^{(0)}\rangle\, h(\epsilon_m^{(0)})\, \langle\psi_m^{(0)}| , \tag{3.24}$$

where $h(\epsilon_m^{(0)})$ is a real and differentiable function of the ground-state energy eigenvalues of the system, $\epsilon_m^{(0)}$. The derivative of $\hat{O}$ with respect to an adiabatic parameter λ is then given by

$$\begin{aligned}\frac{\partial\hat{O}}{\partial\lambda} = &\sum_{m\in\mathcal{M}} \Big(|\psi_m^{(0)}\rangle\, h(\epsilon_m^{(0)})\, \langle\psi_m^{\lambda}| + \text{c.c.}\Big) \\ &+ \sum_{m,n\in\mathcal{M}} \mathcal{G}(\epsilon_m^{(0)},\epsilon_n^{(0)})\, |\psi_n^{(0)}\rangle\, \langle\psi_n^{(0)}|\, \mathcal{H}^{\lambda}\, |\psi_m^{(0)}\rangle\, \langle\psi_m^{(0)}| ,\end{aligned} \tag{3.25}$$

where $\mathcal{G}$ is defined as in our Eq. (3.12), only replacing the occupation function f with h therein. This result essentially corresponds to Eq. (20) of Ref. [115], but recast within a DFPT context. Its proof rests on the following two rules,

$$\begin{aligned}\frac{\partial h(\epsilon_m^{(0)})}{\partial\lambda} &= \frac{\partial h(\epsilon_m^{(0)})}{\partial\epsilon_m^{(0)}}\, \langle\psi_m^{(0)}|\, \hat{\mathcal{H}}^{\lambda}\, |\psi_m^{(0)}\rangle , \\ \frac{\partial\, |\psi_m^{(0)}\rangle}{\partial\lambda} &= |\psi_m^{\lambda}\rangle + \sum_{n\in\mathcal{M}}{}^{'}\, |\psi_n^{(0)}\rangle\, \frac{\langle\psi_n^{(0)}|\, \hat{\mathcal{H}}^{\lambda}\, |\psi_m^{(0)}\rangle}{\epsilon_m^{(0)} - \epsilon_n^{(0)}} ,\end{aligned} \tag{3.26}$$

where the *prime* symbol in the summation indicates that term $n = m$ is not included. Note that, when applied separately, Eq. (3.26) require that there be no degeneracies in the spectrum; conversely, Eq. (3.25) is valid in the general case. Notice that if h corresponds to the occupation function f_m, the operator $\hat{O}$ reduces to the ground-state density operator and Eq. (3.25) becomes Eq. (3.20).

3.3 ANALYTICAL LONG-WAVELENGTH EXPANSION

In this section, our attention will be drawn to our primary objective, which is taking the long-wavelength limit of the second-order energy functional. Before doing so, however, and after rewriting Eq. (3.14) for the case in which the external perturbations are modulated by a wave vector $\mathbf{q}$, we will discuss an important subtlety related to time reversal symmetry. Once the theoretical grounds are well established, including the electrostatic issues related to taking the $\mathbf{q} \to \mathbf{0}$ limit of the potentials, we will give the main result of this chapter in Sec. 3.3.3, which is an analytical expression for first-order spatial dispersion coefficients in metals.

3.3.1 VARIATIONAL SECOND-ORDER ENERGY AT FINITE q

We now apply the formalism presented in the previous subsection to the case of a monochromatic perturbation, which is modulated at a wave vector $\mathbf{q}$, as described in Sec. 2.3.1. As is customary, we shall work with the cell-periodic part of the wave functions and operators. The starting point is once again Eq. (2.109), which decomposes the total energy as a stationary functional plus a nonvariational contribution. Nevertheless, in contrast to Sec. 2.4.4, where TR symmetry is used everywhere to simplify the expressions for insulators, we shall write down the stationary part at finite $\mathbf{q}$ for the most general case; the reason why we do not assume TR symmetry for the time being shall become clear soon. We find,

$$\begin{aligned} E^{\lambda_1\lambda_2}_{\mathrm{st},\mathbf{q}} = \int_{\mathrm{BZ}} [d^3k] \left(\bar{E}^{\lambda_1\lambda_2}_{\mathbf{k},\mathbf{q}} + \bar{E}^{\lambda_1\lambda_2\,*}_{\mathbf{k}+\mathbf{q},-\mathbf{q}} + \Delta E^{\lambda_1\lambda_2}_{\mathbf{k},\mathbf{q}} \right) \\ + \int_{\Omega} \int n^{\lambda_1 *}_{\mathbf{q}}(\mathbf{r}) K_{\mathbf{q}}(\mathbf{r},\mathbf{r}') n^{\lambda_2}_{\mathbf{q}}(\mathbf{r}')\, d^3r\, d^3r'. \end{aligned} \tag{3.27}$$

We shall name the new symbols appearing in Eq. (3.27) as the *wave function* ($\bar{E}$) and *occupation* (ΔE) contributions, which are given by

$$\begin{aligned} \bar{E}^{\lambda_1\lambda_2}_{\mathbf{k},\mathbf{q}} = & \sum_{m\in\mathcal{M}} f_{m\mathbf{k}} \langle u^{\lambda_1}_{m\mathbf{k},\mathbf{q}} | \left(\hat{H}^{(0)}_{\mathbf{k}+\mathbf{q}} + a\hat{P}_{\mathbf{k}+\mathbf{q}} - \epsilon^{(0)}_{m\mathbf{k}} \right) | u^{\lambda_2}_{m\mathbf{k},\mathbf{q}} \rangle \\ & + \sum_{m\in\mathcal{M}} f_{m\mathbf{k}} \langle u^{\lambda_1}_{m\mathbf{k},\mathbf{q}} | \hat{Q}_{\mathbf{k}+\mathbf{q}} \hat{H}^{\lambda_2}_{\mathbf{k},\mathbf{q}} | u^{(0)}_{m\mathbf{k}} \rangle \\ & + \sum_{m\in\mathcal{M}} f_{m\mathbf{k}} \langle u^{(0)}_{m\mathbf{k}} | (\hat{H}^{\lambda_1}_{\mathbf{k},\mathbf{q}})^{\dagger} \hat{Q}_{\mathbf{k}+\mathbf{q}} | u^{\lambda_2}_{m\mathbf{k},\mathbf{q}} \rangle , \end{aligned} \tag{3.28}$$

and

$$\begin{aligned} \Delta E^{\lambda_1\lambda_2}_{\mathbf{k},\mathbf{q}} = & \sum_{m,n\in\mathcal{M}} f^{\lambda_1}_{m\mathbf{k},n\mathbf{k}+\mathbf{q}} \langle u^{(0)}_{n\mathbf{k}+\mathbf{q}} | \hat{H}^{\lambda_2}_{\mathbf{k},\mathbf{q}} | u^{(0)}_{m\mathbf{k}} \rangle \\ & + \sum_{m,n\in\mathcal{M}} \langle u^{(0)}_{m\mathbf{k}} | (\hat{H}^{\lambda_1}_{\mathbf{k},\mathbf{q}})^{\dagger} | u^{(0)}_{n\mathbf{k}+\mathbf{q}} \rangle f^{\lambda_2}_{n\mathbf{k}+\mathbf{q},m\mathbf{k}} \\ & - \sum_{m,n\in\mathcal{M}} f^{\lambda_1}_{m\mathbf{k},n\mathbf{k}+\mathbf{q}} \frac{\epsilon^{(0)}_{n\mathbf{k}+\mathbf{q}} - \epsilon^{(0)}_{m\mathbf{k}}}{f_{n\mathbf{k}+\mathbf{q}} - f_{m\mathbf{k}}} f^{\lambda_2}_{n\mathbf{k}+\mathbf{q},m\mathbf{k}}. \end{aligned} \tag{3.29}$$

In absence of TR symmetry, the first-order electron density is given by

$$\begin{aligned} n^{\lambda}_{\mathbf{q}}(\mathbf{r}) = & \int_{\mathrm{BZ}} [d^3k] \sum_{m\in\mathcal{M}} f_{m\mathbf{k}} \langle u^{(0)}_{m\mathbf{k}} | \mathbf{r} \rangle \langle \mathbf{r} | \hat{Q}_{\mathbf{k}+\mathbf{q}} | u^{\lambda}_{m\mathbf{k},\mathbf{q}} \rangle \\ & + \int_{\mathrm{BZ}} [d^3k] \sum_{m\in\mathcal{M}} f_{m\mathbf{k}+\mathbf{q}} \langle u^{\lambda}_{m\mathbf{k}+\mathbf{q},-\mathbf{q}} | \hat{Q}_{\mathbf{k}} | \mathbf{r} \rangle \langle \mathbf{r} | u^{(0)}_{m\mathbf{k}+\mathbf{q}} \rangle \\ & + \int_{\mathrm{BZ}} [d^3k] \sum_{m,n\in\mathcal{M}} f_{m\mathbf{k}} \langle u^{(0)}_{m\mathbf{k}} | \mathbf{r} \rangle \langle \mathbf{r} | u^{(0)}_{n\mathbf{k}+\mathbf{q}} \rangle f^{\lambda}_{n\mathbf{k}+\mathbf{q},m\mathbf{k}}. \end{aligned} \tag{3.30}$$

Before moving forward, it is useful to recall the following Hermiticity conditions for first-order occupation matrices ($\mathbf{f}^{\lambda}$) and operators ($\hat{O}^{\lambda} = \{\hat{H}^{\lambda}, \hat{\mathcal{H}}^{\lambda}, \hat{\rho}^{\lambda}\}$),

$$f^{\lambda\dagger}_{n\mathbf{k}+\mathbf{q},m\mathbf{k}} = f^{\lambda}_{m\mathbf{k},n\mathbf{k}+\mathbf{q}}, \qquad \hat{O}^{\lambda\dagger}_{\mathbf{k},\mathbf{q}} = \hat{O}^{\lambda}_{\mathbf{k}+\mathbf{q},-\mathbf{q}}, \tag{3.31}$$

which guarantees that the Fourier transforms of the response functions defined here are real. The stationary conditions on $\langle u^{\lambda}_{m\mathbf{k},\mathbf{q}}|$ and $f^{\lambda\dagger}_{n\mathbf{k}+\mathbf{q},m\mathbf{k}}$ of the second-order energy functional give us, respectively, the standard Sternheimer equation for the first-order wave functions, Eq. (2.113), and the finite $\mathbf{q}$ counterpart of Eq. (3.13), which reads as

$$f^{\lambda}_{n\mathbf{k}+\mathbf{q},m\mathbf{k}} = \frac{f_{n\mathbf{k}+\mathbf{q}} - f_{m\mathbf{k}}}{\epsilon^{(0)}_{n\mathbf{k}+\mathbf{q}} - \epsilon^{(0)}_{m\mathbf{k}}} \langle u^{(0)}_{n\mathbf{k}+\mathbf{q}}| \hat{\mathcal{H}}^{\lambda}_{\mathbf{k},\mathbf{q}} |u^{(0)}_{m\mathbf{k}}\rangle . \tag{3.32}$$

To simplify notation, we shall write $f^{\lambda}_{mn\mathbf{k}}$ to indicate $f^{\lambda}_{m\mathbf{k},n\mathbf{k}}$ (the same holds for $\bar{f}_{mn\mathbf{k}}$). As a result, the finite $\mathbf{q}$ counterpart of the nonstationary expression for the second-order energy reported in Sec. 3.2.2 is given by

$$E^{\lambda_1\lambda_2}_{\text{nonst},\mathbf{q}} = \int_{\text{BZ}} [d^3k] \, \text{Tr}\left(\hat{H}^{\lambda_1}_{\mathbf{k}+\mathbf{q},-\mathbf{q}} \hat{\rho}^{\lambda_2}_{\mathbf{k},\mathbf{q}}\right), \tag{3.33}$$

where the integrand is written in a compact form as a trace, and the first-order density operator can be written as

$$\begin{aligned}\hat{\rho}^{\lambda}_{\mathbf{k},\mathbf{q}} = \sum_{m\in\mathcal{M}} \Big(&|u^{\lambda}_{m\mathbf{k},\mathbf{q}}\rangle f_{m\mathbf{k}} \langle u^{(0)}_{m\mathbf{k}}| + |u^{(0)}_{m\mathbf{k}+\mathbf{q}}\rangle f_{m\mathbf{k}+\mathbf{q}} \langle u^{\lambda}_{m\mathbf{k}+\mathbf{q},-\mathbf{q}}| \\ &+ |u^{(0)}_{n\mathbf{k}+\mathbf{q}}\rangle f^{\lambda}_{n\mathbf{k}+\mathbf{q},m\mathbf{k}} \langle u^{(0)}_{m\mathbf{k}}| \Big).\end{aligned} \tag{3.34}$$

As outlined at the very beginning in Sec. 3.1, observable quantities must not depend on the size of the active subspace. It can be readily demonstrated that the nonstationary second-order energy, $E^{\lambda_1\lambda_2}_{\text{nonst},\mathbf{q}}$, is also independent of M. The proof relies on the M-independence of the first-order density operator, $\hat{\rho}^{\lambda_2}_{\mathbf{k},\mathbf{q}}$: if M changes, part of the spectral weight is transferred from the first two terms to the Kubo-like contribution in the second line of Eq. (3.34), but the overall sum remains unchanged. In the limit where M tends to infinity, the active space $\mathcal{M}$ coincides with the entire Hilbert space; then, the first two terms vanish and the entire operator is expressed in a Kubo-like sum-over-all-states [third contribution in Eq. (3.34)] form [116]. Conversely, in gapped systems at zero temperature, i.e., insulators, it is common practice to restrict the active subspace to its bare minimum (i.e., to the valence manifold). In this case, $\Delta E^{\lambda_1\lambda_2}_{\mathbf{k},\mathbf{q}}$ vanishes identically, and the remainder contributions recover the well-known DFPT expressions for insulators that were introduced in Sec. 2.3.

3.3.2 TIME-REVERSAL SYMMETRY

The formulas presented in the previous subsection have the drawback that they require, in principle, solving the Sternheimer problem simultaneously at $\mathbf{q}$ and $-\mathbf{q}$. In the following, we shall specialize our theory to crystals that enjoy TR symmetry, where this inconvenience can be avoided. Indeed, assuming that both perturbations λ_1 and λ_2 are even under a TR operation, we have

$$\langle \mathbf{r} | u^{(0)}_{m\mathbf{k}} \rangle = \langle u^{(0)}_{m-\mathbf{k}} | \mathbf{r} \rangle \,, \quad \langle \mathbf{r} | u^{\lambda}_{m\mathbf{k},\mathbf{q}} \rangle = \langle u^{\lambda}_{m-\mathbf{k},-\mathbf{q}} | \mathbf{r} \rangle \,, \tag{3.35}$$

which implies

$$\bar{E}^{\lambda_1\lambda_2\,*}_{\mathbf{k}+\mathbf{q},-\mathbf{q}} = \bar{E}^{\lambda_1\lambda_2}_{-\mathbf{k}-\mathbf{q},\mathbf{q}} \longrightarrow \bar{E}^{\lambda_1\lambda_2}_{\mathbf{k},\mathbf{q}}. \tag{3.36}$$

Since the latter quantity must be anyway integrated over the Brillouin Zone, we are allowed to operate an arbitrary shift in $\mathbf{k}$-space, such that $-\mathbf{k}-\mathbf{q} \to \mathbf{k}$. This allows us to write the stationary expression for the second-order energy as

$$E^{\lambda_1\lambda_2}_{\mathrm{st},\mathbf{q}} = \int_{\mathrm{BZ}} [d^3k] \left(2\bar{E}^{\lambda_1\lambda_2}_{\mathbf{k},\mathbf{q}} + \Delta E^{\lambda_1\lambda_2}_{\mathbf{k},\mathbf{q}} \right) + \int_{\Omega} \int n^{\lambda_1 *}_{\mathbf{q}}(\mathbf{r}) K_{\mathbf{q}}(\mathbf{r},\mathbf{r}') n^{\lambda_2}_{\mathbf{q}}(\mathbf{r}')\, d^3r\, d^3r', \tag{3.37}$$

with the first-order electron densities defined as

$$\begin{aligned} n^{\lambda}_{\mathbf{q}}(\mathbf{r}) = \int_{\mathrm{BZ}} [d^3k] \Bigg[& 2 \sum_{m\in\mathcal{M}} f_{m\mathbf{k}} \, \langle u^{(0)}_{m\mathbf{k}} | \mathbf{r} \rangle \; \langle \mathbf{r} | \, \hat{Q}_{\mathbf{k}+\mathbf{q}} \, | u^{\lambda}_{m\mathbf{k},\mathbf{q}} \rangle \\ & + \sum_{m,n\in\mathcal{M}} \langle u^{(0)}_{m\mathbf{k}} | \mathbf{r} \rangle \; \langle \mathbf{r} | u^{(0)}_{n\mathbf{k}+\mathbf{q}} \rangle \, f^{\lambda}_{n\mathbf{k}+\mathbf{q},m\mathbf{k}} \Bigg]. \end{aligned} \tag{3.38}$$

Note that the first-order wave functions at $-\mathbf{q}$ are no longer needed. Similarly, after imposing the stationary principles, we arrive at an analogous nonstationary formula for the second derivative of the energy,

$$\begin{aligned} E^{\lambda_1\lambda_2}_{\mathrm{nonst},\mathbf{q}} = \int_{\mathrm{BZ}} [d^3k] \Bigg[& 2 \sum_{m\in\mathcal{M}} f_{m\mathbf{k}} \, \langle u^{(0)}_{m\mathbf{k}} | \, (\hat{H}^{\lambda_1}_{\mathbf{k},\mathbf{q}})^{\dagger} \, | u^{\lambda_2}_{m\mathbf{k},\mathbf{q}} \rangle \\ & + \sum_{m,n\in\mathcal{M}} \langle u^{(0)}_{m\mathbf{k}} | \, (\hat{H}^{\lambda_1}_{\mathbf{k},\mathbf{q}})^{\dagger} \, | u^{(0)}_{n\mathbf{k}+\mathbf{q}} \rangle \, f^{\lambda_2}_{n\mathbf{k}+\mathbf{q},m\mathbf{k}} \Bigg]. \end{aligned} \tag{3.39}$$

The use of TR symmetry in DFPT is, of course, well established; indeed, we have employed it implicitly in Sec. 2.3 in order to simplify the expressions for insulators. The reason for spelling it out explicitly here is related to an important subtlety specific to the metallic case that we believe is worth mentioning. The key point to note is that, because of the shift in $\mathbf{k}$-space that we have operated on the TR-rectified "$-\mathbf{q}$" terms, the *integrands* (i.e., the quantities in the square brackets) in Eq. (3.38) and (3.39) are no longer independent of M: such property is restored only after integration over the full BZ is performed. This observation has an undesirable consequence when operating the parametric differentiation in $\mathbf{q}$ (see next subsection): the accuracy of the result depends on the vanishing of the total $\mathbf{k}$-derivative of $\bar{E}^{\lambda_1\lambda_2}_{\mathbf{k},\mathbf{0}}$. For this requirement to hold, we need $\bar{E}^{\lambda_1\lambda_2}_{\mathbf{k},\mathbf{0}}$ to be a differentiable function of $\mathbf{k}$, which is only true if the active subspace $\mathcal{M}$ forms an isolated group of bands; i.e., it must be separated from higher unoccupied states by a gap. This is illustrated in Fig. 3.1.

There are, of course, some fortunate cases where it is possible to find well-defined energy gaps in the conduction-band region of the spectrum and it is possible to choose M in such a way that $\epsilon^{(0)}_{M\mathbf{k}} - \epsilon^{(0)}_{M+1\mathbf{k}} \neq 0$ over the whole BZ. Less fortunate

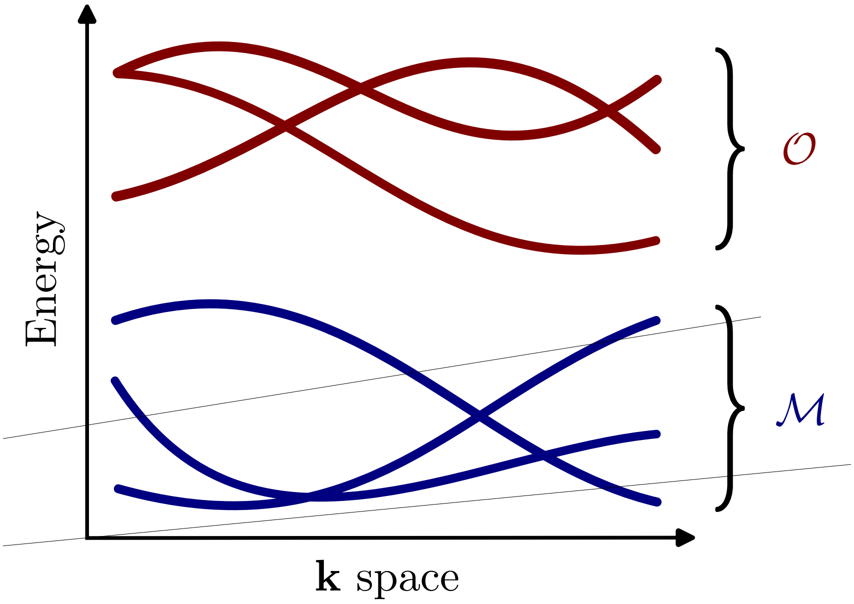

Figure 3.1: Cartoon illustrating the electronic band structure of a hypothetical crystal, where the active subspace $\mathcal{M}$ is separated by an energy gap from the rest of bands forming the group $\mathcal{O}$. For the ensemble DFPT method we have presented in this chapter to be applicable, this requirement needs to hold for all $\mathbf{k}$ points in the Brillouin Zone. However, degeneracies are allowed within each group.

cases might require choosing a different M for distinct $\mathbf{k}$ points, in order to avoid degeneracies between M and $M+1$. (When such degeneracies are present, the linear-response Sternheimer problem becomes ill-conditioned, which makes it difficult or impossible to reach numerical convergence.) Although in principle possible, doing so would require using Eq. (3.27), in place of Eq. (3.37), as a starting point for the long-wave expansion. This would entail a significant revision of the spatial-dispersion formulas already implemented in ABINIT; for practical reasons, we have decided to stick to the TR invariant equations in the following.

A natural question to pose is why the aforementioned energy gap in the spectrum is essential for our scopes, if DFPT calculations on metals have been conducted for decades without consideration of this issue. What is the distinction between the two approaches? To gain a deeper understanding of this matter, it is sufficient to examine the expressions in question. In the nonstationary second-order energy, Eq. (3.39), the first-order wave functions are multiplied by the occupation number of its corresponding state, $f_{m\mathbf{k}}$. If the occupation of such a state is vanishingly small, i.e., $f_{m\mathbf{k}} \sim 0$, there is no need for us to converge the corresponding first-order wave functions. This is in fact the standard strategy employed when dealing with metals: one selects M in such a way that the occupation of the last states in the calculation are negligible, and one reserves the right to leave the highest first-order wave functions unconverged. On the contrary, in the variational expression that we have derived, Eq. (3.37), because of the presence of the terms $\bar{f}_{n\mathbf{k}+\mathbf{q},m\mathbf{k}}$, even if the occupation of a given state is negligible, its contribution to the second-order energy is not. It is therefore imperative that all states that are included in the calculation be converged.

3.3.3 FIRST-ORDER IN q

Our next task consists in taking the analytical derivative of Eq. (3.37) with respect to $\mathbf{q}$. The advantages of the unconstrained variational formulation that have been previously discussed in Sec. 2.4.4 for insulators are applicable in this context. In particular, remember that at first-order in $\mathbf{q}$, the $2n+1$ theorem states that the total derivative in $\mathbf{q}$ coincides with the partial derivative of the second-order energy functional. In the present case, this implies that *both* the first-order wave functions, $|u^{\lambda}_{m\mathbf{k},\mathbf{q}}\rangle$, and occupation matrices, $f^{\lambda}_{m\mathbf{k},n\mathbf{k}+\mathbf{q}}$, are excluded from differentiation. The final result for the $\mathbf{q}$-derivative of the stationary part reads as

$$E^{\lambda_1\lambda_2}_{\mathrm{st},\gamma} = \int_{\mathrm{BZ}} [d^3k] \left(2\bar{E}^{\lambda_1\lambda_2}_{\mathbf{k},\gamma} + \Delta E^{\lambda_1\lambda_2}_{\mathbf{k},\gamma} \right) + \int_{\Omega} \int n^{\lambda_1 *}(\mathbf{r}) K_{\gamma}(\mathbf{r},\mathbf{r}') n^{\lambda_2}(\mathbf{r}')\, d^3r\, d^3r'. \tag{3.40}$$

The wave function term is in the exact same form as in the insulating case [see Eq. (2.119)]. We write it down here to indicate explicitly that the sums are carried out for all states considered in the active subspace $\mathcal{M}$,

$$\begin{aligned}
\bar{E}^{\lambda_1\lambda_2}_{\mathbf{k},\gamma} = &\sum_{m\in\mathcal{M}} f_{m\mathbf{k}} \langle u^{\lambda_1}_{m\mathbf{k}}| \hat{H}^{k_\gamma}_{\mathbf{k}} |u^{\lambda_2}_{m\mathbf{k}}\rangle \\
&- \sum_{m,n\in\mathcal{M}} f_{m\mathbf{k}} \langle u^{\lambda_1}_{m\mathbf{k}}|u^{k_\gamma}_{n\mathbf{k}}\rangle \langle u^{(0)}_{n\mathbf{k}}| \hat{\mathcal{H}}^{\lambda_2}_{\mathbf{k}} |u^{(0)}_{m\mathbf{k}}\rangle \\
&- \sum_{m,n\in\mathcal{M}} f_{m\mathbf{k}} \langle u^{(0)}_{m\mathbf{k}}| (\hat{\mathcal{H}}^{\lambda_1}_{\mathbf{k}})^{\dagger} |u^{(0)}_{n\mathbf{k}}\rangle \langle u^{k_\gamma}_{n\mathbf{k}}|u^{\lambda_2}_{m\mathbf{k}}\rangle \\
&+ \sum_{m\in\mathcal{M}} f_{m\mathbf{k}} \left(\langle u^{\lambda_1}_{m\mathbf{k}}| \hat{H}^{\lambda_2}_{\mathbf{k},\gamma} |u^{(0)}_{m\mathbf{k}}\rangle + \langle u^{(0)}_{m\mathbf{k}}| (\hat{H}^{\lambda_1}_{\mathbf{k},\gamma})^{\dagger} |u^{\lambda_2}_{m\mathbf{k}}\rangle \right).
\end{aligned} \tag{3.41}$$

The occupation term, specific to metals, is given by

$$\begin{aligned}
\Delta E^{\lambda_1\lambda_2}_{\mathbf{k},\gamma} = &\sum_{m,n\in\mathcal{M}} \bar{f}_{mn\mathbf{k}} \langle u^{(0)}_{m\mathbf{k}}| (\hat{\mathcal{H}}^{\lambda_1}_{\mathbf{k}})^{\dagger} |u^{(0)}_{n\mathbf{k}}\rangle \langle u^{(0)}_{n\mathbf{k}}| \hat{H}^{\lambda_2}_{\mathbf{k},\gamma} |u^{(0)}_{m\mathbf{k}}\rangle \\
&+ \sum_{m,n\in\mathcal{M}} \bar{f}_{mn\mathbf{k}} \langle u^{(0)}_{m\mathbf{k}}| (\hat{H}^{\lambda_1}_{\mathbf{k},\gamma})^{\dagger} |u^{(0)}_{n\mathbf{k}}\rangle \langle u^{(0)}_{n\mathbf{k}}| \hat{\mathcal{H}}^{\lambda_2}_{\mathbf{k}} |u^{(0)}_{m\mathbf{k}}\rangle \\
&+ \sum_{m,n\in\mathcal{M}} \bar{f}_{mn\mathbf{k}} \langle u^{(0)}_{m\mathbf{k}}| (\hat{\mathcal{H}}^{\lambda_1}_{\mathbf{k}})^{\dagger} |u^{(0)}_{n\mathbf{k}}\rangle \langle u^{k_\gamma}_{n\mathbf{k}}| \hat{\mathcal{H}}^{\lambda_2}_{\mathbf{k}} |u^{(0)}_{m\mathbf{k}}\rangle \\
&+ \sum_{m,n\in\mathcal{M}} \bar{f}_{mn\mathbf{k}} \langle u^{(0)}_{m\mathbf{k}}| (\hat{\mathcal{H}}^{\lambda_1}_{\mathbf{k}})^{\dagger} |u^{k_\gamma}_{n\mathbf{k}}\rangle \langle u^{(0)}_{n\mathbf{k}}| \hat{\mathcal{H}}^{\lambda_2}_{\mathbf{k}} |u^{(0)}_{m\mathbf{k}}\rangle \\
&+ \sum_{m,n,l\in\mathcal{M}} \mathcal{F}_{mnl\mathbf{k}} \langle u^{(0)}_{m\mathbf{k}}| (\hat{\mathcal{H}}^{\lambda_1}_{\mathbf{k}})^{\dagger} |u^{(0)}_{n\mathbf{k}}\rangle \langle u^{(0)}_{n\mathbf{k}}| \hat{H}^{k_\gamma}_{\mathbf{k}} |u^{(0)}_{l\mathbf{k}}\rangle \langle u^{(0)}_{l\mathbf{k}}| \hat{\mathcal{H}}^{\lambda_2}_{\mathbf{k}} |u^{(0)}_{m\mathbf{k}}\rangle .
\end{aligned} \tag{3.42}$$

The proof of Eq. (3.42) rests on the rules for the differentiation of operators outlined in Sec. 3.2.4, which we apply here to the case $\lambda = q_\gamma$ and $h(\epsilon^{(0)}_{m\mathbf{k}+\mathbf{q}}) = G(\epsilon^{(0)}_{n\mathbf{k}}, \epsilon^{(0)}_{m\mathbf{k}+\mathbf{q}})$. This immediately gives rise to the calligraphic symbol $\mathcal{F}_{mnl\mathbf{k}} \equiv \mathcal{F}(\epsilon_{m\mathbf{k}}, \epsilon_{n\mathbf{k}}, \epsilon_{l\mathbf{k}})$, which is invariant under any permutation of the three band indices. It is defined as [114]

$$\mathcal{F}(x,y,z) = \begin{cases} \frac{G(x,y)-G(x,z)}{y-z}, & y \neq z \\ \frac{1}{6}\left(\frac{\partial^2 f(x)}{\partial x^2} + \frac{\partial^2 f(y)}{\partial y^2} + \frac{\partial^2 f(z)}{\partial z^2}\right), & x = y = z. \end{cases} \tag{3.43}$$

The symmetrization with respect to all three indices in the second line follows the same logic as that used for $G(x,y)$ [see Eq. (3.12) and the comment right after]. We have carefully tested that our implementation of the function $\mathcal{F}(x,y,z)$ is continuous and smooth in the critical $x \simeq y \simeq z$ region. To illustrate the qualitative differences between $\mathcal{F}$ and G, in Fig. 3.2 we present two filled contour plots of the functions $G(x,y)$ and $\mathcal{F}(x,y,0)$; their respective symmetric and antisymmetric nature under the interchange of the two arguments is clear.

3.3.4 FERMI LEVEL SHIFTS

As outlined at the end of Sec. 2.4.4, long-wavelength expansions generally require some care, as the Coulomb potential diverges in the $\mathbf{q} \to 0$ limit. In insulators, this divergence results in a nonanalytic contribution to the response that is due to long-range electric fields. In metals, however, such fields are screened by the redistribution of free carriers, which tends to enforce local charge neutrality. The requirement of charge neutrality becomes strict at $\mathbf{q} = \mathbf{0}$, where it needs to be taken care of explicitly, via the holonomic constraint on particle number in Eq. (3.1). Until now, we have intentionally postponed addressing this matter. In the following discussion, we will provide a comprehensive analysis.

At second-order in the perturbations, the constraint that enforces particle number conservation propagates to the second-order energy functional as $\mu^\lambda \mathrm{Tr}(\mathbf{f}^\lambda)$, where

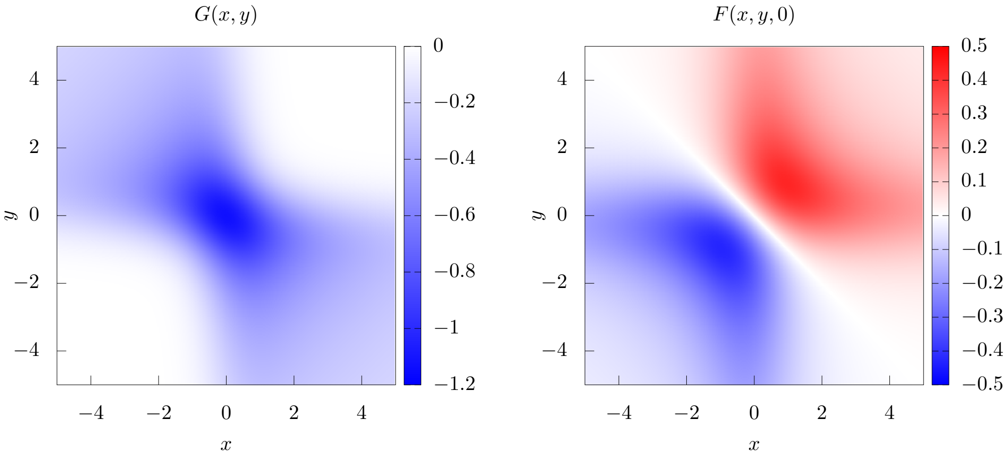

Figure 3.2: Two-dimensional contour plots (in arbitrary units) of the G and $\mathcal{F}$ functions as defined in Eq. (3.12) and Eq. (3.43), respectively. The left panel shows $G(x,y)$ and the right panel $\mathcal{F}(x,y,0)$.

μ^λ plays the role of a first-order Lagrange multiplier [76]. By imposing the stationary condition on the $\mathbf{f}^\lambda$ matrix, one readily obtains the "Fermi level shifts" contribution,

$$\begin{aligned} f^\lambda_{nm\mathbf{k}} &= \bar{f}_{nm\mathbf{k}} \left(\langle u^{(0)}_{n\mathbf{k}} | \hat{\mathcal{H}}^\lambda_{\mathbf{k}} | u^{(0)}_{m\mathbf{k}} \rangle - \delta_{mn}\mu^\lambda \right) \\ &= \bar{f}_{nm\mathbf{k}} \langle u^{(0)}_{n\mathbf{k}} | \left(\hat{\mathcal{H}}^\lambda_{\mathbf{k}} - \mu^\lambda \right) | u^{(0)}_{m\mathbf{k}} \rangle . \end{aligned} \tag{3.44}$$

A closed expression for μ^λ is can be obtained by imposing that the trace of $\mathbf{f}^\lambda$ should vanish. We obtain

$$\mu^\lambda = \frac{\displaystyle\int_{\mathrm{BZ}} [d^3k] \sum_m f'_{m\mathbf{k}} \langle u^{(0)}_{m\mathbf{k}} | \hat{\mathcal{H}}^\lambda_{\mathbf{k}} | u^{(0)}_{m\mathbf{k}} \rangle}{\displaystyle\int_{\mathrm{BZ}} [d^3k] \sum_m f'_{m\mathbf{k}}}, \tag{3.45}$$

where $f'_{m\mathbf{k}} = \frac{\partial f(\epsilon)}{\partial \epsilon}\big|_{\epsilon=\epsilon^{(0)}_{m\mathbf{k}}}$.

It is important to stress that the Fermi-shift-corrected second-order energy at Γ is the exact $\mathbf{q} \to 0$ limit of the second-order energy calculated at a small but finite $\mathbf{q}$; in the latter, the diverging $\mathbf{G} = \mathbf{0}$ term in the Coulomb kernel is still present, and therefore, no correction is needed. Note that the limit is the same regardless of the direction, which is equivalent to observing that adiabatic response functions in metals at finite electronic temperature are always analytic functions of $\mathbf{q}$. This means that, unlike in insulators, the long-wave expansion of the force-constant matrix can be carried out on the whole response function, without the need of artificially suppressing the macroscopic electric field contribution prior to differentiation. This also implies that special care is needed at correctly differentiating such macroscopic electrostatic term with respect to $\mathbf{q}$ in Eq. (3.40). The macroscopic (mac) electrostatic contributions are originated from three different sources: the first contribution comes from the nonvariational term, the second contribution originates from the electrostatic term in Eq. (3.40), and the third contribution arises from the first two lines of the occupation term, Eq. (3.42). All the divergences nullify each other, yielding an additional contribution that is proportional to the Fermi level shifts (μ^λ) produced by the perturbations. For the phonon case,

$$E^{\tau_{\kappa\alpha}\tau_{\kappa'\beta}}_{\mathrm{mac},\gamma} \simeq i\delta_{\alpha\gamma} Z_\kappa \mu^{\tau_{\kappa'\beta}} - i\delta_{\beta\gamma}\mu^{\tau_{\kappa\alpha}} Z_{\kappa'}, \tag{3.46}$$

where Z_κ is the bare nuclear pseudo-charge of sublattice κ. (A detailed derivation of Eq. (3.46) can be found in Appendix A, Sec. A.2 and A.3.)

Since there is no need to remove the (ambiguous) macroscopic fields contributions prior to the long-wave expansion, the adiabatic spatial dispersion coefficients are well-defined bulk properties in metals. In other words, the far-away surfaces cannot contribute electrostatically to the bulk response, and the problematic *potential energy reference* [44] issue inherent to spatial dispersion in insulators is absent in metals.

3.4 APPLICATION TO PHONONS

Up to now, our theory has been presented in a completely general form, and is valid as it stands for any pair of perturbations λ_1 and λ_2. For a numerical validation of the formal results presented thus far, in the following we shall focus our attention to atomic displacements. In particular, we will report first-order spatial dispersion coefficients of zone-center optical phonons of selected metal structures. This application, while primarily intended as a numerical illustration of our methodology, has an obvious practical relevance as well, given the ongoing interest in polar metals.[2]

The basic ingredient for what follows is the force-constant (FC) matrix, $\mathbf{\Phi}^{\mathbf{q}}$, as defined in Eq. (2.77). We write its long-wave expansion in a vicinity of $\mathbf{q}=\mathbf{0}$ as [103, 117]

$$\Phi^{\mathbf{q}}_{\kappa\alpha,\kappa'\beta} \simeq \Phi^{(0)}_{\kappa\alpha,\kappa'\beta} - i\sum_{\gamma} q_\gamma \Phi^{(1,\gamma)}_{\kappa\alpha,\kappa'\beta} - \frac{1}{2}\sum_{\gamma,\delta} q_\gamma q_\delta \Phi^{(2,\gamma\delta)}_{\kappa\alpha,\kappa'\beta}, \tag{3.47}$$

were $\mathbf{\Phi}^{(0)}$ is the zone-center FC matrix, and $\mathbf{\Phi}^{(1)}$ and $\mathbf{\Phi}^{(2)}$ describe its spatial dispersion at first and second order in the momentum $\mathbf{q}$. We shall discuss their physical relevance (and their relation to the theory developed insofar) separately: the first-order in $\mathbf{q}$ case will be addressed in the following lines and we will defer the discussion of $\mathbf{\Phi}^{(2)}$, which plays a central role in the context of flexoelectricity, for Chapter 4. $\Phi^{(1,\gamma)}_{\kappa\alpha,\kappa'\beta}$ is related to the force produced on sublattice κ along α by a displacement pattern of the sublattice κ' that is linearly increasing in space along r_γ. If the lattice Hamiltonian were local (i.e., if the atomic lattice behaved like an array of noninteracting harmonic oscillators), such force would trivially correspond to $R_{\kappa'\gamma}\Phi^{(0)}_{\kappa\alpha,\kappa'\beta}$; $\mathbf{\Phi}^{(1)}$ describes the correction to that value that is due to the nonlocality of the interatomic forces. Historically, $\mathbf{\Phi}^{(1)}$ was first introduced in the context of bulk flexoelectricity, where it mediates an indirect contribution to the lattice response to a macroscopic strain gradient [44, 103] (see Sec. 4.1.2 for a more detailed discussion). Such a contribution is relevant whenever the crystal allows for Raman-active lattice modes, e.g., in diamond-structure crystals (bulk Si or C) and tilted perovskites like $SrTiO_3$ or $LiOsO_3$. More recently, its importance was pointed out in ferroic crystals, where it acquires a central place in the context of nonlinear gradient couplings (most notably, in the form of antisymmetric Dzyaloshinskii-Moriya-like terms [118]) between lattice modes. In chiral crystals such as α-HgS, the main physical consequence of $\mathbf{\Phi}^{(1)}$ consists in the appearance of chiral phonon modes with opposite angular momentum that disperse linearly along the main crystal axis [119]. Such an effect can be regarded as the phonon counterpart of the natural optical activity [4], which we shall study in detail in Chapter 6.

Based on the theory developed thus far, and in combination with the established methodology for insulators that was already presented in Sec. 2.4.4, we calculate $\mathbf{\Phi}^{(1)}$ as

$$\Phi^{(1,\gamma)}_{\kappa\alpha,\kappa'\beta} = -\operatorname{Im}\left(E^{\tau_{\kappa\alpha}\tau_{\kappa'\beta}}_{\mathrm{st},\gamma} + E^{\tau_{\kappa\alpha}\tau_{\kappa'\beta}}_{\mathrm{Ew},\gamma}\right). \tag{3.48}$$

The stationary part is straightforwardly obtained by substituting $\lambda_1 = \tau_{\kappa\alpha}$ and $\lambda_2 = \tau_{\kappa'\beta}$ into Eq. (3.40), while the nonvariational contribution acquires the form of the first $\mathbf{q}$ derivative of the ionic Ewald (Ew) energy, whose explicit expression can be found in Appendix A of Ref. [44].

---

[2] We shall bring our attention to this class of materials in Chapter 4.

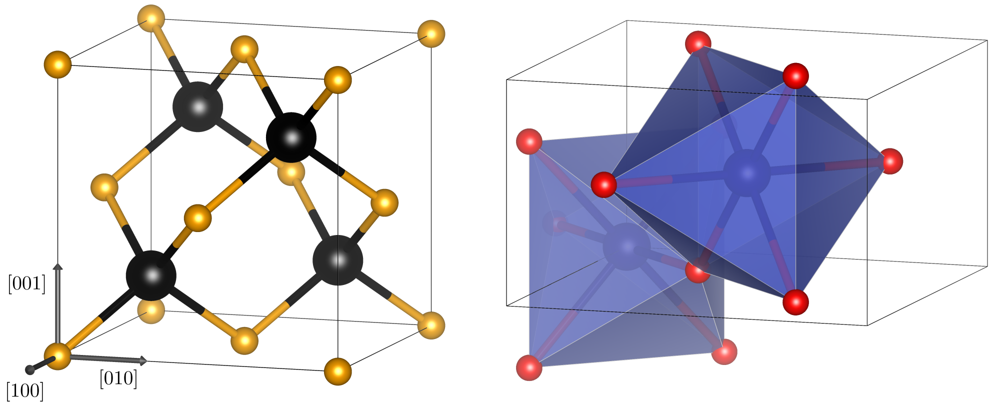

Figure 3.3: Cartoon illustrating the crystal structure of TiB (left) and VO_2 (right). Grey arrows indicate the crystallographic directions that form the Cartesian axes.

3.4.1 A USEFUL SUM RULE

In order to validate our computational strategy for the calculation of the $\mathbf{\Phi}^{(1)}$ tensor, it is useful to recall the following well-established relationship [117],

$$\Lambda^{\kappa}_{\alpha\beta\gamma} = \sum_{\kappa'} \Phi^{(1,\gamma)}_{\kappa\alpha,\kappa'\beta} + f_{\kappa\beta}\delta_{\alpha\gamma}, \tag{3.49}$$

where $f_{\kappa\beta}$ represents the atomic force on the sublattice κ along the Cartesian direction β and $\Lambda^{\kappa}_{\alpha\beta\gamma}$ is the piezoelectric force-response tensor, which can be computed with the metric-tensor formulation as proposed by HWRV [96] (see Sec. 2.3.5 for more details) and is a standard capability of publicly distributed DFT codes. While the sum rule provided by Eq. (3.49) was initially established for insulators [44], we will prove its validity in metals, demonstrating that no additional modifications are required. It should be noted that, unless otherwise stated, we assume that the system under study is at mechanical equilibrium, i.e., forces and stresses tend to zero.

3.4.2 RESULTS

We will consider two types of different structures. First, we will study the zincblende-type structure metals TiB and SiP, which constitute valuable theoretical models for testing our implementation. The selection of the face-centered cubic (fcc) structures for TiB and SiP, which belong to the space group $F\bar{4}3m$ and contain two atoms per unit cell, is motivated by their high symmetry and their structural resemblance to zincblende, an extensively studied compound. We will then turn our attention to VO_2, a more complex material with $P4_2/mnm$ space group that contains 6 atoms per unit cell, where each V atom is bonded to six oxygen atoms, forming a VO_6 octahedron. A schematic representation of the employed crystal structures is given in Fig. 3.3.

3.4.2.1 *Computational parameters*

Our first principles calculations are performed with the DFT and DFPT implementations of the open-source ABINIT [42, 43] package with the Perdew-Wang [81] parametrization of the local density approximation (LDA). Our long-wave ensemble DFPT expressions for the computation of spatial dispersion properties in metals, Eq. (3.40) to (3.42), are incorporated to the ABINIT package after minor modifications to the recently implemented *longwave* module. Norm-conserving pseudopotentials from the Pseudo Dojo [120] website are used as input to the ONCVPSP [88] software, in order to regenerate them without exchange-correlation nonlinear core corrections.[3]

We use a plane-wave cutoff of 60 Ha and a Gaussian smearing of 0.01 Ha for all our test cases. The BZ is sampled with a dense Monkhorst-Pack mesh of $20 \times 20 \times 20$ $\mathbf{k}$ points for TiB and SiP and $16 \times 16 \times 16$ $\mathbf{k}$ points for VO_2. The crystal structures are relaxed until all the forces are smaller than 0.5×10^{-7} Ha/bohr, obtaining a unit cell parameter of $a = 9.176$ bohr and $a = 9.879$ bohr for TiB and SiP, respectively. The calculated lattice parameters for VO_2 are $a = 8.540$ bohr and $c = 5.154$ bohr.

The active subspace is chosen to be $M = 8$ for SiP, $M = 34$ for VO_2 and either $M = 10$ or $M = 14$ for TiB. These choices guarantee that the active subspace forms an isolated group of bands in all cases, following the observations at the end of Sec. 3.3.2. Fig. 3.4 shows the electronic band structure of TiB, SiP and VO_2, where the M-th band is highlighted in red in SiP and VO_2 and in green ($M = 10$) and red ($M = 14$) in TiB. Using two different values for M in the case of TiB allows us to test the consistency of our implementation and, more specifically, the independence of the converged results on the dimension of the active subspace.

3.4.2.2 *TiB and SiP*

We shall start by testing our implementation with the zincblende-type structure metals TiB and SiP. First of all, note that the crystal symmetries of the materials substantially reduce the number of independent components of $\boldsymbol{\Phi}^{(1)}$. Eq. (3.49) reduces to $\phi = \lambda$, since [44]

$$\begin{aligned} \Phi^{(1,\gamma)}_{\kappa\alpha,\kappa'\beta} &= (-1)^{\kappa+1}(1-\delta_{\kappa\kappa'})\phi\left|\epsilon^{\alpha\beta\gamma}\right|, \\ \Lambda^{\kappa}_{\alpha\beta\gamma} &= (-1)^{\kappa+1}\lambda\left|\epsilon^{\alpha\beta\gamma}\right|, \end{aligned} \tag{3.50}$$

where $\epsilon^{\alpha\beta\gamma}$ is the Levi-Civita symbol. In Table 3.1 we show the only independent component of $\boldsymbol{\Phi}^{(1)}$ ($\boldsymbol{\Lambda}$), indicated as ϕ (λ). The sum rule given by Eq. (3.49) is validated to a remarkably high level of accuracy. As an additional test of our implementation, we show in Fig. 3.5 the computed ϕ parameter for TiB as a function of the $\mathbf{k}$-point mesh resolution. Furthermore, in order to prove that our results remain unaltered irrespective of variations in the parameter M (size of the active subspace), we show a comparison between $M = 10$ and $M = 14$. The obtained results reveal a high level of agreement, which corroborates the robustness of our

---

[3] This is a limitation of the *longwave* module of ABINIT during the period this thesis was performed, which affects (at least) versions v9.10 and before. This applies to all the calculations shown in this thesis.

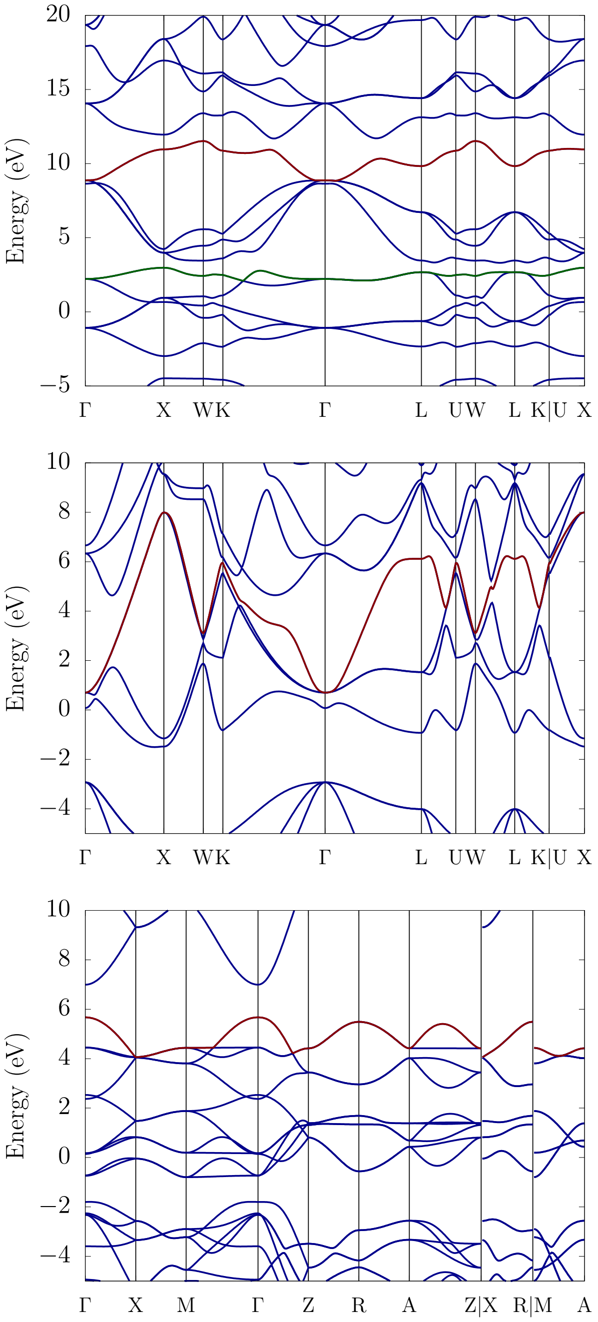

Figure 3.4: Electronic band structures of TiB (top), SiP (middle) and VO_2 (bottom). For TiB, the $M = 10$-th and the $M = 14$-th bands are highlighted, respectively, in green and red. The band depicted in red for the other cases is $M = 8$ for SiP and $M = 34$ for VO_2.

implementation. The discrepancies between the results obtained with $M = 10$ and $M = 14$ in Fig. 3.5 for small **k**-point samplings can be attributed to the shift in **k** space that we discussed in Sec. 3.3.2. Had we adhered to Eq. (3.27), instead of utilizing Eq. (3.37), the results in Fig. 3.5 would have aligned perfectly, regardless of the number of **k** points employed in the calculation.

	ϕ	λ
TiB	224.360	224.368
SiP	287.126	287.340

Table 3.1: A comparison between ϕ and λ for TiB and SiP, in 10^{-3} Ha/bohr units (see Eq. 3.50). ϕ is computed with our long-wave ensemble DFPT formalism presented in this chapter and λ with the standard HWRV implementation.

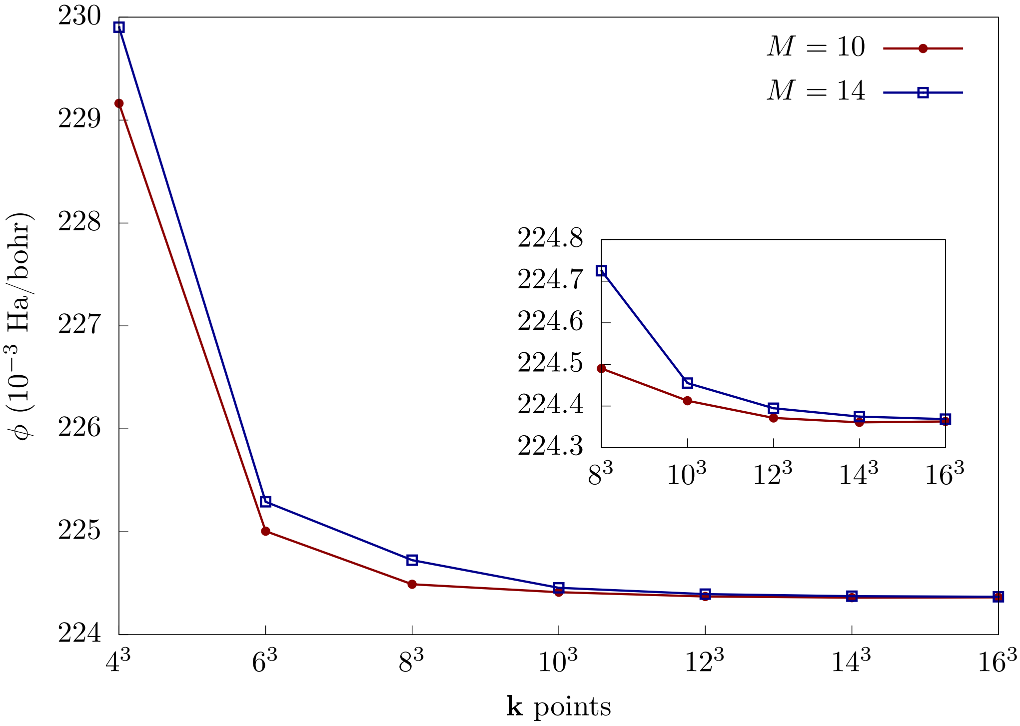

Figure 3.5: Convergence of the ϕ parameter [see Eq. (3.50)] for TiB as a function of the **k** point mesh resolution, for $M = 10$ and $M = 14$. This is a numerical validation that, as long as the highest states considered in the calculation have vanishing occupations, all the observables that can be extracted from the energy functional are independent of the size of the active subspace, M. Solid lines are a guide to the eye.

To conclude with the zincblende structures and in order to validate the sum rule given by Eq. (3.49) in presence of nonvanishing forces, we apply a displacement of 0.3 bohr along the x Cartesian direction to the B atom in TiB. The resulting crystal structure belongs to the space group $Imm2$ and we obtain, in absolute value, maximum interatomic forces of 3×10^{-2} Ha/bohr and stress components of 3.5×10^{-4} Ha^3/bohr. Table 3.2 shows selected tensor elements of $\boldsymbol{\Lambda}^{(1)}$, computed either directly with the HWRV approach or via the sum rule given by Eq. (3.49).

	HWRV	[Eq. (3.49)]′	Eq. (3.49)
$\Lambda^{\mathrm{Ti}}_{xxx}$	64.420	35.140	64.417
$\Lambda^{\mathrm{Ti}}_{xyy}$	−104.004	−104.876	−104.876
$\Lambda^{\mathrm{Ti}}_{xzy}$	−221.380	−220.530	−220.530
$\Lambda^{\mathrm{Ti}}_{yxy}$	−49.769	−78.171	−48.894
$\Lambda^{\mathrm{Ti}}_{yzx}$	−231.073	−231.070	−231.070

Table 3.2: Independent components of the piezoelectric force-response tensor of distorted TiB, computed with the standard HWRV implementation and with the sum rule of Eq. (3.49). The prime symbol indicates that the contributions coming from the interatomic forces have not been taken into account. Values are given in 10^{-3} Ha/bohr.

	HWRV	Eq. (3.49)
$\Lambda^{\mathrm{O}_1}_{xxx}$	64.941	64.914
$\Lambda^{\mathrm{O}_1}_{xyx}$	−15.186	−15.181
$\Lambda^{\mathrm{O}_1}_{yxx}$	3.297	3.300
$\Lambda^{\mathrm{O}_1}_{zzx}$	131.388	131.386
$\Lambda^{\mathrm{O}_1}_{xzz}$	162.162	162.177

Table 3.3: Independent components of the piezoelectric force-response tensor of VO_2, obtained either with the standard HWRV implementation or from the $\mathbf{\Phi}^{(1)}$ tensor with our ensemble DFPT formalism via the lattice sum given by Eq. (3.49).

3.4.2.3 *VO_2*

Due to the crystal symmetries of VO_2, the sum rule given in Eq. (3.49) is non-trivial, meaning that there are more independent components in the $\mathbf{\Phi}^{(1)}$ tensor than in $\mathbf{\Lambda}$. As a consequence, and in contrast with TiB and SiP, the equality only holds after the contributions coming from different sublattices have been summed. This will serve as a further test for the accuracy of our implementation. Fig. 3.6 shows the convergence of selected entries of the piezoelectric force-response tensor as a function of the **k**-mesh, and Table 3.3 displays the converged numerical results.

3.5 SUMMARY AND OUTLOOK

In this chapter, by combining the virtues of ensemble density-functional theory [107] and density-functional perturbation theory [104], we have established a general and powerful first-principles approach for calculating spatial dispersion properties —and more broadly, higher-order derivatives of the total energy— in metals. We have focused our numerical tests on the calculation of the first-order spatial dispersion coefficients of zone-center optical phonons in selected metal structures,

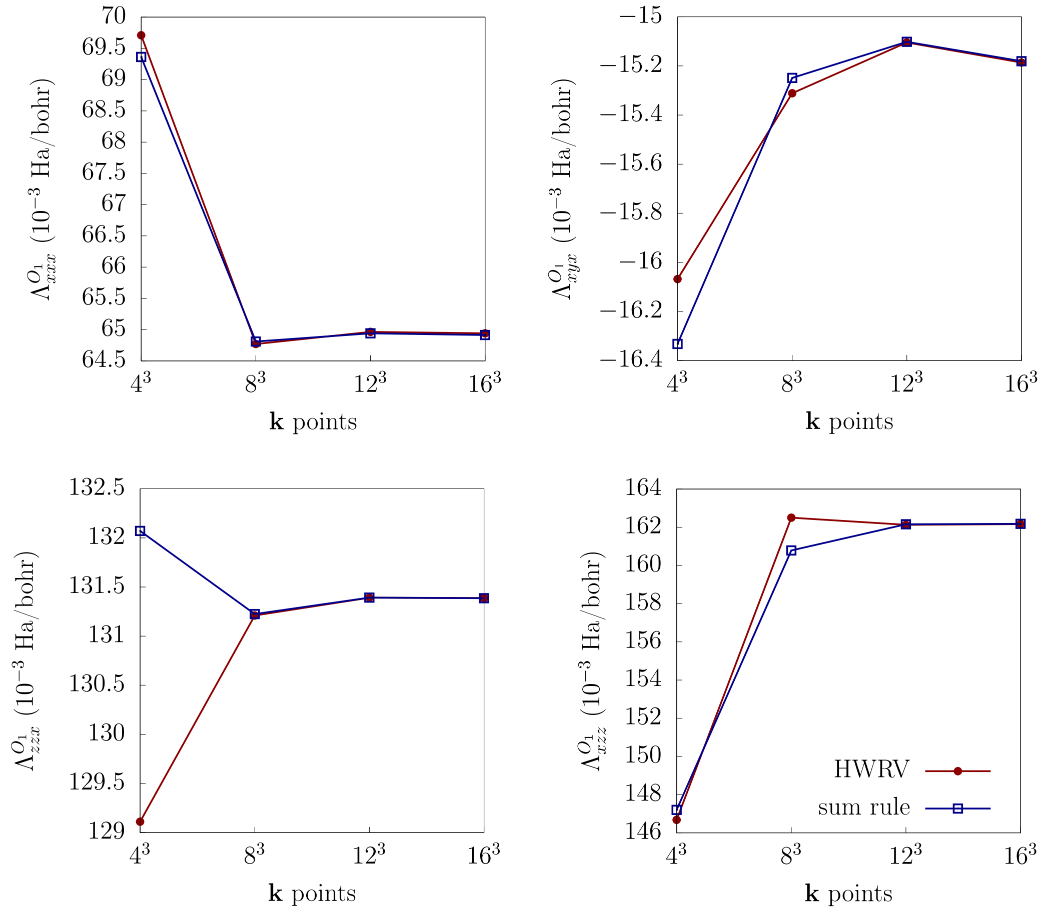

Figure 3.6: Convergence of selected entries of the piezoelectric force-response tensor of VO_2 as a function of the **k** point mesh resolution, where "sum rule" refers to the right hand side of Eq. (3.49). Solid lines are a guide to the eye.

corroborating the accuracy and efficiency of the presented methodology. Our work opens numerous exciting avenues for future studies; we will outline some of them in the following.

- First, the advantages of the approach presented here can be immediately extended to other adiabatic spatial dispersion properties via minor modifications to our formulas. For example, by combining the phonon perturbation with a scalar potential in Eq. (3.40), our method would yield the "adiabatic Born effective charges" as defined in Refs. [121, 122]. The present approach works directly at the Γ point, and hence avoids the need for cumbersome numerical fits. On the other hand, by targeting the adiabatic response to a static (but spatially nonuniform) vector potential field, the present theory could be used to generalize the theory of orbital magnetic susceptibility of Ref. [123] to metals.
- Second, note that the scopes of our work go well beyond the specifics of long-wavelength expansions. One of the main conceptual achievement consists

in generalizing the $2n+1$ theorem [104], one of the mainstays of DFPT in insulators, to metallic systems.[4] This result opens exciting opportunities for calculating not only spatial dispersion effects, but also *nonlinear response* properties in metals, with comparable advantages at the formal and practical level, with respect to the presently available methods, e.g., semiclassical or tight-binding models. The study of nonlinear optics appears as a particularly attractive topic in this context, although its inherent dynamical nature would require generalizing the formalism presented here to the nonadiabatic regime. We regard this as a promising avenue for future developments of our method. We also feel that generalizing the formulas that are currently implemented to TR-broken systems is one of the most pressing priorities; i.e., implementing Eq. (3.27) instead of Eq. (3.37) (see the discussion of Sec. 3.3.2).

For the time being, we shall stick to Eq. (3.37) and our focus will remain on the static regime. We will further prove in the next chapter the great utility of the present approach by applying it in the context of flexoelectricity, i.e., strain gradient mediated effects, with the well-known polar metal $LiOsO_3$.

---

[4] We would like to reiterate the importance of Ref. [108], whose study was carried out essentially in parallel with ours and of which we were not aware at the time of developing our methodology.

4

SWITCHING A POLAR METAL VIA STRAIN GRADIENTS

In this chapter, by pushing the study of flexoelectricity beyond insulators, we demonstrate that strain gradients constitute a viable means to switch the polar order parameter of the so-called “ferroelectric” or polar metals.

It is universally known that the electric polarization is not a well-defined physical property in metals. As such, any parametric derivative of the polarization with respect to an adiabatic parameter (a strain gradient, in the case of flexoelectricity) is also ill-defined. However, as we shall demonstrate shortly, the *flexocoupling* between polar lattice modes and a strain gradient survives even in presence of free carriers. In brief, an applied strain gradient can push the polar order parameter of a material by means of a *geometric* force, which is, at least theoretically, unaffected by the presence of free carriers in the bulk. Still, whether the relevant couplings are strong enough in order to switch the polar order parameter of a real polar metal is currently unknown, as no reported values for the flexocoupling coefficients for metals were available in the literature prior to this work.

This scenario is well-suited for testing our ensemble DFPT methodology of Chapter 3 in the context of strain gradients. Note, however, that this represents an additional challenge compared to the phonon case that was studied in Chapter 3, since it requires, in principle, pushing the long-wavelength expansion of the second-order energy functional up to second order in $\mathbf{q}$. This will enable us to report, for the first time, the flexocoupling coefficients of a metal. As a consistency check, we also develop an alternative method to calculate the flexocoupling tensor in metals, which is based on lattice sums of real-space interatomic force constants.

To validate our strategy, we take $LiOsO_3$ as an example and we try to answer the following physical question: how much do we need to bend a lithium osmate sample in order to reverse its polarity? In practice, everything boils down to estimating the critical bending radius, R_{crit}; i.e., the radius of curvature that needs to be applied in order to switch the polar order parameter. As we shall see, achieving this task involves combining the aforementioned flexocoupling coefficients with a first-principles-based effective Hamiltonian that we will construct by expanding the energy around the centrosymmetric cubic phase. We study the potential energy landscape of $LiOsO_3$ as a function of its main degrees of freedom, i.e., the strain, the polar order parameter and the oxygen octahedral tilts, thus making it possible to identify the most efficient switching paths and the required coercive fields in each case. For comparison, and in order to discuss the experimental viability of our results, we perform an analogous study with $BaTiO_3$, which is arguably one of the most renowned ferroelectric compounds. We find a comparable value of R_{crit} for both materials, and since mechanical switching of polar domains has already been experimentally achieved in $BaTiO_3$ [37] via strain gradients, our work indicates that switching of $LiOsO_3$ mediated by flexoelectricity should also be experimentally feasible.

This chapter is organized as follows. First, in Sec. 4.1 we will make a very brief introduction to flexoelectricity, by defining the fundamental mathematical and physical concepts that are necessary for our intents, most notably the flexoelectric force-response tensor and the flexocoupling coefficients. In Sec. 4.2 the problem to be solved is formally presented and our computational strategy is introduced in Sec. 4.3, where we apply our ensemble DFPT formalism of Chapter 3 in the context of strain gradients. Some of the principal results of this chapter are shown in Sec. 4.4, where the flexocoupling coefficients of $LiOsO_3$ are provided. Sec. 4.5 gives a detailed analysis of the first-principles effective Hamiltonian that we use to study the potential energy landscape of lithium osmate, where the most promising switching paths are discussed. This chapter is concluded with our estimation of the necessary bending radius to switch the polar order parameter of $LiOsO_3$. A comparison with $BaTiO_3$ is also provided. The summary and outlook are presented in Sec. 4.7.

4.1 FLEXOELECTRICITY IN A NUTSHELL

The theory of flexoelectricity has long been plagued with conceptual and methodological challenges that have been successfully addressed [124] over the years. The current state-of-the-art first-principles theory of flexoelectricity allows an accurate and efficient calculation of both electronic and lattice-mediated contributions to the flexoelectric tensor with publicly available DFT codes [41–44]. For this discussion, we will leave aside the continuum models, which have undoubtedly contributed to the phenomenological understanding of flexoelectricity, and we will focus exclusively on first-principles microscopic theories.

Our starting point for this brief introduction to flexoelectricity is the work by Tagantsev [125] in 1985, which was inspired by previous works of Born and Huang [117], and specifically by the method of long-waves. Tagantsev addressed the problem of flexoelectricity in crystalline dielectrics with a microscopic point-charge model. It should be noted, however, that only lattice-mediated contributions were included in this approach. It was not until 2010 that Resta [126] made the first attempt of incorporating the electronic contributions to a first-principles bulk theory of flexoelectricity. By building on the microscopic charge density response induced by a long-wavelength phonon, Resta was able to compute the longitudinal components of the flexoelectric tensor in elemental cubic crystals. This methodology was then generalized to arbitrary insulators by Hong and Vanderbilt [127, 128]. However, it became soon evident that in order to access the full tensorial form of the flexoelectric tensor, the charge density response was insufficient. Later on, Stengel [103] described the complete flexoelectric tensor in an arbitrary insulator within the context of DFPT by means of the microscopic current-density response to a long-wavelength acoustic phonon. Notably, this approach requires only the knowledge of the lowest terms in the Taylor expansion in $\mathbf{q}$ around Γ of linear-response functions that are readily available in standard DFT codes. Soon after, Dreyer *et al.* [98] developed an efficient first-principles current-density implementation for calculating the flexoelectric tensor, which avoided the construction of supercells by directly working with a single unit cell. Yet, this methodology requires numerous linear-response calculations on a $\mathbf{q}$ mesh, followed by a numerical differentiation in $\mathbf{q}$. In the context of the electronic response, the latter issue was resolved in 2019 by Royo and Stengel [41], by means of the analytical long-wavelength DFPT methodology that we have introduced in Sec. 2.4.4, where the flexoelectric tensor represents only a particular case of the general theory. Following the same approach, the lattice-mediated contributions were accounted for in 2022 [44], thus completing the entire picture.

For our scopes, only a handful lattice-mediated contributions are relevant. After providing some basic definitions, we shall study in the next section the ionic flexoelectric response of a crystal from long-wavelength acoustic phonons, following mainly the strategy by Stengel [103].

4.1.1 STRAIN AND STRAIN GRADIENTS

We shall characterize the deformation of a crystal lattice with a three-dimensional vector, $\mathbf{u}(\mathbf{r})$, which describes the displacement of an ion from its equilibrium position, $\mathbf{r}$, as follows,

$$r'_\alpha(\mathbf{r}) = r_\alpha(\mathbf{r}) + u_\alpha(\mathbf{r}), \tag{4.1}$$

where the *primed* vector, $\mathbf{r}'$, represents the new configuration and α is a Cartesian direction. The deformation gradient, i.e., the strain, is then defined as

$$u_{\alpha,\beta}(\mathbf{r}) = \frac{\partial u_\alpha(\mathbf{r})}{\partial r_\beta}, \tag{4.2}$$

which is usually indicated in the literature as the *unsymmetrized* strain tensor. By symmetrizing the indices, one readily obtains its *symmetrized* counterpart,

$$\varepsilon_{\alpha\beta}(\mathbf{r}) = \frac{1}{2}\left(u_{\alpha,\beta}(\mathbf{r}) + u_{\beta,\alpha}(\mathbf{r})\right). \tag{4.3}$$

Flexoelectricity deals with spatial gradients of the strain tensor. Similarly to the uniform strain case, the third-rank strain gradient tensor can be defined in two different ways; either as the gradient of the unsymmetrized strain, commonly known as type-I form,

$$u_{\alpha,\beta\gamma}(\mathbf{r}) = \frac{\partial u_{\alpha,\beta}(\mathbf{r})}{\partial r_\gamma}, \tag{4.4}$$

manifestly invariant under $\beta \leftrightarrow \gamma$ exchange, or in type-II form, i.e., as the gradient of the symmetrized strain,

$$\varepsilon_{\alpha\beta,\gamma}(\mathbf{r}) = \frac{\partial \varepsilon_{\alpha\beta}(\mathbf{r})}{\partial r_\gamma}, \tag{4.5}$$

which is invariant under the exchange $\alpha \leftrightarrow \beta$ by construction. It should be highlighted that both representations, type-I and type-II, contain the same number of independent tensor entries and physical information, but arranged differently. In other words, there exists a one-to-one correspondence between the two representations,

$$u_{\alpha,\beta\gamma}(\mathbf{r}) = \varepsilon_{\alpha\beta,\gamma}(\mathbf{r}) + \varepsilon_{\gamma\alpha,\beta}(\mathbf{r}) - \varepsilon_{\beta\gamma,\alpha}(\mathbf{r}). \tag{4.6}$$

4.1.2 LONG-WAVELENGTH ACOUSTIC PHONONS

One of the most challenging obstacles that one faces when dealing with flexoelectricity is that a strain gradient breaks the periodicity of the crystal lattice and, as a consequence, all the DFT machinery that we have described in Chapter 2 (the Bloch theorem, plane-waves, ...) seems, at first glance, impractical. To circumvent this issue, one considers, following a similar philosophy to that of Sec. 2.4.1, a long-wavelength acoustic phonon modulated by a wave vector **q**. It is then possible to prove [103] that at first and second orders in the wave vector, uniform strain (piezoelectricity) and strain gradient (flexoelectricity) effects are described, respectively. Mathematically, we represent a monochromatic phonon as

$$u^{l}_{\kappa\alpha}(t) = U^{\mathbf{q}}_{\kappa\alpha} e^{i(\mathbf{q}\cdot\mathbf{R}^{l}_{\kappa} - \omega t)}, \tag{4.7}$$

which is Eq. (2.74) but with our phase convention. The eigenvalue problem, as expressed by Eq. (2.75), then becomes

$$M_{\kappa}\omega^{2}_{\mathbf{q}} U^{\mathbf{q}}_{\kappa\alpha} = \sum_{\kappa',\beta} \Phi^{\mathbf{q}}_{\kappa\alpha,\kappa'\beta} U^{\mathbf{q}}_{\kappa'\beta}. \tag{4.8}$$

Following the long-wave strategy of Born and Huang [117], the latter equation is solved perturbatively in a vicinity of $\mathbf{q} = \mathbf{0}$ for the case of an acoustic phonon, i.e., $\omega_{\mathbf{q}\to\mathbf{0}} \longrightarrow 0$. It can be verified that [103, 117]

$$U^{\mathbf{q}}_{\kappa\alpha} = \sum_{\beta} U_{\beta}\left(\delta_{\alpha\beta} + i\sum_{\gamma} q_{\gamma}\Gamma^{\kappa}_{\alpha\beta\gamma} - \sum_{\gamma,\delta} q_{\gamma}q_{\lambda}N^{\kappa}_{\alpha\beta\gamma\lambda}\right) + \mathcal{O}(q^{3}). \tag{4.9}$$

Let us take a moment to discuss the respective significance of each item separately. The piezoelectric internal-strain tensor, $\Gamma^{\kappa}_{\alpha\beta\gamma}$, which appears at first-order in **q**, describes ionic relaxations produced by a strain, $u_{\beta,\gamma}$, and can be obtained by combining the piezoelectric force-response tensor, $\Lambda^{\kappa'}_{\lambda\beta\gamma}$, with the *pseudoinverse*[1] of the singular zone-center FC matrix, $\widetilde{\mathbf{\Phi}}^{(0)}$, as follows,

$$\Gamma^{\kappa}_{\alpha\beta\gamma} = \sum_{\kappa',\lambda} \widetilde{\Phi}^{(0)}_{\kappa\alpha,\kappa'\lambda}\Lambda^{\kappa'}_{\lambda\beta\gamma}. \tag{4.10}$$

The piezoelectric force-response tensor is, in turn, obtained via a summation of one of the sublattices of the first-order term in the long-wavelength expansion of the interatomic force-constants [see Eq. (3.47)],[2]

$$\Lambda^{\kappa}_{\alpha\beta\gamma} = \sum_{\kappa'} \Phi^{(1,\gamma)}_{\kappa\alpha,\kappa'\beta}. \tag{4.11}$$

Its physical interpretation is manifestly obvious: $\Lambda^{\kappa}_{\alpha\beta\gamma}$ accounts for the forces on the sublattice κ along the Cartesian direction α, produced by an applied strain, $u_{\beta,\gamma}$; it is invariant under $\beta \leftrightarrow \gamma$ exchange. Note that the sublattice summation of $\Lambda^{\kappa}_{\alpha\beta\gamma}$ identically vanishes,

$$\sum_{\kappa} \Lambda^{\kappa}_{\alpha\beta\gamma} = 0, \tag{4.12}$$

---

[1] Prescriptions on how to properly build the pseudoinverse of a singular matrix in this context are given in Ref. [129].

[2] The generalization of Eq. (4.11) in presence of nonvanishing forces was given in Eq. (3.49).

which states that a uniform strain does not produce a net force on the whole cell. On the other hand, $N^{\kappa}_{\alpha\beta\gamma\lambda}$, which appears at second order in $\mathbf{q}$ in Eq. (4.9), is the type-I flexoelectric internal-strain tensor, defined as

$$N^{\kappa}_{\alpha\beta\gamma\lambda} = \sum_{\kappa',\rho} \widetilde{\Phi}^{(0)}_{\kappa\alpha,\kappa'\rho} \hat{T}^{\kappa'}_{\rho\beta,\gamma\lambda}, \tag{4.13}$$

where we have also introduced the *mass-compensated* type-I flexoelectric force-response tensor,

$$\hat{T}^{\kappa}_{\alpha\beta,\gamma\lambda} = T^{\kappa}_{\alpha\beta,\gamma\lambda} - \frac{M_\kappa}{M} T_{\alpha\beta,\gamma\lambda}, \tag{4.14}$$

with

$$T^{\kappa}_{\alpha\beta,\gamma\lambda} = [\alpha\beta,\gamma\lambda]^{\kappa} + \frac{1}{2}\Big[(\alpha\gamma,\beta\lambda)^{\kappa} + (\alpha\lambda,\beta\gamma)^{\kappa}\Big], \tag{4.15}$$

where $M = \sum_\kappa M_\kappa$ is the total mass of the unit cell and $\mathbf{T} = \sum_\kappa \mathbf{T}^\kappa$. In Eq. (4.15), the square and round bracket symbols are given by

$$[\alpha\beta,\gamma\delta]^{\kappa} = -\frac{1}{2}\sum_{\kappa'} \Phi^{(2,\gamma\delta)}_{\kappa\alpha,\kappa\beta}, \tag{4.16a}$$

$$(\alpha\lambda,\beta\gamma)^{\kappa} = \sum_{\kappa',\rho} \Phi^{(1,\gamma)}_{\kappa\alpha,\kappa'\rho} \Gamma^{\kappa'}_{\rho\beta\gamma}. \tag{4.16b}$$

We have introduced a number of new symbols in the last few lines; let's pause for a moment to clarify their physical meaning. The (type-I) flexoelectric force-response tensor, $T^{\kappa}_{\alpha\beta,\gamma\lambda}$, describes the forces on the sublattice κ along the Cartesian direction α produced by an applied strain gradient, $u_{\beta,\gamma\lambda}$, where the square bracket symbol accounts for the clamped-ion (CI) response and the round bracket symbol describes the additional forces that are produced due to the ionic relaxations. The latter is a type-II object, meaning that $(\alpha\lambda,\beta\gamma)^{\kappa}$ describes the effect due to a *symmetrized* strain gradient, $\varepsilon_{\beta\gamma,\lambda}$; this explains the symmetrization in Eq. (4.15), since $\mathbf{T}^{\kappa}$ is a type-I object.

In contrast to the piezoelectric force-response tensor, the sublattice summation of $T^{\kappa}_{\alpha\beta,\gamma\lambda}$ does not vanish. This means that some care is required when multiplying it with the pseudoinverse of the zone-center FC matrix in Eq. (4.13). The issue in question has been resolved in Eq. (4.14) by imposing the constraint that $\sum_\kappa \hat{T}^{\kappa} = 0$ via the new *mass-compensated* [103] symbol. In principle, infinitely different *flavors* of $\hat{\mathbf{T}}^{\kappa}$ exist,

$$\hat{T}^{\kappa}_{\alpha\gamma,\beta\lambda} = T^{\kappa}_{\alpha\gamma,\beta\lambda} - \frac{w_\kappa}{\sum_{\kappa''} w_{\kappa''}} \sum_{\kappa'} T^{\kappa'}_{\alpha\gamma,\beta\lambda}, \tag{4.17}$$

where w_κ are arbitrary weights. Within our choice, the weights correspond to the physical atomic masses of the sublattices, but other options are equally valid [128].

4.1.2.1 *Type-II objects and the "elastic sum rule"*

In type-II form, Eq. (4.13) translates to

$$L^{\kappa}_{\rho\lambda,\beta\gamma} = \sum_{\kappa',\gamma} \widetilde{\Phi}^{(0)}_{\kappa\rho,\kappa'\alpha} \hat{C}^{\kappa}_{\alpha\lambda,\beta\gamma}, \tag{4.18}$$

where $\mathbf{L}^{\kappa}$ and $\hat{\mathbf{C}}^{\kappa}$ are, respectively, the type-II flexoelectric internal-strain tensor and the type-II *mass-compensated* flexoelectric force-response tensor. The latter is related to its type-I counterpart by the following rearrangement of the indices,

$$\hat{C}^{\kappa}_{\alpha\lambda,\beta\gamma} = \hat{T}^{\kappa}_{\alpha\beta,\gamma\lambda} + \hat{T}^{\kappa}_{\alpha\gamma,\lambda\beta} - \hat{T}^{\kappa}_{\alpha\lambda,\beta\gamma}. \tag{4.19}$$

In a similar spirit as the approach taken with the type-I objects, $\hat{\mathbf{C}}^{\kappa}$ is defined so that the sublattice sum of its components trivially vanishes,

$$\hat{C}^{\kappa}_{\alpha\lambda,\beta\gamma} = C^{\kappa}_{\alpha\lambda,\beta\gamma} - \frac{M_{\kappa}}{M}\Omega\mathcal{C}_{\alpha\lambda,\beta\gamma}, \tag{4.20}$$

where

$$C^{\kappa}_{\alpha\lambda,\beta\gamma} = [\alpha\beta,\gamma\lambda]^{\kappa} + [\alpha\gamma,\lambda\beta]^{\kappa} - [\alpha\lambda,\beta\gamma]^{\kappa} + (\alpha\lambda,\beta\gamma)^{\kappa} \tag{4.21}$$

and

$$\mathcal{C}_{\alpha\lambda,\beta\gamma} = \frac{1}{\Omega}\sum_{\kappa} C^{\kappa}_{\alpha\lambda,\beta\gamma}, \tag{4.22}$$

where Ω is, as customary, the volume of the unit cell. The advantage of expressing the tensors in their type-II form is that their physical meaning becomes more aparent: $\boldsymbol{\mathcal{C}}$ is, in fact, the elastic tensor [117]. The relationship between the sublattice sum of the type-II flexoelectric force-response tensor and the macroscopic elastic tensor also holds true at the CI level,

$$\bar{\mathcal{C}}^{\text{HWRV}}_{\alpha\lambda,\beta\gamma} = \frac{1}{\Omega}\sum_{\kappa} \bar{C}^{\kappa}_{\alpha\lambda,\beta\gamma}, \tag{4.23}$$

with

$$\bar{C}^{\kappa}_{\alpha\lambda,\beta\gamma} = [\alpha\beta,\gamma\lambda]^{\kappa} + [\alpha\gamma,\lambda\beta]^{\kappa} - [\alpha\lambda,\beta\gamma]^{\kappa}, \tag{4.24}$$

where we have used the label "HWRV" in Eq. (4.23) to explicitly indicate that the sublattice sum of the type-II CI flexoelectric force-response tensor gives rise to the CI macroscopic elastic tensor, which is routinely computed in standard DFT codes with the metric-tensor formulation as proposed by HWRV, as described in Sec. 2.3.5.

4.1.3 FLEXOCOUPLING COEFFICIENTS

One of the most notable physical manifestations of the flexoelectric force-response tensor is the flexocoupling tensor, which accounts for the forces on the zone-center polar modes of the system produced by the applied strain gradient, and can be expressed in the following way [106, 130],

$$f_{\alpha\lambda,\beta\gamma} = \sum_{\kappa,\rho}\sqrt{\frac{M}{M_{\kappa}}}P^{(\alpha)}_{\kappa\rho}\bar{C}^{\kappa}_{\rho\lambda,\beta\gamma}. \tag{4.25}$$

[Note that we are defining the flexocoupling coefficients in Eq. (4.25) in terms of the CI type-II flexoelectric force-response tensor. In general, additional contributions coming from the round bracket symbol are present, see Eq. (4.16b). However, as we shall see shortly, we will restrict our analysis to materials enjoying $Pm\bar{3}m$ cubic

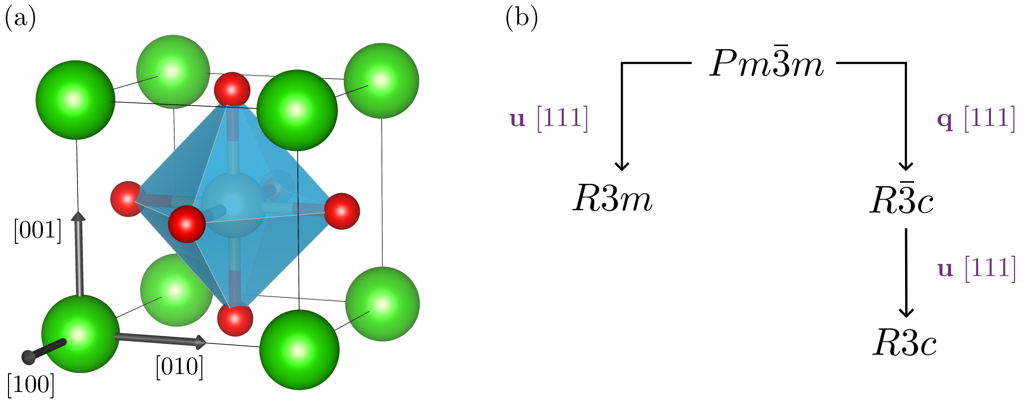

Figure 4.1: (a) Unit cell of cubic $LiOsO_3$. Grey arrows in indicate the crystallographic directions that form the Cartesian axes. (b) Schematic representation of the relevant phases of $LiOsO_3$, where **u** is the polar order parameter and **q** is used to described the antiferrodistortive (AFD) oxygen tilts (see Sec. 4.5).

symmetry, where these contributions identically vanish by symmetry.] In Eq. (4.25), $\mathbf{P}^{(\alpha)}$ is a normalized $3 \times N$ dimensional polar eigenvector of the zone-center ($\mathbf{q} = \mathbf{0}$) dynamical matrix, where N is the number of atoms in the cell and the label α determines which of the eigenvectors that span the polar space is chosen. These vectors satisfy the following eigenvalue problem,

$$[\omega^{(\alpha)}]^2 P^{(\alpha)}_{\kappa\rho} = \sum_{\kappa',\beta} D^{(0)}_{\kappa\rho,\kappa'\beta} P^{(\alpha)}_{\kappa'\beta}, \tag{4.26}$$

where $\omega^{(\alpha)}$ is the frequency and $\mathbf{D}^{(0)}$ is the zone-center dynamical matrix, which is related to the zone-center FC matrix via the usual mass factor,

$$D^{(0)}_{\kappa\alpha,\kappa'\beta} = \frac{\Phi^{(0)}_{\kappa\alpha,\kappa'\beta}}{\sqrt{M_\kappa M_{\kappa'}}}. \tag{4.27}$$

Observe that Eq. (4.25) represents simply the projection of $\bar{\mathbf{C}}^{\kappa}$ on the zone-center polar modes, where the prefactor $\sqrt{M/M_\kappa}$ follows the convention of earlier works [106, 130] and is consistent with the choice we made earlier of identifying the arbitrary weights w_κ with the physical atomic masses of the sublattices. Notice that, by definition, if $\bar{\mathbf{C}}^{\kappa}$ is projected on the acoustic modes in Eq. (4.25), one readily recovers (apart from a trivial volume factor) the CI elastic tensor as defined in Eq. (4.23).

4.2 STATEMENT OF THE PROBLEM

A cartoon representing the cubic phase of $LiOsO_3$ is provided in Fig. 4.1, accompanied by a schematic illustration of its relevant phases upon the release of different degrees of freedom, where $R3c$ is the polar phase of interest. The physical mechanism that allows a strain gradient mediated switching of the polar order parameter

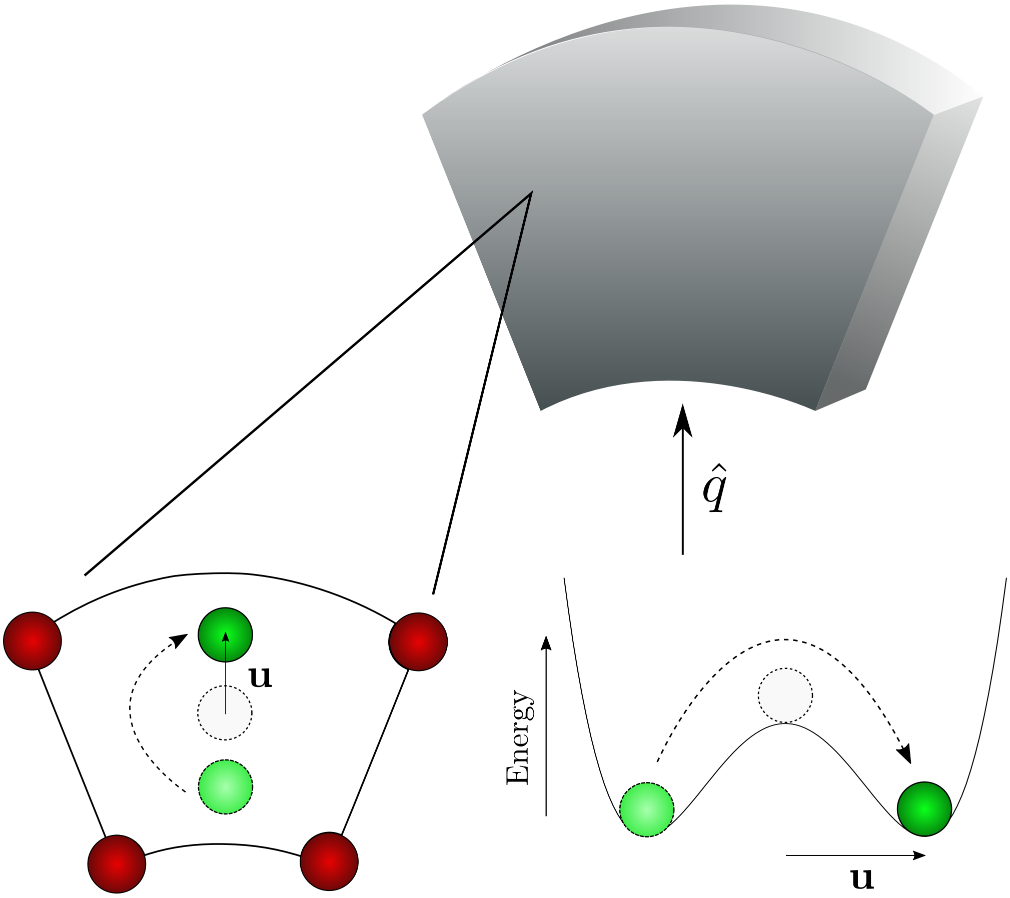

Figure 4.2: A bending-type strain gradient is applied to a macroscopic crystal along the direction $\hat{q}$. The external strain gradient couples to the polar modes resulting in a displacement of the atoms and, as a consequence, the structure evolves to another symmetrically equivalent "ferroelectric" state.

is schematically illustrated in Fig. 4.2. The basic idea here is that the applied macroscopic strain gradient couples to the zone-center polar modes via the flexocouplings defined in Sec. 4.1.3 and, by pushing the atoms via a geometric or elastic force, the structure evolves into another symmetrically equivalent "ferroelectric" state. In a prototypical ferroelectric material, e.g., $BaTiO_3$, the different ferroelectric states are distinguished by measuring the change in the electric polarization when the system evolves from one ferroelectric state to another. When dealing with metals, we will measure the *polarity* of the system by the amplitude of the polar order parameter, and thus, the distinction between two "ferroelectric" states turns out to be purely geometrical [39, 131, 132]. Within the bulk region, the polar order parameter is assumed to be homogeneous and its amplitude will be described by a three dimensional vector, **u**, with the physical dimension of length. Our goal is to estimate the amount of bending that needs to be applied so that the polar order parameter can be switched between two equivalent "ferroelectric" states. This shall be quantified by the critical bending radius, which we compute as

$$R_{\text{crit}} = \frac{f_{\text{eff}}}{F_{\text{coerc}}}, \tag{4.28}$$

where f_{eff} is the effective flexocoupling coefficient associated with the flexural deformation and F_{coerc} is the *generalized* force that is required to cross the energy barrier between two minima. Therefore, the problem can be divided into two separate tasks: (i) determining the coupling between a strain gradient and the polar mode, which is described by f_{eff} and depends on the crystallographic orientation, and (ii) identifying the most likely switching paths and the corresponding energetics. The main technical challenge here resides in (i), since no established methods exist for the calculation of f_{eff} in metals: we shall explain in detail the strategy we shall follow in the next section. In order to tackle task (ii), we will follow the well-established practice with ferroelectrics and assume a Landau-like expansion of the energy around the high-symmetry cubic phase as a function of the relevant parameters, which involves mapping the potential energy landscape of the system as a function of the main degrees of freedom; this procedure has been efficiently applied to a wide variety of materials already [133, 134]. In this context, the computation of F_{coerc} entails no significant challenges.

4.3 COMPUTATIONAL STRATEGY

We now focus on describing the computational strategy that we will follow to compute the flexocoupling coefficients in a metal. According to Eq. (4.25), only two ingredients are required: the zone-center polar eigenvectors of the dynamical matrix, which are straightforward to obtain, and the flexoelectric force-response tensor. We will address the latter in the following.

4.3.1 ANALYTICAL LONG-WAVELENGTH METHOD

The first approach, which we shall prefer from a computational perspective, consists in applying the ensemble DFPT formalism that we have developed in Chapter 3 in the context of strain gradients, so that we can obtain the flexoelectric force-response tensor of metals as an analytical long-wavelength expansion of the second-order energy. Notice that directly applying the formulas of Sec. 3.3.3 to the calculation of $\bar{\mathbf{C}}^{\kappa}$ is not possible, as they target first-order terms in $\mathbf{q}$ and $\bar{\mathbf{C}}^{\kappa}$ is, in fact, related to the *second* $\mathbf{q}$ gradient of the FC matrix, as shown by Eq. (4.16a) and Eq. (4.24). However, observe that the square bracket symbol, from which $\bar{\mathbf{C}}^{\kappa}$ is constructed, only requires the sublattice sum of the $\mathbf{\Phi}^{(2)}$ coefficients, which physically corresponds to the force-response to an acoustic phonon perturbation. We have already seen in Sec. 2.4.1 that acoustic phonons can be conveniently recast, via a coordinate transformation to the comoving frame, into a metric-wave perturbation. This allows us to write the flexoelectric force-response coefficients as the first-order dispersion of the piezoelectric force-response tensor [44]. In light of this, the whole story boils down to applying the ensemble DFPT theory developed in Chapter 3 to the case in which $\lambda_1 = \tau_{\kappa\alpha}$ and $\lambda_2 = \eta_{\beta\delta}$, where $\boldsymbol{\eta}$ denotes the uniform strain perturbation as defined in Sec. 2.3.5. In practice, the type-II representation of the flexoelectric force-response tensor exhibits the following formulation [44],

$$\bar{C}^{\kappa}_{\alpha\gamma,\beta\delta} = E^{\tau_{\kappa\alpha}\eta_{\beta\delta}}_{\mathrm{st},\gamma} + E^{\tau_{\kappa\alpha}\eta_{\beta\delta}}_{\mathrm{nv},\gamma} . \tag{4.29}$$

Remarkably, the nonvariational contribution takes the exact same form as that observed in insulators [44], the only difference being that, instead of assuming that all the active states are completely filled (this is the case in insulators as the active subspace is usually restricted to the valence manifold), the occupation function $f_{m\mathbf{k}}$ must be taken into account for each band m and $\mathbf{k}$ point. The stationary part is given by

$$\begin{aligned} E^{\tau_{\kappa\alpha}\eta_{\beta\delta}}_{\mathrm{st},\gamma} = &\int_{\mathrm{BZ}} [d^3k] \left(2\bar{E}^{\tau_{\kappa\alpha}\eta_{\beta\delta}}_{\mathbf{k},\gamma} + \Delta E^{\tau_{\kappa\alpha}\eta_{\beta\delta}}_{\mathbf{k},\gamma} \right) \\ &+ i \int_{\Omega} \int n^{\tau_{\kappa\alpha}*}(\mathbf{r}) K_{\gamma}(\mathbf{r},\mathbf{r}') n^{\eta_{\beta\delta}}(\mathbf{r}')\, d^3r\, d^3r', \end{aligned} \tag{4.30}$$

where the wave function term acquires [44] the same form as for the insulating case,

$$\begin{aligned} \bar{E}^{\tau_{\kappa\alpha}\eta_{\beta\delta}}_{\mathbf{k},\gamma} =& i \sum_{m\in\mathcal{M}} f_{m\mathbf{k}} \langle u^{\tau_{\kappa\alpha}}_{m\mathbf{k}} | \hat{H}^{k_\gamma}_{\mathbf{k}} | u^{\eta_{\beta\delta}}_{m\mathbf{k}} \rangle \\ &- i \sum_{m,n\in\mathcal{M}} f_{m\mathbf{k}} \langle u^{\tau_{\kappa\alpha}}_{m\mathbf{k}} | u^{k_\gamma}_{n\mathbf{k}} \rangle \, \langle u^{(0)}_{n\mathbf{k}} | \hat{\mathcal{H}}^{\eta_{\beta\delta}}_{\mathbf{k}} | u^{(0)}_{m\mathbf{k}} \rangle \\ &- i \sum_{m,n\in\mathcal{M}} f_{m\mathbf{k}} \langle u^{(0)}_{m\mathbf{k}} | (\hat{\mathcal{H}}^{\tau_{\kappa\alpha}}_{\mathbf{k}})^{\dagger} | u^{(0)}_{n\mathbf{k}} \rangle \, \langle u^{k_\gamma}_{n\mathbf{k}} | u^{\eta_{\beta\delta}}_{m\mathbf{k}} \rangle \\ &+ \sum_{m\in\mathcal{M}} f_{m\mathbf{k}} \left(\frac{1}{2} \langle u^{\tau_{\kappa\alpha}}_{m\mathbf{k}} | \hat{H}^{\eta_{\beta\delta}}_{\mathbf{k},\gamma} | u^{(0)}_{m\mathbf{k}} \rangle + i \langle u^{(0)}_{m\mathbf{k}} | (\hat{\mathcal{H}}^{\tau_{\kappa\alpha}}_{\mathbf{k}})^{\dagger} | u^{\eta_{\beta\delta}}_{m\mathbf{k}} \rangle \right), \end{aligned} \tag{4.31}$$

and the occupation term, specific to metals, reads as

$$\begin{aligned} \Delta E^{\tau_{\kappa\alpha}\eta_{\beta\delta}}_{\mathbf{k},\gamma} =& i \sum_{m,n\in\mathcal{M}} \bar{f}_{mn\mathbf{k}} \langle u^{(0)}_{m\mathbf{k}} | (\hat{H}^{\tau_{\kappa\alpha}}_{\mathbf{k},\gamma})^{\dagger} | u^{(0)}_{n\mathbf{k}} \rangle \, \langle u^{(0)}_{n\mathbf{k}} | \hat{\mathcal{H}}^{\eta_{\beta\delta}}_{\mathbf{k}} | u^{(0)}_{m\mathbf{k}} \rangle \\ &+ \frac{1}{2} \sum_{m,n\in\mathcal{M}} \bar{f}_{mn\mathbf{k}} \langle u^{(0)}_{m\mathbf{k}} | (\hat{\mathcal{H}}^{\tau_{\kappa\alpha}}_{\mathbf{k}})^{\dagger} | u^{(0)}_{n\mathbf{k}} \rangle \, \langle u^{(0)}_{n\mathbf{k}} | \hat{H}^{(\beta\delta)}_{\mathbf{k},\gamma} | u^{(0)}_{m\mathbf{k}} \rangle \\ &+ i \sum_{m,n\in\mathcal{M}} \bar{f}_{mn\mathbf{k}} \langle u^{(0)}_{m\mathbf{k}} | (\hat{\mathcal{H}}^{\tau_{\kappa\alpha}}_{\mathbf{k}})^{\dagger} | u^{k_\gamma}_{n\mathbf{k}} \rangle \, \langle u^{(0)}_{n\mathbf{k}} | \hat{\mathcal{H}}^{\eta_{\beta\delta}}_{\mathbf{k}} | u^{(0)}_{m\mathbf{k}} \rangle \\ &+ i \sum_{m,n\in\mathcal{M}} \bar{f}_{mn\mathbf{k}} \langle u^{(0)}_{m\mathbf{k}} | (\hat{\mathcal{H}}^{\tau_{\kappa\alpha}}_{\mathbf{k}})^{\dagger} | u^{(0)}_{n\mathbf{k}} \rangle \, \langle u^{k_\gamma}_{n\mathbf{k}} | \hat{\mathcal{H}}^{\eta_{\beta\delta}}_{\mathbf{k}} | u^{(0)}_{m\mathbf{k}} \rangle \\ &+ i \sum_{m,n,l\in\mathcal{M}} \mathcal{F}_{mnl\mathbf{k}} \langle u^{(0)}_{m\mathbf{k}} | (\hat{\mathcal{H}}^{\tau_{\kappa\alpha}}_{\mathbf{k}})^{\dagger} | u^{(0)}_{n\mathbf{k}} \rangle \, \langle u^{(0)}_{n\mathbf{k}} | \hat{H}^{k_\gamma}_{\mathbf{k}} | u^{(0)}_{l\mathbf{k}} \rangle \, \langle u^{(0)}_{l\mathbf{k}} | \hat{\mathcal{H}}^{\eta_{\beta\delta}}_{\mathbf{k}} | u^{(0)}_{m\mathbf{k}} \rangle . \end{aligned} \tag{4.32}$$

The additional contributions coming from the macroscopic electrostatics, which were discussed for phonons in Sec. 3.3.4, should also be taken into account in the present context with strain gradients. Once again, the second derivatives in $\mathbf{q}$ can be avoided by treating the acoustic phonon perturbation in the comoving frame as a metric-wave perturbation. It is straightforward to verify, starting from Eq. (3.46), that the macroscopic electrostatic contribution reads as

$$E_{\mathrm{mac},\gamma}^{\tau_{\kappa\alpha}\eta_{\beta\delta}} \simeq -\delta_{\alpha\gamma} Z_{\kappa} \mu^{\eta_{\beta\delta}}, \tag{4.33}$$

where $\mu^{\eta_{\beta\delta}}$ is the Fermi level shift produced by a uniform strain.

4.3.2 LATTICE SUMS OF REAL-SPACE IFC

An alternative, although less sophisticated approach, involves expressing the derivatives in **q** of the FC matrix as real-space sums of the IFCs,

$$\Phi_{\kappa\alpha,\kappa'\beta}^{(2,\gamma\delta)} = \sum_{l} \Phi_{\kappa\alpha,\kappa'\beta}(0,l)(\mathbf{R}_{\kappa}^{0} - \mathbf{R}_{\kappa'}^{l})_{\gamma}(\mathbf{R}_{\kappa}^{0} - \mathbf{R}_{\kappa'}^{l})_{\delta}. \tag{4.34}$$

One can then obtain $\bar{\mathbf{C}}^{\kappa}$ via Eq. (4.16a) and Eq. (4.24). It is important to note that Eq. (4.34) relies on an underlying assumption: the rapid decay of the IFCs as a function of $\left|\mathbf{R}_{\kappa}^{0} - \mathbf{R}_{\kappa'}^{l}\right|$. This condition is clearly violated in insulators, where the long-range nature of the electrostatic interactions thwarts obtaining a convergent result for the sums. Long-range interactions can also be present in metals when working at very low temperatures. The reason for this, which was already briefly discussed in Sec. 2.3.2, is that the Fermi-Dirac occupation function might suffer from sharp discontinuities near the Fermi level, which leads to the so-called Kohn anomalies. In practice, a finite electronic temperature, which we impose by smearing the occupation function, guarantees that the IFCs are short-ranged and that the lattice sums of Eq. (4.34) will eventually converge to the correct physical value when a dense enough **q**-point mesh is used in the calculations.

4.3.3 EFFECTIVE FLEXOCOUPLING COEFFICIENTS IN CUBIC CRYSTALS

It is also pertinent to stress that the flexocoupling coefficients computed from Eq. (4.25) require manipulation prior to obtaining the effective flexocoupling that appears in the denominator of Eq. (4.28). This involves two steps. First, one needs to define the geometry of the system to which the flexural deformation is applied, e.g., a beam or a slab. Here, we shall consider a beam sample, where one of the dimensions of the system, e.g., the length, is much greater than its width and height.

In cubic crystals, there are only three linearly independent components of the flexocoupling tensor, which are commonly denoted in the literature as longitudinal ($f_{11} = f_{xx,xx}$), transverse ($f_{12} = f_{xx,yy}$) and shear ($f_{44} = f_{xy,xy}$); the same holds for the elastic tensor as well. It is shown in Ref. [135] that

$$\begin{aligned} f_{\mathrm{eff}}^{100} &= \frac{-\mathcal{C}_{12}}{\mathcal{C}_{11}+\mathcal{C}_{12}} f_{11} + \frac{\mathcal{C}_{11}}{\mathcal{C}_{11}+\mathcal{C}_{12}} f_{12}, \\ f_{\mathrm{eff}}^{110} &= A f_{11} + B f_{12} - 2(1-A) f_{44}, \\ f_{\mathrm{eff}}^{111} &= \frac{\mathcal{C}_{44}}{\mathcal{C}_{11}+2\mathcal{C}_{12}+\mathcal{C}_{44}}(f_{11}+2f_{12}) - \frac{\mathcal{C}_{11}+2\mathcal{C}_{12}}{\mathcal{C}_{11}+2\mathcal{C}_{12}+\mathcal{C}_{44}} f_{44}, \end{aligned} \tag{4.35}$$

with

$$
\begin{aligned}
A &= \frac{2\mathcal{C}_{11}\mathcal{C}_{44}}{(\mathcal{C}_{11}-\mathcal{C}_{12})(\mathcal{C}_{11}+2\mathcal{C}_{12})+2\mathcal{C}_{11}\mathcal{C}_{44}}, \\
B &= \frac{2(\mathcal{C}_{11}-2\mathcal{C}_{12})\mathcal{C}_{44}}{(\mathcal{C}_{11}-\mathcal{C}_{12})(\mathcal{C}_{11}+2\mathcal{C}_{12})+2\mathcal{C}_{11}\mathcal{C}_{44}},
\end{aligned}
\tag{4.36}
$$

where f_{eff}^{100}, f_{eff}^{110} and f_{eff}^{111} are the effective flexocoupling coefficients for the [100], [110] and [111] orientations of the sample for the beam-bending limit. Notice that an accurate calculation of $\boldsymbol{\mathcal{C}}$ is a necessary and crucial preliminary step, since the elastic tensor is by itself a key ingredient in the calculation of the effective flexocoupling coefficients.

Second, one should take into account that for each surface orientation $\hat{\mathbf{q}}$, the effective flexocoupling describes the force induced by the flexural deformation acting on the polar modes along $\hat{\mathbf{q}}$. However, such force might not be parallel to the direction $\hat{\mathbf{s}}$ along which the polar order parameter evolves during switching. In such cases, the effective flexocoupling needs to be scaled by the projection $\hat{\mathbf{q}} \cdot \hat{\mathbf{s}}$. Implications of the latter shall be discussed in the following subsections with $LiOsO_3$ and $BaTiO_3$ as test cases.

4.4 FLEXOCOUPLING COEFFICIENTS OF $LiOsO_3$

We now turn to one of the central themes of this chapter: the computation of the flexocoupling tensor in a metal.

Our calculations on cubic $LiOsO_3$ are carried out with norm-conserving pseudopotentials under the generalized gradient approximation (GGA) with Perdew-Burke-Ernzerhof (PBE) exchange-correlation functionals [82], which we take from the Pseudo Dojo [120] website. In order to test the robustness of our analytical long-wavelength DFPT methodology (see Sec. 4.3.1), we also employ pseudopotentials with the Perdew-Wang [81] parametrization of the local density approximation (LDA). With the long-wave DFPT methodology, we use a plane-wave cutoff of 60 Ha, a Gaussian smearing of 0.01 Ha and the Brillouin Zone is sampled with a dense $20 \times 20 \times 20$ $\mathbf{k}$-mesh. With the alternative method based on lattice sums of the IFCs, we also employ a plane-wave cutoff of 60 Ha and a Gaussian smearing of 0.01 Ha, but the BZ is sampled with $16 \times 16 \times 16$ $\mathbf{k}$ points.[3]

To start with, we show in Fig. 4.3 the convergence of the flexocoupling coefficients of cubic $LiOsO_3$ and the elastic tensor, computed either with our long-wave DFPT approach via Eq. (4.23) or directly with the HWRV method. For comparison purposes, we also present in Fig. 4.4 the convergence of the flexocoupling and elastic tensor as a function of the two dimensional grid of $\mathbf{q}$ points, for a fixed $\mathbf{k}$-point mesh, computed with the alternative methodology based on sums of the real-space IFCs, see Eq. (4.34). (For cubic systems, a two dimensional grid of $\mathbf{q}$ points is

---

[3] The reason why we did not go up to $20 \times 20 \times 20$ $\mathbf{k}$ points with the latter method is that, in contrast to the analytical long-wave DFPT approach, which works directly at the Γ point, the method based on sums of the IFCs involves computing the FC matrix in a dense $\mathbf{q}$-point mesh, making it computationally more demanding. It is, however, adequate to double check our recently implemented long-wave DFPT methodology in metals.

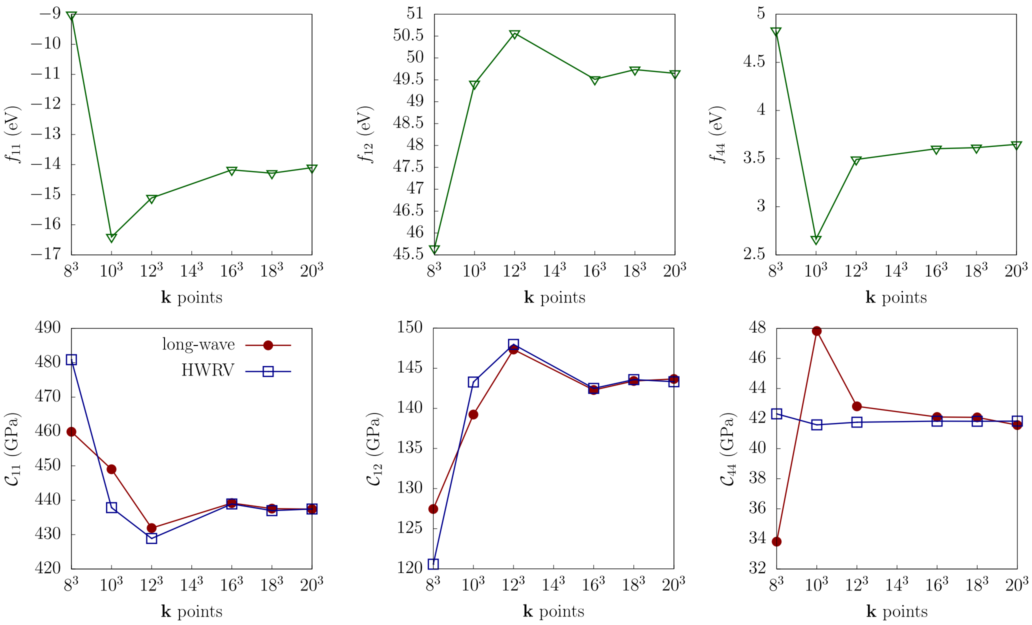

Figure 4.3: Convergence of the three independent components of the flexocoupling tensor (top) and the elastic tensor (bottom) of cubic LiOsO$_3$, as a function of the **k** mesh. Results are obtained with the Perdew-Wang parametrization of the LDA. Solids lines are a guide to the eye.

enough to calculate the three independent components of the mentioned tensors.) Note that in Fig. 4.4, for a $16 \times 16 \times 1$ mesh of **q** points convergence is reached for the elastic constants (the reference values obtained with the HWRV method are indicated with dashed lines) and, as a consequence, for the flexocoupling tensor. Remember that both calculations are carried out using the same method, so similar convergence rates and errors are expected.

Table 4.1 presents the numerical values of the calculated independent components for the flexoelectric force-response tensor, along with the numerical validation of the elastic sum rule, Eq. (4.23), which is verified to a high degree of accuracy. Additionally, the last two rows of Table 4.1 display the independent components of the flexocoupling tensor, computed by means of Eq. (4.25). The penultimate row shows the numerical values obtained with the analytical long-wave method, whereas the last row corresponds to the results obtained via sums of real-space IFCs. The agreement between the results derived from the analytical long-wave method and those obtained through lattice sums of the real-space IFCs is remarkable, particularly given the diverse computational strategies employed with each method. Regarding the effect of different schemes for the exchange-correlation functional, we observe that the equilibrium volume slightly differs between LDA and GGA, following the expected trends: we obtain $\Omega = 362.756$ bohr^3 and $\Omega = 381.532$ bohr^3, respectively. In general, the calculated values for the flexoelectric force-response tensor and the flexocoupling coefficients show only a small dependence on the choice of the exchange and correlation model.

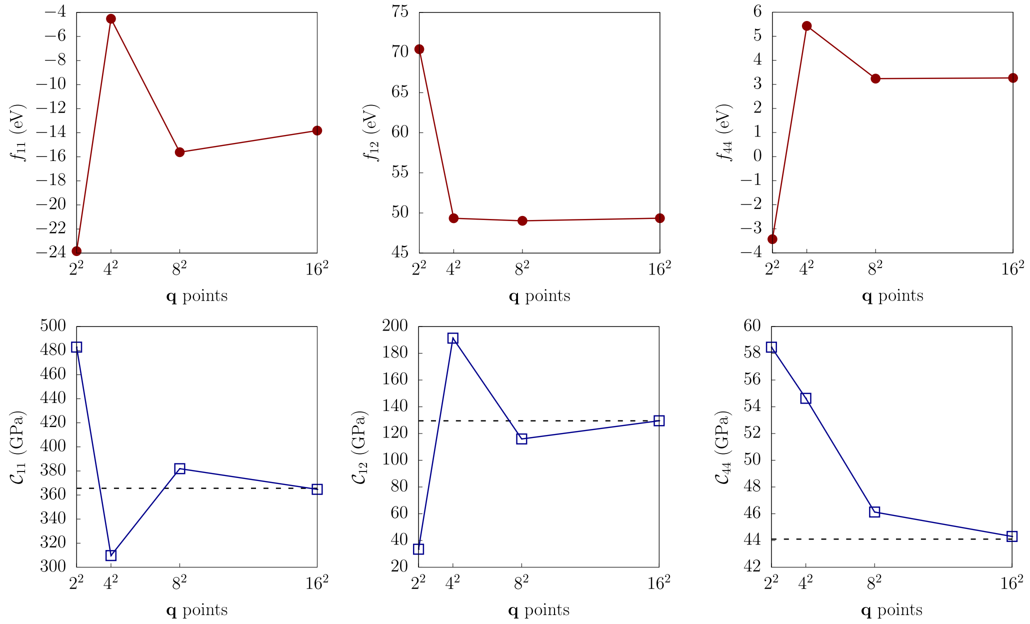

Figure 4.4: Convergence of the three independent components of the flexocoupling (top) and the elastic (bottom) tensor, computed via lattice sums of the real-space IFCs, Eq. (4.34), with respect to the two-dimensional grid of **q** points. Dashed lines represent the reference values of the elastic constants computed with DFPT. Solids lines are a guide to the eye.

	xx, xx		xx, yy		xy, xy	
Atom	LDA	PBE	LDA	PBE	LDA	PBE
Li	0.95	0.75	10.22	9.99	0.30	0.32
Os	62.97	58.18	24.77	22.67	16.02	15.90
O_1	−1.08	−0.99	−2.80	−2.44	−3.28	−3.37
O_2	−1.08	−0.99	9.84	10.13	−0.63	−0.01
O_3	85.00	71.51	6.17	5.07	1.54	2.70
$\bar{C}_{\alpha\gamma,\beta\delta}$	437.42	364.05	143.67	128.73	41.57	44.04
$\bar{C}^{\text{HWRV}}_{\alpha\gamma,\beta\delta}$	437.44	364.19	143.31	128.63	41.83	44.16
Sums of IFCs	...	364.72	...	129.54	...	44.30
$f_{\alpha\gamma,\beta\delta}$	−14.10	−14.24	49.65	47.56	3.69	3.33
Sums of IFCs	...	−13.81	...	49.35	...	3.26

Table 4.1: Linearly independent components of the flexoelectric force-response tensor (in eV), the clamped-ion elastic tensor (in GPa) and the flexocoupling tensor (in eV) for cubic LiOsO_3. Values are obtained either with the Perdew-Wang parametrization of the LDA or with the PBE parametrization of the GGA.

	C_{11}	C_{12}	C_{44}	f_{11}	f_{12}	f_{44}
Long-wave	353.09	121.44	137.74	−55.75	3.87	−41.26
HWRV	353.47	121.79	137.75	⋯	⋯	⋯

Table 4.2: Independent components of the calculated elastic (in GPa) and flexocoupling (in eV) tensor of cubic $BaTiO_3$. The *n*-type flexocoupling coefficients [106] of $BaTiO_3$ are shown.

	$\lvert f_{\mathrm{eff}}^{100}\rvert$	$\lvert f_{\mathrm{eff}}^{110}\rvert$	$\lvert f_{\mathrm{eff}}^{111}\rvert$
$LiOsO_3$	40.1	5.3	2.5
$BaTiO_3$	17.1	25.9	24.5

Table 4.3: Effective flexocoupling coefficients (absolute values in eV units) for [100], [110] and [111] oriented samples, in the beam-bending limit.

Clearly, the largest flexocoupling coefficient (in absolute value) of cubic $LiOsO_3$ is f_{12}. It should be noted that prior to this study, there were no values in the literature for flexocoupling coefficients in metals, which makes it difficult to evaluate whether the obtained coupling parameters are in fact relevant in magnitude or not. To contextualize these results, we show in Table 4.2 the calculated flexocoupling coefficients of cubic $BaTiO_3$, along with the elastic constants, which are calculated either directly with DFPT via the HWRV method, or with the elastic sum rule given by Eq. (4.23). (In order to avoid any potential disruption to the reading, we show in the main text the final results and we shall defer all the details concerning the study of $BaTiO_3$ to Appendix B.) It is worth noting that $BaTiO_3$ behaves very similarly to $SrTiO_3$ [106], which is natural to expect given the affinities in the electronic and atomic structure. The absolute values of the flexocoupling coefficients of $LiOsO_3$ and $BaTiO_3$ are similar overall, which provides a first indication that the flexocoupling is comparably strong in these two materials.

To make further progress, we compute the effective flexocouplings for three representative orientations of the sample by means of Eq. (4.35). The obtained numerical results[4] are shown in Table 4.3. It is indisputably [100] the bending direction that produces the largest flexocoupling in lithium osmate. The situation in $BaTiO_3$ seems to be more balanced overall, with a slight preference for [110] and [111] directions over [100].

Nevertheless, as we have previously stated, this is just one of the two necessary ingredients for the computation of the critical bending radius, Eq. (4.28). In the following, we shall study the possible switching paths of the polar order parameter by means of a first-principles based effective Hamiltonian.

---

[4] To construct the effective flexocoupling coefficients of lithium osmate, we use our calculations with the PBE parametrization of the GGA from Table 4.1, obtained via the lattice sums of the IFCs. In any case, the flexocoupling coefficients are sufficiently robust with respect to the employed computational methodology (i.e., analytical long-wave DFPT method or lattice sums of the IFCs) to ensure that the results of Table 4.3 remain consistent, regardless of the previous choice.

4.5 FIRST-PRINCIPLES EFFECTIVE HAMILTONIAN

In order to extract information about the possible switching paths for the polar order parameter, we construct a Landau-Ginzburg-Devonshire-type first-principles effective Hamiltonian by expanding the energy around the reference cubic phase, with $P3\bar{m}3$ symmetry, in terms of the relevant degrees of freedom. We consider the strain in Voigt notation, s_i, the tilts of the oxygen ocathedra, q_i, where q_i represents the displacements of the oxygen atoms perpendicular to the rotation axis and the polar order parameter, u_i. The continuum model for the effective Hamiltonian that we shall use to describe the relevant phases in LiOsO$_3$ (see Fig. 4.1) is given by the following expression,

$$H_{\text{eff}}[\mathbf{s},\mathbf{q},\mathbf{u}] = H_{\text{s}}[\mathbf{s}] + H_{\text{q}}[\mathbf{q}] + H_{\text{u}}[\mathbf{u}] + H_{\text{sq}}[\mathbf{s},\mathbf{q}] + H_{\text{su}}[\mathbf{s},\mathbf{u}] + H_{\text{uq}}[\mathbf{u},\mathbf{q}], \tag{4.37}$$

where the individual contributions are defined as

$$H_{\text{s}}[\mathbf{s}] = \frac{\widetilde{\Omega}}{2}\mathcal{C}_{11}(s_1^2+s_2^2+s_3^2) + \widetilde{\Omega}\mathcal{C}_{12}(s_1s_2+s_1s_3+s_2s_3) + \frac{\widetilde{\Omega}}{2}\mathcal{C}_{44}(s_4^2+s_5^2+s_6^2), \tag{4.38}$$

$$H_{\text{q}}[\mathbf{q}] = \beta_1(q_1^2+q_2^2+q_3^2) + \beta_2(q_1^4+q_2^4+q_3^4) + \beta_3(q_2^2q_3^2+q_1^2q_3^2+q_1^2q_2^2), \tag{4.39}$$

$$\begin{aligned} H_{\text{u}}[\mathbf{u}] =& \zeta_1(u_1^2+u_2^2+u_3^2) + \zeta_2(u_1^4+u_2^4+u_3^4) + \zeta_3(u_2^2u_3^2+u_1^2u_3^2+u_1^2u_2^2) \\ &+ \zeta_4(u_1^6+u_2^6+u_3^6) + \zeta_5[u_1^4(u_2^2+u_3^2) + u_2^4(u_1^2+u_3^2) + u_3^4(u_1^2+u_2^2)] \\ &+ \zeta_6(u_1^8+u_2^8+u_3^8), \end{aligned} \tag{4.40}$$

$$\begin{aligned} H_{\text{sq}}[\mathbf{s},\mathbf{q}] =& \lambda_1(s_1q_1^2+s_2q_2^2+s_3q_3^2) + \lambda_2[s_1(q_2^2+q_3^2) \\ &+ s_2(q_1^2+q_3^2) + s_3(q_1^2+q_2^2)] \\ &+ \lambda_3(s_4q_2q_3+s_5q_1q_3+s_6q_1q_2) + \lambda_4(s_1q_1^4+s_2q_2^4+s_3q_3^4) \\ &+ \lambda_5(s_4q_2^2q_3^2+s_5q_1^2q_3^2+s_6q_1^2q_2^2), \end{aligned} \tag{4.41}$$

$$\begin{aligned} H_{\text{su}}[\mathbf{s},\mathbf{u}] =& \rho_1(s_1u_1^2+s_2u_2^2+s_3u_3^2) + \rho_2[s_1(u_2^2+u_3^2) \\ &+ s_2(u_1^2+u_3^2) + s_3(u_1^2+u_2^2)] \\ &+ \rho_3(s_4u_2u_3+s_5u_1u_3+s_6u_1u_2) + \rho_4(s_1u_1^4+s_2u_2^4+s_3u_3^4) \\ &+ \rho_5(s_4u_2^2u_3^2+s_5u_1^2u_3^2+s_6u_1^2u_2^2) \\ &+ \rho_6[s_1(u_2^4+u_3^4) + s_2(u_1^4+u_3^4) + s_3(u_1^4+u_2^4)] \end{aligned} \tag{4.42}$$

and

$$H_{\text{uq}}[\mathbf{u},\mathbf{q}] = \gamma_1(u_1^2q_1^2+u_2^2q_2^2+u_3^2q_3^2) + \gamma_2(u_1^2q_1^4+u_2^2q_2^4+u_3^2q_3^4). \tag{4.43}$$

($\widetilde{\Omega} = 2\Omega$ is the volume of the 10-atom cell and $\mathcal{C}_{ij}$ are the components of the macroscopic elastic tensor, which are given in Table 4.1.) $H_{\text{s}}[\mathbf{s}]$, $H_{\text{q}}[\mathbf{q}]$ and $H_{\text{u}}[\mathbf{u}]$ describe the energetics of the system under application of strain, oxygen octahedral tilts and the polar order parameter, respectively; whereas the terms $H_{\text{sq}}[\mathbf{s},\mathbf{q}]$, $H_{\text{su}}[\mathbf{s},\mathbf{u}]$ and $H_{\text{uq}}[\mathbf{u},\mathbf{q}]$ account for the coupling between different degrees of freedom. The calculated parameters for the effective Hamiltonian, which are obtained by fitting first-principles DFT calculations to our continuum model, are given in Table 4.4.

As a first step for the validation of H_{eff}, we compute the energy of the most relevant phases that can be obtained by combining antiferrodistortive (i.e., oxygen

Parameter	Value	Units	Parameter	Value	Units
β_1	-4.31	eV/Å^2	λ_3	-12.38	eV/Å^2
β_2	8.03	eV/Å^4	λ_4	-32.82	eV/Å^4
β_3	5.97	eV/Å^4	λ_5	16.33	eV/Å^4
ζ_1	-35.43	eV/Å^2	ρ_1	81.43	eV/Å^2
ζ_2	8.68×10^2	eV/Å^4	ρ_2	-1.36×10^2	eV/Å^2
ζ_3	2.20×10^3	eV/Å^4	ρ_3	-1.11×10^2	eV/Å^2
ζ_4	-6.98×10^3	eV/Å^6	ρ_4	-3.09×10^2	eV/Å^4
ζ_5	5.91×10^4	eV/Å^6	ρ_5	-1.43×10^4	eV/Å^4
ζ_6	2.06×10^4	eV/Å^8	ρ_6	-1.18×10^4	eV/Å^4
λ_1	38.25	eV/Å^2	γ_1	3.48×10^2	eV/Å^4
λ_2	19.09	eV/Å^2	γ_2	-9.90×10^2	eV/Å^6

Table 4.4: Calculated model parameters for the first-principles Hamiltonian of LiOsO$_3$. First-principles DFT calculations were carried out with the PBE parametrization of the GGA, with a plane-wave energy cutoff of 60 Ha, a Gaussian smearing of 0.01 Ha and the Brillouin Zone was sampled with $16 \times 16 \times 16$ **k** points.

octahedral tilts) and polar instabilities, compared with the cubic $P3\bar{m}3$ structure, whose energy is taken as reference. The structural ground state of $R3c$ symmetry contains both polar distortions and antiphase octahedral tilts ($a^-a^-a^-$ in Glazer notation) oriented along the [111] pseudocubic direction. Other important phases are the centrosymmetric $R\bar{3}c$ and the polar $R3m$, where either the polar or the antiferrodistortive modes are suppressed.

Numerical minimization of our effective Hamiltonian is carried out with the Monte Carlo simulated annealing method. The structure of the system is described in a generalized parameter space by a *state-vector*, $\mathbf{v}$, that contains the information of the strain, the oxygen octahedral tilts and the polar order parameter. The state-vector is randomly initialized and, in each time step, t, a new configuration is proposed, such that $\mathbf{v}_{t+1} = \mathbf{v}_t + \delta$, where δ is the step that brings the system from its current configuration into a new one. If the energy of the proposed new configuration is lower that the present one, the new configuration is accepted, i.e., if $\Delta E_t < 0$ then $\mathbf{v}_t \rightarrow \mathbf{v}_{t+1}$, where $\Delta E_t = H_{\text{eff}}[\mathbf{v}_{t+1}] - H_{\text{eff}}[\mathbf{v}_t]$. If $\Delta E_t >= 0$, the new configuration is accepted with a probability $p_t = e^{-\Delta E_t/T}$, where T is the *temperature* of the system and controls the *randomness* of the acceptance of configurations with higher energies during the minimization procedure. The simulation is initialized with a temperature large enough to allow to escape from local minima and it is then constantly reduced in each time step until the global minimum is achieved.

As we can see from the calculated values in Table 4.5, our continuum model accurately reproduces the first-principles results obtained by fully relaxing the crystal cell within the given symmetry. In particular, this first-principles Hamiltonian almost perfectly describes the energy difference between the lowest-energy

	DFT		Effective Hamiltonian	
	ΔE	$\Delta V(\%)$	ΔE	$\Delta V(\%)$
$R3m$	-149	1.1	-157	1.3
$R\bar{3}c$	-908	-11.4	-906	-11.5
$R3c$	-930	-12.0	-929	-11.9

Table 4.5: Volume and energy comparison between first-principles calculations and our model. Energies are in meV / f.u. units.

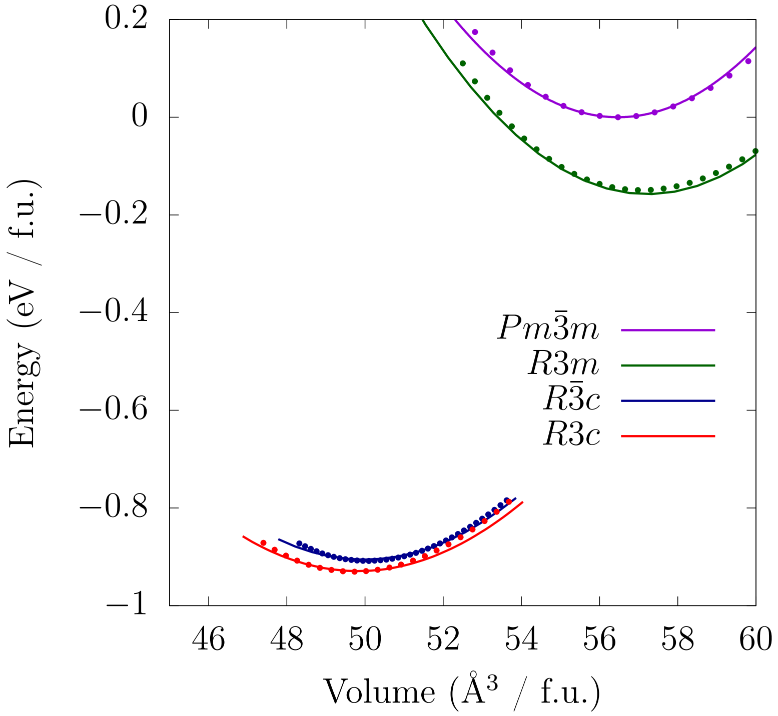

Figure 4.5: Energy per formula unit as a function of the volume of the perovskite formula unit of $Pm\bar{3}m$, $R3m$, $R\bar{3}c$, and $R3c$ phases of $LiOsO_3$. Data points are computed via explicit first-principles calculations and solid lines are obtained from our effective Hamiltonian.

$R\bar{3}c$ and $R3c$ phases, which are the most relevant for the switching of the polar order parameter: -22 meV/f.u. with DFT and -23 meV/f.u. with our effective Hamiltonian, were f.u. stands for perovskite formula unit. As a further test, we study the phase diagram of $LiOsO_3$ as a function of cell volume, which we control by applying uniaxial strain. The dots shown in Fig. 4.5 are obtained from DFT calculations by fully relaxing the ionic positions for each fixed cell volume. These results are in excellent agreement with experimental values [28] and previous first-principles studies [136]. Solid lines represent the energies obtained with our continuum model, again showing excellent agreement with first-principles results.

Now that the reliability of our effective Hamiltonian has been rigorously verified, we are ready to study the most favorable switching paths for the polar order parameter. We tackle this problem by constraining one of the components of the polar vector (u_1 in our case) and by minimizing the effective Hamiltonian with respect to the other parameters, while the system evolves along some specific structural path. Before doing so, however, it is useful to recall the structural properties of $LiOsO_3$ (see Fig. 4.1). The ground state of $LiOsO_3$, $R3c$, contains both polar distortions and antiphase octahedral tilts, both oriented along the [111] pseudocubic direction. Since the energy associated to the oxygen octahedral tilts is substantially larger than that associated to $\mathbf{u}$ (see Fig. 4.5), the former are very unlikely to be affected by the latter. In other words, the polar order parameter is forced to switch between the [111] and $[\bar{1}\bar{1}\bar{1}]$ states, while the AFD oxygen tilts remain practically unaltered. Nonetheless, different switching paths might be possible.

In Fig. 4.6 we show two potential switching paths. The first and probably more naive option involves an homogeneous evolution of the polar modes along the [111] direction (this means applying the constraint $u_1 = u_2 = u_3$), while passing through the noncentrosymmetric $R\bar{3}c$ phase. This is illustrated by the dashed lines in Fig. 4.6. The coercive field associated to this switching path is $F_{\mathrm{coerc}} = 0.69$ eV/Å. However, in order for this to be the actual switching path of the polar order parameter, the $R\bar{3}c$ phase (characterized by $u_1 = u_2 = u_3 = 0$) would need to be stable, and previous first-principles calculations [136] have already shown that this is not to be expected. This is nicely confirmed by the "butterfly-diagram" (solid lines in Fig. 4.6) that we obtain when plotting the energy as a function of u_1 and letting the remaining parameters evolve freely (no constraints). To help better clarify the meaning of this butterfly diagram, we also show in Fig. 4.6 the evolution of the perpendicular components of the polar modes, i.e., u_2 and u_3, as a function of u_1, which indicates the presence of an in-plane polarization switching at $u_1 = 0$. The coercive field in this case is $F_{\mathrm{coerc}} = 0.34$ eV/Å. As expected, this is significantly smaller than that of the constrained path along the [111] direction.

In this context, it is also beneficial to consider the case of barium titanate (more details can be found in Appendix B). For $BaTiO_3$ the polarization cannot be constrained by the oxygen tilts, since the latter are absent in this material. At low-temperature, $BaTiO_3$ has $R3m$ symmetry, and we find that the lowest switching barrier occurs when the polarization continuously rotates from [111] to $[\bar{1}11]$ by passing through an orthorhombic [110] saddle point; see Fig. 4.7. (The path is roughly oriented along [100]). We find a critical coercive field of $F_{\mathrm{coerc}} = 0.14$ eV/Å for such a switching path. For comparison to room-temperature experiments, where $BaTiO_3$ adopts a tetragonal structure, we also calculate the hypothetical barrier that one would obtain by constraining $\mathbf{P} \parallel [100]$ (i.e., by setting the in-plane components of $\mathbf{P}$ to zero). We find $F_{\mathrm{coerc}} = 0.29$ eV/Å. This is a substantially larger value than the aforementioned threshold for polarization rotation, in line with literature results. Since the relevant paths in $BaTiO_3$ involve [100]-oriented switching, such geometrical factor reduces its [110] and [111] effective flexocoupling coefficients of Table 4.3 by $\sqrt{2}$ and $\sqrt{3}$, respectively, bringing all three values of f_{eff} to a similar magnitude.

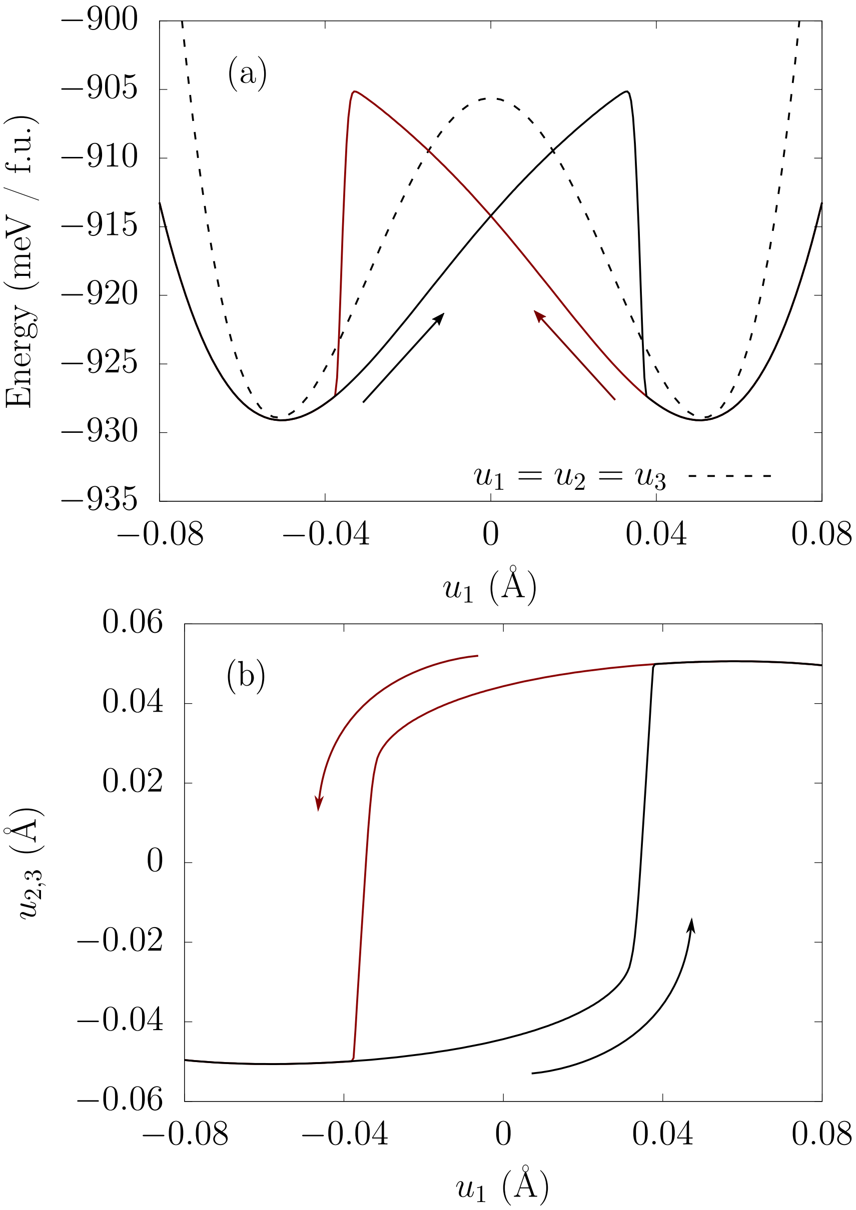

Figure 4.6: (a) Potential energy landscape of LiOsO$_3$ from our first principles effective Hamiltonian, obtained by minimizing the energy at fixed values of u_1. A typical double-well like curve is obtained when $u_1 = u_2 = u_3$ is enforced (dashed line) and a butterfly-like diagram emerges when all the parameters are allowed to evolve freely (solid line). Colors and arrows are used to illustrate the switching path, either for the case in which u_1 linearly increases or decreases. (b) Evolution of u_2 and u_3 as a function of u_1.

4.6 CRITICAL BENDING RADIUS

We are now ready to estimate the critical bending radius needed to switch the polar order parameter of LiOsO$_3$. Combining the effective flexocoupling coefficients of Table 4.3 with the critical coercive fields of the previous section, by means of Eq.

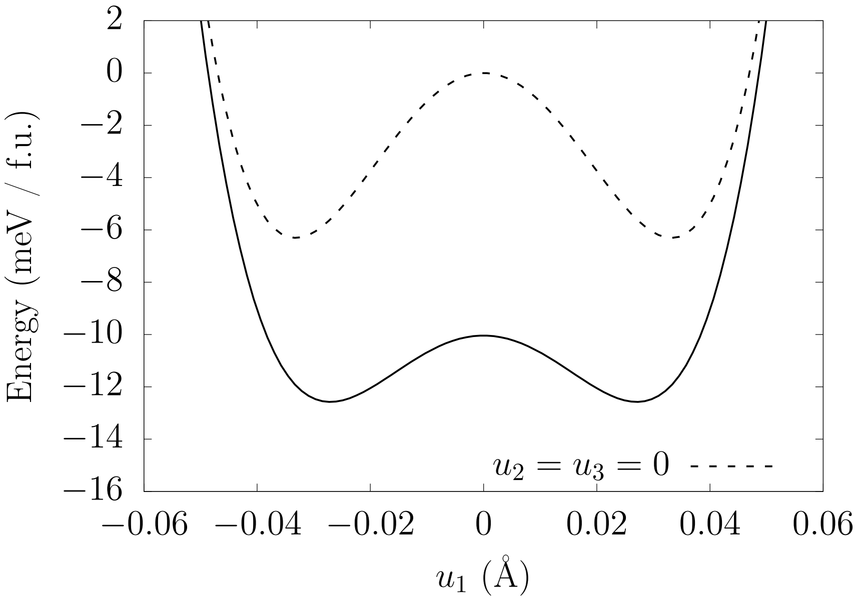

Figure 4.7: Potential energy landscape of $BaTiO_3$. The dashed line represents the study under the $u_2 = u_3 = 0$ constraint, and the solid line the case with no constraints.

(4.28), we obtain $R_{\text{crit}} \sim 118$ Å for $LiOsO_3$ and $R_{\text{crit}} \sim 130$ Å for the rhombohedral $BaTiO_3$ and $R_{\text{crit}} \sim 63$ Å for tetragonal $BaTiO_3$. Remarkably, the calculated critical bending radius of $LiOsO_3$ is twice as large as that of tetragonal $BaTiO_3$, essentially matching the calculated value of rhombohedral $BaTiO_3$.

Our results for $BaTiO_3$ are in good agreement with the ones reported in Ref. [137] where a critical bending radius of 110 Å was estimated. This is substantially smaller than the available experimental estimates (a value of $R_{\text{crit}} \sim 300$ Å was observed in $BaTiO_3$ [38]). This is expected, since theoretical estimations of coercive fields in ferroelectrics that are based on the homogeneous Landau potential are typically overestimated by one or two orders of magnitude [138]. Consideration of more realistic mechanisms (e.g., domain wall nucleation and motion) would drastically complicate our study, and bring us far from our main scope. We stress in any case that our underestimation of the critical bending radii compared to experiments should be ascribed to an overestimation of F_{coerc}, while we regard our calculation of the flexocoupling coefficients as accurate. In this context, it is necessary to mention that in the $R\bar{3}c$ phase of $LiOsO_3$, the flexocoupling coefficients are expected to acquire additional contributions coming from the oxygen octahedral tilt gradients, which are neglected in this work. While certainly present, we consider it unlikely to qualitatively affect our conclusions.

4.7 SUMMARY AND OUTLOOK

The following points summarize the achievements of the work presented in this chapter:

- We have proposed strain gradients as a viable and promising way of switching polarity at the bulk level in polar metals, thus solving one of the long-standing issues that has been a challenge to unravel for some time.
- Our work also opens the door to a previously unexplored research field of flexoelectricity in metals, where strain gradient mediated effects have the potential to become as relevant as they are with standard insulating ferroelectrics.
- We have computed, for the first time, the flexocoupling coefficients of a metal from first-principles, by means of the ensemble DFPT approach presented in Chapter 3. After extensively verifying the accuracy of our results via the elastic sum rule that was presented in Sec. 4.23, we also proposed an alternative methodology for computing the flexocouplings in metals, which is based on lattice sums of real-space IFCs.
- We have estimated the needed critical bending radius to switch the polarity of $LiOsO_3$, which is comparable in magnitude to that of $BaTiO_3$. Since mechanical switching of polar domains in tetragonal barium titanate has already been experimentally achieved [37, 38] via strain gradients, our results indicate that this is very likely to be feasible in $LiOsO_3$ as well.

As an outlook, we hope that the results presented here will stimulate further experimental work to verify our theoretical predictions. Along these lines, it is worth mentioning Ref. [139], where the spontaneous polarization of $LiOsO_3$ is found to be comparable to that of $BaTiO_3$, in line with our predictions about the critical bending radii of these materials. Additionally, it will be interesting to estimate the magnitude of the flexocoupling coefficients in a broader range of polar metals and identify candidates where the effect is especially strong. Our long-wave DFPT methodology presented in Chapter 3 appears to be an excellent tool for this task. We expect it to greatly facilitate the first-principles-based modeling of polar metals, which are currently under intense scrutiny within the research community.

5

ROTATIONAL g FACTORS AND LORENTZ FORCES

In this chapter we establish, in the framework of first-principles density-functional perturbation theory (DFPT), an accurate and computationally efficient methodology to compute both generalized Lorentz forces and g factors in molecules and solids.

Our strategy consists in defining both quantities in terms of the microscopic electronic and nuclear currents, $\mathbf{J}(\mathbf{r})$, that accompany the adiabatic evolution of the system along the atomic trajectories. In particular, the first spatial moment of $\mathbf{J}(\mathbf{r})$ can be regarded as a geometric orbital magnetic moment, $\mathbf{m}$, which couples linearly to the external $\mathbf{B}$ field and acts as an effective vector potential in the classical ionic Lagrangian. At the leading order in the ionic velocities, $\mathbf{v}$, the calculation of $\mathbf{m}$ can be carried out within the framework of DFPT via a long-wave expansion of the macroscopic polarization response to a phonon. Such expansion, in turn, is written [103] in terms of two linear-response tensors: the macroscopic polarization induced by an atomic displacement, $\mathbf{J}^{(0)}$, corresponding to the Born effective charges (BECs), and its first-order spatial dispersion, $\mathbf{J}^{(1)}$. The main technical challenge resides in the calculation of $\mathbf{J}^{(1)}$, since the BECs are routinely calculated in many publicly-available DFT codes [77, 140].

We have implemented and used two different approaches for accessing $\mathbf{J}^{(1)}$, and compared their mutual consistency as part of our numerical tests. The first method, based on Ref. [98], consists in performing the DFPT calculations of the polarization response at finite $\mathbf{q}$, and subsequently taking their long-wave expansion via numerical differentiation. The second method, which we shall prefer from the point of view of computational convenience, consists in taking the long-wave expansion analytically [41], following the prescriptions of Sec. 2.4.4. Note, however, that the implementation that is currently available in ABINIT doesn't capture the full tensorial form of $\mathbf{J}^{(1)}$. For its implementation, we have further extended the capabilities of ABINIT by incorporating the wave function response to an orbital $\mathbf{B}$ field. One can show that the resulting formulation of the geometric orbital magnetization recovers the theory of Ref. [17], including the additional *topological* contribution derived therein (see Appendix E for more details).

To demonstrate our method, we first consider the rotational g factor, which depends on the magnetic moment that is associated with a uniform and rigid rotation of a finite body. We show that our formula, based on the calculation of $\mathbf{J}^{(1)}$, consistently yields a vanishing magnetic moment in the case of a neutral closed-shell atom, and correctly transforms upon a change of the assumed center of rotation. Our numerical results for several representative molecules show excellent agreement with experiment and with earlier calculations, where available; the elements of $\mathbf{J}^{(1)}$ that we obtained via either finite-difference or analytical long-wave expansions nicely match in all tested cases. For comparison, we also test an alternative formulation, based on a coordinate transformation to the comoving frame [100] of the rotating molecule, and discuss its performance regarding numerical convergence and other technical issues (e.g., related to the use of nonlocal pseudopotentials).

Next, we consider the magnetization induced by a circularly polarized optical phonon, which we express as a generalized Lorentz force in presence of a uniform magnetic field. As a physical manifestation of this effect, we calculate the splitting of the soft polar transverse-optical (TO) mode frequencies of $SrTiO_3$ at Γ due to an external magnetic field. Our motivation for revisiting this system comes the very recent measurement of a giant phonon Hall effect [141] in the same material. As in the case of the molecular g factors, we base our discussion on the calculation of the $\mathbf{J}^{(1)}$ tensor, which we perform both via the approach of Ref. [98], and via the analytical long-wave method; again, we find excellent numerical agreement between the two.

The remainder of this chapter is organized as follows. Sec. 5.1 and Sec. 5.2 are devoted to introducing the formalism and computational implementation for calculating molecular g factors and generalized Lorentz forces in extended solids. In Sec. 5.3 we present our numerical results of the rotational g factors of selected molecules and the generalized Lorentz force in cubic $SrTiO_3$. The latter enables the calculation of the frequency splitting of the TO modes in presence of a magnetic field. We conclude the chapter in Sec. 5.4 with a summary and a brief outlook.

5.1 THEORY

5.1.1 LAGRANGIAN FOR A SOLID UNDER AN APPLIED MAGNETIC FIELD

Our starting point is the following nonadiabatic Ehrenfest Lagrangian of a crystalline system under an applied magnetic field,

$$\mathcal{L} = \sum_{l,\kappa,\alpha} \frac{1}{2} M_\kappa (\dot{R}^l_{\kappa\alpha})^2 + \sum_{l,\kappa} Z_\kappa \dot{\mathbf{R}}^l_\kappa \cdot \mathbf{A}(\mathbf{R}^l_\kappa) + \sum_m \langle \psi_m | \left[i\partial_t - \hat{H}(\mathbf{A}) \right] | \psi_m \rangle , \tag{5.1}$$

where $\mathbf{A}(\mathbf{R}^l_\kappa)$ is the magnetic vector potential (the electromagnetic gauge origin at $\mathbf{R}^l_\kappa$ is explicitly indicated), $\mathbf{R}^l_\kappa$ represents, as usual, the position of ion $l\kappa$ within the crystal (κ is a sublattice index and l refers to the cell), M_κ is the mass of ion κ and Z_κ its bare pseudo-charge. Regarding the electronic part, ψ_m are the Kohn-Sham orbitals and $\hat{H}(\mathbf{A})$ is the electronic Hamiltonian, depending parametrically on the ionic positions,

$$\hat{H}(\mathbf{A}) = \frac{1}{2} \left(\hat{\mathbf{p}} + \hat{\mathbf{A}} \right)^2 + \hat{V}_{\mathrm{KS}}, \tag{5.2}$$

where $\hat{V}_{\mathrm{KS}}$ is the KS effective potential given in Eq. (2.13), and accounts for the Hartree (H), exchange-correlation (xc) and and the electron-nucleus interaction. (We shall distinguish between $\hat{H}(\mathbf{A})$, which takes into account the effects of the applied $\mathbf{B}$ field via the incorporation of the vector potential in Eq. (5.2), and $\hat{H}$, which is the Hamiltonian in absence of any external fields. In addition, note that the parametric dependence on ionic positions, $\{\mathbf{R}^l_\kappa\}$, and velocities, $\{\dot{\mathbf{R}}^l_\kappa\}$, of the objects entering the Lagrangian is kept implicit.) If we assume that the external magnetic field is small (an excellent approximation in the vast majority of cases), we can work at linear order in the vector potential and write

$$\begin{aligned}\mathcal{L} = &\sum_{l,\kappa,\alpha} \frac{1}{2} M_\kappa (\dot{R}^l_{\kappa\alpha})^2 + \sum_{l,\kappa} Z_\kappa \dot{\mathbf{R}}^l_\kappa \cdot \mathbf{A}(\mathbf{R}^l_\kappa) + \int \mathbf{A}(\mathbf{r}) \cdot \mathbf{J}^{\text{el}}(\mathbf{r}) d^3 r \\ &+ \sum_m \langle \psi_m | \left(i\partial_t - \hat{H} \right) | \psi_m \rangle ,\end{aligned} \tag{5.3}$$

where the microscopic electronic (el) currents, in zero external field, are defined as

$$\mathbf{J}^{\text{el}}(\mathbf{r}) = -\frac{1}{2} \sum_m \langle \psi_m | \left(\hat{\mathbf{p}} |\mathbf{r}\rangle\langle\mathbf{r}| + |\mathbf{r}\rangle\langle\mathbf{r}| \hat{\mathbf{p}} \right) | \psi_m \rangle . \tag{5.4}$$

(Later on in this chapter we will apply the prescriptions of Sec. 2.4.3 for the correct treatment of the current-density operator in presence of non-local pseudopotentials.) As we treat the nuclei as classical point charges, the ionic (ion) currents read as

$$\mathbf{J}^{\text{ion}}(\mathbf{r}) = \sum_{l,\kappa} Z_\kappa \dot{\mathbf{R}}^l_\kappa \delta(\mathbf{r} - \mathbf{R}^l_\kappa). \tag{5.5}$$

This allows us to reabsorb the effects of the external vector potential in a single interaction term,

$$\mathcal{L} = \sum_{l,\kappa,\alpha} \frac{1}{2} M_\kappa (\dot{R}^l_{\kappa\alpha})^2 + \int \mathbf{A}(\mathbf{r}) \cdot \mathbf{J}(\mathbf{r})\, d^3 r + \sum_m \langle \psi_m | \left(i\partial_t - \hat{H} \right) | \psi_m \rangle , \tag{5.6}$$

where $\mathbf{J} = \mathbf{J}^{\text{el}} + \mathbf{J}^{\text{ion}}$. By choosing the symmetric gauge, $\mathbf{A} = \frac{1}{2}\mathbf{B} \times \mathbf{r}$, we can equivalently write

$$\int \mathbf{A}(\mathbf{r}) \cdot \mathbf{J}(\mathbf{r})\, d^3 r = \mathbf{B} \cdot \mathbf{m}, \tag{5.7}$$

where $\mathbf{m} = 1/2 \int \mathbf{r} \times \mathbf{J}\, d^3 r$ is the geometric orbital magnetic moment associated with the dynamical evolution of the ions along their trajectories, which implicitly depends both on the ionic positions and velocities. We are now ready to take the adiabatic approximation in a regime where the ionic velocities are small,

$$\mathcal{L} = \sum_{l,\kappa,\alpha} \frac{1}{2} M_\kappa (\dot{R}^l_{\kappa\alpha})^2 + \mathbf{B} \cdot \sum_{l,\kappa,\alpha} \dot{R}^l_{\kappa\alpha} \mathbf{m}^l_{\kappa\alpha} - E, \tag{5.8}$$

where the two new terms are the Born-Oppenheimer potential energy surface in zero field, E, plus a term that depends on the *dynamical orbital magnetic moment tensor*,

$$\mathbf{m}^l_{\kappa\alpha} = \left. \frac{\partial \mathbf{m}}{\partial \dot{R}^l_{\kappa\alpha}} \right|_{\dot{R}^l_{\kappa\alpha}=0} . \tag{5.9}$$

The latter quantity differs from the Born effective charge (BEC) tensor in that the adiabatic macroscopic $\mathbf{m}$, rather than the adiabatic macroscopic current $\mathbf{J}$, is differentiated with respect to the ionic velocities. Note that $\mathbf{m}^l_{\kappa\alpha}$ generally depends on the electromagnetic gauge, unlike the BECs. However, as we shall see shortly, its consequences on ionic dynamics are gauge-independent. This is a common feature of physical problems that involve an applied external $\mathbf{B}$ field. Indeed, the velocity-dependent potential

$$\mathcal{A}^l_{\kappa\alpha} = \mathbf{B} \cdot \mathbf{m}^l_{\kappa\alpha}, \tag{5.10}$$

can be regarded as an effective vector potential, $\boldsymbol{\mathcal{A}}^l_\kappa$, acting on the ion $l\kappa$, whose magnitude depends on the specific atom under consideration. This leads to the following expression for the classical Hamiltonian of the ions,

$$H^{\text{ion}} = \sum_{l,\kappa,\alpha} \frac{1}{2M_\kappa} \left(P^l_{\kappa\alpha} - \mathcal{A}^l_{\kappa\alpha} \right)^2 + E, \quad \text{with} \quad P^l_{\kappa\alpha} = \partial \mathcal{L} / \partial \dot{R}^l_{\kappa\alpha}, \tag{5.11}$$

which is good up to linear order in the ionic velocities, and where the vector potential emerges from the breakdown of time-reversal (TR) symmetry that is associated with the external **B** field. One can show that this treatment is fully consistent with more conventional expressions [142] where $\mathcal{A}^l_{\kappa\alpha}$ is written as a Berry connection in the parameter space of the ionic coordinates. The advantage of the present formulation rests on the availability of efficient first-principles methods to compute directly $\mathbf{m}^l_{\kappa\alpha}$, and hence the vector potential $\mathcal{A}^l_{\kappa\alpha}$, without the need of incorporating an external **B** field in the simulation. We shall discuss this point in the next subsection.

5.1.2 GEOMETRIC ORBITAL MAGNETIZATION

The basic quantity we shall be dealing with is the microscopic polarization response to the displacement of *an isolated atom* [103],

$$\boldsymbol{\mathcal{P}}_{\kappa\beta}(\mathbf{r} - \mathbf{R}^l_\kappa) = \left. \frac{\partial \mathbf{J}(\mathbf{r})}{\partial \dot{R}^l_{\kappa\beta}} \right|_{\dot{R}^l_{\kappa\beta}=0}. \tag{5.12}$$

Eq. (5.12) always sets the coordinate origin to the atomic site; therefore, the functions $\boldsymbol{\mathcal{P}}_{\kappa\beta}(\mathbf{r})$ do not depend on the cell index l. Note that the vector fields contain both electronic and ionic contributions, i.e.,

$$\mathcal{P}_{\alpha,\kappa\beta}(\mathbf{r}) = \mathcal{P}^{\text{el}}_{\alpha,\kappa\beta}(\mathbf{r}) + \mathcal{P}^{\text{ion}}_{\alpha,\kappa\beta}(\mathbf{r}), \tag{5.13}$$

where the α subscript indicates the Cartesian component. The ionic contribution comes in the form of a Dirac delta function that carries the bare nuclear (or pseudopotential) charge Z_κ,

$$\mathcal{P}^{\text{ion}}_{\alpha,\kappa\beta}(\mathbf{r}) = Z_\kappa \delta_{\alpha\beta} \delta(\mathbf{r}). \tag{5.14}$$

The relationship between the localized functions we have just introduced, $\boldsymbol{\mathcal{P}}_{\kappa\beta}(\mathbf{r})$, and the polarization response to a collective phonon mode as described in Sec. 2.3.3, $\mathbf{P}_{\kappa\beta}(\mathbf{r})$, which can be obtained from Eqs. (2.102) and (2.106), is straightforward [103],

$$\mathbf{P}^{\mathbf{q}}_{\kappa\beta}(\mathbf{r}) = \sum_l \boldsymbol{\mathcal{P}}_{\kappa\beta}(\mathbf{r} - \mathbf{R}^l_\kappa) e^{i\mathbf{q}\cdot(\mathbf{R}^l_\kappa - \mathbf{r})}. \tag{5.15}$$

The Taylor expansion of Eq. (5.15) in $\mathbf{q}$ around $\mathbf{q} = \mathbf{0}$ reads as

$$P^{\mathbf{q}}_{\alpha,\kappa\beta} \simeq P^{(0)}_{\alpha,\kappa\beta} - i \sum_\gamma q_\gamma P^{(1,\gamma)}_{\alpha,\kappa\beta} - \frac{1}{2} \sum_{\gamma,\delta} q_\gamma q_\delta P^{(2,\gamma\delta)}_{\alpha,\kappa\beta}, \tag{5.16}$$

where α is a Cartesian direction and we have followed the same sign conventions as with the FC matrix in Eq. (3.47). In terms of the localized functions, for the lowest orders in $\mathbf{q}$, we obtain

$$\begin{aligned} P^{(0)}_{\alpha,\kappa\beta}(\mathbf{r}) &= \sum_l \mathcal{P}_{\alpha,\kappa\beta}(\mathbf{r}-\mathbf{R}^l_\kappa), \\ P^{(1,\gamma)}_{\alpha,\kappa\beta}(\mathbf{r}) &= \sum_l \mathcal{P}_{\alpha,\kappa\beta}(\mathbf{r}-\mathbf{R}^l_\kappa)(\mathbf{r}-\mathbf{R}^l_\kappa)_\gamma, \\ P^{(2,\gamma\delta)}_{\alpha,\kappa\beta}(\mathbf{r}) &= \sum_l \mathcal{P}_{\alpha,\kappa\beta}(\mathbf{r}-\mathbf{R}^l_\kappa)(\mathbf{r}-\mathbf{R}^l_\kappa)_\gamma(\mathbf{r}-\mathbf{R}^l_\kappa)_\delta. \end{aligned} \tag{5.17}$$

For most practical purposes, it is convenient to introduce the moments of the localized functions as the following integrals over all space,[1]

$$\begin{aligned} J^{(0)}_{\alpha,\kappa\beta} &= \int \mathcal{P}_{\alpha,\kappa\beta}(\mathbf{r})\, d^3r, \\ J^{(1,\gamma)}_{\alpha,\kappa\beta} &= \int \mathcal{P}_{\alpha,\kappa\beta}(\mathbf{r}) r_\gamma\, d^3r. \end{aligned} \tag{5.18}$$

Here, $\mathbf{J}^{(0)}$ corresponds to the Born effective charge tensor and $\mathbf{J}^{(1)}$ is the first moment of the polarization response, whose symmetric part corresponds to the dynamical quadrupole tensor [41, 103]

$$Q^{(2,\alpha\gamma)}_{\kappa\beta} = J^{(1,\gamma)}_{\alpha,\kappa\beta} + J^{(1,\alpha)}_{\gamma,\kappa\beta}. \tag{5.19}$$

On the other hand, the antisymmetric part of $\mathbf{J}^{(1)}$ contributes to the magnetization response to the atomic velocity, and can be expressed as

$$\mathcal{M}_{\alpha,\kappa\beta} = \frac{1}{2}\sum_{\gamma,\delta} \epsilon^{\alpha\gamma\delta} J^{(1,\gamma)}_{\delta,\kappa\beta}, \tag{5.20}$$

where $\epsilon^{\alpha\gamma\delta}$ is the Levi-Civita symbol. More precisely, $\boldsymbol{\mathcal{M}}$ is the magnetic moment of the electronic currents calculated with respect to the unperturbed atomic position, which follows from the definition of $\mathbf{J}^{(1)}$ in Eq. (5.18).

The above definitions lead to the following formula for the geometric magnetic moment associated with the adiabatic motion of the ion $l\kappa$,

$$\begin{aligned} \mathbf{m}^l_{\kappa\beta} &= \frac{1}{2}\int \mathbf{r} \times \boldsymbol{\mathcal{P}}_{\kappa\beta}(\mathbf{r}-\mathbf{R}^l_\kappa)\, d^3r \\ &= \frac{1}{2}\mathbf{R}^l_\kappa \times \mathbf{Z}^*_{\kappa\beta} + \boldsymbol{\mathcal{M}}_{\kappa\beta}, \end{aligned} \tag{5.21}$$

where $Z^*_{\alpha,\kappa\beta} = J^{(0)}_{\alpha,\kappa\beta}$ is the α Cartesian component of the polarization induced by a displacement of atom κ along β, i.e., the Born effective charge, as defined in Eq. (2.83). This expression clarifies the gauge-dependence of $\mathbf{m}^l_{\kappa\beta}$ that we have

---

[1] Note that this is completely equivalent to performing the cell-average of the *extended* functions; for example, at first-order in $\mathbf{q}$,

$$J^{(1,\gamma)}_{\alpha,\kappa\beta} = \int_\Omega P^{(1,\gamma)}_{\alpha,\kappa\beta}(\mathbf{r})\, d^3r = \int \mathcal{P}^{(1,\gamma)}_{\alpha,\kappa\beta}(\mathbf{r}) r_\gamma\, d^3r,$$

where the first integral is carried out only for the unit cell, and the second one over the whole space.

anticipated in the previous subsection: this quantity depends explicitly on the absolute atomic position, and hence on the arbitrary choice of the coordinate origin.

In the case of an isolated and neutral molecule, it is insightful to consider the sublattice sum of $\mathbf{m}_{\kappa\beta} = \mathbf{m}^0_{\kappa\beta}$, which corresponds physically to the magnetic moment associated with a rigid translation of the body. Because of the acoustic sum rule, the origin indeterminacy disappears. Then, by using the following *dipolar sum rule* for molecules (see Appendix C for a detailed derivation),

$$\sum_\kappa \left(J^{(1,\gamma)}_{\alpha,\kappa\beta} + \tau_{\kappa\alpha} Z^*_{\alpha,\kappa\beta} \right) = \delta_{\alpha\beta} \mathcal{D}_\gamma, \tag{5.22}$$

we arrive at

$$\sum_\kappa m_{\alpha,\kappa\beta} = \frac{1}{2} \sum_\gamma \epsilon^{\beta\alpha\gamma} \mathcal{D}_\gamma, \tag{5.23}$$

where $\boldsymbol{\mathcal{D}}$ is the static dipolar moment of the molecule,

$$\boldsymbol{\mathcal{D}} = \int \mathbf{r}\, n^{(0)}(\mathbf{r})\, d^3r. \tag{5.24}$$

This is precisely the expected result for the uniform rigid motion of a distribution of classical charges whose local density equals $n^{(0)}(\mathbf{r})$.

5.1.3 MAGNETIZATION BY ROTATION: ROTATIONAL g FACTORS

We now derive the rotational g factor, which is relevant for molecules and other finite systems. Consider an isolated molecule to which we apply a time-dependent counter-clockwise rotation along the axis b by an angle θ_b. In general, the magnetic moment can be expressed as [143, 144]

$$m_a = \frac{1}{2} \sum_j g_{aj} L_j, \tag{5.25}$$

where g_{aj} is the rotational $\mathbf{g}$ tensor. On the other hand, L_j is the angular momentum, given by

$$L_j = \sum_b I_{jb} \omega_b, \tag{5.26}$$

where $\mathbf{I}$ is the moment of inertia matrix and $\omega_b = \dot{\theta}_b$ is the angular velocity, defined as time derivative of the rotation angle. Thus,

$$\frac{\partial m_a}{\partial \omega_b} = \frac{1}{2} \sum_j g_{aj} I_{jb}. \tag{5.27}$$

In the reference frame where $\mathbf{I}$ is diagonal, the $\mathbf{g}$ tensor can then be written as

$$g_{ab} = \frac{2}{I_{bb}} \frac{\partial m_a}{\partial \omega_b}. \tag{5.28}$$

We will now derive a closed formula for the magnetic moment induced by a uniform rotation of the molecule. We shall present two alternative results, the first calculated in the standard Cartesian frame based on the quantities introduced in the previous section, and the second based on the comoving frame theory of Ref. [100].

5.1.3.1 *Cartesian frame*

A rigid rotation about an arbitrary axis can be represented as the following displacement of the individual atoms [100],

$$\mathbf{u}_\kappa = \boldsymbol{\theta} \times \boldsymbol{\tau}_\kappa, \tag{5.29}$$

where we have introduced the rotation pseudovector $\boldsymbol{\theta} = \theta \hat{r}_b$. By combining Eq. (5.29) with Eq. (5.21), the magnetic moment associated with the rigid rotation of the sample can be expressed in terms of the Born effective charge tensor and the dynamical magnetization defined in the previous subsection,

$$\frac{\partial m_a}{\partial \omega_b} = \sum_{\kappa,\rho,\beta} \epsilon^{b\rho\beta} \tau_{\kappa\rho} \left[\mathcal{M}_{a,\kappa\beta} + \frac{1}{2} \sum_{\gamma,\alpha} \epsilon^{a\gamma\alpha} \tau_{\kappa\gamma} J^{(0)}_{\alpha,\kappa\beta} \right]. \tag{5.30}$$

This formula, containing the first moment of the dynamical magnetic dipoles and the second moment of the dynamical electrical dipoles, is valid only if the electromagnetic gauge origin coincides with the center of rotation of the molecule; this ensures, via rotational symmetry, that the linear-response result corresponds with the average geometric magnetization accumulated in a cyclic loop [100].

Consider now a simultaneous shift of the gauge origin and center of rotation by $\mathbf{R}$ in Eq. (5.30), giving rise to $\frac{\partial m_a(\mathbf{R})}{\partial \omega_b}$. We want to see how that quantity is related to $\frac{\partial m_a(\mathbf{0})}{\partial \omega_b} \equiv \frac{\partial m_a}{\partial \omega_b}$, which is indeed Eq. (5.30). Following the above considerations,

$$\begin{aligned} \frac{\partial m_a(\mathbf{R})}{\partial \omega_b} &= \sum_{\kappa,\rho,\beta} \epsilon^{b\rho\beta} (\tau_{\kappa\rho} - R_\rho) \left[\mathcal{M}_{a,\kappa\beta} + \frac{1}{2} \sum_{\gamma,\alpha} \epsilon^{a\gamma\alpha} (\tau_{\kappa\gamma} - R_\gamma) J^{(0)}_{\alpha,\kappa\beta} \right] \\ &= - \sum_{\kappa,\rho,\beta} \epsilon^{b\rho\beta} R_\rho \left[\mathcal{M}_{a,\kappa\beta} + \frac{1}{2} \sum_{\gamma,\alpha} \epsilon^{a\gamma\alpha} \tau_{\kappa\gamma} J^{(0)}_{\alpha,\kappa\beta} \right] \\ &\quad - \frac{1}{2} \sum_{\kappa,\rho,\beta} \epsilon^{b\rho\beta} \tau_{\kappa\rho} \sum_{\gamma,\alpha} \epsilon^{a\gamma\alpha} R_\gamma J^{(0)}_{\alpha,\kappa\beta} + \frac{\partial m_a(\mathbf{0})}{\partial \omega_b}. \end{aligned} \tag{5.31}$$

We will now rearrange some terms and make use of i) the definition of the dynamical orbital magnetic moment tensor given in Eq. (5.21) and ii) the sum rule of Eq. (5.23), in order to obtain

$$\begin{aligned} \frac{\partial m_a(\mathbf{R})}{\partial \omega_b} - \frac{\partial m_a(\mathbf{0})}{\partial \omega_b} &= - \frac{1}{2} \sum_{\rho,\beta,\gamma} \epsilon^{b\rho\beta} \epsilon^{a\gamma\beta} R_\rho D_\gamma \\ &\quad + \frac{1}{2} \sum_{\rho,\beta} \epsilon^{b\rho\beta} \sum_{\gamma,\alpha} \epsilon^{a\gamma\alpha} R_\gamma \left(\sum_\kappa J^{(1,\rho)}_{\alpha,\kappa\beta} - \mathcal{D}_\rho \delta_{\alpha\beta} \right). \end{aligned} \tag{5.32}$$

For the first term on the right hand side of Eq. (5.32), it is useful to observe the following property of the Levi-Civita symbol,

$$\sum_\alpha \epsilon^{\alpha mk} \epsilon^{\alpha nl} = \delta_{mn} \delta_{kl} - \delta_{ml} \delta_{nk}, \tag{5.33}$$

which leads to

$$-\frac{1}{2} \sum_{\rho,\beta\gamma} \epsilon^{b\rho\beta} \epsilon^{a\gamma\beta} R_\rho \mathcal{D}_\gamma = -\frac{1}{2} \left(\delta_{ab} \mathbf{R} \cdot \boldsymbol{\mathcal{D}} - R_a \mathcal{D}_b \right). \tag{5.34}$$

For the second contribution on the right hand side of Eq. (5.32), we will once again invoke the dipolar sum rule given in Eq. (5.22) and observe that the sublattice sum of the $J^{(1,\gamma)}_{\alpha,\kappa\beta}$ tensor coincides with the clamped-ion *proper* piezoelectric tensor times a trivial volume factor [see Eq. (C.4) in Appendix C], and is therefore symmetric with respect to $\beta \leftrightarrow \gamma$ exchange. As a consequence, the latter contribution vanishes. (An antisymmetric contribution would describe a steady macroscopic current that is generated by a rotating body in its comoving reference frame, and must vanish [100] on general physical grounds.) We obtain,

$$-\frac{1}{2}\sum_{\rho,\beta}\epsilon^{b\rho\beta}\sum_{\gamma,\alpha}\epsilon^{a\gamma\alpha}R_\gamma\mathcal{D}_\gamma\delta_{\alpha\beta} = -\frac{1}{2}\left(\delta_{ab}\mathbf{R}\cdot\boldsymbol{\mathcal{D}} - R_a\mathcal{D}_b\right). \tag{5.35}$$

Collecting all the contributions, we finally arrive at the following expression,

$$\frac{\partial m_a(\mathbf{R})}{\partial \omega_b} - \frac{\partial m_a(\mathbf{0})}{\partial \omega_b} = \frac{1}{2}\left(R_a\mathcal{D}_b + R_b\mathcal{D}_a\right) - \delta_{ab}\mathbf{R}\cdot\boldsymbol{\mathcal{D}}, \tag{5.36}$$

which describes the translational symmetry properties of the geometric magnetization derived in Eq. (5.30) upon a simultaneous shift of the gauge origin and the center of rotation. What are the key conclusions we can deduce from the above derivations? In short, Eq. (5.36) is telling us that $\partial m_a(\mathbf{R})/\partial \omega_b$ is origin independent in nonpolar molecules, i.e., molecules with vanishing static dipole. In all other cases, the result depends on the assumed center of rotation, which is usually set as the center of mass of the system.

5.1.3.2 *Comoving frame*

In the reference that is comoving (rotating) with the system, the rotational geometric magnetization can be expressed as [100, 145]

$$\begin{aligned}
\frac{\partial m_a}{\partial \omega_b} &= -2\chi^{\text{mag}}_{ab} + \frac{1}{2}\int \frac{\partial[\mathbf{r}\times(\boldsymbol{\omega}\times\mathbf{r})]_a}{\partial \omega_b} n^{(0)}(\mathbf{r})\, d^3r \\
&= -2\chi^{\text{mag}}_{ab} + \frac{1}{2}\sum_{\alpha,\delta,\beta}\epsilon^{a\alpha\beta}\epsilon^{b\delta\beta}\int r_\alpha r_\delta n^{(0)}(\mathbf{r})\, d^3r \\
&= -2\chi^{\text{mag}}_{ab} + \frac{1}{2}\int(\delta_{ab}r^2 - r_a r_b)n^{(0)}(\mathbf{r})\, d^3r.
\end{aligned} \tag{5.37}$$

The first term is proportional to the magnetic susceptibility, and originates from the electronic currents in the reference frame that is rigidly rotating with the sample; the second term describes the magnetic moment generated by the rigid rotation of the ground-state charge density of the molecule, and serves to convert the result to the laboratory frame. Upon a shift of the gauge origin, χ^{mag}_{ab} remains unaltered while the second term trivially transforms as in Eq. (5.36). (Clearly, the quadrupole becomes origin-dependent whenever a nonzero dipolar moment is also present, consistent with the above arguments.)

As part of the validation of our implementation, we shall compute the geometric magnetization by using both methods, Eq. (5.30) and Eq. (5.37). We can anticipate, however, that Eq. (5.30) is preferable in practical applications, for the following reasons. First, the widespread use of nonlocal pseudopotentials is a concern in regard to Eq. (5.37). [In particular, the equivalence between Eq. (5.30) and Eq. (5.37) rests on the translational invariance at the quadrupolar order, see the discussion around Eq. (C.18) in Appendix C.] Because of this issue, we find that Eq. (5.37) yields qualitatively incorrect results for systems where $\partial m_a / \partial \omega_b$ must vanish identically, e.g., in isolated noble gas atoms or molecular dimers that rotate about their axis. Second, even in cases where Eq. (5.37) is exact (e.g., in the H_2 molecule whenever hydrogen is described by a local pseudopotential), its numerical implementation involves the calculation of the static quadrupolar moment of the molecule, which might converge slowly as a function of the cell size. We shall illustrate this point in practice in Sec. 5.3.1.

5.1.4 MAGNETIZATION INDUCED BY CIRCULARLY POLARIZED OPTICAL PHONONS: GENERALIZED LORENTZ FORCE

We now turn to extended systems, and consider the case of a circularly polarized optical phonon describing a cyclic path along orbits in a given plane. In presence of time-reversal (TR) symmetry, the clockwise and counterclockwise orbits are degenerate. Here, we take the approach of breaking TR symmetry via an external **B** field oriented along γ, and discuss the implications on lattice dynamics within the harmonic regime of small displacements.

The starting point is the Lagrangian of Eq. (5.8). The Euler-Lagrange equations of motion are obtained from

$$\frac{d}{dt}\frac{\partial \mathcal{L}}{\partial \dot{u}^0_{\kappa\alpha}} - \frac{\partial \mathcal{L}}{\partial u^0_{\kappa\alpha}} = 0, \tag{5.38}$$

where $\mathbf{u}^l_\kappa$ and $\dot{\mathbf{u}}^l_\kappa$ are, respectively, the ionic displacements and velocities. (The former brings the position of ion $l\kappa$ from $\mathbf{R}^l_\kappa$ to $\mathbf{R}^l_\kappa + \mathbf{u}^l_\kappa$.) In order to compute the derivatives of the Lagrangian with respect to the ionic displacements and velocities, we expand the total orbital magnetic moment of the system up to first order both in $\mathbf{u}^l_\kappa$ and $\dot{\mathbf{u}}^l_\kappa$, and the Kohn-Sham energy up to second order in $\mathbf{u}^l_\kappa$ (harmonic approximation). The Lagrangian of Eq. (5.8) then reads as

$$\begin{aligned}\mathcal{L} = {} & \sum_{l,\kappa,\alpha} \frac{1}{2} M_\kappa (\dot{u}^l_{\kappa\alpha})^2 + \sum_{l,\kappa,\alpha} \left(\frac{\partial m_\gamma}{\partial \dot{R}^l_{\kappa\alpha}} \dot{u}^l_{\kappa\alpha} B_\gamma - \frac{\partial E}{\partial R^l_{\kappa\alpha}} u^l_{\kappa\alpha} \right) \\ & + \sum_{\substack{l,\kappa,\alpha \\ l',\kappa',\beta}} \left(\frac{\partial^2 m_\gamma}{\partial R^l_{\kappa\alpha} \partial \dot{R}^{l'}_{\kappa'\beta}} u^l_{\kappa\alpha} \dot{u}^{l'}_{\kappa'\beta} B_\gamma - \frac{1}{2} \frac{\partial^2 E}{\partial R^l_{\kappa\alpha} \partial R^{l'}_{\kappa'\beta}} u^l_{\kappa\alpha} u^{l'}_{\kappa'\beta} \right).\end{aligned} \tag{5.39}$$

The first line consists, next to the kinetic term, in a constant vector potential field acting on individual ions, which can be gauged out; and in the static forces in the initial configuration, which we assume to vanish. Based on these observations, the Euler-Lagrange equations of motion immediately lead to

$$M_\kappa \ddot{u}^0_{\kappa\alpha}(t) = - \sum_{l,\kappa',\beta} \left(\Phi_{\kappa\alpha,\kappa'\beta}(0,l) u^l_{\kappa'\beta}(t) - \Phi^\gamma_{\kappa\alpha,\kappa'\beta}(0,l) \dot{u}^l_{\kappa'\beta}(t) B_\gamma \right), \tag{5.40}$$

where the time dependence of $\mathbf{u}^l_\kappa(t)$ has been made explicit. $\Phi_{\kappa\alpha,\kappa'\beta}(0,l)$ is the usual real-space interatomic force-constant matrix and we have defined

$$\Phi^{\gamma}_{\kappa\alpha,\kappa'\beta}(0,l) = \frac{\partial^2 m_\gamma}{\partial R^0_{\kappa\alpha}\partial \dot{R}^l_{\kappa'\beta}} - \frac{\partial^2 m_\gamma}{\partial \dot{R}^0_{\kappa\alpha}\partial R^l_{\kappa'\beta}}, \tag{5.41}$$

which is the (antisymmetric) generalized Lorentz force produced by the external magnetic field. In accordance with the treatment of the FC matrix [see Eq. (2.72)], we can sum all cell contributions and write the following for the $\mathbf{q} = \mathbf{0}$ case,

$$\Phi^{\gamma}_{\kappa\alpha,\kappa'\beta} = \sum_l \Phi^{\gamma}_{\kappa\alpha,\kappa'\beta}(0,l). \tag{5.42}$$

By using this result in combination with Eq. (5.9) and Eq. (5.21), we obtain

$$\Phi^{\gamma}_{\kappa\alpha,\kappa'\beta} = \Phi^{\mathrm{pc},\gamma}_{\kappa\alpha,\kappa'\beta} + \Phi^{\mathrm{di},\gamma}_{\kappa\alpha,\kappa'\beta} + \Phi^{\mathrm{ea},\gamma}_{\kappa\alpha,\kappa'\beta}. \tag{5.43}$$

The meaning of the three terms on the right hand side goes as follows. First, we have an on-site contribution that only depends on the Born effective charges,

$$\Phi^{\mathrm{pc},\gamma}_{\kappa\alpha,\kappa'\beta} = \frac{1}{2}\delta_{\kappa\kappa'}\sum_\rho \left(\epsilon^{\gamma\alpha\rho} Z^*_{\rho,\kappa\beta} - \epsilon^{\gamma\beta\rho} Z^*_{\rho,\kappa\alpha}\right). \tag{5.44}$$

The "point-charge" (pc) denomination indicates that, in absence of electrons, the BEC tensor becomes a constant, $Z^*_{\rho,\kappa\alpha} = Z_\kappa \delta_{\alpha\rho}$, and Eq. (5.44) reduces to the well-known Lorentz force (L) acting on a classical test particle of charge Z_κ,

$$\Phi^{\mathrm{L},\gamma}_{\kappa\alpha,\kappa'\beta} = \delta_{\kappa\kappa'} Z_\kappa \epsilon^{\gamma\alpha\beta}. \tag{5.45}$$

This term was described in Refs. [20] and [21]. Next, we have a "dispersion" (di) contribution, which stems from the fact that the electronic currents associated with ionic motion are spread out in space around the nuclear site,

$$\Phi^{\mathrm{di},\gamma}_{\kappa\alpha,\kappa'\beta} = \frac{\partial \mathcal{M}_{\gamma,\kappa'\beta}}{\partial \tau_{\kappa\alpha}} - \frac{\partial \mathcal{M}_{\gamma,\kappa\alpha}}{\partial \tau_{\kappa'\beta}}. \tag{5.46}$$

This additional term was neglected in earlier studies; its explicit calculation constitutes one of the main technical advances of this work. Finally, we have a third contribution in the form

$$\Phi^{\mathrm{ea},\gamma}_{\kappa\alpha,\kappa'\beta} = \frac{1}{2}\sum_{\delta,\rho} \epsilon^{\gamma\delta\rho} \left(\tau_{\kappa'\delta} \frac{\partial Z^*_{\rho,\kappa'\beta}}{\partial \tau_{\kappa\alpha}} - \tau_{\kappa\delta} \frac{\partial Z^*_{\rho,\kappa\alpha}}{\partial \tau_{\kappa'\beta}} \right), \tag{5.47}$$

which is different from zero only when $\kappa \neq \kappa'$, and corresponds to the *electrical anharmonicity* (ea) tensor discussed by Roman *et al.* [146]. This term is present only if the site symmetries of the occupied Wyckoff position lack the space inversion operation; if, on the other hand, every atom in the crystal sits at an inversion center (e.g., cubic perovskites like $\mathrm{SrTiO_3}$), $\Phi^{\mathrm{ea},\gamma}_{\kappa\alpha,\kappa'\beta}$ vanishes identically. One can also verify that all three contributions are antisymmetric under $\kappa\alpha \leftrightarrow \kappa'\beta$ exchange, consistent with the definition of Eq. (5.41) and that they are independent of the choice of the coordinate origin. In addition, note that Eqs. (5.44), (5.46) and (5.47) can be computed with DFPT by considering only the unit cell of the system; details about our computational implementation are given in Sec. 5.2.

As a final comment, we expect all the three terms contributing to Eq. (5.41) to vanish for large interatomic distances, although there may be long-range contributions mediated by electrostatic forces; their detailed analysis, while interesting, goes beyond the scope of our work, as we will only focus on zone-center phonons.

5.1.5 PHONON g FACTOR AND FREQUENCY SPLITTING

We now demonstrate how the formalism of the last subsection can be used to calculate the g factor for the phonon modes of an extended solid [20, 21, 59]. In order to find a solution for the equations of motion of the ions given by Eq. (5.40), as usual, we try the following *ansatz*,

$$u^l_{\kappa\beta}(t) = U^{\mathbf{q}}_{\kappa\beta} e^{i(\mathbf{q}\cdot\mathbf{R}^l_\kappa - \omega t)}, \tag{5.48}$$

where ω is the frequency. We shall specialize to the $\mathbf{q} = \mathbf{0}$ case henceforth, and thus remove the $\mathbf{q}$ subscript. We obtain,

$$\omega^2 \tilde{U}_{\kappa\alpha} = \sum_{\kappa',\beta} \left(D^{(0)}_{\kappa\alpha,\kappa'\beta} + i\omega B_\gamma D^{\gamma}_{\kappa\alpha,\kappa'\beta} \right) \tilde{U}_{\kappa'\beta}, \tag{5.49}$$

with $U_{\kappa\alpha} = \tilde{U}_{\kappa\alpha} / \sqrt{M_\kappa}$ and

$$\begin{aligned} D^{(0)}_{\kappa\alpha,\kappa'\beta} &= \frac{1}{\sqrt{M_\kappa M_{\kappa'}}} \sum_l \Phi_{\kappa\alpha,\kappa'\beta}(0,l), \\ D^{\gamma}_{\kappa\alpha,\kappa'\beta} &= \frac{1}{\sqrt{M_\kappa M_{\kappa'}}} \sum_l \Phi^{\gamma}_{\kappa\alpha,\kappa'\beta}(0,l). \end{aligned} \tag{5.50}$$

The term that is linear in $\mathbf{B}$ in Eq. (5.49) shall be treated as a perturbation of the $\mathbf{B} = \mathbf{0}$ phonon dynamics in the following. The system we shall consider is a cubic crystal with a two-fold degenerate transverse optical mode at the Γ point (e.g., the “soft” [147] polar mode in cubic $SrTiO_3$). The unperturbed ($\mathbf{B} = \mathbf{0}$) frequency, $\omega^{(0)}$, can be determined from the following eigenvalue problem,

$$[\omega^{(0)}_i]^2 V^{(i)}_{\kappa\alpha} = \sum_{\kappa',\beta} D^{(0)}_{\kappa\alpha,\kappa'\beta} V^{(i)}_{\kappa'\beta}, \tag{5.51}$$

where i runs over the degenerate modes and $V^{(i)}_{\kappa'\beta}$ are the eigenvector components, where κ' runs from 1 to N (number of ions in the cell) and β runs over the Cartesian directions. We choose $i = 1, 2$ to span the plane orthogonal to $\mathbf{B}$ in such a way that they form a right handed coordinate system. We can now apply degenerate perturbation theory to Eq. (5.51) by choosing the unperturbed eigenvectors as

$$\begin{aligned} |+\rangle &= \frac{1}{\sqrt{2}} \left(|V^{(1)}\rangle + i\,|V^{(2)}\rangle \right), \\ |-\rangle &= \frac{1}{\sqrt{2}} \left(|V^{(1)}\rangle - i\,|V^{(2)}\rangle \right), \end{aligned} \tag{5.52}$$

where $\langle\kappa'\beta|V^{(i)}\rangle = V^{(i)}_{\kappa'\beta}$. Here $|\kappa'\beta\rangle$ stands for a unit displacement of ion κ' along the Cartesian direction β while the rest of ions remain still; $|V^{(i)}\rangle$ is therefore a $3\times N$ dimensional vector. $|+\rangle$ and $|-\rangle$ are circularly polarized phonon modes expressed as a superposition of linearly polarized modes. In order to account for the frequency splitting and to verify that the eigenvectors given by Eq. (5.52) diagonalize the perturbation, we build the perturbation matrix g_{ij},

$$g_{ij} = i\begin{pmatrix} \langle +|\,\mathbf{D}^{\gamma}\,|+\rangle & \langle +|\,\mathbf{D}^{\gamma}\,|-\rangle \\ \langle -|\,\mathbf{D}^{\gamma}\,|+\rangle & \langle -|\,\mathbf{D}^{\gamma}\,|-\rangle \end{pmatrix}, \tag{5.53}$$

which we identify with the gyromagnetic g_{ij} tensor of the phonon modes [20, 21, 58, 59]. Assuming cubic symmetry, this reduces to

$$g_{ij} = \begin{pmatrix} g & 0 \\ 0 & -g \end{pmatrix}, \tag{5.54}$$

where

$$\begin{aligned} g &= i\,\langle +|\,\mathbf{D}^{\gamma}\,|+\rangle \\ &= i\,\langle +|\,(\mathbf{D}^{\mathrm{pc},\gamma} + \mathbf{D}^{\mathrm{di},\gamma})\,|+\rangle \\ &= g^{\mathrm{pc}} + g^{\mathrm{di}} \end{aligned} \tag{5.55}$$

is the g factor of the phonon modes. We have explicitly indicated the two contributions on $\mathbf{D}^{\gamma}$ coming from Eq. (5.44) and Eq. (5.46); there is only a difference of a mass factor between $\mathbf{\Phi}^{\gamma}$ and $\mathbf{D}^{\gamma}$, which is indicated in Eq. (5.50). Once the g factor is computed it is easy to give an expression for the frequency splitting of the modes,

$$\omega^{(\pm)} \simeq \omega^{(0)} \pm \frac{1}{2} g B_{\gamma}. \tag{5.56}$$

Before closing this section, we will briefly comment on the relationship between our methodology to calculate the phonon g factors and previous first-principles approaches. Spaldin and coworkers [20, 21] calculated the "pc" contribution, while the "di" term was systematically neglected, resulting in a point-charge approximation to the full g factor; we will show later that for the soft polar mode in $SrTiO_3$, both terms are of the same order of magnitude. In Ref. [59], Ceresoli presents a point charge model, in addition to a similar perturbative treatment to our Eq. (5.49). In the latter, it was assumed that the Born effective charge tensor was isotropic for each sublattice κ, which is not the case for cubic perovskites like $SrTiO_3$. Also, Ceresoli's version of our dispersion contribution $\mathbf{D}^{\mathrm{di},\gamma}$ was in the form of a Berry curvature. While formally equivalent to our expression, which can be seen by writing the Lagrangian in terms of the effective vector potential given by Eq. (5.10), it is more computationally demanding compared to the DFPT implementation given here.

5.2 IMPLEMENTATION

We now discuss the practical calculation of the dynamical magnetic moments, $\boldsymbol{\mathcal{M}}$, in the framework of density-functional perturbation theory. The other physical property entering the g factors, i.e., the Born effective charge tensor $\mathbf{Z}^*$, is straightforward to calculate within standard implementations of DFPT [77, 140].

5.2.1 POLARIZATION RESPONSE TO A LONG-WAVELENGTH PHONON

The polarization response to a phonon (times a trivial volume factor) is just a particular case of Eq. (2.106), where the perturbation is identified with $\lambda = \tau_{\kappa\alpha}$. For clarity, we write it down explicitly,

$$J^{\mathbf{q}}_{\alpha,\kappa\beta} = -2 \int_{\mathrm{BZ}} [d^3k] \sum_{m\in\mathcal{V}} f_{m\mathbf{k}} \, \langle i u^{A_\alpha}_{m\mathbf{k},\mathbf{q}} | u^{\tau_{\kappa\beta}}_{m\mathbf{k},\mathbf{q}} \rangle \, . \tag{5.57}$$

The implementation described in Ref. [98] allows for the calculation of $\mathbf{J}^{\mathbf{q}}_{\kappa\beta}$ directly via Eq. (5.57); $J^{(1,\gamma)}_{\alpha,\kappa\beta}$ can be then obtained by taking numerical derivatives around $\mathbf{q} = 0$. The same finite-$\mathbf{q}$ implementation [98] enables the computation of the magnetic susceptibility of the system, which we shall use in our numerical tests of Eq. (5.37). This finite-$\mathbf{q}$ methodology will be used to double check the results that will be obtained from an alternative method, which consists in the application of the analytical long-wave DFPT approach described in Sec. (2.4.4) to the polarization case.

5.2.2 ANALYTICAL LONG-WAVE EXPANSION

The treatment of the polarization response to a long-wavelength phonon is described in detailed in Ref. [41], where the long-wave limit of a second-order energy, with respect to a modulated electric field and a phonon perturbation, is taken analytically. The final expression reads as

$$J^{(1,\gamma)}_{\alpha,\kappa\beta} = -\mathrm{Im}\, E^{\mathcal{E}_\alpha \tau_{\kappa\beta}}_{\gamma}, \tag{5.58}$$

where

$$E^{\mathcal{E}_\alpha \tau_{\kappa\beta}}_{\gamma} = 2 \int_{\mathrm{BZ}} [d^3k] E^{\mathcal{E}_\alpha \tau_{\kappa\beta}}_{\mathbf{k},\gamma} + \int_{\Omega} \int n^{\mathcal{E}_\alpha}(\mathbf{r}) K_\gamma(\mathbf{r},\mathbf{r}') n^{\tau_{\kappa\beta}} \, d^3r \, d^3r', \tag{5.59}$$

and the quantity that needs to be integrated over the BZ is given by

$$\begin{aligned} E^{\mathcal{E}_\alpha \tau_{\kappa\beta}}_{\mathbf{k},\gamma} = & \sum_{m\in\mathcal{V}} f_{m\mathbf{k}} \, \langle u^{\mathcal{E}_\alpha}_{m\mathbf{k}} | \, \hat{H}^{k_\gamma}_{\mathbf{k}} \, | u^{\tau_{\kappa\beta}}_{m\mathbf{k}} \rangle \\ & - \sum_{m,n\in\mathcal{V}} f_{m\mathbf{k}} \left(\langle u^{\mathcal{E}_\alpha}_{m\mathbf{k}} | u^{k_\gamma}_{n\mathbf{k}} \rangle \, \langle u^{(0)}_{m\mathbf{k}} | \, \hat{\mathcal{H}}^{\tau_{\kappa\beta}}_{\mathbf{k}} \, | u^{(0)}_{m\mathbf{k}} \rangle + \langle u^{(0)}_{m\mathbf{k}} | \, \hat{V}^{\mathcal{E}_\alpha} \, | u^{(0)}_{n\mathbf{k}} \rangle \, \langle u^{k_\gamma}_{n\mathbf{k}} | u^{\tau_{\kappa\beta}}_{m\mathbf{k}} \rangle \right) \\ & + \sum_{m\in\mathcal{V}} f_{m\mathbf{k}} \left(\langle u^{\mathcal{E}_\alpha}_{m\mathbf{k}} | \, \hat{H}^{\tau_{\kappa\beta}}_{\mathbf{k},\gamma} \, | u^{(0)}_{m\mathbf{k}} \rangle + \langle i u^{A_\alpha}_{m\mathbf{k},\gamma} | u^{\tau_{\kappa\beta}}_{m\mathbf{k}} \rangle \right) . \end{aligned} \tag{5.60}$$

The reason why we think it is worth writing down those expressions explicitly is related to a term that appears in the third line of Eq. (5.60), $|u^{A_\alpha}_{m\mathbf{k},\gamma}\rangle$, which describes the wave function response to a long-wavelength electromagnetic vector potential field. Although the theoretical basis for its computation within a DFPT framework is well established (see Appendix A of Ref. [41]), this is not a standard capability of publicly available codes like ABINIT. In fact, the existing implementation [41] focuses on the dynamical quadrupoles $Q^{(2,\alpha\gamma)}_{\kappa\beta}$, which are symmetric under exchange of Cartesian indices $\alpha \leftrightarrow \gamma$, as shown in Eq. (5.19). Therefore, only the

Molecule	Geometry	Molecule	Geometry
H_2	$d = 1.446$	FCCH	$d_{\mathrm{FC}} = 2.396$, $d_{\mathrm{CC}} = 2.260$, $d_{\mathrm{CH}} = 2.022$
N_2	$d = 2.066$	HNC	$d_{\mathrm{HN}} = 1.908$, $d_{\mathrm{NC}} = 2.202$
F_2	$d = 2.622$	H_2O	$d_{\mathrm{HO}} = 1.835$, $\angle\mathrm{HOH} = 104.8°$
HF	$d = 1.760$	HN_3	$d_{\mathrm{NH}} = 1.930$, $\angle\mathrm{HNH} = 107.3°$
CH_4	$d_{\mathrm{CH}} = 2.070$	...	...

Table 5.1: Geometry of selected molecules after relaxation. Distances are in bohr and ∠ABC represents the bond angle of atoms A, B and C.

symmetric components of $|u^{A_\alpha}_{m\mathbf{k},\gamma}\rangle$ are currently available. To access the *antisymmetric* components, as required for the full tensorial form of $J^{(1,\gamma)}_{\alpha,\kappa\beta}$, additional coding effort is required.

Even though the implementation of the wave function response $|u^{A_\beta}_{m\mathbf{k},\gamma}\rangle$ constitutes a crucial aspect of the methodology we have presented in this chapter, we have decided to leave all the details for Appendix D.

5.2.3 COMPUTATIONAL PARAMETERS

For the numerical validation of the methodology presented in the previous sections, we use the Perdew-Wang [81] parametrization of the local density approximation (LDA) and Optimized Norm-Conserving Vanderbilt Pseudopotentials (ONCVPSP) [88] in all the DFT and DFPT calculations.

Our numerical results on rotational g factors of molecules are obtained employing a large cell of $20 \times 20 \times 20$ bohr^3 to avoid interactions between neighboring images. A maximum plane-wave cutoff of 100 Ha (60 Ha for CH_4, C_5H_5N and C_6H_5F) is used and the Brillouin Zone is sampled with a single $\mathbf{k}$ point at Γ. The structural optimization for the geometry of the molecules is performed to a tolerance of 5×10^{-7} Ha/bohr on the residual forces. The relaxed molecular geometries employed in our calculations are shown in Table 5.1 and Table 5.2.

For our calculations on $SrTiO_3$, we use the five-atom primitive cubic cell, with a plane-wave cutoff of 80 Ha and an $8 \times 8 \times 8$ mesh of $\mathbf{k}$ points to sample the Brillouin Zone; with this setup we obtain an optimized cell parameter of $a_0 = 7.288$ bohr. For the derivative with respect to the displacement of atoms appearing in Eq. (5.46), $\partial/\partial\tau_{\kappa\alpha}$, we apply a displacement of 0.01 bohr to atom κ along the Cartesian direction α and compute the derivative via finite differences; this means that $3N$ (where N is the number of atoms in the cell) of such calculations are needed to compute the full $\mathbf{D}^\gamma$ matrix. This number could be reduced significantly via use of symmetries; however, in our calculations we opt for a straightforward calculation of all components, and check that the resulting generalized Lorentz force tensor enjoys the expected symmetries as part of the validation procedure.

Atom	x	y	Atom	x	y
F	0.000	-4.138	C_1	2.510	0.070
C_1	0.000	-1.605	C_2	1.303	-2.249
C_2	-2.281	-0.352	C_3	-1.308	-2.295
C_3	2.281	-0.352	C_4	-2.599	-0.026
C_4	-2.264	2.262	C_5	-1.219	2.196
C_5	2.264	2.262	N	1.289	2.261
H_1	0.000	3.573	H_1	4.577	0.172
H_2	-4.034	-1.435	H_2	2.402	-3.993
H_3	4.034	-1.435	H_3	-2.328	-4.088
H_4	-4.051	3.289	H_4	-4.659	0.034
H_5	4.051	3.289	H_5	-2.185	4.026
H_6	0.000	5.633	…	…	…

Table 5.2: Relaxed Cartesian coordinates (in bohr) of C_6H_5F (left) and C_5H_5N (right) molecules, which lie in the xy plane with $z = 0$.

5.3 RESULTS

5.3.1 ROTATIONAL g FACTOR OF MOLECULES

To begin with, we present a detailed study of the H_2, N_2, and F_2 molecules, since they constitute the simplest nontrivial test of our methodology. In the case of elemental diatomic molecules, the rotational g factor is only defined for rotations about an axis that is perpendicular to the bond. Assuming that the bond is aligned with the x Cartesian direction, and that the rotation axis passes through the center of mass, the g factor reduces to

$$g = \frac{J^{(1,x)}_{y,1y} - J^{(1,y)}_{x,1y}}{I}, \tag{5.61}$$

where $I = Md^2/2$ is the moment of inertia and $\kappa = 1$ is the label for one of the ions of the elemental diatomic molecule; d stands for the interatomic distance, and M is the atomic mass in units of the proton mass. Fig. 5.1 shows the convergence with respect to the plane-wave energy cutoff of the g factor of H_2 using the experimental geometry (d_{exp}=1.4 bohr), calculated with the analytical long-wave approach described in Sec. 5.2.2. We see that the result is well-converged at a relatively modest (for a molecule in a box) energy cutoff of 50 Ha. We can compare the converged value of 0.8956 to the finite-$\mathbf{q}$ calculations, which gives precisely 0.8956. For N_2 (d_{exp}=2.074 bohr) and F_2 (d_{exp}=2.668 bohr), the analytical long-wave approach gives -0.2704 and -0.1043, also in excellent agreement with the finite-difference method, which yields -0.2708 and -0.1045, respectively. The excellent agreement confirms the accuracy of our implementation described in Sec. 5.2.2.

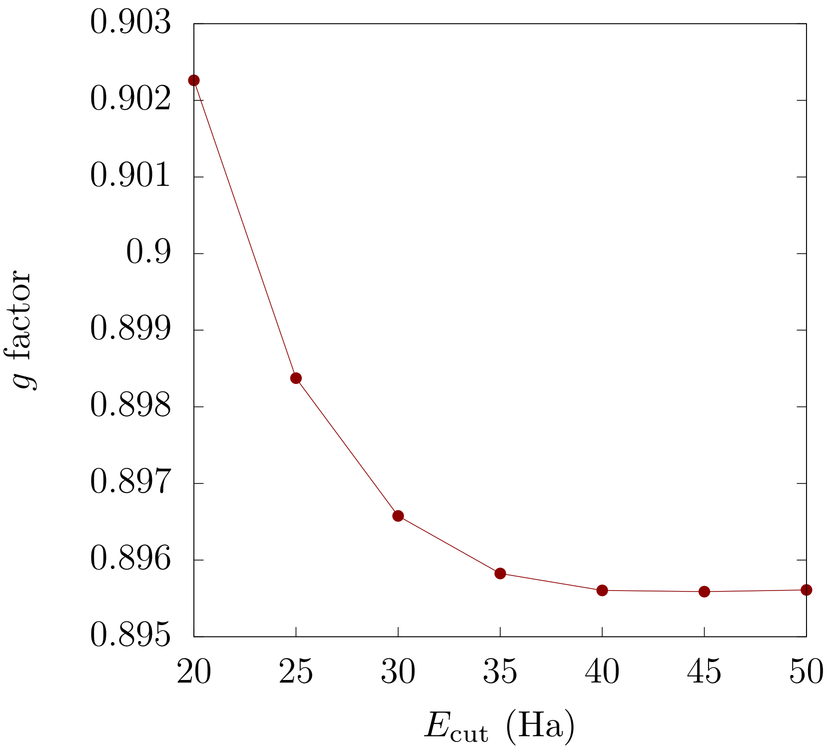

Figure 5.1: Convergence of the g factor of H_2 (with $d_{\mathrm{exp}} = 1.4$ bohr) with respect to the plane-wave cutoff, E_{cut}. Calculations are performed using a single $\mathbf{k}$ point (Γ) with a box size of $20 \times 20 \times 20$ bohr^3. Solids lines are a guide to the eye.

Since the H atom is well described by a local pseudopotential, we can use the H_2 molecule to benchmark the performance of the two alternative formulations of $\partial m_a / \partial \omega_b$; i.e., Eq. (5.30) —which reduces to Eq. (5.61) in this case— and Eq. (5.37). In Fig. 5.2 (a) we the plot the calculated g factor of H_2 versus inverse cell size by using both methods. As anticipated in Sec. 5.1.3.2, we find that Eq. (5.37) is quite challenging to converge, while the corresponding results of Eq. (5.61) display an optimally fast convergence. To understand the origin of such a behavior, we show in Fig. 5.2 (b) a decomposition of Eq. (5.37) into the two contributions on the right hand side. This analysis clarifies that the convergence is limited by the quadrupole term [i.e., the second term in Eq. (5.37)], while the magnetic susceptibility of the molecule is already converged at a relatively small box size. If we extrapolate this term to the limit of an infinitely large cell parameter ($1/a \to 0$, purple dashed curve), then we see that our g factor indeed converges to the value we obtain using the methodology of Sec. 5.2.2 [purple cross on Fig. 5.2 (a)]. The agreement for large cell sizes provides an independent confirmation of the accuracy of our approach, though the methodology of Sec. 5.2.2 is clearly superior from a computational perspective.

As anticipated, a further issue with Eq. (5.37) consists in the fact that it may yield qualitatively incorrect results when nonlocal pseudopotentials are used, i.e., in the vast majority of first-principles simulations that are being performed nowadays. An obvious example is that of a neutral (and isolated) closed-shell atom, where

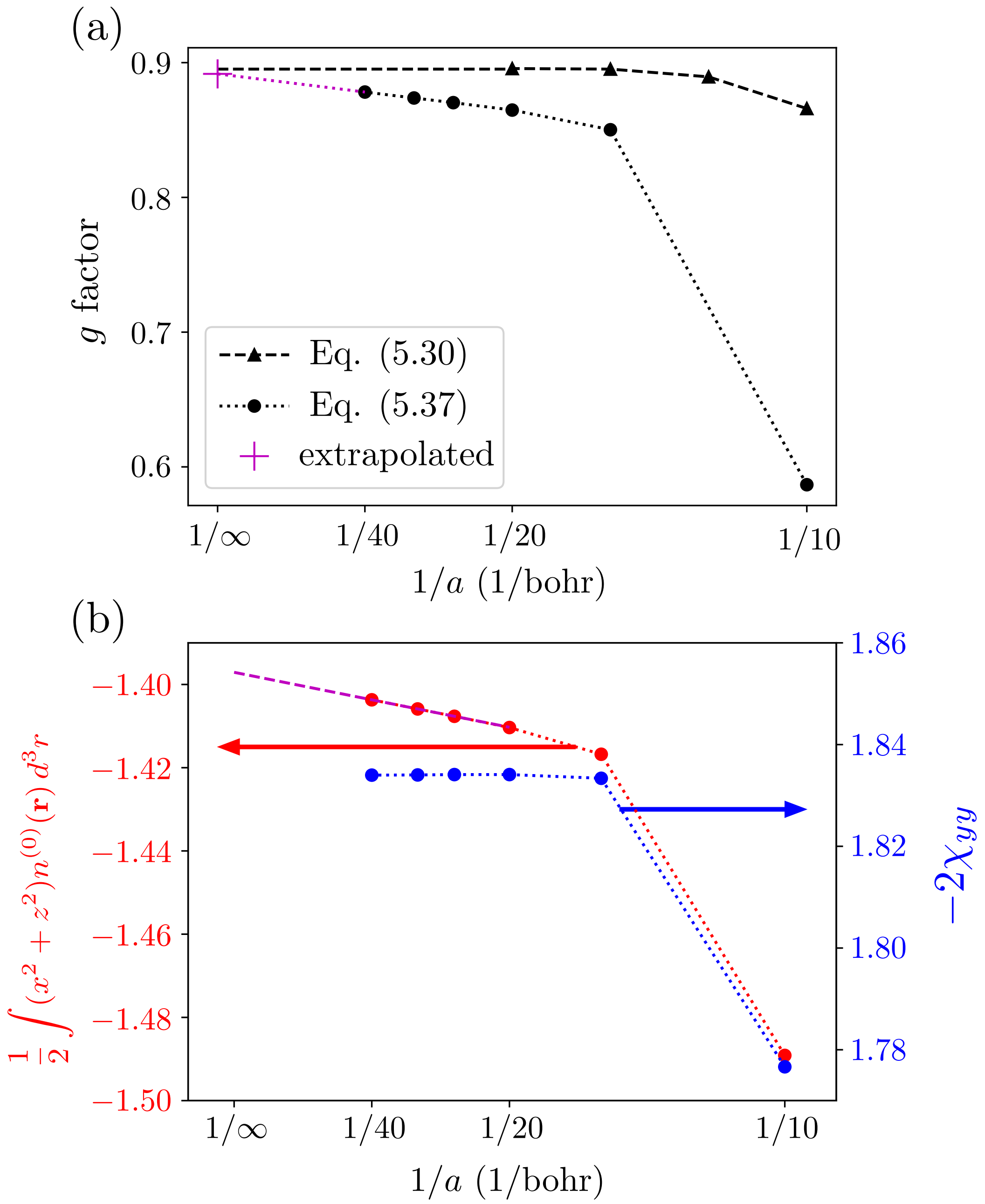

Figure 5.2: (a) Calculation of rotational g factor of H_2 (with d_{exp}=1.4 bohr) using the expression for $\partial m_a/\partial \omega_b$ from Eq. (5.37) (dots) and from Eq. (5.30) (triangles) versus inverse of the simulation cell size side length. (b) Convergence of terms in Eq. (5.37) versus inverse of the simulation cell size. Purple dashed line in (b) is the extrapolated value for the quadrupole term; the purple cross in (a) is the g factor calculated with the extrapolated quadrupole term.

the rotationally induced magnetization must vanish exactly. This requirement is trivially fulfilled by our Eq. (5.30): both dynamical charges and dynamical magnetic moments identically vanish in this system due to charge neutrality and inversion symmetry. In the context of Eq. (5.37) one would also expect a vanishing result: Langevin's theory of diamagnetism expresses the susceptibility as the quadrupolar moment of the spherical atomic charge, which should cancel out exactly with the second term on the right hand side. In presence of nonlocal pseudopotentials, however, Langevin's result no longer holds, and Eq. (5.37) yields a nonzero value for all noble gas atoms except He. (The latter, just like H, is well described by a local pseudopotential.) We regard this as a serious concern in this context, and we therefore caution against a straightforward application of Eq. (5.37) to the calculation of rotational g factors.

In addition to the aforementioned elemental diatomic molecules, we consider several other examples: HF, HNC, and FCCH (still linear, but with a finite dipole moment), nonlinear molecules such as NH_3, H_2O, and CH_4, and the aromatic compounds C_5H_5F and C_6H_5F. At difference with H_2 and related structures, in all these cases Eq. (5.28) contains a nonzero contribution from the Born effective charges; therefore, these additional examples offer the opportunity to test the full formula, Eq. (5.30) —in combination with Eq. (5.28)—, rather than its simplified version, Eq. (5.61). In order to calculate the g factor, the rotation axis is taken to be perpendicular to the molecular axis in linear molecules (H_2 , N_2 , F_2 , HF, HNC, and FCCH), perpendicular to the molecular plane for C_5H_5N, C_6H_5F and H_2O, along one of the bonds in CH_4 and perpendicular to the plane formed by the H atoms in NH_3; it is assumed that the magnetic field is parallel to the rotation axis in all cases.

In Table 5.3 we compare our results for the rotational g factors to experimental measurements from Refs. [148] and [56]. In addition, we report the results of previous calculations using Hartree-Fock (HF) and post Hartree-Fock methods [57], as well as DFT calculations using the Berry-phase method [58, 149]. Since the inclusion of electron-electron correlations, either at the level of Møller-Plesset (MP) perturbation theory or coupled cluster with double excitations (CCD), seems to improve the agreement with experiment in many cases, [57] we include those data as well for comparison. We see that our DFPT based method compares well even with the best theoretical values obtained via more computationally demanding methods. Our results in Table 5.3 are also in excellent agreement with experiment, where available; CH_4 appears to be the only exception, though the reason for the larger discrepancy is not clear.

5.3.2 SOFT-MODE FREQUENCY SPLITTING OF CUBIC $SrTiO_3$

We now turn our attention to the splitting of the soft polar TO mode at the zone-center in cubic $SrTiO_3$. As we did in the case of the rotational g factors in Sec. 5.3.1, we can test the accuracy of the generalized Lorentz forces by comparing the implementation described in Sec. 5.2.2 with the alternative finite-$\mathbf{q}$ approach of Sec. 5.2.1. In Table 5.4, we present the linearly independent components of $D^{\mathrm{di},\gamma=z}_{\kappa\alpha,\kappa'\beta}$ for cubic $SrTiO_3$ using both methods. Note that our labeling convention for the oxygen is, in reduced coordinates: $O_1 = (0, 1/2, 1/2)$, $O_2 = (1/2, 0, 1/2)$, $O_3 = (1/2, 1/2, 0)$. The additional $(\kappa\alpha, \kappa'\beta)$ tensor components can be determined

	Rotational g factor			
	This work	HF/DFT	MP/CDD	Exp.
H_2	0.8901	0.9103[a] 0.8755[b]	0.8899[a]	0.8829[c]
N_2	−0.2699	−0.2872[a]	−0.2653[a]	−0.2593[c]
F_2	−0.1003	−0.0900[a]	−0.1136[a]	−0.1208[c]
HF	0.7603	0.7624[a]	0.7488[a]	0.7392[c]
HNC	−0.1004	−0.0996[a]	−0.0968[a]	···
FCCH	−0.0065	···	···	−0.0077[d]
H_2O	0.6699	0.6640[a]	0.6507[a]	0.6450[c]
NH_3	0.5289	0.5061[a]	0.5044[a]	···
CH_4	0.3629	0.3019[a] 0.2985[e]	0.3190[a]	0.3133[c]
C_5H_5N	0.0411	···	···	0.0428[d]
C_6H_5F	0.0276	···	···	0.0266[d]

Table 5.3: Calculated rotational g factors for selected simple molecules compared with the relevant literature data. "HF/DFT" and "MP/CCD" stand for computational results at various level of theory (Hartree-Fock / Density Functional Theory, and Møller-Plesset perturbation theory / Coupled-Cluster with Double excitations); "Exp." refers to experimental measurements. Theoretical values from other works are taken from:

[a] Ref. [57]
[b] Ref. [58]
[c] Ref. [148]
[d] Ref. [56]
[e] Ref. [149]

from symmetry considerations. Overall, we see quite good agreement, to the second or third decimal places, between the very distinct implementations; this confirms the accuracy of our methodology.

With the information of Table 5.4 we can readily obtain the g factor for the low-frequency TO phonon modes by means of Eq. (5.55), where we can identify contributions coming from $\mathbf{J}^{(0)}$ (g^{pc}) and $\mathbf{J}^{(1)}$ (g^{di}) terms. We obtain, in atomic units, the following numerical values,

$$g = -1.2083 \times 10^{-4}, \qquad g^{\text{pc}} = 0.6679 \times 10^{-4}, \qquad g^{\text{di}} = -1.8763 \times 10^{-4}. \quad (5.62)$$

As mentioned earlier, some works [20, 21] have only accounted for the terms depending on the Born effective charges within a point-charge approximation, roughly corresponding to our calculated g^{pc}. It is immediately clear from our results in Eq. (5.62) that such an approximation is inappropriate: the remainder (g^{di}) has opposite sign and is almost three times larger (in absolute value) than

$(\kappa\alpha, \kappa'\beta)$	DFPT	Finite $\mathbf{q}$	$(\kappa\alpha, \kappa'\beta)$	DFPT	Finite $\mathbf{q}$
(Sr x, Sr y)	1.5320	1.5317	(Ti x, O$_3$ y)	3.7315	3.7336
(Sr x, Ti y)	2.4483	2.4526	(O$_1$ x, O$_2$ y)	-6.3272	-6.3416
(Sr x, O$_1$ y)	-0.4487	-0.4489	(O$_2$ x, O$_1$ y)	3.9400	3.9416
(Sr x, O$_2$ y)	-2.3829	-2.3874	(O$_2$ x, O$_2$ y)	8.3977	8.3987
(Sr x, O$_3$ y)	-1.1537	-1.1542	(O$_3$ x, O$_1$ y)	-0.3842	-0.3845
(Ti x, Ti y)	8.4125	8.4037	(O$_3$ x, O$_2$ y)	-2.0026	-2.0041
(Ti x, O$_1$ y)	-9.6112	-9.6131	(O$_3$ x, O$_3$ y)	0.0642	0.0653
(Ti x, O$_2$ y)	-2.4061	-2.3937	...	...	...

Table 5.4: $D^{\mathrm{di},z}_{\kappa\alpha,\kappa'\beta}$ elements [see Eq. (5.46)] for cubic SrTiO$_3$ calculated with the analytical long-wave DFPT implementation described in Sec. 5.2.2, and the finite-$\mathbf{q}$ implementation described in Sec. 5.2.1. Values are given in Hartree atomic units.

the contribution coming from g^{pc}; as a result, the total g factor disagrees with g^{pc} both in magnitude and sign. This indicates that an accurate computation of the $\mathbf{J}^{(1)}$ tensor is crucial in this particular case and that these terms should not be neglected.

For a more quantitative comparison, note that Ref. [59] and Ref. [21] computed g^{pc} for tetragonal SrTiO$_3$, obtaining values of $g^{\mathrm{pc}} = 5.76 \times 10^{-5}\,\mathrm{cm}^{-1}/\mathrm{T}$ and $g^{\mathrm{pc}} = 4.78 \times 10^{-5}\,\mathrm{cm}^{-1}/\mathrm{T}$, respectively. In those units, our result for cubic SrTiO$_3$ is $g^{\mathrm{pc}} = 6.23 \times 10^{-5}\mathrm{cm}^{-1}/\mathrm{T}$. The agreement is rather good, especially considering that: (i) we are considering the full tensorial form of the Born effective charge tensor and (ii) our analysis is carried out in the cubic, and not tetragonal, phase of SrTiO$_3$. Note that Ref. [59] also reports a result for the total g factor; they obtain $g = -7.95 \times 10^{-5}\,\mathrm{cm}^{-1}/\mathrm{T}$, which again compares well to our calculated value of $g = -11.28 \times 10^{-5}\,\mathrm{cm}^{-1}/\mathrm{T}$.

To gain some insight on the physics, we perform a further decomposition of g^{pc} and g^{di} into the individual contributions of each atomic sublattice. In the case of g^{pc}, such a decomposition is straightforward, as this term mediates an on-site coupling between the displacement of each atom and its own velocity. (This can be appreciated by observing that the corresponding contribution to the generalized Lorentz force, Eq. (5.44), contains a $\delta_{\kappa\kappa'}$ prefactor.) The case of g^{di} is less obvious: the nondiagonal (on the atomic index) nature of $\mathbf{D}^{\mathrm{di},\gamma}$ implies that the velocity of a given atom can produce forces not only onto itself, but also on its neighbors. Thus, prior to attempting a decomposition of g^{di}, we first isolate the basis-diagonal $\kappa = \kappa'$ terms in $\mathbf{D}^{\mathrm{di},\gamma}$, and use them to define an on-site contributions to g^{di} (indicated as $g^{\mathrm{di}}_{\kappa=\kappa'}$ henceforth). Apart from enabling the aforementioned decomposition, this analysis also gives a flavor of the overall importance of the off-site contributions to g^{di}. The results are summarized in Table 5.5. Regarding g^{pc}, we find that the contribution of the oxygen atoms largely dominates over the rest, consistent with the conclusions of Ref. [59]. Due to their smaller mass, oxygens evolve along larger orbits, which amplifies their contribution to the magnetic moment. Regarding g^{di}, we find that the on-site terms represent more than the 75% of the total g^{di} factor,

	Sr	Ti	O_1	O_2	O_3	Total
g^{pc}	-0.0197	-0.1082	0.2985	0.2985	0.1987	0.6679
$g^{\text{di}}_{\kappa=\kappa'}$	-0.0118	-0.1246	-0.6429	-0.6429	-0.0062	-1.4284

Table 5.5: Contribution of each atom to g^{pc} and $g^{\text{di}}_{\kappa=\kappa'}$, which are defined as the on-site ($\kappa = \kappa'$) contributions to g^{di}. Values are in 10^{-4} atomic units.

which indicates that intersite couplings have a relatively minor importance. At the level of $g^{\text{di}}_{\kappa=\kappa'}$, we find that the contribution of the equatorial oxygens is by far the largest, and primarily responsible for reversing the sign of the overall g factor.

Finally, we use the above results to calculate the frequency splitting of the TO modes. Considering a magnetic field of $B = 100$ T we obtain $gB \sim 0.01\,\text{cm}^{-1}$, of the same order as predicted in Ref. [20]. This is, however, a very small value that appears challenging to resolve even for the most powerful experimental techniques available nowadays.

It is noteworthy to mention that spin-orbit coupling (SOC) effects have also been discussed in the literature [22] in this context. Although SOC has been systematically neglected in our calculations, it can make an impact on the calculated phonon g factor primarily in two different ways. First, the inclusion of SOC could directly affect the phonon dispersion of $SrTiO_3$; however, previous first-principles calculations [22] have demonstrated that these effects are almost negligible and therefore insufficient to alter the phonon band structure of cubic $SrTiO_3$ significantly. Second, the effects of SOC on our calculated $\mathbf{J}^{(1)}$ remain to be tested. For the time being, the implementation we have described in Sec. 5.2.2 prevents the use of SOC in our first-principles calculations. The main limitation in this regard is our implementation for the wave function response to a long-wavelength electromagnetic vector potential, as described in Appendix D. However, we do not expect SOC to have considerable impact on the final numerical results.

5.4 SUMMARY AND OUTLOOK

In this chapter we have developed a complete theoretical approach for calculating orbital magnetization from rotations and pseudorotations (circularly polarized optical phonons) within the context of first-principles theory. The following points summarize the accomplishments of this chapter along with the primary strengths of our method.

- Our approach is based on density-functional perturbation theory calculations of the polarization induced by an atomic displacement (i.e., Born effective charges), and its first real-space moment, denoted as $\mathbf{J}^{(1)}$. We have demonstrated an implementation to calculate the latter quantity via generalization of the existing long-wave approach [41] to the dynamical quadrupoles; thus establishing a connection between spatial dispersion phenomena and orbital magnetism. Our coding efforts have resulted in new capabilities that have been incorporated to the ABINIT package; namely the wave function response to an orbital magnetic field, as described in Appendix D. (This is also a key ingredient for the natural optical activity, which we shall study in the next chapter.)

- Our methodology allows for an efficient and optimally accurate computation of $\mathbf{J}^{(1)}$, and works equally well for molecules and solids. Finite-$\mathbf{q}$ calculations have been used to corroborate the accuracy of our implementation.
- We have used this approach to determine rotational g factors of some simple molecules, and demonstrated excellent agreement with experimental results, where available.
- Finally, we have developed a strategy to calculate the generalized Lorentz force that enters the equations of motion of the ions in presence of a magnetic field, and utilized it to study the splitting of the soft TO phonons modes in cubic $SrTiO_3$. In this case, we have demonstrated that contributions to the phonon g factor from the first moment of the induced polarization, which had been neglected in some previous approaches, dominate the response.

As a last note, we would like the mention that in spite of the additional contributions coming from $\mathbf{J}^{(1)}$, our calculated overall phonon g factor for cubic $SrTiO_3$ remains of the same order of magnitude as the values quoted in Refs. [20, 59]. Therefore, our theory as it stands appears unlikely to explain the large phonon Hall [141] effects reported experimentally. To move forward in this direction and find an explanation for the large discrepancy between experiments and microscopic theories, we suspect that it may be necessary to take into account the quantum paraelectric nature of $SrTiO_3$ at low temperatures, e.g., by going beyond the Ehrenfest Lagrangian of Eq. (5.1). We regard this as an exciting avenue for further study.

6

NATURAL OPTICAL ACTIVITY

In this chapter we introduce, within the framework of long-wave DFPT, a novel first-principles approach to calculate the natural optical activity (NOA), which overcomes most of the limitations that currently available methods have been facing. These include numerical differentiation with respect to the wave vector, the appropriate treatment of SCF terms and cumbersome sums over empty states. In addition, our approach addresses an additional technical subtlety, namely the correct treatment of the current-density response in presence of nonlocal pseudopotentials [98]. Our methodology is equally valid for molecules and extended solids and brings the calculation of the natural optical activity to comparable accuracy and computational efficiency to that of standard linear-response properties, e.g., the dielectric tensor.

This chapter is organized as follows. We start in Sec. 6.1 by providing some fundamental concepts and mathematical definitions. In Sec. 6.2 we give a detailed explanation of the computational approach that we use to study the NOA, highlighting the advantages with respect to the currently available implementations and establishing a formal connection between our methodology and commonly used formulas for the NOA in molecules. In addition, we also address some formal aspects of the theory; in particular, the non-uniqueness of the analytic expression for the gyration coefficients. Our numerical results are presented in Sec. 6.3, where we validate our implementation by computing the natural optical activity tensor both in representative chiral crystals (trigonal Se, α-HgS, and α-SiO$_2$) and molecules ($C_4H_4O_2$). The summary and prospects for future research are presented in Sec. 6.4.

6.1 PRELIMINARY CONSIDERATIONS

Our starting point is the double Fourier transform in frequency ω and wave vector $\mathbf{q}$ of the dielectric permittivity function, $\epsilon_{\alpha\beta}(\omega,\mathbf{q})$. By expanding $\epsilon_{\alpha\beta}(\omega,\mathbf{q})$ in powers of the wave vector $\mathbf{q}$, around $\mathbf{q}=\mathbf{0}$, we obtain

$$\epsilon_{\alpha\beta}(\omega,\mathbf{q}) = \epsilon_{\alpha\beta}(\omega,\mathbf{q}=\mathbf{0}) + i\sum_{\gamma} q_\gamma \eta_{\alpha\beta\gamma}(\omega) + \ldots, \tag{6.1}$$

where $\eta_{\alpha\beta\gamma}(\omega)$ is the natural optical activity tensor [4]. In absence of dissipation (i.e., in the transparent regime), $\epsilon_{\alpha\beta}(\omega,\mathbf{q})$ is a 3×3 Hermitian matrix. At $\mathbf{q}=\mathbf{0}$ it becomes real symmetric in crystals with time-reversal (TR) symmetry, which we assume in the following. The frequency-dependent natural optical activity tensor is then also real and satisfies $\eta_{\alpha\beta\gamma}(\omega) = -\eta_{\beta\alpha\gamma}(\omega)$, which means that only 9 of the 27 components of $\eta_{\alpha\beta\gamma}$ are independent. As a consequence, $\eta_{\alpha\beta\gamma}$ is often rearranged into the second-rank *gyration* or *gyrotropic* tensor, $g_{\alpha\beta}$, [4]

$$g_{\alpha\beta}(\omega) = \frac{1}{2}\sum_{\gamma,\delta} \epsilon^{\gamma\delta\alpha}\eta_{\gamma\delta\beta}(\omega), \tag{6.2}$$

where $\epsilon^{\gamma\alpha\delta}$ is the Levi-Civita symbol. Due to crystal symmetries, the number of independent components of $g_{\alpha\beta}$ can be further reduced. To avoid unnecessary complexity, we will assume from now on that the symmetries of the solid under study are compatible with the crystallographic point group 32 (trigonal Se, α-HgS and α-SiO$_2$, which are the solids that we analyse in Sec 6.3, belong to this crystal class). Considering that the optical axis is oriented along the z Cartesian direction [49], we obtain

$$\boldsymbol{g}(\omega) = \begin{pmatrix} g_{11}(\omega) & 0 & 0 \\ 0 & g_{11}(\omega) & 0 \\ 0 & 0 & g_{33}(\omega) \end{pmatrix}, \tag{6.3}$$

where $g_{11} = \eta_{231}$ and $g_{33} = \eta_{123}$. Even for simple cases, extracting all individual components of the gyration tensor in an experiment is a challenging task. Instead, it is easier to measure the optical rotation, $\rho(\omega)$, also known as the optical rotatory power, which quantifies the extent to which the plane of polarization of the incident light is rotated as it passes through the system. For a crystal with the 32 point group, this is directly related [49] to the g_{33} component of the gyration tensor,

$$\rho(\omega) = \frac{\omega^2}{2c^2} g_{33}(\omega), \tag{6.4}$$

where c is the speed of light. In this work, we shall focus on the $\omega \to 0$ limit, where the components of both $\boldsymbol{g}$ and $\boldsymbol{\eta}$ tend to a finite constant [4],

$$\eta_{\alpha\beta\gamma} = \eta_{\alpha\beta\gamma}(\omega \to 0), \qquad g_{\alpha\beta} = g_{\alpha\beta}(\omega \to 0). \tag{6.5}$$

At leading order in the frequency, this yields a rotatory power of

$$\rho(\omega) \simeq (\hbar\omega)^2 \bar{\rho}, \qquad \bar{\rho} = \frac{g_{33}}{2(\hbar c)^2}, \tag{6.6}$$

where $\hbar$ is the reduced Planck constant. The constant $\bar{\rho}$ is usually expressed in units of deg/[mm (eV)^2] and can be directly compared to experimental measurements.

6.2 COMPUTATIONAL APPROACH

The strategy we shall follow in order to obtain a first-principles expression for the natural optical activity is based on the analytical long-wavelength DFPT methodology introduced in Sec. 2.4.4. First of all, we express the electronic contribution[1] to the dielectric permittivity function in the low-frequency limit as a second derivative of the ground state energy with respect to two spatially modulated [77] electric fields ($\boldsymbol{\mathcal{E}}$) as described in Sec. 2.4.2,

$$\epsilon_{\alpha\beta}(\mathbf{q}) = \delta_{\alpha\beta} - \frac{4\pi}{\Omega} E_{\mathbf{q}}^{\mathcal{E}_\alpha \mathcal{E}_\beta}, \tag{6.7}$$

---

[1] While undoubtedly present [77], the lattice-mediated contributions are not accounted for in the present work.

where Ω is the volume of the unit cell. This allows us to write the natural optical activity tensor as the first derivative of $\epsilon_{\alpha\beta}(\mathbf{q})$ with respect to q_γ,

$$\eta_{\alpha\beta\gamma} = -\frac{4\pi}{\Omega}\mathrm{Im}\, E_\gamma^{\mathcal{E}_\alpha\mathcal{E}_\beta}, \qquad E_\gamma^{\mathcal{E}_\alpha\mathcal{E}_\beta} = \left.\frac{\partial E_{\mathbf{q}}^{\mathcal{E}_\alpha\mathcal{E}_\beta}}{\partial q_\gamma}\right|_{\mathbf{q}=\mathbf{0}}. \tag{6.8}$$

At this stage, we invoke the $2n+1$ theorem and follow the logic of Sec. 2.4.4 for the case in which both perturbations are electric fields modulated by a wave vector $\mathbf{q}$ (see Sec. 2.4.2). We obtain

$$E_\gamma^{\mathcal{E}_\alpha\mathcal{E}_\beta} = 2\int_{\mathrm{BZ}}[d^3k]E_{\mathbf{k},\gamma}^{\mathcal{E}_\alpha\mathcal{E}_\beta} + \int_\Omega\int n^{\mathcal{E}_\alpha}(\mathbf{r})K_\gamma(\mathbf{r},\mathbf{r}')n^{\mathcal{E}_\beta}\, d^3r\, d^3r', \tag{6.9}$$

where

$$E_{\mathbf{k},\gamma}^{\mathcal{E}_\alpha\mathcal{E}_\beta} = \mathcal{X}_{\mathbf{k}}^{\mathcal{E}_\alpha k_\gamma \mathcal{E}_\beta} + \mathcal{Y}_{\mathbf{k}}^{\mathcal{E}_\alpha\mathcal{E}_\beta k_\gamma} + \mathcal{Y}_{\mathbf{k}}^{k_\gamma\mathcal{E}_\alpha\mathcal{E}_\beta} + \mathcal{W}_{\mathbf{k}}^{\alpha,\beta\gamma} + \left(\mathcal{W}_{\mathbf{k}}^{\beta,\alpha\gamma}\right)^*. \tag{6.10}$$

For the sake of convenience, we have expressed Eq. (6.10) in terms of the $\mathcal{X}_{\mathbf{k}}$, $\mathcal{Y}_{\mathbf{k}}$ and $\mathcal{W}_{\mathbf{k}}$ symbols, which we shall explain in the following. (This notation, which might look unnecessary now, will become useful shortly.) For three generic perturbations, λ_1, λ_2 and λ_3, we define

$$\mathcal{X}_{\mathbf{k}}^{\lambda_1\lambda_2\lambda_3} = \sum_{m\in\mathcal{V}} f_{m\mathbf{k}}\, \langle u_{m\mathbf{k}}^{\lambda_1}|\, \hat{\mathcal{H}}_{\mathbf{k}}^{\lambda_2}\, |u_{m\mathbf{k}}^{\lambda_3}\rangle \tag{6.11}$$

and

$$\mathcal{Y}_{\mathbf{k}}^{\lambda_1\lambda_2\lambda_3} = -\sum_{m,n\in\mathcal{V}} f_{m\mathbf{k}}\, \langle u_{m\mathbf{k}}^{\lambda_1}|u_{n\mathbf{k}}^{\lambda_3}\rangle\, \langle u_{n\mathbf{k}}^{(0)}|\, \hat{\mathcal{H}}_{\mathbf{k}}^{\lambda_2}\, |u_{m\mathbf{k}}^{(0)}\rangle\,, \tag{6.12}$$

which are well-known objects in the context of DFPT. Note that $\hat{\mathcal{H}}_{\mathbf{k}}^{k_\gamma} = \hat{H}_{\mathbf{k}}^{k_\gamma}$ as there is no SCF contribution to the derivative in $\mathbf{k}$-space, and $\hat{\mathcal{H}}_{\mathbf{k}}^{\mathcal{E}_\alpha} = \hat{V}^{\mathcal{E}_\alpha}$ in the above equations since the "external potential" is a purely cross-gap operator in the electric-field case [41] (see Sec. 2.3.4). The third contribution in Eq. (6.10), denoted by the symbol $\mathcal{W}_{\mathbf{k}}$, is given by

$$\mathcal{W}_{\mathbf{k}}^{\alpha,\beta\gamma} = i\sum_{m\in\mathcal{V}} f_{m\mathbf{k}}\, \langle u_{m\mathbf{k}}^{\mathcal{E}_\alpha}|u_{m\mathbf{k},\gamma}^{A_\beta}\rangle\,, \tag{6.13}$$

where $|u_{m\mathbf{k},\gamma}^{A_\beta}\rangle$ is the wave function response to a long-wavelength electromagnetic vector potential (see Appendix D for more details). By exploiting the symmetric and antisymmetric nature of its corresponding perturbing operator, we can express $\mathcal{W}_{\mathbf{k}}^{\alpha,\beta\gamma}$ as a sum of two contributions that are symmetric ($\mathcal{S}_{\mathbf{k}}^{\alpha,\beta\gamma}$) and antisymmetric ($\mathcal{A}_{\mathbf{k}}^{\alpha,\beta\gamma}$) with respect to $\beta \leftrightarrow \gamma$ exchange:

$$\mathcal{W}_{\mathbf{k}}^{\alpha,\beta\gamma} = \mathcal{S}_{\mathbf{k}}^{\alpha,\beta\gamma} + \mathcal{A}_{\mathbf{k}}^{\alpha,\beta\gamma}, \tag{6.14}$$

where

$$\mathcal{S}_{\mathbf{k}}^{\alpha,\beta\gamma} = \frac{i}{2}\sum_{m\in\mathcal{V}} f_{m\mathbf{k}}\, \langle u_{m\mathbf{k}}^{\mathcal{E}_\alpha}|\partial^2_{\beta\gamma} u_{m\mathbf{k}}^{(0)}\rangle \tag{6.15}$$

and

$$\mathcal{A}_{\mathbf{k}}^{\alpha,\beta\gamma} = \frac{1}{2}\sum_\delta \epsilon^{\delta\beta\gamma}\sum_{m\in\mathcal{V}} f_{m\mathbf{k}}\, \langle u_{m\mathbf{k}}^{\mathcal{E}_\alpha}|u_{m\mathbf{k}}^{B_\delta}\rangle\,. \tag{6.16}$$

In Eq. (6.15), $\partial^2_{\beta\gamma} = \partial^2/\partial_{k_\beta}\partial_{k_\delta}$ represents a second derivative in $\mathbf{k}$ space. The $|\partial^2_{\beta\gamma} u^{(0)}_{m\mathbf{k}}\rangle$ functions in $\mathcal{S}_\mathbf{k}$ are the well-known $d^2/dk_\beta dk_\gamma$ wave functions; whereas in Eq. (6.16), $|u^{B_\delta}_{m\mathbf{k}}\rangle$ gives the orbital contribution of the wave function response to a uniform magnetic field, B_δ, as defined by Essin *et al.* [102]. Upon preliminary inspection of Eq. (6.9) to Eq. (6.16), we can already highlight some of the advantages that the present methodology exhibits over previous approaches:

- Only occupied states are included in our equations, which avoids cumbersome sums over empty states of previous methods.
- Differentiation with respect to the wave vector $\mathbf{q}$ is taken analytically. Thus, undesired numerical errors caused by taking the derivative via finite differences are completely absent.
- Our methodology complies with the necessary prescriptions for the appropriate treatment of the current-density response in the presence of nonlocal pseudopotentials [98].
- SCF terms are naturally included in the formalism, either explicitly via $\hat{\mathcal{H}}^{\mathcal{E}_\beta}_\mathbf{k} = \hat{H}^{\mathcal{E}_\beta}_\mathbf{k} + \hat{V}^{\mathcal{E}_\beta}$, where $\hat{V}^{\mathcal{E}_\beta}$ is the SCF potential, or implicitly via the first-order wave functions, $|u^{\mathcal{E}_\beta}_{m\mathbf{k}}\rangle$. (The effect of SCF terms are studied in detail in Sec. 6.3, both for crystals and molecules.)
- Thanks to the $2n+1$ theorem, only response functions to uniform field perturbations are needed. (Strictly speaking, $|u^{A_\beta}_{m\mathbf{k},\gamma}\rangle$ should be considered an exception, but as shown in Appendix D, its calculation solely involves solving a standard Sternheimer equation.)
- Our methodology is equally applicable to both extended and finite systems; i.e., solids and molecules.

6.2.1 MOLECULAR LIMIT

Historically, the natural optical activity has been mostly studied in finite system like molecules, where the NOA tensor acquires contributions from well-defined [150] physical observables: magnetic dipoles, as well as electric dipoles and quadrupoles. Consequently, it is expected that the expression for the NOA that we have obtained in the last section might seem unfamiliar at first sight. The goal of this section is to establish a formal link between our method and previous approaches for the NOA, and prove that our Eq. (6.9) exactly recovers, in the molecular limit, the established formulas that have been used for years in quantum chemistry calculations.

We start by removing SCF terms from the NOA tensor, which involves excluding the electrostatic Hxc term from Eq. (6.9) and the $\mathcal{Y}_\mathbf{k}$ contributions from Eq. (6.10), as well as replacing the first-order wave functions, $|u^{\mathcal{E}_\alpha}_{m\mathbf{k}}\rangle$, with their non-self-consistent counterparts, $|\tilde{u}^{\mathcal{E}_\alpha}_{m\mathbf{k}}\rangle$. These are obtained from Eq. (2.80) once the SCF potential $\hat{V}^{\mathcal{E}_\alpha}$ is suppressed:

$$(\hat{H}^{(0)}_\mathbf{k} + a\hat{P}_\mathbf{k} - \epsilon^{(0)}_{m\mathbf{k}})\, |\tilde{u}^{\mathcal{E}_\alpha}_{m\mathbf{k}}\rangle = -i\, |u^{k_\alpha}_{m\mathbf{k}}\rangle\,. \tag{6.17}$$

(We use the "tilde" symbol to indicate that SCF terms are excluded.) Without self-consistency, the natural optical activity tensor reads as

$$\tilde{\eta}_{\alpha\beta\gamma} = -\frac{4\pi}{\Omega} \mathrm{Im}\, \tilde{E}_{\gamma}^{\mathcal{E}_\alpha \mathcal{E}_\beta}, \tag{6.18}$$

where

$$\tilde{E}_{\gamma}^{\mathcal{E}_\alpha \mathcal{E}_\beta} = 2 \int_{\mathrm{BZ}} [d^3k] \tilde{E}_{\mathbf{k},\gamma}^{\mathcal{E}_\alpha \mathcal{E}_\beta}. \tag{6.19}$$

The quantity that needs to be integrated over the whole BZ is given by

$$\tilde{E}_{\mathbf{k},\gamma}^{\mathcal{E}_\alpha \mathcal{E}_\beta} = \tilde{\mathcal{X}}_{\mathbf{k}}^{\mathcal{E}_\alpha k_\gamma \mathcal{E}_\beta} + \tilde{\mathcal{W}}_{\mathbf{k}}^{\alpha,\beta\gamma} + \left(\tilde{\mathcal{W}}_{\mathbf{k}}^{\beta,\alpha\gamma} \right)^*, \tag{6.20}$$

where

$$\begin{aligned} \tilde{X}_{\mathbf{k}}^{\mathcal{E}_\alpha k_\gamma \mathcal{E}_\beta} &= \sum_{m\in\mathcal{V}} f_{m\mathbf{k}} \langle \tilde{u}_{m\mathbf{k}}^{\mathcal{E}_\alpha} | \hat{H}_{\mathbf{k}}^{k_\gamma} | \tilde{u}_{m\mathbf{k}}^{\mathcal{E}_\beta} \rangle, \\ \tilde{W}_{\mathbf{k}}^{\alpha,\beta\gamma} &= i \sum_{m\in\mathcal{V}} f_{m\mathbf{k}} \langle \tilde{u}_{m\mathbf{k}}^{\mathcal{E}_\alpha} | u_{m\mathbf{k},\gamma}^{A_\beta} \rangle. \end{aligned} \tag{6.21}$$

For finite samples like molecules, it is useful to recall the following relationships:

$$\hat{H}_{\mathbf{k}}^{\mathcal{E}_\alpha} \to \hat{r}_\alpha, \qquad \partial_\gamma \hat{H}_{\mathbf{k}}^{(0)} \to \hat{v}_\gamma = i[\hat{H}, \hat{r}_\gamma], \qquad \partial_\gamma \hat{P}_{\mathbf{k}} \to i[\hat{P}, \hat{r}_\gamma], \tag{6.22}$$

where $\hat{v}_\beta$ and $\hat{r}_\beta$ represent, respectively, the β Cartesian component of the velocity and position operators. (When working with molecules, and in view of simplifying notation, we will use $|u_{m\mathbf{k}}^{(0)}\rangle \to |\psi_m\rangle$, $\hat{H}_{\mathbf{k}}^{(0)} \to \hat{H}$ and $\epsilon_{m\mathbf{k}}^{(0)} \to \epsilon_m$, where the wave vector label is dropped. We shall also omit the "(0)" superscript, since this should not lead to any confusion.) We will omit some tedious but otherwise straightforward intermediate steps and provide the final expressions for $\tilde{\mathcal{X}}$ and $\tilde{\mathcal{W}}$ appearing in Eq. (6.20) [for a detailed derivation, see Appendix F]. The $\tilde{\mathcal{X}}$ term reads as

$$\begin{aligned} \tilde{\mathcal{X}}^{\mathcal{E}_\alpha k_\gamma \mathcal{E}_\beta} = i \sum_{m\in\mathcal{V}} \sum_{l\in\mathcal{C}} f_m \Bigg[& \frac{\langle \psi_m | \hat{r}_\alpha \hat{Q} \hat{r}_\gamma | \psi_l \rangle \langle \psi_l | \hat{r}_\beta | \psi_m \rangle}{\epsilon_l - \epsilon_m} \\ & - \frac{\langle \psi_m | \hat{r}_\alpha | \psi_l \rangle \langle \psi_l | \hat{r}_\gamma \hat{Q} \hat{r}_\beta | \psi_m \rangle}{\epsilon_l - \epsilon_m} \Bigg], \end{aligned} \tag{6.23}$$

where m runs over the valence ($\mathcal{V}$) manifold only and l runs over the empty states that belong to the conduction ($\mathcal{C}$) manifold. Of course,

$$\sum_{m\in\mathcal{V}} |\psi_m\rangle \langle\psi_m| + \sum_{l\in\mathcal{C}} |\psi_l\rangle \langle\psi_l| = \mathbb{1}. \tag{6.24}$$

Regarding $\tilde{\mathcal{W}}$, it can be expressed as follows,

$$\begin{aligned} \tilde{\mathcal{W}}^{\alpha,\beta\gamma} =& \frac{i}{2} \sum_{m\in\mathcal{V}} \sum_{l\in\mathcal{C}} f_m \frac{\langle \psi_m | \hat{r}_\alpha | \psi_l \rangle}{\epsilon_l - \epsilon_m} \langle \psi_l | \left(\hat{r}_\beta \hat{r}_\gamma - 2 \hat{r}_\gamma \hat{P} \hat{r}_\beta \right) | \psi_m \rangle \\ &+ \frac{1}{2} \sum_{m\in\mathcal{V}} \sum_{l\in\mathcal{C}} f_m \frac{\langle \psi_m | \hat{r}_\alpha | \psi_l \rangle}{(\epsilon_l - \epsilon_m)^2} \langle \psi_l | \left(\hat{r}_\beta \hat{v}_\gamma - \hat{r}_\gamma \hat{v}_\beta \right) | \psi_m \rangle. \end{aligned} \tag{6.25}$$

In the end, summing all contributions, we arrive at the following expression for the NOA tensor (excluding SCF terms) in finite samples,

$$\tilde{\eta}_{\alpha\beta\gamma} = -\frac{4\pi}{\Omega}\,\mathrm{Im}\sum_{m\in\mathcal{V}}\sum_{l\in C} f_m\,\tilde{\eta}^{ml}_{\alpha\beta\gamma}, \tag{6.26}$$

where we have defined

$$\begin{aligned}\tilde{\eta}^{ml}_{\alpha\beta\gamma} =& \frac{1}{(\epsilon_l-\epsilon_m)^2}\Big[\langle\psi_m|\,\hat{r}_\alpha\,|\psi_l\rangle\,\langle\psi_l|\,(\hat{r}_\beta\hat{v}_\gamma-\hat{r}_\gamma\hat{v}_\beta)\,|\psi_m\rangle \\ &\qquad -\langle\psi_m|\,\hat{r}_\beta\,|\psi_l\rangle\,\langle\psi_l|\,(\hat{r}_\alpha\hat{v}_\gamma-\hat{r}_\gamma\hat{v}_\alpha)\,|\psi_m\rangle\Big] \\ &+\frac{i}{\epsilon_l-\epsilon_m}\Big[\langle\psi_m|\,\hat{r}_\beta\,|\psi_l\rangle\,\langle\psi_l|\,\hat{r}_\alpha\hat{r}_\gamma\,|\psi_m\rangle-\langle\psi_m|\,\hat{r}_\alpha\,|\psi_l\rangle\,\langle\psi_l|\,\hat{r}_\beta\hat{r}_\gamma\,|\psi_m\rangle\Big].\end{aligned} \tag{6.27}$$

This is the same expression that can be obtained, e.g., from Ref. [51], where the first two lines in Eq. (6.27) contain contributions from the electric and magnetic dipoles and the third line accounts for the electric dipoles and quadrupoles.

Regarding optical rotation, the quantity of relevance in molecular systems is the optical rotatory parameter, β, which is related to the rotatory power, usually denoted by the symbol $\alpha(\omega)$, via [151–153]

$$\alpha(\omega) = \frac{N_A\omega^2}{Mc^2}\beta, \qquad \beta = \frac{\Omega}{4\pi}\frac{1}{2}\sum_\alpha\frac{1}{3}g_{\alpha\alpha}. \tag{6.28}$$

Here, N_A is the Avogadro number, M is the molar mass of the molecule and Ω is the volume of the simulation cell. Recalling the relationship between $g_{\alpha\beta}$ and $\eta_{\alpha\beta\gamma}$ [see Eq. (6.2)], and using x, y, z to indicate Cartesian directions, we obtain

$$\begin{aligned}\beta = -\frac{1}{3}\,\mathrm{Im}\sum_{m\in\mathcal{V}}\sum_{l\in C} f_m\frac{1}{(\epsilon_l-\epsilon_m)^2}\Big[&\langle\psi_m|\,\hat{r}_x\,|\psi_l\rangle\,\langle\psi_l|\,\big(\hat{r}_y\hat{v}_z-\hat{r}_z\hat{v}_y\big)\,|\psi_m\rangle \\ &+\langle\psi_m|\,\hat{r}_y\,|\psi_l\rangle\,\langle\psi_l|\,\big(\hat{r}_z\hat{v}_x-\hat{r}_x\hat{v}_z\big)\,|\psi_m\rangle \\ &+\langle\psi_m|\,\hat{r}_z\,|\psi_l\rangle\,\langle\psi_l|\,\big(\hat{r}_x\hat{v}_y-\hat{r}_y\hat{v}_x\big)\,|\psi_m\rangle\Big],\end{aligned} \tag{6.29}$$

again, matching the analytical expressions that can be found in the literature.

6.2.2 ELECTROMAGNETIC GAUGE FREEDOM

We have seen in the last section that for finite system like molecules our formalism recovers the magnetic dipole and electric dipole and quadrupole contributions to the NOA, which were identified long ago. At this point, a natural question to ask is whether it is possible to decompose the total gyration coefficients into separate contributions with well-defined physical significance in extended systems like solids. Two inequivalent definitions of $E^{\mathcal{E}^*_\alpha\mathcal{E}_\beta}_{\mathbf{k},\gamma}$ can, at most, differ by a vanishing Brillouin Zone integral; so the question boils down to asking whether we can combine the individual pieces in Eq. (6.10) in such a way that the result is the total $\mathbf{k}$-derivative of some function $f(\mathbf{k})$. An obvious choice for $f(\mathbf{k})$ consists in identifying it with the $\mathbf{k}$-derivative of the macroscopic dielectric tensor. Indeed, by applying the $2n+1$ theorem to the stationary expression [75–77] for $E_{\mathbf{k},\mathbf{q}=\mathbf{0}}^{\mathcal{E}_\alpha^* \mathcal{E}_\beta}$, we find

$$\begin{aligned} \frac{\partial E_{\mathbf{k},\mathbf{q}}^{\mathcal{E}_\alpha^* \mathcal{E}_\beta}}{\partial k_\gamma}\bigg|_{\mathbf{q}=\mathbf{0}} =& \mathcal{X}_{\mathbf{k}}^{\mathcal{E}_\alpha \mathcal{E}_\beta k_\gamma} + \mathcal{X}_{\mathbf{k}}^{k_\gamma \mathcal{E}_\alpha \mathcal{E}_\beta} + \mathcal{X}_{\mathbf{k}}^{\mathcal{E}_\alpha k_\gamma \mathcal{E}_\beta} \\ &+ \mathcal{Y}_{\mathbf{k}}^{\mathcal{E}_\alpha \mathcal{E}_\beta k_\gamma} + \mathcal{Y}_{\mathbf{k}}^{\mathcal{E}_\alpha k_\gamma \mathcal{E}_\beta} + \mathcal{Y}_{\mathbf{k}}^{k_\gamma \mathcal{E}_\alpha \mathcal{E}_\beta} \\ &+ 2\mathcal{S}_{\mathbf{k}}^{\alpha,\beta\gamma} + 2\left(\mathcal{S}_{\mathbf{k}}^{\beta,\alpha\gamma}\right)^*. \end{aligned} \tag{6.30}$$

Then, by subtracting the latter expression from Eq. (6.10), we obtain another equally valid formula for the integrand in $\mathbf{k}$ space for the NOA,

$$\left[E_{\mathbf{k},\gamma}^{\mathcal{E}_\alpha \mathcal{E}_\beta}\right]' = -\left(\mathcal{X}_{\mathbf{k}}^{\mathcal{E}_\alpha \mathcal{E}_\beta k_\gamma} + \mathcal{X}_{\mathbf{k}}^{k_\gamma \mathcal{E}_\alpha \mathcal{E}_\beta} + \mathcal{Y}_{\mathbf{k}}^{\mathcal{E}_\alpha k_\gamma \mathcal{E}_\beta}\right) - \mathcal{W}_{\mathbf{k}}^{\alpha,\gamma\beta} - \left(\mathcal{W}_{\mathbf{k}}^{\beta,\gamma\alpha}\right)^*. \tag{6.31}$$

Numerical tests confirm the consistency of Eq. (6.10) and (6.31) to a very high degree of accuracy. This arbitrariness can be regarded a direct consequence of the *electromagnetic* (EM) gauge freedom. Indeed, the $\mathcal{W}$ terms in both Eq. (6.10) and Eq. (6.31) have the physical meaning of Berry curvatures in the parameter space spanned by a uniform magnetic field (**B**) and an electric field. Such curvatures are insensitive to the choice of the coordinate origin and the wave function gauge. This result is achieved by expressing the **B**-field response function in a cell-periodic form, consistent with the density-operator theory of Essin *et al.* [102]. Notwithstanding these undeniable advantages, the aforementioned Berry curvatures retain an inherent dependence on the EM-gauge [154]. More specifically, the symbol $\mathcal{W}^{\alpha,\beta\gamma}$ is expressed in a Landau gauge where the β component of the **A**-field increases linearly along γ; so when going from Eq. (6.10) to Eq. (6.31) we have essentially switched between two Landau gauges in the $\mathcal{W}$ terms, and collected the leftovers in the form of $\mathcal{X}$ and $\mathcal{Y}$. It is, of course, possible to define other variants of Eq. (6.10), where either the contributions from the symmetric ($\mathcal{S}$) or antisymmetric ($\mathcal{A}$) terms of $\mathcal{W}$ cancel out, at the expense of having a slightly longer list of $\mathcal{X}$- and $\mathcal{Y}$-symbols. Ideally, one would like to exploit this freedom to obtain an intuitive separation between well-defined (and possibly individually measurable) physical observables; whether such a choice exists is an interesting open question.

6.3 RESULTS

We will now validate our computational approach both with finite and extended systems, i.e., molecules and solids. Our numerical results are obtained using the DFT and DFPT implementations of the ABINIT package with the Perdew-Wang [81] parametrization of the local density approximation (LDA). We use norm-conserving pseudopotentials from the Pseudo Dojo [120] website and we regenerate them without exchange-correlation nonlinear core corrections using the ONCVPSP [88] software. Spin-orbit coupling (SOC) is neglected in all of our first-principles calculations.

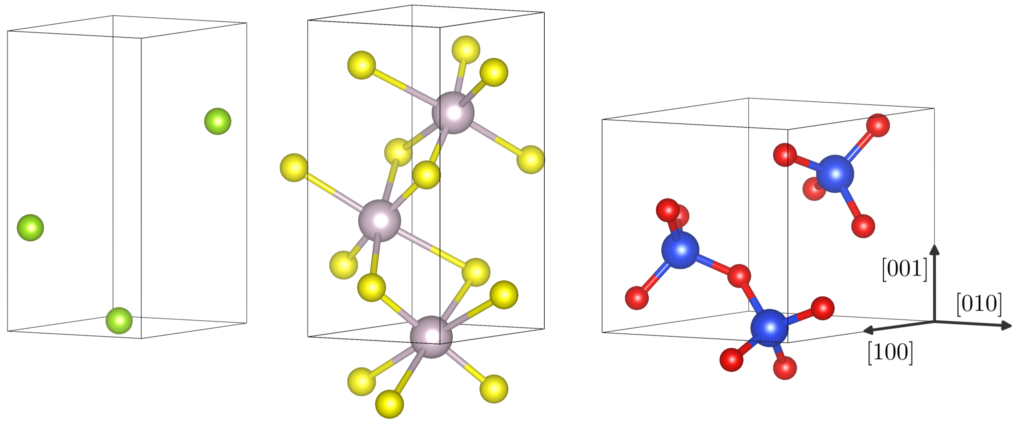

Figure 6.1: Cartoon illustrating the crystal structure of a) trigonal Se, b) α-HgS and c) α-SiO$_2$. Grey arrows indicate the crystallographic directions that form the Cartesian axes.

	g_{11}	g_{33}	$\bar{\rho}$
Se	-1.307 (-1.547)	-1.913 (-0.458)	-74.5 (-17.8)
α-HgS	0.775 (0.554)	-1.861 (-1.274)	-72.5 (-49.6)
α-SiO$_2$	-0.071 (-0.001)	0.125 (0.019)	4.9 (0.7)

Table 6.1: Calculated independent components of the gyration tensor (in bohr) and the optical rotatory power $\bar{\rho}$ defined in Eq. 6.6 (in deg/[mm (eV)^2] units). Values in brackets are computed neglecting the SCF terms.

6.3.1 CHIRAL SOLIDS: TRIGONAL Se, α-HgS AND α-SiO$_2$

All the crystals studied in this work, trigonal Se and α-HgS and α-SiO$_2$, belong to the point group 32, but they may crystallize in two enantiomorphic structures with space groups $P3_121$ and $P3_221$. These structures with opposite handedness have the same rotatory power in magnitude, but with opposite sign. We shall consider the $P3_121$ space group structure for the three crystals under study. The crystal structure is either set to the experimental one (Ref. [155] for Se), or relaxed to mechanical equilibrium until the forces are smaller than 10^{-6} Ha/bohr (Table 6.3 shows the structural parameters used in our calculations). A schematic representation of these crystals is shown in Fig. 6.1, where the chiral axis is oriented along the c crystallographic direction in all cases.

Converged values for the NOA tensor are obtained by sampling the BZ with 24^3, 16^3 and 8^3 $\mathbf{k}$ points and with a plane-wave energy cutoff of 50 Ha, 40 Ha and 50 Ha, for trigonal Se, α-HgS and α-SiO$_2$, respectively. Table 6.1 shows the obtained numerical values for the independent components of the gyration tensor and the optical rotatory power in our test set of trigonal crystals, where values in brackets are computed by neglecting SCF terms. Our results are in fairly good agreement with literature values, even if some studies have applied an *ad-hoc* correction [55] to the LDA band gap via a scissor operator. The latter consists in applying a rigid shift, Δ, to the conduction band energies that are used as an input to the sum-over-states formula for the optical conductivity, and is aimed at correcting the systematic underestimation of the fundamental optical gap that one obtains with the local density approximation (LDA).

Let us first analyze the case of α-HgS. Ref. [16] reports a value of $\bar{\rho} \sim -83$ deg/[mm (eV)^2] for the optical rotatory power, measured at a single wave length of $\lambda = 6328$ Å ($\omega \sim 1.96$ eV). The agreement with our computed result is very good, especially considering that the value detailed in Ref. [16] was not extrapolated to the $\omega \to 0$ limit.

For trigonal Se and α-SiO$_2$ we shall take as reference Ref. [55], where the optical rotatory power is computed, either including or neglecting the contributions of SCF local fields, in the $\omega \to 0$ limit, with ($\Delta \neq 0$) and without ($\Delta = 0$) corrections coming from a scissor operator. For trigonal Se, without correction ($\Delta = 0$) Ref. [55] reports a value of $\bar{\rho} = -131$ deg/[mm (eV)^2]. With $\Delta = 1.1$ eV their result of $\bar{\rho} = -55$ deg/[mm (eV)^2] drastically improves, and almost perfectly matches the experimental[2] value [55] of $\bar{\rho} = \pm 56 \pm 30$ deg/[mm (eV)^2]. However, as the authors of Ref. [55] state, due to the sensitivity of the optical rotatory power with respect to Δ, this level of accuracy might be accidental. Our result falls within the error bars of the experiment, and significantly improves the $\Delta = 0$ result of Ref. [55].

For α-SiO$_2$, the uncorrected $\Delta = 0$ value quoted by Ref. [55] is $\bar{\rho} = 6.8$ deg/[mm (eV)^2]; whereas when a correction of Δ = 1.8 eV is added to the conduction energies, they obtain $\bar{\rho}$= 5.6 deg/[mm (eV)^2]. The robustness of the results with respect to Δ makes α-SiO$_2$ the ideal candidate to validate our theoretical results. Our converged value for the optical rotatory power, $\bar{\rho}$ = 4.9 deg/[mm (eV)^2], is in excellent agreement with Ref. [55], as well as with experimental data, $\bar{\rho} = \pm 4.6 \pm 0.1$ deg/[mm (eV)^2]. A very recent first-principles study [156] of the rotatory power in α-SiO$_2$ reports a value of $\bar{\rho}$ = -5.9 deg/[mm (eV)^2] for $\lambda = 589.44$ nm ($\hbar\omega \sim 4.42$ eV); this is again in good agreement with our results in spite of the differences in our respective computational approaches. (A structure with opposite handedness compared to the one studied in this work is used in Ref. [156], which explains the sign discrepancy.) As a further validation, we can compare the other independent component of the gyration tensor with the literature. Ref. [55] obtains $g_{11} = -4.8$ pm, and the experimental value is known [55] to lie between -3 pm and -4 pm. In those units, our calculated value is $g_{11} = -3.8$ pm, which is again in excellent agreement with the available literature reports. Regarding the effects of self-consistency, without SCF terms we obtain $\bar{\rho} = 0.7$ deg/[mm (eV)^2], indicating a correction by a factor of $+7$ to the optical rotatory power, which matches the conclusions of Ref. [55]. We summarize some of these results in Table 6.2.

Overall, our results confirm the crucial importance of local-field SCF contributions, consistent with the conclusions of Ref. [55]. Given the large impact of SCF fields, we decided to repeat our calculations with the Perdew-Burke-Ernzerhof (PBE) [82] parametrization of the generalized gradient approximation (GGA). This topic is further addressed in the subsequent section.

---

[2] The sign uncertainty of the optical rotatory power obtained from experiments appears to be a common issue. Consequently, for a meaningful comparison with our theoretical results, we should focus exclusively on the absolute values of the reported experimental measurements.

$\bar{\rho}$	This work	Ref. [55]		Experiment
Se	-74.5	-131 ($\Delta = 0$)	-55 ($\Delta = 1.1$ eV)	$\pm 56 \pm 30$ [a]
α-HgS	-72.5	$\cdots$	$\cdots$	-83 [b]
α-SiO_2	4.9	6.8 ($\Delta = 0$)	5.6 ($\Delta = 1.8$ eV)	$\pm 4.6 \pm 0.1$ [a]

Table 6.2: Optical rotatory power for trigonal Se, α-HgS and α-SiO_2, in deg/[mm $(\text{eV})^2$] units. Reference values from other works are taken from:
[a] Taken from Ref. [55].
[b] Ref. [16], with $\hbar\omega \sim 1.959$ eV.

Structure	Functional	a (bohr)	c (bohr)	Ω (bohr^3)	band gap (eV)
Se (exp)	LDA	8.201	9.354	544.894	0.850
Se (exp)	PBE	8.201	9.354	544.894	0.948
Se (exp)	PBEsol	8.201	9.354	544.894	0.895
Se (LDA)	LDA	7.431	9.695	463.605	0.225
Se (PBE)	PBE	8.463	9.564	593.187	0.961
Se (PBEsol)	PBEsol	7.600	9.698	485.172	0.399
α-HgS (LDA)	LDA	7.629	17.530	883.498	0.995
α-HgS (PBE)	PBE	8.434	18.430	1135.414	1.829
α-SiO_2 (LDA)	LDA	9.174	10.110	736.974	5.987
α-SiO_2 (PBE)	PBE	9.489	10.411	811.792	5.768

Table 6.3: Structural parameters and electronic band gap of Se, α-HgS and α-SiO_2, with LDA and PBE. In the "Structure" column, "exp" refers to the experimental structure, while "Se (LDA)" means that the structure was relaxed with LDA, for example. The "Functional" column specifies the exchange and correlation functional employed in the calculation of the electronic band structure.

6.3.2 EFFECT OF THE EXCHANGE-CORRELATION FUNCTIONAL: LDA vs PBE

The aim of this section is to examine how the exchange and correlation functional affects the structural characteristics and electronic band structure (in particular, the band gap) of the solids being analyzed, and how this translates to the natural optical activity tensor.

To start with, we show in Table 6.3 the obtained structural parameters and the electronic band gap for different combinations of the geometrical structure of the system (either relaxed or experimental setup) and the XC functional employed for the calculation of the electronic band structure. For α-SiO_2, we obtain structural data that are reasonably consistent between LDA and PBE. On the contrary, trigonal Se and α-SiO_2 seem to be really challenging to reproduce within the standard approximations of DFT. We shall focus our discussion on the specific case of trigonal Se in the following, since the disagreement seems to be especially dramatic in this particular case, although most of the considerations apply to some extent to α-HgS as well.

None of the exchange and correlation functionals[3] that we tested appears to provide an accurate description of the equilibrium volume of trigonal Se, with somewhat larger deviations than the expected trends: both LDA and PBEsol yield a strong underestimation (-15 % and -11 %, respectively), whereas PBE significantly overestimates it ($+9$ %). The volume, however, is not always correlated to the quality of the calculation: both LDA and PBE are characterized by systematic volume errors that are more or less common to all crystals and, in spite of that, their physical predictions are in many cases correct. Internal degrees of freedom tend to be more reliable indicators of the overall accuracy; in our case, an obvious structural parameter to look at is the relaxed aspect ratio of the cell. In this regard, the PBE structure ($c/a = 1.13$) is by far the most accurate, closely matching the experimental value of $c/a = 1.14$. This result correlates well with the excellent agreement between the Kohn-Sham gap and the gyration coefficients that we obtain using either crystal structure (see Table 6.4). At the other extreme, both LDA ($c/a = 1.30$) and PBEsol ($c/a = 1.27$) strongly overestimate this structural parameter. Such failure appears to be the primary culprit for the near-closure of the Kohn-Sham gap (and the consequent difficulties at calculating meaningful optical properties) that we observe in both cases. Since the PBEsol structure is very similar to the LDA one, we won't discuss it further, and focus on the comparison between LDA and PBE henceforth.

When the structure of trigonal Se is relaxed with LDA, the band gap drastically decreases and, in fact, it becomes so small (around 0.2 eV) that even standard DFPT calculations, e.g., the dielectric permittivity, fail to converge. In general, we observe that the larger the band gap, the faster the convergence is, which might explain the slightly faster convergence of the natural optical activity with PBE, in contrast to LDA. As an illustrative example, we show in Fig. 6.2 the convergence of the independent components of the NOA tensor of α-SiO$_2$; we observe similar convergence rates for α-HgS and trigonal Se. The corresponding converged numerical values for the natural optical activity of the studied chiral crystals, obtained either with LDA or PBE, are shown in Table 6.4. Interestingly, for a given crystal structure the choice between the LDA and PBE seems to have a relatively small influence on the calculated coefficients, except for the g_{33} component of trigonal Se, where such deviation reaches $\sim 50\%$. Conversely, the structural parameters do appear to have a significant impact on the final result.

6.3.3 THE $C_4H_4O_2$ MOLECULE

In order to validate our methodology with finite systems, we now turn our attention to the $C_4H_4O_2$ molecule. Our calculations are performed with a plane-wave energy

---

[3] Since neither LDA or PBE were able to accurately reproduce the structural characteristics of triginal Se, we decided to try with the PBEsol parametrization [157] of the GGA as well, which is specifically designed to improve the description of equilibrium bulk properties of densely packed solids; it differs from the *standard* PBE parametrization of the GGA [82] only in a few parameters.

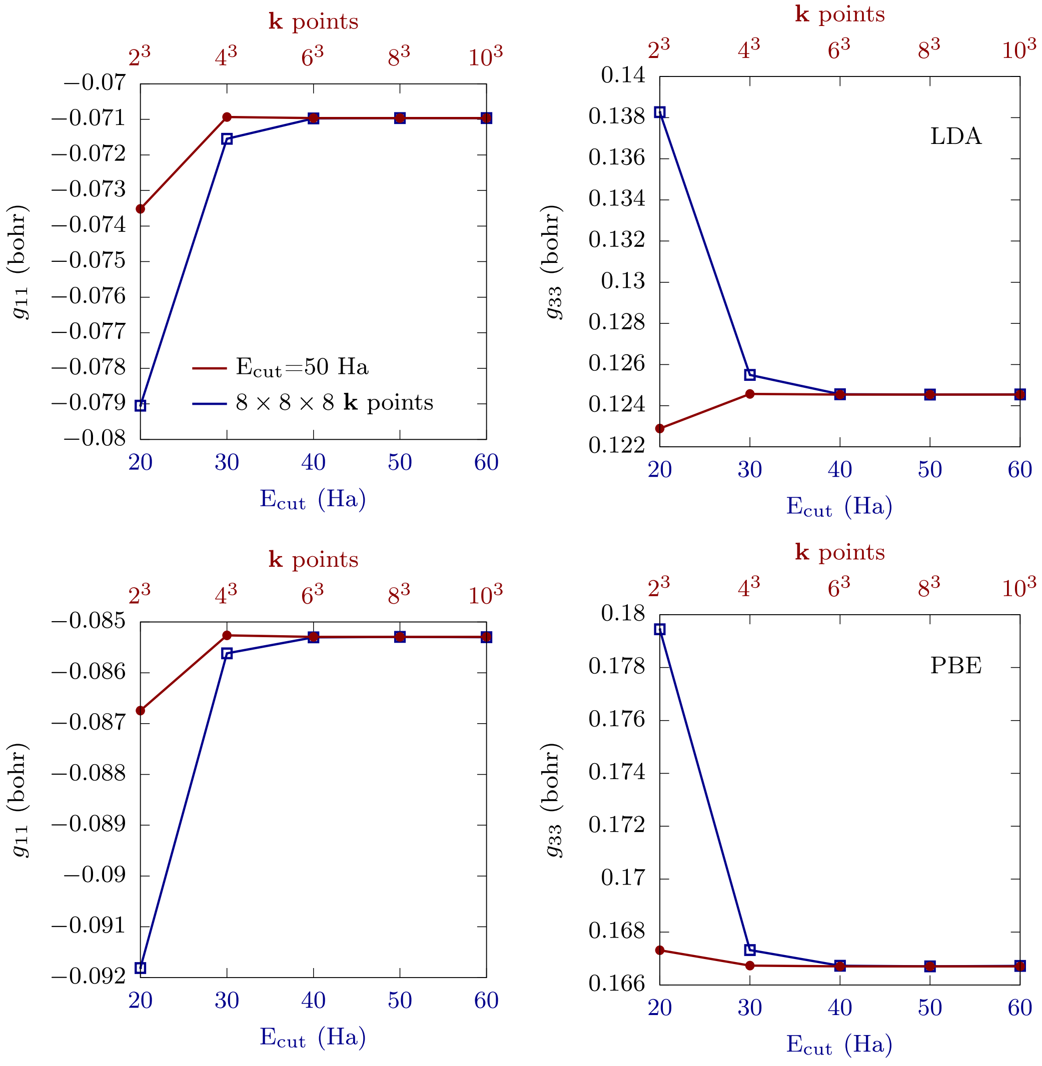

Figure 6.2: Convergence of the independent components of the gyration tensor, g_{11} and g_{33}, of α-SiO$_2$ with respect to the plane-wave cutoff and the density of the **k**-point mesh. The top panel shows the obtained results with LDA, whereas the bottom panel shows the results obtained with the PBE parametrization of the GGA. Solids lines are a guide to the eye.

cutoff of 50 Ha and a box with sides of $a = 35$ bohr ($\Omega = a^3$) is used in order to simulate an isolated molecule. We show in Table 6.5 the Cartesian coordinates used in our simulations.

Table 6.6 shows our computed gyration tensor (multiplied by the volume of the simulation cell), with and without SCF terms; as in periodic crystals, the latter have a huge impact on some components. We also report the optical rotatory parameter, β, as previously defined in Eq. (6.28). Our computed value of β almost exactly matches the value of $\beta = -2.29$ that is reported in Ref. [159]. Although such a level of agreement gives us confidence in the correctness of our implementation, we suspect that it may be to some extent coincidental, given the differences in our respective approximations and computational schemes.

	g_{11} (bohr)		g_{33} (bohr)	
Structure	LDA	PBE	LDA	PBE
Se (exp)	−1.307	−1.301	−1.913	−1.329
Se (PBE)	−1.408	−1.431	−1.802	−1.216
α-HgS (LDA)	0.775	0.663	−1.861	−1.645
α-HgS (PBE)	−0.716	−0.692	−0.065	−0.065
α-SiO_2 (LDA)	−0.071	−0.071	0.125	0.125
α-SiO_2 (PBE)	−0.085	−0.085	0.168	0.167

Table 6.4: Comparison between LDA and GGA for the independent components of the gyration tensor for Se, α-HgS and α-SiO_2, for different structures. In the "Structure" column, "exp" refers to the experimental structure, while Se (LDA) means that the structure was relaxed with LDA, for example.

Atom	x	y	z	Atom	x	y	z
O_1	0.6434	1.2364	−2.0775	C_4	−0.1201	−2.5557	0.1166
O_2	−0.6434	−1.2364	−2.0775	H_1	0.1171	4.5743	−0.2216
C_1	−0.1201	1.3735	2.3318	H_2	−0.4960	2.4271	4.0404
C_2	0.1201	2.5557	0.1166	H_3	−0.1171	−4.5743	−0.2216
C_3	0.1201	−1.3735	2.3318	H_4	0.4960	−2.4271	4.0404

Table 6.5: Geometry of $C_4H_4O_2$ used in our calculations. The non-relaxed Cartesian coordinates shown in this table (in bohr) are taken from Ref. [158].

	Ωg_{11}	Ωg_{22}	Ωg_{33}	$\frac{\Omega}{2}(g_{12}+g_{21})$	β
With SCF	−69.69	−68.12	−33.98	−267.32	−2.28
Without SCF	−72.52	−56.18	144.90	−629.35	0.21

Table 6.6: Calculated independent components of the gyration tensor times the volume of the simulation cell (Ω) for $C_4H_4O_2$. Values are given in Hartree atomic units.

6.4 SUMMARY AND OUTLOOK

In this chapter we have presented an efficient and accurate first-principles methodology for the calculation of natural optical activity within the framework of density-functional perturbation theory. Our methodology brings the first-principles calculation of the NOA tensor to the same level of accuracy and computational ease as standard linear-response properties, e.g., the dielectric tensor. Our approach solves the major issues that previous first-principles theories had completely neglected or had only partially addressed. An overview of the accomplishments of this chapter is given below.

- Our long-wave DFPT approach for the computation of the NOA avoids sums over excited states, takes the derivative in momentum **q** analytically and, last but not least, accounts for SCF terms.
- We have shown, both with trigonal crsytals (Se, α-Hgs and α-SiO$_2$) and with the C$_4$H$_4$O$_2$ molecule, that the aforementioned SCF contributions are essential for a correct description of the NOA. Our numerical results are in general in excellent agreement with experiments and with previous (computationally more demanding) first-principles calculations.
- We have also discussed some formal aspects of the theory, e.g., the non-uniqueness of the analytical expression of the gyration coefficients, which we relate to the gauge freedom of electromagnetism. Whether it is possible to decompose the gyration coefficients into physically meaningful quantities in extended systems like solids remains an open question.

As an outlook, we consider that one of the most pressing priorities is to include spin-orbit coupling (SOC) effects into our formalism, which would help us better quantify the magnitude of the effect in crystals containing heavier elements, e.g., trigonal Se and α-HgS. In addition, a natural step forward consists in generalizing our method to finite frequencies and to magnetic materials with broken time-reversal symmetry. Finally, it would be especially interesting to combine the present theory with the formalism developed in Chapter 3 in order to capture optical dispersion effects in metals [160, 161]. While this would likely entail additional methodological challenges (e.g., in order to describe the Fermi-surface contributions in the dynamical regime), doing so appears well within reach. Given the growing interest in this class of phenomena, we regard this as an exciting avenue for further exploration.

7

CONCLUSIONS

In this thesis we have focused on advancing the theoretical understanding of several material properties related to spatial dispersion. We have committed our efforts towards diverse areas, including natural optical activity, molecular g factors, Lorentz forces and flexoelectricity in polar metals. Our work required significant amount of methodological and code development, where we used DFPT —and, in particular, long-wave DFPT— as general framework.

A crucial characteristic of our work is that we have developed, tested and implemented new methods that enable the study of selected spatial dispersion properties with greater accuracy and efficiency than was previously possible. These new methodologies have been developed in response to a lack of adequate computational tools at the time this thesis was initiated. We have already capitalized on this opportunity by solving pressing and fundamental physical problems, e.g., the bulk polarization switching of "ferroelectric" metals via external fields. We now proceed to outline the main results achieved in this thesis.

- Spatial dispersion in metals

  We have established a first-principles theory of spatial dispersion in metals by generalizing the long-wavelength DFPT technique of Ref. [41] to conductors. Our methodology enjoys all the benefits derived from the application of the $2n + 1$ theorem to DFPT, just like in the insulating case. Most importantly, SCF contributions are inherently accounted for and first-order spatial dispersion coefficients are accessed without the need of explicitly calculating the response to nonuniform field perturbations. We have validated the accuracy and computational efficiency of this methodology with phonons (Chapter 3) and strain gradients (Chapter 4).

- Switching a polar metal via strain gradients

  We have demonstrated that strain gradients can be used to switch the bulk polar order parameter of the so-called "ferroelectric" or polar metals, thereby solving a long-standing issue that this class of materials have been facing. Our claims are supported by our results on $LiOsO_3$, the first and arguably the best known polar metal since its experimental observation in 2013. We have calculated the critical bending radius to switch its polar order parameter, and find it to be similar in magnitude to that of $BaTiO_3$. Therefore, our theoretical predictions should be experimentally feasible. From a historical perspective, experimental efforts in flexoelectricity have long been oriented at showing that *whatever an electric field can do, a strain gradient can accomplish equally well*. In this context, our work can be regarded as a paradigm shift, by showing that *strain gradients can achieve even what electric fields cannot*.

- ROTATIONAL g FACTORS AND GENERALIZED LORENTZ FORCES

  We have established a formalism to compute the rotational g factors in molecules and generalized Lorentz forces in crystals, which only requires the knowledge of two linear-response quantities: the macroscopic polarization induced by an atomic displacement (i.e., Born effective charge tensor) and its first-order spatial dispersion, $\mathbf{J}^{(1)}$. Physically, the presence of the latter contribution means that the electronic orbital current accompanying the adiabatic evolution of atoms along closed trajectories are spread out in space; i.e., they do not behave like point charges. For rotational g factors of molecules, we find that our method yields results that are in excellent agreement with reference literature values, although at a much lower computational cost. Regarding solids, we have taken cubic $SrTiO_3$ as a test case and we have computed the generalized Lorentz force on the ions produced by an applied magnetic field and the phonon g factor of the low-frequency TO phonon modes. One of our primary achievements has been to prove that the *dispersive* contributions coming from $\mathbf{J}^{(1)}$, which had been systematically neglected in previous studies, can dominate the response.

- NATURAL OPTICAL ACTIVITY

  We have developed a first-principles method, based on the long-wavelength DFPT technique, to compute the natural optical activity, which works equally well both in molecules and solids. Our methodology avoids cumbersome sums over empty states, takes care of the $\mathbf{q}$ derivative analytically and, last but not least, includes SCF contributions into the formalism in a natural manner. We have demonstrated that our method displays remarkably fast convergence with respect to the energy cutoff and $\mathbf{k}$ mesh with selected chiral crystals as test examples. We find that self-consistent fields, which had been seldom accounted for by previous approaches, have huge impact on the final result; this is true both in molecules and solids. We also reach the conclusion that the analytical expression for the gyration coefficients is not unique, which we ascribe to the electromagnetic gauge freedom. This point has also been validated by numerical first-principles calculations.

We emphasize that we have incorporated our new implementations to the ABINIT package [42, 43], which is distributed under the General Public License (GNU). This means that all of our contributions are freely available to the public and that the users are allowed to share and modify the software. One of our main contributions is the long-wavelength DFPT implementation for the natural optical activity (Chapter 6). In addition, we have expanded the linear-response capabilities of the ABINIT package in order to account for contributions of orbital magnetization to spatial dispersion. In particular, we have implemented the wave function response to an electromagnetic vector potential in the long-wavelength limit, corresponding to a uniform orbital magnetic field (Appendix D). The latter is an essential ingredient both for the calculation of the natural optical activity and the rotational g factors and generalized Lorentz forces studied in Chapter 5. Although it has not been directly relevant for the scopes of this thesis, it is worth noting that the wave function response to an orbital magnetic field is ubiquitous in the calculation of spatial dispersion properties, including the flexoelectric tensor [41]. Beforehand, the computation of the flexoelectric tensor was restricted to systems enjoying specific crystal symmetries where this contribution vanishes by symmetry.

Our work opens many avenues for future research. These have already been briefly discussed at the end of each chapter; for completeness, we summarize some of these ideas here. In the context of applications, it would be interesting to explore a wider range of polar metals in order to identify cases that exhibit the most pronounced strain gradient-induced polar distortions. Our generalization of the long-wave DFPT for conductors developed in Chapter 3 seems the ideal framework for this purpose. In this context, it is worth mentioning the very recent work [162] on the experimental observation of flexoelectric-induced polarization in the otherwise centrosymmetric $SrRuO_3$ metal. After our theoretical prediction of a strong flexocoupling effect in $LiOsO_3$, Ref. [162] represents, to the best of our knowledge, the first experimental validation of our claims. Regarding natural optical activity, note that our implementation as described in this thesis exclusively accounts for electronic mediated effects. It is well known [1] that lattice effects might be important in the infrared range of the spectrum; however, no first-principles theory of these effects is currently available. Finally, the giant phonon Hall effect in $SrTiO_3$ reported in experiments remains a mystery to the first-principles community, since all the microscopic explanations fail to predict this effect by orders of magnitude. While our results do not offer a conclusive answer on this issue, it is our hope that the computational tools developed in this thesis for the calculation of Lorentz forces in crystals stimulate research that allow for a more efficient screening of candidate materials where this effect is specially strong, and therefore, experimentally measurable.

On the methodological front, our newly implemented first-principles tools offer exciting opportunities for future developments. First, the long-wave DFPT for spatial dispersion in metals that we have presented in Chapter 3 can be expanded to access other adiabatic spatial dispersion properties. As an illustrative example, note that the "adiabatic Born effective charges" as introduced in Refs. [121, 122] can be obtained after minor modifications to our implementation. (We have already achieved preliminary promising results in this direction; however, we have decided not to include this material in this thesis.) A key characteristic of our method is that it works directly at the Γ point, meaning that cumbersome numerical fits are entirely avoided. In addition, the formalism for orbital magnetic susceptibility developed in Ref. [123] could be generalized to metals, by considering the adiabatic response to a static, though spatially nonuniform, electromagnetic vector potential field. Generalizing our ensemble DFPT formalism for metals presented in Chapter 3 to the dynamical ($\omega \neq 0$) regime seems particularly compelling, especially given the increasing interest in nonlinear optics and optical dispersion in conductors. Most of the calculations that have been reported so far rely on semiclassical or tight-binding models. In this context, our approach has the potential to address the current gap in first-principles methods. Regarding our implementation for the natural optical activity, and as previously discussed at the end of Chapter 6, some of the most urgent priorities include generalizing our methodology to finite frequencies and to magnetic materials with broken time-reversal symmetry; as well as the inclusion of spin-orbit coupling effects. In addition, generalizing our long-wave DFPT method presented in Chapter 6 in order to account for lattice-mediated contributions to the natural optical activity seems well within reach.

Even in their current form, we believe that the methods we have presented in this thesis can become the preferred choice within their respective areas of relevance. Paraphrasing Lev Landau, to a considerable degree we have adhered to a philosophy in which *a method is more important than a discovery, since the right method will lead to new and even more important discoveries*. Our hope is that our methodological work will find widespread use within the condensed matter community.

APPENDIX

A

TREATMENT OF THE MACROSCOPIC ELECTROSTATIC TERM IN THE $q = 0$ LIMIT

This appendix takes care of the macroscopic electrostatic term in the limit where $\mathbf{q}$ approaches zero, and is divided into three sections. First, we will justify why this contribution is problematic in insulators and we will explain the solution to address it. Next, in Sec. A.2 we will examine the long-wave limit of external potentials both in insulators and metals, with the intention of identifying the distinctions between the two. In Sec. A.3 we will take the first $\mathbf{q}$ derivative of the macroscopic electrostatic term within the framework of ensemble DFPT. This is relevant in the context of spatial dispersion in metals, particularly in relation to our Chapter 3.

A.1 SUPPRESSION OF THE MACROSCOPIC ELECTRIC FIELD TERM IN INSULATORS

The analytical long-wavelength approach of Sec. 2.4.4 serves as the methodological framework for the study of spatial dispersion properties. However, prior to taking the analytical derivative (around Γ) with respect to the wave vector of the response functions of interest, it is necessary to take care of the macroscopic electric fields that are generated by phonons in insulators. In order to identify the source of the issue, let us write [103] the induced electric field as

$$\frac{d\mathcal{E}_\alpha(\mathbf{r})}{d\lambda^{\mathbf{q}}_{\kappa\beta}} = \mathcal{E}^{\mathbf{q}}_{\alpha,\kappa\beta} e^{i\mathbf{q}\cdot\mathbf{r}}, \tag{A.1}$$

where $\mathcal{E}^{\mathbf{q}}_{\alpha,\kappa\beta}$ is the cell-periodic part of the response, whose macroscopic component is related to $\mathbf{G} = \mathbf{0}$ Fourier component in reciprocal space. Its expansion in powers of $\mathbf{q}$ is problematic for $\mathbf{q} \to \mathbf{0}$,

$$\mathcal{E}^{\mathbf{q}\to\mathbf{0}}_{\alpha,\kappa\beta}(\mathbf{G} = \mathbf{0}) \simeq -\frac{4\pi}{\Omega}\hat{q}_\alpha \frac{(\mathbf{q}\cdot\mathbf{Z}^*_\kappa)_\beta}{\hat{\mathbf{q}}\cdot\boldsymbol{\epsilon}\cdot\hat{\mathbf{q}}}, \tag{A.2}$$

where $\hat{\mathbf{q}} = \mathbf{q}/q$, $Z^*_{\alpha,\kappa\beta}$ is the Born effective charge tensor and $\boldsymbol{\epsilon}$ is the macroscopic dielectric tensor. The crucial point to be emphasized here is that Eq. (A.2) is a direction dependent constant in the neighborhood of Γ. This nonanalytic behaviour propagates to other response functions, thwarting their Taylor expansion in powers of $\mathbf{q}$ around $\mathbf{q} = \mathbf{0}$. A natural and widely used solution to overcome this problem is to suppress the problematic macroscopic electric fields, by adopting *short-circuit* electrical boundary conditions. Nevertheless, there is no unique method of suppressing the aforementioned macroscopic electric fields. In presence of strain gradients, this implies that certain response functions are only well-defined up to a constant. Consequences of the latter are more thoroughly examined Sec. B.2, with the particular case of bulk flexocoupling coefficients.

A.2 LONG-WAVE LIMIT OF EXTERNAL POTENTIALS

We shall now review the long-wavelength behavior of the external potentials, highlighting the differences between insulators and metals.

A.2.1 INSULATORS

The external potential at first-order in response to an atomic displacement perturbation is usually expressed as a sum of a local plus a separable part [41, 74]. For our scopes, the latter can be omitted, as no divergences associated to the separable part are present in the long-wave limit. The macroscopic component ($\mathbf{G} = \mathbf{0}$) of the local part is given by [74]

$$V_{\mathbf{q}}^{\mathrm{loc},\tau_{\kappa\alpha}}(\mathbf{G} = \mathbf{0}) \sim -i\frac{q_\alpha}{\Omega}\left(-\frac{4\pi Z_\kappa}{q^2} + \frac{F_\kappa''}{2}\right), \tag{A.3}$$

where F_κ'' is the second derivative in q of $F_\kappa(q) = q^2 v_\kappa^{\mathrm{loc}}(q)$, with $v_\kappa^{\mathrm{loc}}(q) \sim -4\pi Z_\kappa/q^2$, and Z_κ is the bare nuclear pseudo-charge. The Hartree potential, on the other hand, is given by

$$V_{\mathbf{q}}^{\mathrm{H},\tau_{\kappa\alpha}} = \frac{4\pi}{q^2} n_{\tau_{\kappa\alpha}}^{\mathbf{q}}, \tag{A.4}$$

where the lower terms in the Taylor expansion of the first-order electron density (in powers of $\mathbf{q}$) are given by[1]

$$n_{\tau_{\kappa\alpha}}^{\mathbf{q}} \sim -i\sum_\gamma q_\gamma n_{\tau_{\kappa\alpha}}^{(1,\gamma)} - \frac{1}{2}\sum_{\gamma,\delta} q_\gamma q_\delta n_{\tau_{\kappa\alpha}}^{(2,\gamma\delta)} + \ldots \tag{A.5}$$

The sum of the local and Hartree potentials then reads as (we omit terms that vanish in the $\mathbf{q} \to \mathbf{0}$ limit)

$$V_{\mathbf{q}}^{\mathrm{loc+H},\tau_{\kappa\alpha}} \simeq \frac{4\pi}{\Omega}\left(\sum_\gamma \frac{iq_\gamma Z_{\kappa\alpha}^{(\gamma)}}{q^2} + \sum_{\gamma,\delta}\frac{q_\gamma q_\delta}{2q^2} Q_{\kappa\alpha}^{(\gamma\delta)}\right), \tag{A.6}$$

where the tensors $Z_{\kappa\alpha}^{(\gamma)}$ and $Q_{\kappa\alpha}^{(\gamma\delta)}$ are, respectively, the *screened* (short-circuit electrical boundary conditions are assumed) "Born effective charges" and "dynamical quadrupoles",

$$\begin{aligned} Z_{\kappa\alpha}^{(\gamma)} &= Z_\kappa \delta_{\alpha\gamma} - \Omega n_{\tau_{\kappa\alpha}}^{(1,\gamma)}, \\ Q_{\kappa\alpha}^{(\gamma\delta)} &= -\Omega n_{\tau_{\kappa\alpha}}^{(2,\gamma\delta)}. \end{aligned} \tag{A.7}$$

As a consequence, as long as the "Born effective charges" do not vanish, in an insulator the potential given by Eq. (A.6) diverges as $\mathcal{O}(q^{-1})$, corresponding to the well-known Frölich term in the scattering potential.

---

[1] For notational convenience, we will use $n_\lambda^{\mathbf{q}}$ instead of $n_{\mathbf{q}}^\lambda$ in this appendix to indicate the first-order electron density at finite $\mathbf{q}$ to an external perturbation, λ.

A.2.2 METALS

In metals the potential should be an analytic function of the wave vector $\mathbf{q}$, which implies that the divergences that we have encountered in Eq. (A.6) should disappear. This involves

$$Z^{(\gamma)}_{\kappa\alpha} = 0, \quad \Omega n^{(1,\gamma)}_{\tau_{\kappa\alpha}} = \delta_{\alpha\gamma} Z_\kappa. \tag{A.8}$$

In addition, the quadrupoles must be isotropic,

$$Q^{(\gamma\delta)}_{\kappa\alpha} = \delta_{\delta\gamma} Q_{\kappa\alpha}. \tag{A.9}$$

We reach the conclusion that in a metal, the first-order electron density in response to an atomic displacement acquires the following form,

$$\Omega n^{\mathbf{q}}_{\tau_{\kappa\alpha}} \sim -i q_\alpha Z_\kappa + \frac{q^2}{2} Q_{\kappa\alpha}. \tag{A.10}$$

When summing the local and the Hartree potential terms, the divergencies cancel out and, at leading order in $\mathbf{q}$, the scattering potential tends to a direction-independent constant,

$$V^{\text{loc+H},\tau_{\kappa\alpha}}_{\mathbf{q}} \sim \frac{2\pi}{\Omega} Q_{\kappa\alpha}, \tag{A.11}$$

which is uniquely determined by the charge neutrality of the unit cell and corresponds to the Fermi level shifts defined in Sec. 3.3.4,

$$\frac{2\pi}{\Omega} Q_{\kappa\alpha} = -\mu^{\tau_{\kappa\alpha}}. \tag{A.12}$$

A.3 FIRST q DERIVATIVE OF THE MACROSCOPIC ELECTROSTATIC ENERGY

We want to take the first $\mathbf{q}$ derivative of the three terms that contribute to the macroscopic electrostatic energy in metals, within the framework of variational spatial dispersion theory, as described in Chapter 3. To this end, we shall write down the finite $\mathbf{q}$ expressions and we shall take the $\mathbf{q} \to \mathbf{0}$ limit once the divergencies coming from all the three terms have been properly treated.

The first contribution to the macroscopic electrostatics comes from the ion-ion Ewald (Ew) term,

$$\begin{aligned} E^{\tau_{\kappa\alpha}\tau_{\kappa'\beta}}_{\text{Ew},\mathbf{q}}(\mathbf{G}=\mathbf{0}) &= Z_\kappa Z_{\kappa'} \frac{4\pi}{\Omega} \frac{q_\alpha q_\beta}{q^2} e^{-\frac{q^2}{4\Lambda^2}} \\ &\simeq Z_\kappa Z_{\kappa'} \frac{4\pi}{\Omega} \left(\frac{q_\alpha q_\beta}{q^2} - \frac{q_\alpha q_\beta}{4\Lambda^2} + \dots \right), \end{aligned} \tag{A.13}$$

where Λ is a range-separation parameter that can assume any value in order to accelerate convergence [77], and the dots stand for an analytic sum of higher-order terms containing even powers of $\mathbf{q}$. Its partial derivative with respect to the wave vector q_γ is

$$E^{\tau_{\kappa\alpha}\tau_{\kappa'\beta}}_{\text{Ew},\gamma} \simeq \left[\frac{4\pi}{\Omega} \frac{Z_\kappa Z_{\kappa'}}{q^2} \left(\delta_{\alpha\gamma} q_\beta + \delta_{\beta\gamma} q_\alpha \right) - \frac{8\pi}{\Omega} Z_\kappa Z_{\kappa'} \frac{q_\alpha q_\beta q_\gamma}{q^4} \right]_{\mathbf{q}=\mathbf{0}}. \tag{A.14}$$

In Eq. (A.14) and in the following derivations, we omit terms that vanish in the $\mathbf{q} = \mathbf{0}$ limit, and we also exclude the $\mathbf{G} = \mathbf{0}$ label in order to keep the notation as simple as possible.

The second contribution comes from the second line of Eq. (3.27), which we shall refer to as the "elst" term, and can be equivalently written in reciprocal space as

$$E^{n_{\kappa\alpha}\tau_{\kappa'\beta}}_{\text{elst},\mathbf{q}} = \Omega(n^{\mathbf{q}}_{\tau_{\kappa\alpha}})^{*} K_{\mathbf{q}} n^{\mathbf{q}}_{\tau_{\kappa'\beta}}, \tag{A.15}$$

where $K_{\mathbf{q}} = 4\pi/q^2$ is the Coulomb kernel. The partial derivative of Eq. (A.15) with respect to q_γ, within the context of our variational spatial dispersion theory, i.e., excluding the partial $\mathbf{q}$ derivatives of the first-order electron densities, is given by

$$\begin{aligned} E^{\tau_{\kappa\alpha}\tau_{\kappa'\beta}}_{\text{elst},\gamma} &= \left[\Omega(n^{\mathbf{q}}_{\tau_{\kappa\alpha}})^{*} K_{\gamma} n^{\mathbf{q}}_{\tau_{\kappa'\beta}}\right]_{\mathbf{q}=\mathbf{0}} \\ &\simeq \frac{1}{\Omega}\left(iq_\alpha Z_\kappa + \frac{q^2}{2}Q_{\kappa\alpha}\right)\left(-\frac{8\pi q_\gamma}{q^4}\right)\left(-iq_\beta Z_{\kappa'} + \frac{q^2}{2}Q_{\kappa'\beta}\right)\Bigg|_{\mathbf{q}=\mathbf{0}} \\ &\simeq \left[-\frac{8\pi}{\Omega}Z_\kappa Z_{\kappa'}\frac{q_\alpha q_\beta q_\gamma}{q^4} + 2\left(i\delta_{\alpha\gamma}Z_\kappa \mu^{\tau_{\kappa'\beta}} - i\delta_{\beta\gamma}\mu^{\tau_{\kappa\alpha}}Z_{\kappa'}\right)\right]_{\mathbf{q}=\mathbf{0}}. \end{aligned} \tag{A.16}$$

In order to compute the third and last contribution to the macroscopic electrostatic energy, which comes from the local (loc) potentials in the first two lines of the occupation term, Eq. (3.42), we need the first $\mathbf{q}$ derivative of the local part of the psuedopotential given in Eq. (A.3),

$$V^{\text{loc},\tau_{\kappa\alpha}}_{\gamma} \simeq \frac{4\pi i}{\Omega}\left[Z_\kappa \frac{\delta_{\alpha\gamma}}{q^2} - 2Z_\kappa \frac{q_\alpha q_\gamma}{q^4}\right]_{\mathbf{q}=\mathbf{0}}. \tag{A.17}$$

This leads to

$$\begin{aligned} E^{\tau_{\kappa\alpha}\tau_{\kappa\beta}}_{\text{loc},\gamma} &= \left[\Omega(n^{\mathbf{q}}_{\tau_{\kappa\alpha}})^{*} V^{\text{loc},\tau_{\kappa'\beta}}_{\gamma} + \Omega(V^{\text{loc},\tau_{\kappa\alpha}}_{\gamma})^{*} n^{\mathbf{q}}_{\tau_{\kappa'\beta}}\right]_{\mathbf{q}=\mathbf{0}} \\ &\simeq \Bigg[\left(iq_\alpha Z_\kappa + \frac{q^2}{2}Q_{\kappa\alpha}\right)\frac{4\pi i}{\Omega}\left(Z_{\kappa'}\frac{\delta_{\beta\gamma}}{q^2} - 2Z_{\kappa'}\frac{q_\beta q_\gamma}{q^4}\right) \\ &\qquad - \frac{4\pi i}{\Omega}\left(Z_\kappa \frac{\delta_{\alpha\gamma}}{q^2} - 2Z_\kappa \frac{q_\alpha q_\gamma}{q^4}\right)\left(-iq_\beta Z_{\kappa'} + \frac{q^2}{2}Q_{\kappa'\beta}\right)\Bigg]_{\mathbf{q}=\mathbf{0}} \\ &\simeq \Bigg[-\frac{4\pi}{\Omega}\frac{Z_\kappa Z_{\kappa'}}{q^2}\left(\delta_{\alpha\gamma}q_\beta + \delta_{\beta\gamma}q_\alpha\right) + \frac{16\pi}{\Omega}Z_\kappa Z_{\kappa'}\frac{q_\alpha q_\beta q_\gamma}{q^4} \\ &\qquad + i\delta_{\beta\gamma}\mu^{\tau_{\kappa\alpha}}Z_{\kappa'} - i\delta_{\alpha\gamma}Z_\kappa \mu^{\tau_{\kappa'\beta}}\Bigg]_{\mathbf{q}=\mathbf{0}}. \end{aligned} \tag{A.18}$$

When the three contributions are treated together, all the divergences cancel out, and we are left with the following final result,

$$\begin{aligned} E^{\tau_{\kappa\alpha}\tau_{\kappa'\beta}}_{\text{mac},\gamma} &= E^{\tau_{\kappa\alpha}\tau_{\kappa'\beta}}_{\text{Ew},\gamma} + E^{\tau_{\kappa\alpha}\tau_{\kappa'\beta}}_{\text{elst},\gamma} + E^{\tau_{\kappa\alpha}\tau_{\kappa'\beta}}_{\text{loc},\gamma} \\ &\simeq i\delta_{\alpha\gamma}Z_\kappa \mu^{\tau_{\kappa'\beta}} - i\delta_{\beta\gamma}\mu^{\tau_{\kappa\alpha}}Z_{\kappa'}, \end{aligned} \tag{A.19}$$

which is Eq. (3.46) of the main text.

B

POLARIZATION SWITCHING OF BARIUM TITANATE VIA STRAIN GRADIENTS

This appendix offers supplementary information regarding the results presented in Chapter 4 on $BaTiO_3$. Our analysis on barium titanate will be more concise than that of lithium osmate. This is because the computation of the flexocoupling coefficients in insulators nowadays does not present any significant challenges, and because the potential energy landscape of $BaTiO_3$ is considerably simpler, since the AFD oxygen tilts do not need to be considered.

B.1 COMPUTATIONAL PARAMETERS

Calculations for $BaTiO_3$ are performed by using norm-conserving pseudopotentials with the Perdew-Wang [81] parametrization of the local density approximation (LDA), which we regenerate with the ONCVPSP [88] software in order to remove exchange-correlation nonlinear core corrections. We use a plane-wave energy cutoff of 60 Ha and the Brillouin Zone is sampled with $12 \times 12 \times 12$ $\mathbf{k}$ points. The obtained relax cell parameter is $a = 7.428$ bohr.

B.2 FLEXOCOUPLING COEFFICIENTS

The linearly independent components of the flexoelectric force-response tensor of cubic $BaTiO_3$ are shown in Table B.1. These are calculated using the standard long-wave DFPT implementation for insulators available in ABINIT, which is described in Sec. 2.4.4. One can easily check that the elastic sum rule given by Eq. (4.23) is readily satisfied, as shown in Table 4.2. The direct application of the definition of the flexocoupling coefficients, as indicated by Eq. (4.25), results in the values that are shown in the last column of Table B.1, which definitely disagree with those reported in Table 4.2.

What is the reason for this discrepancy? As explained in Sec. A.1, in order to ensure that the long-wave expansion of the physical quantities of interest in insulators do not contain undesired nonanalicities coming from macroscopic electric fields, we have suppressed the macroscopic component ($\mathbf{G} = \mathbf{0}$ term) of the self-consistent electrostatic potential; i.e., short-circuit electrical boundary conditions have been adopted. But there is not a unique way of doing so. This ambiguity (or gauge freedom) in suppressing the macroscopic electric field is completely innocuous when dealing with uniform strains, i.e., piezoelectricity. The case of flexoelectricity is more subtle, since a strain gradient changes the electronic energy of each of the states at a different rate; thus the bulk flexocoupling tensor of an insulator depends on which energy level we choose as reference. (In metals, this problematic energy reference is unambiguously defined by the Fermi level.) As a consequence, we reach the conclusion that the bulk flexocoupling coefficients of an insulator are defined only modulo an arbitrary constant [103, 105]. This is expected, since the bulk flexoelectric tensor suffers from the same reference potential ambiguity, which is intimately related to the theory of deformation potentials [163, 164].

By default, the *longwave* module of ABINIT places the energy reference at the average electrostatic potential. For a meaningful comparison with metallic $LiOsO_3$, we decided to use the conduction-band minimum (CBM) energy as reference, giving rise to the so-called n-type [106] flexocoupling coefficients, which are the values that are shown in Table 4.2 in the main text. The flexocoupling coefficients defined with respect to the average electrostatic potential are related to their n-type counterparts by the following constant,

$$\Delta f_{\alpha\beta,\gamma\delta} = Z^*_{\alpha\beta}\frac{\partial V_{c\mathbf{k}}}{\partial \varepsilon_{\gamma\delta}}. \tag{B.1}$$

Here, $Z^*_{\alpha\beta}$ is the dynamical charge associated with the β-th mode, which is defined as [103, 165]

$$Z^*_{\alpha\beta} = \sum_{\kappa,\rho}\sqrt{\frac{M}{m_\kappa}}Z^*_{\kappa,\alpha\rho}P^{(\beta)}_{\kappa\rho}, \tag{B.2}$$

where $Z^*_{\kappa,\alpha\rho}$ are the Born effective charges and $\mathbf{P}^{(\beta)}$ is a normalized polar eigenvector of the dynamical matrix, as introduced in Eq. (4.25). On the other hand, $V_{c\mathbf{k}} = -\epsilon^{(0)}_{c\mathbf{k}}/e + \bar{V}$ is the relative potential of the conduction band minimum, $\epsilon^{(0)}_{c\mathbf{k}}$, with respect to the average electrostatic potential, $\bar{V}$. Note the minus sign in the $-e$ factor, indicating the electron charge. For cubic $BaTiO_3$, we obtain

$$\frac{\partial \epsilon^{(0)}_{c\mathbf{k}}}{\partial \varepsilon_{\delta\delta}} = -11.38\text{ eV}, \quad \frac{\partial \bar{V}}{\partial \varepsilon_{\delta\delta}} = 5.58\text{ eV}, \quad Z^*_{\alpha\alpha} = 28.89\, e, \tag{B.3}$$

which gives, via Eq. (B.1), a correction of $\Delta f = 490.20$ eV to the linearly independent entries $f_{xx,xx}$ and $f_{xx,yy}$. The $f_{xy,xy}$ component, on the other hand, is independent of the chosen potential reference. The addition of Δf to the flexocoupling coefficients of Table B.1 immediately gives rise to the n-type flexocoupling coefficients of cubic $BaTiO_3$, as shown in Table 4.2.

Atom	xx,xx	xx,yy	xy,xy
Ba	−21.71	−27.78	11.14
Ti	−77.55	−108.79	8.03
O_1	147.69	101.65	13.40
O_2	42.72	41.41	16.10
O_3	42.72	39.54	3.55
$f_{\alpha\gamma,\beta\delta}$	−545.94	−486.32	−41.26

Table B.1: Linearly independent components of the flexoelectric force-response tensor (in eV) and the flexocoupling tensor (in eV) of cubic $BaTiO_3$. The energy reference is placed at the average electrostatic potential.

Parameter	Value	Units	Parameter	Value	Units
ζ_1	-11.54	$\mathrm{eV/\AA^2}$	ρ_3	-99.21	$\mathrm{eV/\AA^2}$
ζ_2	7.29×10^3	$\mathrm{eV/\AA^4}$	ρ_4	-2.92×10^4	$\mathrm{eV/\AA^4}$
ζ_3	3.44×10^3	$\mathrm{eV/\AA^4}$	ρ_5	3.11×10^4	$\mathrm{eV/\AA^4}$
ρ_1	-9.11×10^2	$\mathrm{eV/\AA^2}$	ρ_6	9.69×10^3	$\mathrm{eV/\AA^4}$
ρ_2	-97.06	$\mathrm{eV/\AA^2}$	...	...	...

Table B.2: Calculated model parameters for the first-principles Hamiltonian of BaTiO$_3$.

B.3 EFFECTIVE HAMILTONIAN

We use the following expression for the effective Hamiltonian of BaTiO$_3$,

$$E_{\mathrm{eff}}[\mathbf{s},\mathbf{u}] = H_{\mathrm{s}}[\mathbf{s}] + H_{\mathrm{u}}[\mathbf{u}] + H_{\mathrm{su}}[\mathbf{s},\mathbf{u}], \tag{B.4}$$

where

$$H_{\mathrm{s}}[\mathbf{s}] = \frac{\Omega}{2}\mathcal{C}_{11}(s_1^2+s_2^2+s_3^2) + \Omega\mathcal{C}_{12}(s_1s_2+s_1s_3+s_2s_3) + \frac{\Omega}{2}\mathcal{C}_{44}(s_4^2+s_5^2+s_6^2), \tag{B.5}$$

$$H_{\mathrm{u}}[\mathbf{u}] = \zeta_1(u_1^2+u_2^2+u_3^2) + \zeta_2(u_1^4+u_2^4+u_3^4) + \zeta_3(u_2^2u_3^2+u_1^2u_3^2+u_1^2u_2^2) \tag{B.6}$$

and

$$\begin{aligned} H_{\mathrm{su}}[\mathbf{s},\mathbf{u}] =& \rho_1(s_1u_1^2+s_2u_2^2+s_3u_3^2) + \rho_2[s_1(u_2^2+u_3^2)+s_2(u_1^2+u_3^2)+s_3(u_1^2+u_2^2)] \\ &+ \rho_3(s_4u_2u_3+s_5u_1u_3+s_6u_1u_2) + \rho_4(s_1u_1^4+s_2u_2^4+s_3u_3^4) \\ &+ \rho_5(s_4u_2^2u_3^2+s_5u_1^2u_3^2+s_6u_1^2u_2^2) \\ &+ \rho_6[s_1(u_2^4+u_3^4)+s_2(u_1^4+u_3^4)+s_3(u_1^4+u_2^4)]. \end{aligned} \tag{B.7}$$

(Remember that s_i and u_i represent, respectively, the strain in Voigt notation and the amplitude of the polar order parameter. In addition, Ω is the volume of the unit cell and $\mathcal{C}_{ij}$ are the elastic constants, which are given in Table 4.2.) The obtained model parameters are shown in Table B.2. In Fig. B.1 we validate our model by computing the phase diagram of the $Pm\bar{3}m$ and $R3m$ phases of BaTiO$_3$ as a function of the cell volume, which shows excellent agreement with first principles calculations.

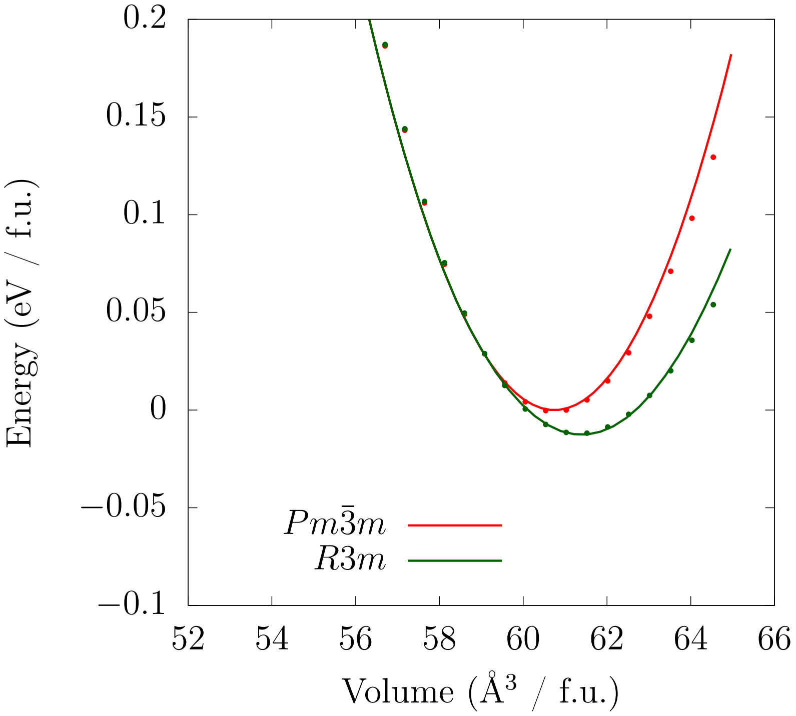

Figure B.1: Energy per formula unit as a function of the volume of the perovskite formula unit of $Pm\bar{3}m$ and $R3m$ phases of $BaTiO_3$. Dots represent direct DFT calculations and solid lines are obtained from our effective Hamiltonian.

C

DIPOLAR SUM RULE FOR MOLECULES

This appendix is devoted to proving the following sum rule, which is valid for an isolated molecule in open electrostatic boundary conditions,

$$\sum_\kappa \left(J^{(1,\gamma)}_{\alpha,\kappa\beta} + \tau_{\kappa\gamma} Z^*_{\alpha,\kappa\beta} \right) = \delta_{\alpha\beta} \mathcal{D}_\gamma, \tag{C.1}$$

where $\mathbf{J}^{(1)}$ is the first moment of the polarization response to an atomic displacement, $\mathbf{Z}^*$ corresponds to the Born effective charge tensor and $\boldsymbol{\mathcal{D}}$ is the static dipole moment of the molecule,

$$\mathcal{D}_\gamma = \int r_\gamma n^{(0)}(\mathbf{r})\, d^3r. \tag{C.2}$$

In absence of nonlocal pseudopotentials the proof is straightforward: it suffices to use the definition of the $J^{(n)}_{\alpha,\kappa\beta}$ moments provided in the main text [see Eq. (5.18)] together with the following relation (translational invariance) for the microscopic polarization response [97],

$$\sum_\kappa \mathcal{P}_{\alpha,\kappa\beta}(\mathbf{r} - \boldsymbol{\tau}_\kappa) = \delta_{\alpha\beta} n^{(0)}(\mathbf{r}). \tag{C.3}$$

If nonlocal pseudopotentials are present, Eq. (C.3) breaks down; however, we will show that Eq. (C.1) is exact even in that case. To prove Eq. (C.1) without passing through Eq. (C.3), we will use another (exact) sum rule, relating the $J^{(1,\gamma)}_{\alpha,\kappa\beta}$ moments to the clamped-ion piezoelectric tensor [129],

$$-\frac{1}{\Omega} \sum_\kappa J^{(1,\gamma)}_{\alpha,\kappa\beta} = \bar{e}_{\alpha,\beta\gamma}. \tag{C.4}$$

To apply this rule, we need to place the isolated molecule in a large box of volume Ω, and work in periodic boundary conditions. Then, Eq. (C.4) describes the clamped-ion *proper* piezoelectric response of the resulting crystal lattice to an infinitesimal strain. (In order to avoid complications due to long-range interactions between repeated images, we assume that the Coulomb kernel is cut off at the boundary of the box, and that all objects entering Eq. (C.1) are consistently calculated in such conditions.) Since the images of the molecule are isolated in space, the macroscopic polarization of the crystal is exactly given by the Clausius-Mossotti formula as the static dipole moment divided by the volume,

$$\mathbf{P} = \frac{\boldsymbol{\mathcal{D}}}{\Omega}. \tag{C.5}$$

However, $\bar{e}_{\alpha,\beta\gamma}$ is not defined as a straightforward strain derivative of $\mathbf{P}$, as this would give rise to the so-called clamped-ion *improper* piezoelectric[1] tensor, $\bar{e}^{\text{impr}}_{\alpha,\beta\gamma}$

---

[1] The relationship between the *proper* and *improper* (impr) piezoelectric tensors [129] reads as follows: $\bar{e}_{\alpha,\beta\gamma} = \bar{e}^{\text{impr}}_{\alpha,\beta\gamma} - \delta_{\beta\gamma} P_\alpha + \delta_{\alpha\beta} P_\beta$, where $\mathbf{P}$ is the polarization of the reference configuration, i.e., prior to applying the strain.

[129, 166]. To arrive at $\bar{e}_{\alpha,\beta\gamma}$, we first need to introduce the *reduced* (tilded) polarization [129],

$$\tilde{P}_i = \frac{1}{2\pi}\Omega \mathbf{b}_i \cdot \mathbf{P} = \frac{1}{2\pi}\mathbf{b}_i \cdot \boldsymbol{\mathcal{D}}, \tag{C.6}$$

where $\mathbf{a}_i$ and $\mathbf{b}_i$ are, respectively, the primitive real and reciprocal space lattice vectors, fulfilling $\mathbf{a}_i \cdot \mathbf{b}_j = 2\pi\delta_{ij}$, as defined in Eq. (2.24). We are now ready to introduce the clamped-ion *proper* piezoelectric tensor [129, 167],

$$\bar{e}_{\alpha,\beta\gamma} = \frac{1}{\Omega}\sum_i a_{i\alpha}\frac{\partial \tilde{P}_i}{\partial \eta_{\beta\gamma}}, \tag{C.7}$$

where $a_{i\alpha}$ represents the α Cartesian component of the primitive real space lattice vector $\mathbf{a}_i$ and $\boldsymbol{\eta}$ is the Cauchy infinitesimal strain tensor. This leads to the following formula, without factors of volume,

$$\begin{aligned} \sum_\kappa J^{(1,\gamma)}_{\alpha,\kappa\beta} &= -\frac{1}{2\pi}\sum_i a_{i\alpha}\frac{\partial(\mathbf{b}_i \cdot \boldsymbol{\mathcal{D}})}{\partial \eta_{\beta\gamma}} \\ &= -\frac{1}{2\pi}\sum_i a_{i\alpha}\left[\mathbf{b}_i \cdot \frac{\partial \boldsymbol{\mathcal{D}}}{\partial \eta_{\beta\gamma}} + \frac{\partial \mathbf{b}_i}{\partial \eta_{\beta\gamma}} \cdot \boldsymbol{\mathcal{D}}\right]. \end{aligned} \tag{C.8}$$

In order to calculate the derivatives with respect to $\eta_{\beta\gamma}$, note that an infinitesimal strain corresponds to the following linear transformation of the atomic coordinates and primitive real space lattice vectors,

$$\boldsymbol{\tau}'_\kappa = (\mathbf{I} + \boldsymbol{\eta})\boldsymbol{\tau}_\kappa, \tag{C.9a}$$

$$\mathbf{a}'_i = (\mathbf{I} + \boldsymbol{\eta})\mathbf{a}_i, \tag{C.9b}$$

where the prime symbol indicates the new vectors after application of strain and $\mathbf{I}$ is the identity matrix. The first relation yields

$$\frac{\partial \tau_{\kappa\sigma}}{\partial \eta_{\beta\gamma}} = \delta_{\beta\sigma}\tau_{\kappa\gamma}. \tag{C.10}$$

By using the definition of the Born effective charge tensor, one immediately obtains,

$$\frac{\partial \mathcal{D}_\alpha}{\partial \eta_{\beta\gamma}} = \sum_{\kappa,\sigma}\frac{\partial \mathcal{D}_\alpha}{\partial \tau_{\kappa\sigma}}\frac{\partial \tau_{\kappa\sigma}}{\partial \eta_{\beta\gamma}} = \sum_\kappa Z^*_{\alpha,\kappa\beta}\tau_{\kappa\gamma}. \tag{C.11}$$

The second relation, Eq. (C.9b), is useful for determining the transformation law for their dual vectors, $\mathbf{b}_i$. The orthonormality condition given in Eq. (2.24) needs to be preserved up to linear order in the strain, which leads to the following result,

$$\mathbf{b}'_i \simeq (\mathbf{I} - \boldsymbol{\eta}^{\mathrm{T}})\mathbf{b}_i, \tag{C.12}$$

where the symbol T indicates the transpose of the matrix, i.e., $(\boldsymbol{\eta}^{\mathrm{T}})_{\alpha\beta} = \eta_{\beta\alpha}$. From this, we deduce

$$\frac{\partial b_{i\rho}}{\partial \eta_{\beta\gamma}} = -\delta_{\gamma\rho}b_{i\beta}. \tag{C.13}$$

Collecting all the pieces, Eq. (C.4) can be rewritten as

$$\sum_\kappa J^{(1,\gamma)}_{\alpha,\kappa\beta} = -\frac{1}{2\pi}\sum_i a_{i\alpha}\sum_\rho\left[b_{i\rho}\sum_\kappa Z^*_{\rho,\kappa\beta}\tau_{\kappa\gamma} - \delta_{\gamma\rho}b_{i\beta}\mathcal{D}_\rho\right]. \tag{C.14}$$

By using the orthonormality rule $\sum_i a_{i\alpha} b_{i\beta} = 2\pi\delta_{\alpha\beta}$, we eventually arrive at

$$\sum_\kappa J^{(1,\gamma)}_{\alpha,\kappa\beta} = \delta_{\alpha\beta}\mathcal{D}_\gamma - \sum_\kappa Z^*_{\alpha,\kappa\beta}\tau_{\kappa\gamma}, \tag{C.15}$$

thereby concluding the proof.

The above results allow us to further specify the validity of Eq. (C.3) in the case of an isolated molecule. While the microscopic formula breaks down in presence of nonlocal pseudopotentials, one can expand both sides into Cartesian multipoles and ask at what order the equality no longer holds. At order zero the equality clearly is satisfied,

$$\sum_\kappa \int \mathcal{P}_{\alpha,\kappa\beta}(\mathbf{r})\, d^3r = \delta_{\alpha\beta} \int n^{(0)}(\mathbf{r})\, d^3r, \tag{C.16}$$

since macroscopic currents are well described; in the case of a neutral molecule, Eq. (C.16) reduces to the acoustic sum rule on the Born charge tensor components. In this appendix, we have provided a formal proof that Eq. (C.3) works equally well at first order,

$$\sum_\kappa \int r_\gamma \mathcal{P}_{\alpha,\kappa\beta}(\mathbf{r})\, d^3r = \delta_{\alpha\beta} \int r_\gamma n^{(0)}(\mathbf{r})\, d^3r. \tag{C.17}$$

On the other hand, we already know from earlier works [98, 100] that the second order doesn't work if nonlocal potentials are used in the calculation,

$$\sum_\kappa \int r_\gamma r_\lambda \mathcal{P}_{\alpha,\kappa\beta}(\mathbf{r})\, d^3r \neq \delta_{\alpha\beta} \int r_\gamma r_\lambda n^{(0)}(\mathbf{r})\, d^3r. \tag{C.18}$$

This breakdown of translational invariance at the quadrupolar level explains why Eq. (5.30) and Eq. (5.37) disagree in presence of nonlocal potentials.

D

RESPONSE TO A LONG-WAVELENGTH ELECTROMAGNETIC VECTOR POTENTIAL FIELD

We consider a monochromatic electromagnetic vector potential field that is modulated by a wave vector $\mathbf{q}$, such that $A_\beta = A^{\mathbf{q}}_\beta e^{i\mathbf{q}\cdot\mathbf{r}}$. The corresponding wave function response at finite $\mathbf{q}$, which we denote as $|u^{A_\beta}_{m\mathbf{k},\mathbf{q}}\rangle$, can be obtained from the following Sternheimer equation [41],

$$\left(\hat{H}^{(0)}_{\mathbf{k}+\mathbf{q}} + a\hat{P}_{\mathbf{k}+\mathbf{q}} - \epsilon^{(0)}_{m\mathbf{k}}\right) |u^{A_\beta}_{m\mathbf{k},\mathbf{q}}\rangle = -\hat{Q}_{\mathbf{k}+\mathbf{q}}\hat{H}^{A_\beta}_{\mathbf{k},\mathbf{q}} |u^{(0)}_{m\mathbf{k}}\rangle , \tag{D.1}$$

where $\hat{H}^{A_\beta}_{\mathbf{k},\mathbf{q}}$ is the first-order Hamiltonian, as defined by Eq. (2.100); notice the absence of SCF terms in Eq. (D.1). At $\mathbf{q} = \mathbf{0}$, it reduces to $\hat{H}^{A_\beta}_{\mathbf{k},\mathbf{q}=\mathbf{0}} = \partial_\beta \hat{H}^{(0)}_{\mathbf{k}}$, and we recover the well-known d/dk_β wave functions,

$$|u^{A_\beta}_{m\mathbf{k},\mathbf{q}=\mathbf{0}}\rangle = \partial_\beta \hat{P}_{\mathbf{k}} |u^{(0)}_{m\mathbf{k}}\rangle = |u^{k_\beta}_{m\mathbf{k}}\rangle . \tag{D.2}$$

The response at first order in the wave vector $\mathbf{q}$ can be obtained by deriving both sides of Eq. (D.1) with respect to q_γ,

$$\begin{aligned}\left(\hat{H}^{(0)}_{\mathbf{k}} + a\hat{P}_{\mathbf{k}} - \epsilon^{(0)}_{m\mathbf{k}}\right) |u^{A_\beta}_{m\mathbf{k},\gamma}\rangle = \Big(&\partial_\gamma \hat{H}^{(0)}_{\mathbf{k}} \partial_\beta \hat{Q}_{\mathbf{k}} - a\partial_\gamma \hat{P}_{\mathbf{k}} \partial_\beta \hat{P}_{\mathbf{k}} \\ &- \partial_\gamma \hat{Q}_{\mathbf{k}} \partial_\beta \hat{H}^{(0)}_{\mathbf{k}} - \frac{1}{2}\hat{Q}_{\mathbf{k}} \partial^2_{\beta\gamma} \hat{H}^{(0)}_{\mathbf{k}}\Big) |u^{(0)}_{m\mathbf{k}}\rangle .\end{aligned} \tag{D.3}$$

After some tedious but otherwise straightforward algebra, it can be shown [41] that the wave function response to an electromagnetic vector potential at first order in the modulation wave vector $\mathbf{q}$, which we denote as $|u^{A_\beta}_{m\mathbf{k},\gamma}\rangle$, is given by

$$|u^{A_\beta}_{m\mathbf{k},\gamma}\rangle = |\bar{u}^{A_\beta}_{m\mathbf{k},\gamma}\rangle - \frac{1}{2}[\partial_\gamma \hat{P}_{\mathbf{k}}, \partial_\beta \hat{P}_{\mathbf{k}}] |u^{(0)}_{m\mathbf{k}}\rangle . \tag{D.4}$$

The second term in the right-hand side of Eq. (D.4) is a purely *geometric* contribution, in the sense that it only depends on the unperturbed ground-state wave functions, and the first term is a linear-response quantity that can be obtained from the following Sternheimer equation [41],

$$\left(\hat{H}^{(0)}_{\mathbf{k}} + a\hat{P}_{\mathbf{k}} - \epsilon^{(0)}_{m\mathbf{k}}\right) |\bar{u}^{A_\beta}_{m\mathbf{k},\gamma}\rangle = -\hat{Q}_{\mathbf{k}} \hat{O}^{\beta\gamma}_{\mathbf{k}} |u^{(0)}_{m\mathbf{k}}\rangle , \tag{D.5}$$

where the perturbing operator $\hat{O}^{\beta\gamma}_{\mathbf{k}}$ is given by

$$\hat{O}^{\beta\gamma}_{\mathbf{k}} = \partial_\gamma \hat{H}^{(0)}_{\mathbf{k}} \partial_\beta \hat{P}_{\mathbf{k}} - \partial_\gamma \hat{P}_{\mathbf{k}} \partial_\beta \hat{H}^{(0)}_{\mathbf{k}} + \frac{1}{2}\partial^2_{\beta\gamma} \hat{H}^{(0)}_{\mathbf{k}} . \tag{D.6}$$

The symbols $\partial_\gamma \equiv \partial/\partial_{k_\gamma}$ and $\partial^2_{\beta\gamma} \equiv \partial^2/\partial_{k_\gamma}\partial_{k_\beta}$ represent, respectively, the first and second derivatives in $\mathbf{k}$ space. The physical interpretation of the perturbing operator given by Eq. (D.6) becomes clearer once it is expressed as a sum of a symmetric ($\hat{O}_{\mathbf{k}}^{\mathrm{S},\beta\gamma}$) plus an antisymmetric ($\hat{O}_{\mathbf{k}}^{\mathrm{A},\beta\gamma}$) contribution with respect to $\beta \leftrightarrow \gamma$ exchange,

$$\hat{O}_{\mathbf{k}}^{\beta\gamma} = \frac{1}{2}\left(\hat{O}_{\mathbf{k}}^{\mathrm{S},\beta\gamma} + \hat{O}_{\mathbf{k}}^{\mathrm{A},\beta\gamma}\right), \tag{D.7}$$

where

$$\hat{O}_{\mathbf{k}}^{\mathrm{S},\beta\gamma} = \partial_\gamma \hat{H}_{\mathbf{k}}^{(0)} \partial_\beta \hat{P}_{\mathbf{k}} + \partial_\beta \hat{H}_{\mathbf{k}}^{(0)} \partial_\gamma \hat{P}_{\mathbf{k}} - \partial_\gamma \hat{P}_{\mathbf{k}} \partial_\beta \hat{H}_{\mathbf{k}}^{(0)} - \partial_\beta \hat{P}_{\mathbf{k}} \partial_\gamma \hat{H}_{\mathbf{k}}^{(0)} + \partial_{\beta\gamma}^2 \hat{H}_{\mathbf{k}}^{(0)} \tag{D.8}$$

and

$$\hat{O}_{\mathbf{k}}^{\mathrm{A},\beta\gamma} = \partial_\gamma \hat{H}_{\mathbf{k}}^{(0)} \partial_\beta \hat{P}_{\mathbf{k}} - \partial_\beta \hat{H}_{\mathbf{k}}^{(0)} \partial_\gamma \hat{P}_{\mathbf{k}} - \partial_\gamma \hat{P}_{\mathbf{k}} \partial_\beta \hat{H}_{\mathbf{k}}^{(0)} + \partial_\beta \hat{P}_{\mathbf{k}} \partial_\gamma \hat{H}_{\mathbf{k}}^{(0)}. \tag{D.9}$$

Notably, $\hat{O}_{\mathbf{k}}^{\mathrm{S},\beta\gamma}$ is the perturbing operator that enters the Sternheimer equation for the $|\partial_{\beta\gamma}^2 u_{m\mathbf{k}}^{(0)}\rangle$ wave functions (commonly denoted as $d^2/dk_\gamma dk_\beta$) and the antisymmetric $\hat{O}_{\mathbf{k}}^{\mathrm{A},\beta\gamma}$ operator is intimately related to the perturbing operator that describes the orbital wave function response to a uniform magnetic field, $\hat{O}_{\mathbf{k}}^{B_\delta}$, as defined by Essin *et al.* [102],

$$\hat{O}_{\mathbf{k}}^{B_\delta} = \frac{i}{2} \sum_{\beta,\gamma} \epsilon^{\delta\beta\gamma} \hat{O}_{\mathbf{k}}^{A,\beta\gamma}. \tag{D.10}$$

While the theoretical basis for the wave function response to a long-wavelength electromagnetic vector potential had already been well-established in earlier works [41], its practical implementation in a publicly available DFT code is one of the achievements of this thesis.

E

GEOMETRIC ORBITAL MAGNETIZATION BY ROTATION

The main objective of this appendix is to establish a formal link between the geometric orbital magnetization as we have presented in Chapter 5 and the theory discussed in Ref. [17]. In the latter work, Trifunovic, Ono and Watanabe developed a general theory for periodic adiabatic processes that include as special cases the scenarios we have addressed in Chapter 5; i.e., rigid rotations of molecules and pseudorotations in solids induced by circularly polarized phonons.

We will consider the magnetization induced by a rotation in a molecule as introduced in Chapter 5 and we will prove that our DFPT treatment of the orbital magnetic field response exactly recovers the topological and nontopological contributions to the geometric orbital magnetization as described in Ref. [17].

E.1 MAGNETIZATION BY ROTATION

Following the strategy of Ceresoli and Tosatti [58], we consider an adiabatic parameter $\theta(t)$, which describes the rotation angle of the molecule. The Hamiltonian and the instantaneous Bloch wave functions of a given molecule depend on θ and fulfill the following Schrödinger equation,

$$\hat{H}^{(0)}_{\mathbf{k}}(\theta)\,|u^{(0)}_{m\mathbf{k}}(\theta)\rangle = \epsilon^{(0)}_{m\mathbf{k}}\,|u^{(0)}_{m\mathbf{k}}(\theta)\rangle\,. \tag{E.1}$$

(Note that the eigenenergies $\epsilon^{(0)}_{m\mathbf{k}}$ are independent of θ, since the energy of the system is invariant under any unitary transformation, e.g., rotations.) Assuming that the rotation axis is oriented along the δ Cartesian direction,

$$|u^{(0)}_{m\mathbf{k}}(\theta)\rangle = \hat{R}_\delta(\theta)\,|u^{(0)}_{m\mathbf{k}}(0)\rangle\,, \quad \text{with} \quad \hat{R}_\delta(\theta) = e^{-i\theta\hat{L}_\delta}, \tag{E.2}$$

where $\hat{R}_\delta(\theta)$ is the rotation operator, $\hat{L}_\delta$ is the angular momentum operator and we impose periodicity in θ, i.e., $|u^{(0)}_{m\mathbf{k}}(0)\rangle = |u^{(0)}_{m\mathbf{k}}(2\pi)\rangle$. It is then easy to see that the Berry connection $\mathcal{A}^{\theta}_{nm\mathbf{k}}$ is a constant with respect to θ,

$$\mathcal{A}^{\theta}_{nm\mathbf{k}} \equiv \langle u^{(0)}_{n\mathbf{k}}|i\partial_\theta u^{(0)}_{m\mathbf{k}}\rangle = \langle u^{(0)}_{n\mathbf{k}}|\,\hat{L}_\delta\,|u^{(0)}_{m\mathbf{k}}\rangle\,, \tag{E.3}$$

which means [17, 100] that we will be able to safely evaluate the induced magnetization at $\theta = 0$; i.e., there is no need to integrate over the whole cycle. The Berry phase accumulated around a closed loop, at linear order in the applied external magnetic field, which is assumed to be oriented along the δ Cartesian direction as well, can be written as

$$\varphi_{B_\delta} = 2\pi B_\delta \Omega_{B_\delta\theta}, \tag{E.4}$$

where $\Omega_{B_\delta \theta}$ is the Berry curvature [154] in the (B_δ, θ) parameter space,

$$\begin{aligned}\Omega_{B_\delta \theta} &= \sum_{m\in\mathcal{V}} \int_{\mathrm{BZ}} [d^3k] \left(\partial_{B_\delta} \mathcal{A}^{\theta}_{m m\mathbf{k}} - \partial_{\theta} \mathcal{A}^{B_\delta}_{m m\mathbf{k}}\right) \\ &=2\,\mathrm{Im} \sum_{m\in\mathcal{V}} \int_{\mathrm{BZ}} [d^3k] \, \langle u^{\theta}_{m\mathbf{k}} | u^{B_\delta}_{m\mathbf{k}} \rangle \,.\end{aligned} \tag{E.5}$$

(Notice that in absence of the applied external magnetic field, the Berry phase due to a rigid rotation of the molecule, as specified in Eq. (E.4), identically vanishes; this is the reason why we include explicitly the B_δ subscript in φ.) It can also be demonstrated [58, 100] that the magnetization by rotation is directly related to the Berry phase accumulated around a closed loop in presence of a uniform magnetic field,

$$\varphi_{B_\delta} = 2\pi B_\delta \frac{\partial m_z}{\partial \dot{\theta}}, \tag{E.6}$$

which implies that

$$\frac{\partial m_\delta}{\partial \dot{\theta}} = \Omega_{B_\delta \theta}. \tag{E.7}$$

In short, Eq. (E.7) is telling us that the magnetization by rotation in a molecule reduces to a Berry curvature in the two-dimensional (B_δ, θ) parameter space. All the expressions we have summarized in the previous lines are well established results that can be found in the literature [58, 100]. The remainder of this appendix will be devoted to expand the wave function response to B_δ appearing in Eq. (E.5) in order to prove that we indeed recover the topological and nontopological contributions to the orbital magnetization as defined in Ref. [17].

We shall obtain the wave function response to a magnetic field that enters the Berry curvature from the response to an electromagnetic vector potential field in the symmetric gauge, i.e., $\mathbf{A} = \frac{1}{2}\mathbf{B} \times \mathbf{r}$. From Eq. (D.4) and Eq. (D.10) of Appendix D, we deduce that the wave function response to an orbital magnetic field can be written as a sum of two contributions,

$$|u^{B_\delta}_{m\mathbf{k}}\rangle = |\bar{u}^{B_\delta}_{m\mathbf{k}}\rangle + \frac{i}{2} \sum_{\beta,\gamma} \epsilon^{\delta\beta\gamma} [\partial_\gamma \hat{P}_{\mathbf{k}}, \partial_\beta \hat{P}_{\mathbf{k}}] \, |u^{(0)}_{m\mathbf{k}}\rangle \,. \tag{E.8}$$

The first term on the right hand side of Eq. (E.8) is obtained as a solution of the following Sternheimer equation,

$$(\hat{H}_{\mathbf{k}} + a\hat{P}_{\mathbf{k}} - \epsilon^{(0)}_{m\mathbf{k}}) \, |\bar{u}^{B_\delta}_{m\mathbf{k}}\rangle = -\hat{Q}_{\mathbf{k}} \hat{O}^{B_\delta}_{\mathbf{k}} \, |u^{(0)}_{m\mathbf{k}}\rangle \,, \tag{E.9}$$

where the perturbing operator $\hat{O}^{B_\delta}_{\mathbf{k}}$ is given by Eq. (D.10). By inserting Eq. (E.8) into Eq. (E.7), we obtain

$$\frac{\partial m_\delta}{\partial \dot{\theta}} = \frac{\partial}{\partial \dot{\theta}} m^{\mathrm{top}}_\delta + \frac{\partial}{\partial \dot{\theta}} m^{\mathrm{nontop}}_\delta, \tag{E.10}$$

where the topological (top) and nontopological (nontop) contributions are examined in more detail in the following sections.

E.2 TOPOLOGICAL RESPONSE

The topological contribution to the orbital magnetization induced by a rotation in a molecule comes from the second term on the right hand side of Eq. (E.8). Substituting this term into Eq. (E.7), one immediately obtains

$$\frac{\partial}{\partial\dot{\theta}} m_\delta^{\text{top}} = \int_{\text{BZ}} [d^3k] \sum_{\beta,\gamma} \epsilon^{\delta\beta\gamma} \, \text{Tr} \left(\hat{P}_{\mathbf{k}} \partial_\theta \hat{P}_{\mathbf{k}} [\partial_\gamma \hat{P}_{\mathbf{k}}, \partial_\beta \hat{P}_{\mathbf{k}}] \right), \tag{E.11}$$

where ∂_θ is the derivative with respect to the rotation angle and $\partial_\gamma \equiv \partial/\partial k_\gamma$ represents a covariant derivative in $\mathbf{k}$ space. For simplicity, we will now assume that both the applied magnetic field and the rotation axis are parallel to the z Cartesian direction. It is then interesting to note that Eq. (E.11) can be written as a third Chern-Simons form,

$$\frac{\partial}{\partial\dot{\theta}} m_z^{\text{top}} = \int_{\text{BZ}} [d^3k] \, \text{Tr} \left(\boldsymbol{\mathcal{A}}_{\mathbf{k}}^{\mathbf{Y}} \cdot \nabla_{\mathbf{Y}} \times \boldsymbol{\mathcal{A}}_{\mathbf{k}}^{\mathbf{Y}} - \frac{2i}{3} \boldsymbol{\mathcal{A}}_{\mathbf{k}}^{\mathbf{Y}} \cdot \boldsymbol{\mathcal{A}}_{\mathbf{k}}^{\mathbf{Y}} \times \boldsymbol{\mathcal{A}}_{\mathbf{k}}^{\mathbf{Y}} \right), \tag{E.12}$$

where we have introduced the Berry connection $\boldsymbol{\mathcal{A}}_{\mathbf{k}}^{\mathbf{Y}}$ in the $\mathbf{Y} = (\theta, k_x, k_y)$ space,

$$(\boldsymbol{\mathcal{A}}_{\mathbf{k}}^{\mathbf{Y}})_{nm} = \langle u_{n\mathbf{k}}^{(0)} | i \nabla_{\mathbf{Y}} u_{m\mathbf{k}}^{(0)} \rangle, \quad \text{with} \quad \nabla_{\mathbf{Y}} = (\partial_\theta, \partial_{k_x}, \partial_{k_y}). \tag{E.13}$$

Eq. (E.12) is presented as it appears in Ref. [17].

E.3 NONTOPOLOGICAL RESPONSE

The nontopological contribution to the orbital magnetization comes from the linear-response term in Eq. (E.8), which is indicated with a "bar" symbol. We obtain

$$\frac{\partial}{\partial\dot{\theta}} m_\delta^{\text{nontop}} = 2\,\text{Im} \sum_{m\in\mathcal{V}} \int_{\text{BZ}} [d^3k] \, \langle u_{m\mathbf{k}}^{\theta} | \bar{u}_{m\mathbf{k}}^{B_\delta} \rangle, \tag{E.14}$$

where $|\bar{u}_{m\mathbf{k}}^{B_\delta}\rangle$ can be expressed as a sum over unoccupied states belonging to the conduction-band manifold ($\mathcal{C}$). From Eq. (E.9), we can write the following,

$$\begin{aligned} |\bar{u}_{m\mathbf{k}}^{B_\delta}\rangle &= \sum_{n\in\mathcal{C}} |u_{n\mathbf{k}}^{(0)}\rangle \frac{\langle u_{n\mathbf{k}}^{(0)} | \hat{O}_{\mathbf{k}}^{B_\delta} | u_{m\mathbf{k}}^{(0)} \rangle}{\epsilon_{m\mathbf{k}}^{(0)} - \epsilon_{n\mathbf{k}}^{(0)}} \\ &= \sum_{n\in\mathcal{C}} \sum_{\beta,\gamma} \frac{i}{2} \epsilon^{\delta\beta\gamma} |u_{n\mathbf{k}}^{(0)}\rangle \frac{\langle u_{n\mathbf{k}}^{(0)} | \left(\{\partial_\gamma \hat{H}_{\mathbf{k}}, \partial_\beta \hat{P}_{\mathbf{k}}\} - \{\partial_\beta \hat{H}_{\mathbf{k}}, \partial_\gamma \hat{P}_{\mathbf{k}}\} \right) | u_{m\mathbf{k}}^{(0)} \rangle}{\epsilon_{m\mathbf{k}}^{(0)} - \epsilon_{n\mathbf{k}}^{(0)}}, \end{aligned} \tag{E.15}$$

where the *curly* brackets indicate the anticommutator relation, $\{\hat{A}, \hat{B}\} = \hat{A}\hat{B} + \hat{B}\hat{A}$. It is then straightforward to obtain the nontopological contribution as expressed in Ref. [17],

$$\frac{\partial}{\partial\dot{\theta}} m_\delta^{\text{nontop}} = \int_{\text{BZ}} [d^3k] \sum_{m\in\mathcal{V}} \sum_{n\in\mathcal{C}} m_{\delta,nm\mathbf{k}}^{\text{nontop}}, \tag{E.16}$$

where we have defined

$$m_{\delta,nm\mathbf{k}}^{\text{nontop}} = \sum_{\beta,\gamma} \epsilon^{\delta\beta\gamma} \frac{\langle u_{m\mathbf{k}}^{(0)} | \partial_\theta \hat{P}_{\mathbf{k}} | u_{n\mathbf{k}}^{(0)} \rangle \; \langle u_{n\mathbf{k}}^{(0)} | \{\partial_\gamma \hat{H}_{\mathbf{k}}^{(0)}, \partial_\beta \hat{H}_{\mathbf{k}}^{(0)}\} | u_{m\mathbf{k}}^{(0)} \rangle}{\epsilon_{m\mathbf{k}}^{(0)} - \epsilon_{n\mathbf{k}}^{(0)}} + \text{c.c.}, \tag{E.17}$$

which brings this appendix to an end.

F

NATURAL OPTICAL ACTIVITY IN MOLECULES

In this appendix we derive explicitly the $\tilde{\mathcal{X}}^{\mathcal{E}_\alpha k_\gamma \mathcal{E}_\beta}$ and $\tilde{\mathcal{W}}^{\alpha,\beta\gamma}$ terms appearing in Eq. (6.20) for the natural optical activity tensor in finite samples. Remember that the "tilde" symbol indicates that SCF contributions are neglected. The relationships given in Eq. (6.22) are used throughout, in conjunction with the following expression for the first-order wave functions,

$$|\tilde{\psi}_m^{\mathcal{E}_\alpha}\rangle = \sum_{l\in\mathcal{C}} |\psi_l\rangle \frac{\langle\psi_l|\,\hat{r}_\alpha\,|\psi_m\rangle}{\epsilon_m-\epsilon_l}. \tag{F.1}$$

F.1 COMPUTATION OF THE $\tilde{\mathcal{X}}^{\mathcal{E}_\alpha k_\gamma \mathcal{E}_\beta}$ TERM

We start from the definition for the $\tilde{\mathcal{X}}$ term and express the velocity operator and the first-order wave functions in terms of unperturbed quantities, by means of Eq. (6.22) and Eq. (F.1), respectively. This leads to

$$\begin{aligned}\tilde{\mathcal{X}}^{\mathcal{E}_\alpha k_\gamma \mathcal{E}_\beta} &= \sum_{m\in\mathcal{V}} f_m \langle\tilde{\psi}_m^{\mathcal{E}_\alpha}|\,\hat{H}^{k_\gamma}\,|\tilde{\psi}_m^{\mathcal{E}_\beta}\rangle \\ &= i\sum_{m\in\mathcal{V}}\sum_{l,s\in\mathcal{C}} f_m \frac{\langle\psi_m|\,\hat{r}_\alpha\,|\psi_l\rangle\,\langle\psi_l|\,[\hat{H},\hat{r}_\gamma]\,|\psi_s\rangle\,\langle\psi_s|\,\hat{r}_\beta\,|\psi_m\rangle}{(\epsilon_l-\epsilon_m)(\epsilon_s-\epsilon_m)}.\end{aligned} \tag{F.2}$$

After expanding the commutator and rearranging some terms, we obtain

$$\begin{aligned}\tilde{\mathcal{X}}^{\mathcal{E}_\alpha k_\gamma \mathcal{E}_\beta} =& i\sum_{m\in\mathcal{V}}\sum_{l,s\in\mathcal{C}} f_m \left[\frac{\langle\psi_m|\,\hat{r}_\alpha\,|\psi_l\rangle\,\langle\psi_l|\,\hat{H}\hat{r}_\gamma\,|\psi_s\rangle\,\langle\psi_s|\,\hat{r}_\beta\,|\psi_m\rangle}{(\epsilon_l-\epsilon_m)(\epsilon_s-\epsilon_m)}\right. \\ &\left. -\frac{\langle\psi_m|\,\hat{r}_\alpha\,|\psi_l\rangle\,\langle\psi_l|\,\hat{r}_\gamma\hat{H}\,|\psi_s\rangle\,\langle\psi_s|\,\hat{r}_\beta\,|\psi_m\rangle}{(\epsilon_l-\epsilon_m)(\epsilon_s-\epsilon_m)}\right] \\ =& i\sum_{m\in\mathcal{V}}\sum_{l,s\in\mathcal{C}} f_m(\epsilon_l-\epsilon_s)\frac{\langle\psi_m|\,\hat{r}_\alpha\,|\psi_l\rangle\,\langle\psi_l|\,\hat{r}_\gamma\,|\psi_s\rangle\,\langle\psi_s|\,\hat{r}_\beta\,|\psi_m\rangle}{(\epsilon_l-\epsilon_m)(\epsilon_s-\epsilon_m)}.\end{aligned} \tag{F.3}$$

We now use $\epsilon_l-\epsilon_s=(\epsilon_l-\epsilon_m)+(\epsilon_m-\epsilon_s)$ in order to write

$$\begin{aligned}\tilde{\mathcal{X}}^{\mathcal{E}_\alpha k_\gamma \mathcal{E}_\beta} =& i\sum_{m\in\mathcal{V}}\sum_{l,s\in\mathcal{C}} f_m \left[\frac{\langle\psi_m|\,\hat{r}_\alpha\,|\psi_l\rangle\,\langle\psi_l|\,\hat{r}_\gamma\,|\psi_s\rangle\,\langle\psi_s|\,\hat{r}_\beta\,|\psi_m\rangle}{\epsilon_s-\epsilon_m}\right. \\ &\left. -\frac{\langle\psi_m|\,\hat{r}_\alpha\,|\psi_l\rangle\,\langle\psi_l|\,\hat{r}_\gamma\,|\psi_s\rangle\,\langle\psi_s|\,\hat{r}_\beta\,|\psi_m\rangle}{\epsilon_l-\epsilon_m}\right].\end{aligned} \tag{F.4}$$

Bringing up the definition of the conduction-band projector, $\hat{Q} = \sum_{l\in\mathcal{C}} |\psi_l\rangle \langle\psi_l|$, one immediately obtains the following,

$$\begin{aligned}\tilde{\mathcal{X}}^{\mathcal{E}_\alpha k_\gamma \mathcal{E}_\beta} =& i \sum_{m\in\mathcal{V}} \sum_{l\in\mathcal{C}} f_m \Bigg[\frac{\langle\psi_m| \hat{r}_\alpha \hat{Q} \hat{r}_\gamma |\psi_l\rangle \langle\psi_l| \hat{r}_\beta |\psi_m\rangle}{\epsilon_l - \epsilon_m} \\ & - \frac{\langle\psi_m| \hat{r}_\alpha |\psi_l\rangle \langle\psi_l| \hat{r}_\gamma \hat{Q} \hat{r}_\beta |\psi_m\rangle}{\epsilon_l - \epsilon_m} \Bigg].\end{aligned} \tag{F.5}$$

F.2 COMPUTATION OF THE $\tilde{\mathcal{W}}^{\alpha,\beta\gamma}$ TERM

We now turn our attention to the $\tilde{\mathcal{W}}$ term, which is given by

$$\begin{aligned}\tilde{\mathcal{W}}^{\alpha,\beta\gamma} =& \sum_{m\in\mathcal{V}} f_m \langle \tilde{\psi}^{\mathcal{E}_\alpha}_m | i \psi^{A_\beta}_{m,\gamma} \rangle \\ =& i \sum_{m\in\mathcal{V}} \sum_{l\in\mathcal{C}} f_m \frac{\langle\psi_m| \hat{r}_\alpha |\psi_l\rangle \langle\psi_l| \hat{O}^{\beta\gamma} |\psi_m\rangle}{(\epsilon_m - \epsilon_l)^2},\end{aligned} \tag{F.6}$$

where $\hat{O}^{\beta\gamma}$ represents the perturbing operator of Eq. (D.7) and where we have used, along with the definition of the first-order wave functions given in Eq. (F.1), the following relationship for the wave function response to a long-wavelength vector potential field,

$$\langle \psi_l | \psi^{A_\beta}_{m,\gamma} \rangle = \frac{\langle\psi_l| \hat{O}^{\beta\gamma} |\psi_m\rangle}{\epsilon_m - \epsilon_l}, \qquad m \in \mathcal{V},\, l \in \mathcal{C}. \tag{F.7}$$

The latter can be directly derived from the Sternheimer equation given by Eq. (D.5). We will compute independently the symmetric (S) and antisymmetric (A) parts of the numerator in Eq. (F.7),

$$\langle\psi_l| \hat{O}^{\beta\gamma} |\psi_m\rangle = \frac{1}{2} \langle\psi_l| \left(\hat{O}^{\mathrm{S},\beta\gamma} + \hat{O}^{\mathrm{A},\beta\gamma} \right) |\psi_m\rangle, \tag{F.8}$$

where the operators $\hat{O}^{\mathrm{S},\beta\gamma}$ and $\hat{O}^{\mathrm{A},\beta\gamma}$ are given in Eqs. (D.8) and (D.9), respectively. (Even if not explicitly stated, for the remainder of this appendix one should implicitly assume that $m \in \mathcal{V}$ and $l \in \mathcal{C}$.)

F.2.1 SYMMETRIC PART

We start with the symmetric contribution,

$$\langle\psi_l| \hat{O}^{\mathrm{S},\beta\gamma} |\psi_m\rangle = S_1 + S_2, \tag{F.9}$$

where we have defined

$$\begin{aligned}S_1 =& - \langle\psi_l| [\hat{H}, \hat{r}_\gamma][\hat{P}, \hat{r}_\beta] |\psi_m\rangle - \langle\psi_l| [\hat{H}, \hat{r}_\beta][\hat{P}, \hat{r}_\gamma] |\psi_m\rangle \\ & - \langle\psi_l| [[\hat{H}, \hat{r}_\gamma], \hat{r}_\beta] |\psi_m\rangle\end{aligned} \tag{F.10}$$

and

$$S_2 = \langle\psi_l|\,[\hat{P},\hat{r}_\beta][\hat{H},\hat{r}_\gamma]\,|\psi_m\rangle + \langle\psi_l|\,[\hat{P},\hat{r}_\gamma][\hat{H},\hat{r}_\beta]\,|\psi_m\rangle\,. \tag{F.11}$$

Let us first focus on the S_1 term,

$$\begin{aligned} S_1 = & \underbrace{-\langle\psi_l|\,[\hat{H},\hat{r}_\gamma]\hat{r}_\beta\,|\psi_m\rangle + \langle\psi_l|\,[\hat{H},\hat{r}_\beta]\hat{r}_\gamma\,|\psi_m\rangle - \langle\psi_l|\,[[\hat{H},\hat{r}_\gamma],\hat{r}_\beta]\,|\psi_m\rangle}_{S_1^{(a)}} \\ & \underbrace{-\langle\psi_l|\,[\hat{H},\hat{r}_\gamma]\hat{P}\hat{r}_\beta\,|\psi_m\rangle - \langle\psi_l|\,[\hat{H},\hat{r}_\beta]\hat{P}\hat{r}_\gamma\,|\psi_m\rangle}_{S_2^{(b)}}\,. \end{aligned} \tag{F.12}$$

The $S_1^{(a)}$ term can be simplified as follows,

$$\begin{aligned} S_1^{(a)} &= \langle\psi_l|\,\hat{H}\hat{r}_\beta\hat{r}_\gamma\,|\psi_m\rangle - \langle l|\,\hat{r}_\beta\hat{H}\hat{r}_\gamma\,|\psi_m\rangle + \langle\psi_l|\,\hat{H}\hat{r}_\beta\hat{r}_\gamma\,|\psi_m\rangle \\ &\quad - \langle\psi_l|\,\hat{r}_\gamma\hat{H}\hat{r}_\beta\,|\psi_m\rangle - \langle\psi_l|\,[\hat{H},\hat{r}_\gamma]\hat{r}_\beta\,|\psi_m\rangle + \langle\psi_l|\,\hat{r}_\beta[\hat{H},\hat{r}_\gamma]\,|\psi_m\rangle \\ &= \langle\psi_l|\,\hat{H}\hat{r}_\gamma\hat{r}_\beta\,|\psi_m\rangle - \langle\psi_l|\,\hat{r}_\gamma\hat{r}_\beta\hat{H}\,|\psi_m\rangle \\ &= \langle\psi_l|\,[\hat{H},\hat{r}_\gamma\hat{r}_\beta]\,|\psi_m\rangle\,. \end{aligned} \tag{F.13}$$

We can simplify the $S_1^{(b)}$ term in a similar fashion, where only two terms survive, as we have a conduction-band state on the left,

$$\begin{aligned} S_1^{(b)} &= \langle\psi_l|\,[\hat{P},\hat{r}_\beta][\hat{H},\hat{r}_\gamma]\,|\psi_m\rangle + \langle\psi_l|\,[\hat{P},\hat{r}_\gamma][\hat{H},\hat{r}_\beta]\,|\psi_m\rangle \\ &= -\langle\psi_l|\,\hat{r}_\beta\hat{P}[\hat{H},\hat{r}_\gamma]\,|\psi_m\rangle - \langle\psi_l|\,\hat{r}_\gamma\hat{P}[\hat{H},\hat{r}_\beta]\,|\psi_m\rangle\,. \end{aligned} \tag{F.14}$$

Collecting all terms, $S_1 + S_2$, we obtain

$$\begin{aligned} \langle\psi_l|\,\hat{O}^{\mathrm{S},\beta\gamma}\,|\psi_m\rangle &= \langle\psi_l|\,[\hat{H},\hat{r}_\beta\hat{r}_\gamma]\,|\psi_m\rangle - \langle\psi_l|\,[\hat{H},\hat{r}_\gamma]\hat{P}\hat{r}_\beta\,|\psi_m\rangle - \langle\psi_l|\,[\hat{H},\hat{r}_\beta]\hat{P}\hat{r}_\gamma\,|\psi_m\rangle \\ &\quad - \langle\psi_l|\,\hat{r}_\beta\hat{P}[\hat{H},\hat{r}_\gamma]\,|\psi_m\rangle - \langle\psi_l|\,\hat{r}_\gamma\hat{P}[\hat{H},\hat{r}_\beta]\,|\psi_m\rangle \\ &= \langle\psi_l|\,[\hat{H},\hat{r}_\beta\hat{r}_\gamma]\,|\psi_m\rangle - \langle\psi_l|\,\hat{H}\hat{r}_\gamma\hat{P}\hat{r}_\beta\,|\psi_m\rangle + \cancel{\langle\psi_l|\,\hat{r}_\gamma\hat{H}\hat{P}\hat{r}_\beta\,|\psi_m\rangle} \\ &\quad - \langle\psi_l|\,\hat{H}\hat{r}_\beta\hat{P}\hat{r}_\gamma\,|\psi_m\rangle + \cancel{\langle\psi_l|\,\hat{r}_\beta\hat{H}\hat{P}\hat{r}_\gamma\,|\psi_m\rangle} - \cancel{\langle\psi_l|\,\hat{r}_\beta\hat{P}\hat{H}\hat{r}_\gamma\,|\psi_m\rangle} \\ &\quad + \langle\psi_l|\,\hat{r}_\beta\hat{P}\hat{r}_\gamma\hat{H}\,|\psi_m\rangle - \cancel{\hat{r}_\gamma\hat{P}\hat{H}\hat{r}_\beta\,|\psi_m\rangle} + \langle\psi_l|\,\hat{r}_\gamma\hat{P}\hat{r}_\beta\hat{H}\,|\psi_m\rangle \\ &= \langle\psi_l|\,[\hat{H},\hat{r}_\beta\hat{r}_\gamma]\,|\psi_m\rangle - \langle\psi_l|\,\hat{H}\hat{r}_\gamma\hat{P}\hat{r}_\beta\,|\psi_m\rangle - \langle\psi_l|\,\hat{H}\hat{r}_\beta\hat{P}\hat{r}_\gamma\,|\psi_m\rangle \\ &\quad + \langle\psi_l|\,\hat{r}_\beta\hat{P}\hat{r}_\gamma\hat{H}\,|\psi_m\rangle + \langle\psi_l|\,\hat{r}_\gamma\hat{P}\hat{r}_\beta\hat{H}\,|\psi_m\rangle\,. \end{aligned} \tag{F.15}$$

Therefore, the symmetric part yields a purely *geometric* contribution to the wave function response, in the sense that there are only contributions coming from ground-state wave functions,

$$\langle\psi_l|\,\hat{O}^{\mathrm{S},\beta\gamma}\,|\psi_m\rangle = (\epsilon_l - \epsilon_m)\,\langle\psi_l|\left(\hat{r}_\beta\hat{r}_\gamma - \hat{r}_\beta\hat{P}\hat{r}_\gamma - \hat{r}_\gamma\hat{P}\hat{r}_\beta\right)|\psi_m\rangle\,. \tag{F.16}$$

F.2.2 ANTISYMMETRIC PART

Let's now discuss the antisymmetric contribution of Eq. (F.8). We start with the following,

$$\begin{aligned} \langle\psi_l|\,\hat{O}^{\mathrm{A},\beta\gamma}\,|\psi_m\rangle = & \underbrace{-\langle\psi_l|\,[\hat{H},\hat{r}_\gamma][\hat{P},\hat{r}_\beta]\,|\psi_m\rangle + \langle\psi_l|\,[\hat{H},\hat{r}_\beta][\hat{P},\hat{r}_\gamma]\,|\psi_m\rangle}_{A_1} \\ & + \underbrace{\langle\psi_l|\,[\hat{P},\hat{r}_\gamma][\hat{H},\hat{r}_\beta]\,|\psi_m\rangle - \langle\psi_l|\,[\hat{P},\hat{r}_\beta][\hat{H},\hat{r}_\gamma]\,|\psi_m\rangle}_{A_2}\,. \end{aligned} \tag{F.17}$$

Regarding the A_1 term, we have

$$\begin{aligned} A_1 =& - \langle\psi_l| \left(\hat{H}\hat{r}_\gamma - \hat{r}_\gamma\hat{H}\right)\left(\hat{P}\hat{r}_\beta - \hat{r}_\beta\hat{P}\right)|\psi_m\rangle + \langle\psi_l| \left(\hat{H}\hat{r}_\beta - \hat{r}_\beta\hat{H}\right)\left(\hat{P}\hat{r}_\gamma - \hat{r}_\gamma\hat{P}\right)|\psi_m\rangle \\ =& - \langle\psi_l| \hat{H}\hat{r}_\gamma\hat{P}\hat{r}_\beta |\psi_m\rangle + \cancel{\langle\psi_l| \hat{H}\hat{r}_\gamma\hat{r}_\beta |\psi_m\rangle} + \langle\psi_l| \hat{r}_\gamma\hat{H}\hat{P}\hat{r}_\beta |\psi_m\rangle - \langle\psi_l| \hat{r}_\gamma\hat{H}\hat{r}_\beta |\psi_m\rangle \\ & + \langle\psi_l| \hat{H}\hat{r}_\beta\hat{P}\hat{r}_\gamma |\psi_m\rangle - \cancel{\langle\psi_l| \hat{H}\hat{r}_\beta\hat{r}_\gamma |\psi_m\rangle} - \langle\psi_l| \hat{r}_\beta\hat{H}\hat{P}\hat{r}_\gamma |\psi_m\rangle + \langle\psi_l| \hat{r}_\beta\hat{H}\hat{r}_\gamma |\psi_m\rangle \\ =& - \epsilon_l \langle\psi_l| \hat{r}_\gamma\hat{P}\hat{r}_\beta |\psi_m\rangle + \langle\psi_l| \hat{r}_\gamma\hat{H}\hat{P}\hat{r}_\beta |\psi_m\rangle - \langle\psi_l| \hat{r}_\gamma\hat{H}\hat{r}_\beta |\psi_m\rangle \\ & + \epsilon_m \langle\psi_l| \hat{r}_\beta\hat{P}\hat{r}_\gamma |\psi_m\rangle - \langle\psi_l| \hat{r}_\beta\hat{H}\hat{P}\hat{r}_\gamma |\psi_m\rangle + \langle\psi_l| \hat{r}_\beta\hat{H}\hat{r}_\gamma |\psi_m\rangle . \end{aligned} \tag{F.18}$$

Let's work through A_2. Notice that some terms identically vanish, as we have a conduction-band state on the left,

$$\begin{aligned} A_2 =& \langle\psi_l| [\hat{P},\hat{r}_\gamma][\hat{H},\hat{r}_\beta] |\psi_m\rangle - \langle\psi_l| [\hat{P},\hat{r}_\beta][\hat{H},\hat{r}_\gamma] |\psi_m\rangle \\ =& \langle\psi_l| \left(\hat{P}\hat{r}_\gamma - \hat{r}_\gamma\hat{P}\right)\left(\hat{H}\hat{r}_\beta - \hat{r}_\beta\hat{H}\right)|\psi_m\rangle - \langle\psi_l| \left(\hat{P}\hat{r}_\beta - \hat{r}_\beta\hat{P}\right)\left(\hat{H}\hat{r}_\gamma - \hat{r}_\gamma\hat{H}\right)|\psi_m\rangle \\ =& - \langle\psi_l| \hat{r}_\gamma\hat{P}\hat{H}\hat{r}_\beta |\psi_m\rangle + \langle\psi_l| \hat{r}_\gamma\hat{P}\hat{r}_\beta\hat{H} |\psi_m\rangle + \langle\psi_l| \hat{r}_\beta\hat{P}\hat{H}\hat{r}_\gamma |\psi_m\rangle \\ & - \langle\psi_l| \hat{r}_\beta\hat{P}\hat{r}_\gamma\hat{H} |\psi_m\rangle \\ =& - \langle\psi_l| \hat{r}_\gamma\hat{P}\hat{H}\hat{r}_\beta |\psi_m\rangle + \epsilon_m \langle\psi_l| \hat{r}_\gamma\hat{P}\hat{r}_\beta |\psi_m\rangle + \langle\psi_l| \hat{r}_\beta\hat{P}\hat{H}\hat{r}_\gamma |\psi_m\rangle \\ & - \epsilon_m \langle\psi_l| \hat{r}_\beta\hat{P}\hat{r}_\gamma |\psi_m\rangle . \end{aligned} \tag{F.19}$$

Everything together,

$$\begin{aligned} \langle\psi_l| \hat{O}^{\mathrm{A},\beta\gamma} |\psi_m\rangle =& \left(\epsilon_l - \epsilon_m\right) \langle\psi_l| \left(\hat{r}_\beta\hat{P}\hat{r}_\gamma - \hat{r}_\gamma\hat{P}\hat{r}_\beta\right)|\psi_m\rangle \\ & + \langle\psi_l| \left(\hat{r}_\beta\hat{H}\hat{r}_\gamma - \hat{r}_\gamma\hat{H}\hat{r}_\beta\right)|\psi_m\rangle . \end{aligned} \tag{F.20}$$

For convenience, we shall write the second term as

$$\begin{aligned} \langle\psi_l| \left(\hat{r}_\beta\hat{H}\hat{r}_\gamma - \hat{r}_\gamma\hat{H}\hat{r}_\beta\right)|\psi_m\rangle =& \langle\psi_l| \left(\hat{r}_\beta[\hat{H},\hat{r}_\gamma] - \hat{r}_\gamma[\hat{H},\hat{r}_\beta]\right)|\psi_m\rangle \\ =& - i \langle\psi_l| \left(\hat{r}_\beta\hat{v}_\gamma - \hat{r}_\gamma\hat{v}_\beta\right)|\psi_m\rangle , \end{aligned} \tag{F.21}$$

where we have used $\hat{v}_\alpha = i[\hat{H},\hat{r}_\alpha]$. Therefore, the antisymmetric contribution reads as

$$\langle\psi_l| \hat{O}^{\mathrm{A},\beta\gamma} |\psi_m\rangle = -i \langle\psi_l| \left(\hat{r}_\beta\hat{v}_\gamma - \hat{r}_\gamma\hat{v}_\beta\right)|\psi_m\rangle + \left(\epsilon_l - \epsilon_m\right) \langle\psi_l| \left(\hat{r}_\beta\hat{P}\hat{r}_\gamma - \hat{r}_\gamma\hat{P}\hat{r}_\beta\right)|\psi_m\rangle . \tag{F.22}$$

F.2.3 SYMMETRIC + ANTISYMMETRIC CONTRIBUTIONS

We can now compute the full $\tilde{\mathcal{W}}^{\alpha,\beta\gamma}$ tensor given by Eq. (F.6),

$$\begin{aligned} \tilde{\mathcal{W}}^{\alpha,\beta\gamma} =& \frac{i}{2} \sum_{m\in\mathcal{V}} \sum_{l\in\mathcal{C}} f_m \frac{\langle\psi_m| \hat{r}_\alpha |\psi_l\rangle \ \langle\psi_l| \left(\hat{O}^{\mathrm{S},\beta\gamma} + \hat{O}^{\mathrm{A},\beta\gamma}\right)|\psi_m\rangle}{(\epsilon_m - \epsilon_l)^2} \\ =& \frac{i}{2} \sum_{m\in\mathcal{V}} \sum_{l\in\mathcal{C}} f_m \frac{\langle\psi_m| \hat{r}_\alpha |\psi_l\rangle}{(\epsilon_m - \epsilon_l)^2} \Bigg[\left(\epsilon_l - \epsilon_m\right) \langle\psi_l| \left(\hat{r}_\beta\hat{r}_\gamma - \cancel{\hat{r}_\beta\hat{P}\hat{r}_\gamma} - \hat{r}_\gamma\hat{P}\hat{r}_\beta\right)|\psi_m\rangle \\ & + \left(\epsilon_l - \epsilon_m\right) \langle\psi_l| \left(\cancel{\hat{r}_\beta\hat{P}\hat{r}_\gamma} - \hat{r}_\gamma\hat{P}\hat{r}_\beta\right)|\psi_m\rangle - i \langle\psi_l| \left(\hat{r}_\beta\hat{v}_\gamma - \hat{r}_\gamma\hat{v}_\beta\right)|\psi_m\rangle \Bigg] . \end{aligned} \tag{F.23}$$

In the end, we get

$$\begin{aligned}\tilde{\mathcal{W}}^{\alpha,\beta\gamma} =& \frac{i}{2}\sum_{m\in\mathcal{V}}\sum_{l\in\mathcal{C}} f_m \frac{\langle\psi_m|\,\hat{r}_\alpha\,|\psi_l\rangle}{(\epsilon_l-\epsilon_m)}\,\langle\psi_l|\left(\hat{r}_\beta\hat{r}_\gamma - 2\hat{r}_\gamma\hat{P}\hat{r}_\beta\right)|\psi_m\rangle \\ &+ \frac{1}{2}\sum_{m\in\mathcal{V}}\sum_{l\in\mathcal{C}} f_m \frac{\langle\psi_m|\,\hat{r}_\alpha\,|\psi_l\rangle}{(\epsilon_l-\epsilon_m)^2}\,\langle\psi_l|\left(\hat{r}_\beta\hat{v}_\gamma - \hat{r}_\gamma\hat{v}_\beta\right)|\psi_m\rangle .\end{aligned} \tag{F.24}$$

F.3 COMPUTATION OF THE $\tilde{\eta}_{\alpha\beta\gamma}$ TENSOR

We now use the previous results, Eq. (F.4) and Eq. (F.24), in order to compute $\tilde{\eta}_{\alpha\beta\gamma}$,

$$\begin{aligned}\tilde{\eta}_{\alpha\beta\gamma} &= -\frac{4\pi}{\Omega}2\,\mathrm{Im}\left[\tilde{\mathcal{X}}^{\mathcal{E}_\alpha k_\gamma \mathcal{E}_\beta} + \tilde{\mathcal{W}}^{\alpha,\beta\gamma} + \left(\tilde{\mathcal{W}}^{\beta,\alpha\gamma}\right)^*\right] \\ &= -\frac{4\pi}{\Omega}\,\mathrm{Im}\sum_{m\in\mathcal{V}}\sum_{l\in\mathcal{C}} f_m\,\tilde{\eta}^{ml}_{\alpha\beta\gamma},\end{aligned} \tag{F.25}$$

where we have defined

$$\begin{aligned}\tilde{\eta}^{ml}_{\alpha\beta\gamma} =& 2i\frac{\langle\psi_m|\,\hat{r}_\alpha\hat{Q}\hat{r}_\gamma\,|\psi_l\rangle\,\langle\psi_l|\,\hat{r}_\beta\,|\psi_m\rangle}{\epsilon_l-\epsilon_m} - 2i\frac{\langle\psi_m|\,\hat{r}_\alpha\,|\psi_l\rangle\,\langle\psi_l|\,\hat{r}_\gamma\hat{Q}\hat{r}_\beta\,|\psi_m\rangle}{\epsilon_l-\epsilon_m} \\ &+ i\frac{\langle\psi_m|\,\hat{r}_\alpha\,|\psi_l\rangle\,\langle\psi_l|\left(\hat{r}_\beta\hat{r}_\gamma - 2\hat{r}_\gamma\hat{P}\hat{r}_\beta\right)|\psi_m\rangle}{\epsilon_l-\epsilon_m} \\ &+ \frac{\langle\psi_m|\,\hat{r}_\alpha\,|\psi_l\rangle\,\langle\psi_l|\left(\hat{r}_\beta\hat{v}_\gamma - \hat{r}_\gamma\hat{v}_\beta\right)|\psi_m\rangle}{(\epsilon_l-\epsilon_m)^2} \\ &- i\frac{\langle\psi_m|\left(\hat{r}_\alpha\hat{r}_\gamma - 2\hat{r}_\alpha\hat{P}\hat{r}_\gamma\right)|\psi_l\rangle\,\langle\psi_l|\,\hat{r}_\beta\,|\psi_m\rangle}{\epsilon_l-\epsilon_m} \\ &+ \frac{\langle\psi_m|\left(\hat{r}_\alpha\hat{v}_\gamma - \hat{r}_\gamma\hat{v}_\alpha\right)|\psi_l\rangle\,\langle\psi_l|\,\hat{r}_\beta\,|\psi_m\rangle}{(\epsilon_l-\epsilon_m)^2}.\end{aligned} \tag{F.26}$$

We now make use of the identity $\hat{P}+\hat{Q}=\mathbb{1}$ to simplify some terms,

$$\begin{aligned}\tilde{\eta}^{ml}_{\alpha\beta\gamma} =& \frac{1}{(\epsilon_l-\epsilon_m)^2}\Big[\langle\psi_m|\,\hat{r}_\alpha\,|\psi_l\rangle\,\langle\psi_l|\left(\hat{r}_\beta\hat{v}_\gamma - \hat{r}_\gamma\hat{v}_\beta\right)|\psi_m\rangle \\ &\qquad + \langle\psi_m|\left(\hat{r}_\alpha\hat{v}_\gamma - \hat{r}_\gamma\hat{v}_\alpha\right)|\psi_l\rangle\,\langle\psi_l|\,\hat{r}_\beta\,|\psi_m\rangle\Big] \\ &+ \frac{i}{(\epsilon_l-\epsilon_m)}\left[\langle\psi_m|\,\hat{r}_\alpha\hat{r}_\gamma\,|\psi_l\rangle\,\langle\psi_l|\,\hat{r}_\beta\,|\psi_m\rangle - \langle\psi_m|\,\hat{r}_\alpha\,|\psi_l\rangle\,\langle\psi_l|\,\hat{r}_\gamma\hat{r}_\beta\,|\psi_m\rangle\right].\end{aligned} \tag{F.27}$$

As a final step, we use the fact that $\mathrm{Im}\big[a-ib\big]=-b$ and $\mathrm{Im}\big[i(a-ib)\big]=a$, in order to obtain the following expression for the natural optical activity in finite samples,

$$\begin{aligned}\tilde{\eta}^{ml}_{\alpha\beta\gamma} =& \frac{1}{(\epsilon_l-\epsilon_m)^2}\Big[\langle\psi_m|\,\hat{r}_\alpha\,|\psi_l\rangle\,\langle\psi_l|\left(\hat{r}_\beta\hat{v}_\gamma - \hat{r}_\gamma\hat{v}_\beta\right)|\psi_m\rangle \\ &\qquad - \langle\psi_m|\,\hat{r}_\beta\,|\psi_l\rangle\,\langle\psi_l|\left(\hat{r}_\alpha\hat{v}_\gamma - \hat{r}_\gamma\hat{v}_\alpha\right)|\psi_m\rangle\Big] \\ &+ \frac{i}{\epsilon_l-\epsilon_m}\Big[\langle\psi_m|\,\hat{r}_\beta\,|\psi_l\rangle\,\langle\psi_l|\,\hat{r}_\alpha\hat{r}_\gamma\,|\psi_m\rangle - \langle\psi_m|\,\hat{r}_\alpha\,|\psi_l\rangle\,\langle\psi_l|\,\hat{r}_\beta\hat{r}_\gamma\,|\psi_m\rangle\Big],\end{aligned} \tag{F.28}$$

which is Eq. (6.27) of the main text.

BIBLIOGRAPHY

[1] L. D. Barron, *Molecular light scattering and optical activity* (Cambridge University Press, 2009).

[2] E. U. Condon, "Theories of optical rotatory power," Rev. Mod. Phys. **9**, 432–457 (1937).

[3] P. S. Halasyamani and K. R. Poeppelmeier, "Noncentrosymmetric oxides," Chem. Mater. **10**, 2753–2769 (1998).

[4] L. D. Landau and E. M. Lifshitz, *Electrodynamics of continuous media, landau and lifshitz course of theoretical physics, vol. 8* (Pergamon Press, 1984).

[5] P. J. Stephens, F. J. Devlin, J. R. Cheeseman, and M. J. Frisch, "Calculation of optical rotation using density functional theory," J. Phys. Chem. A **105**, 5356–5371 (2001).

[6] J. Autschbach, T. Ziegler, S. J. A. van Gisbergen, and E. J. Baerends, "Chiroptical properties from time-dependent density functional theory. I. circular dichroism spectra of organic molecules," J. Chem. Phys. **116**, 6930–6940 (2002).

[7] J. Autschbach, S. Patchkovskii, T. Ziegler, S. J. A. van Gisbergen, and E. Jan Baerends, "Chiroptical properties from time-dependent density functional theory. II. optical rotations of small to medium sized organic molecules," J. Chem. Phys. **117**, 581–592 (2002).

[8] P. L. Polavarapu, "Ab initio molecular optical rotations and absolute configurations," Mol. Phys. **91**, 551–554 (1997).

[9] B. C. Mort and J. Autschbach, "Magnitude of zero-point vibrational corrections to optical rotation in rigid organic molecules: a time-dependent density functional study," J. Phys. Chem. A **109**, 8617–8623 (2005).

[10] J. Jerphagnon and D. S. Chemla, "Optical activity of crystals," J. Chem. Phys. **65**, 1522–1529 (1976).

[11] S. Ades and C. H. Champness, "Optical activity of tellurium to 20 µm," J. Opt. Soc. Am. **65**, 217–218 (1975).

[12] K Stadnicka, A. Glazer, and J. Moxon, "The structural chirality and optical activity of α-LiIO3," J. Appl. Cryst. **18**, 237–240 (1985).

[13] S. Fukuda, T. Shiosaki, and A. Kawabata, "Infrared optical activity in tellurium," Phys. Status Solidi B **68**, K107–K110.

[14] K. C. Nomura, "Optical activity in tellurium," Phys. Rev. Lett. **5**, 500–501 (1960).

[15] G. W. Day, "Linear and nonlinear optical properties of trigonal selenium," Appl. Phys. Lett. **18**, 347–349 (1971).

[16] V. Devarajan and A. M. Glazer, "Theory and computation of optical rotatory power in inorganic crystals," Acta Crystallogr. A **42**, 560–569 (1986).

[17] L. Trifunovic, S. Ono, and H. Watanabe, “Geometric orbital magnetization in adiabatic processes,” Phys. Rev. B **100**, 054408 (2019).

[18] D. Ceresoli, R. Marchetti, and E. Tosatti, “Electron-corrected lorentz forces in solids and molecules in a magnetic field,” Phys. Rev. B **75**, 161101 (2007).

[19] T. Qin, J. Zhou, and J. Shi, “Berry curvature and the phonon hall effect,” Phys. Rev. B **86**, 104305 (2012).

[20] D. M. Juraschek and N. A. Spaldin, “Orbital magnetic moments of phonons,” Phys. Rev. Mater. **3**, 064405 (2019).

[21] D. M. Juraschek, M. Fechner, A. V. Balatsky, and N. A. Spaldin, “Dynamical multiferroicity,” Phys. Rev. Mater. **1**, 014401 (2017).

[22] K. Sun, Z. Gao, and J.-S. Wang, “Phonon hall effect with first-principles calculations,” Phys. Rev. B **103**, 214301 (2021).

[23] S. M. Kogan, “Piezoelectric effect during inhomogeneous deformation and acoustic scattering of carriers in crystals,” Soviet Physics-Solid State **5**, 2069–2070 (1964).

[24] X. Liang, S. Hu, and S. Shen, “Nanoscale mechanical energy harvesting using piezoelectricity and flexoelectricity,” SMS **26**, 035050 (2017).

[25] S. Zhang, K. Liu, M. Xu, and S. Shen, “A curved resonant flexoelectric actuator,” Appl. Phys. Lett. **111**, 082904 (2017).

[26] X Yan, W. Huang, S. Kwon, S. Yang, X. Jiang, and F. Yuan, “Design of a curvature sensor using a flexoelectric material,” in Sensors and smart structures technologies for civil, mechanical, and aerospace systems, Vol. 8692 (SPIE, 2013), pp. 193–202.

[27] P. W. Anderson and E. I. Blount, “Symmetry considerations on martensitic transformations: “ferroelectric” metals?” Phys. Rev. Lett. **14**, 217–219 (1965).

[28] Y. Shi, Y. Guo, X. Wang, A. J. Princep, D. Khalyavin, P. Manuel, Y. Michiue, A. Sato, K. Tsuda, S. Yu, et al., “A ferroelectric-like structural transition in a metal,” Nat. Mater. **12**, 1024–1027 (2013).

[29] C. Ma and K. Jin, “Design strategy for ferroelectric-based polar metals with dimensionality-tunable electronic states,” Science China Physics, Mechanics & Astronomy **61**, 97011 (2018).

[30] S. Yip, “Noncentrosymmetric superconductors,” Annu. Rev. Condens. Mat. Phys. **5**, 15–33 (2014).

[31] E. Bauer and M. Sigrist, *Non-centrosymmetric superconductors: introduction and overview*, Vol. 847 (Springer Science & Business Media, 2012).

[32] C.-K. Lu and S. Yip, “Spin current in topologically trivial and nontrivial noncentrosymmetric superconductors,” Phys. Rev. B **82**, 104501 (2010).

[33] N. A. Benedek and T. Birol, “*Ferroelectric* metals reexamined: fundamental mechanisms and design considerations for new materials,” J. Mat. Chem. C **4**, 4000–4015 (2016).

[34] S. Bhowal and N. A. Spaldin, “Polar metals: principles and prospects,” Annu. Rev. Mater. Res. **53**, 53–79 (2023).

[35] W. X. Zhou and A. Ariando, “Review on ferroelectric/polar metals,” JJAP **59**, SI0802 (2020).

[36] Z. Fei, W. Zhao, T. A. Palomaki, B. Sun, M. K. Miller, Z. Zhao, J. Yan, X. Xu, and D. H. Cobden, “Ferroelectric switching of a two-dimensional metal,” Nature **560**, 336–339 (2018).

[37] H. Lu, C.-W. Bark, D. E. de los Ojos, J. Alcala, C. B. Eom, G. Catalan, and A. Gruverman, “Mechanical writing of ferroelectric polarization,” Science **336**, 59–61 (2012).

[38] J. Očenášek, Jiří, H. Lu, C. W. Bark, C. B. Eom, J. Alcalá, G. Catalan, and A. Gruverman, “Nanomechanics of flexoelectric switching,” Phys. Rev. B **92**, 035417 (2015).

[39] G. Catalan, “Metal poles around the bend,” Nature Physics **20**, 358–359 (2024).

[40] X. Gonze, D. C. Allan, and M. P. Teter, “Dielectric tensor, effective charges, and phonons in α-quartz by variational density-functional perturbation theory,” Phys. Rev. Lett. **68**, 3603–3606 (1992).

[41] M. Royo and M. Stengel, “First-principles theory of spatial dispersion: dynamical quadrupoles and flexoelectricity,” Phys. Rev. X **9**, 021050 (2019).

[42] X. Gonze, B. Amadon, G. Antonius, F. Arnardi, L. Baguet, J.-M. Beuken, J. Bieder, F. Bottin, J. Bouchet, E. Bousquet, et al., “The ABINIT project: Impact, environment and recent developments,” Comput. Phys. Commun. **248**, 107042 (2020).

[43] X. Gonze, B. Amadon, P.-M. Anglade, J.-M. Beuken, F. Bottin, P. Boulanger, F. Bruneval, D. Caliste, R. Caracas, M. Côté, et al., “ABINIT: First-principles approach to material and nanosystem properties,” Comput. Phys. Commun. **180**, 2582–2615 (2009).

[44] M. Royo and M. Stengel, “Lattice-mediated bulk flexoelectricity from first principles,” Phys. Rev. B **105**, 064101 (2022).

[45] M. Springolo, M. Royo, and M. Stengel, “Direct and converse flexoelectricity in two-dimensional materials,” Phys. Rev. Lett. **127**, 216801 (2021).

[46] M. Springolo, M. Royo, and M. Stengel, “In-plane flexoelectricity in two-dimensional D_{3d} crystals,” Phys. Rev. Lett. **131**, 236203 (2023).

[47] M. C. Tam, N. J. Russ, and T. D. Crawford, “Coupled cluster calculations of optical rotatory dispersion of (s)-methyloxirane,” J. Chem. Phys. **121**, 3550–3557 (2004).

[48] P. Norman, K. Ruud, and T. Helgaker, “Density-functional theory calculations of optical rotatory dispersion in the nonresonant and resonant frequency regions,” J. Chem. Phys. **120**, 5027–5035 (2004).

[49] H. Zhong, Z. H. Levine, D. C. Allan, and J. W. Wilkins, “Band-theoretic calculations of the optical-activity tensor of α-quartz and trigonal Se,” Phys. Rev. B **48**, 1384–1403 (1993).

[50] H. Zhong, Z. H. Levine, D. C. Allan, and J. W. Wilkins, “Optical activity of selenium: a nearly first-principles calculation,” Phys. Rev. Lett. **69**, 379–382 (1992).

[51] A. Malashevich and I. Souza, “Band theory of spatial dispersion in magnetoelectrics,” Phys. Rev. B **82**, 245118 (2010).

[52] Óscar Pozo Ocaña and I. Souza, “Multipole theory of optical spatial dispersion in crystals,” SciPost Phys. **14**, 118 (2023).

[53] X. Wang and Y. Yan, “Optical activity of solids from first principles,” Phys. Rev. B **107**, 045201 (2023).

[54] S. S. Tsirkin, P. A. Puente, and I. Souza, “Gyrotropic effects in trigonal tellurium studied from first principles,” Phys. Rev. B **97**, 035158 (2018).

[55] L. Jönsson, Z. H. Levine, and J. W. Wilkins, “Large local-field corrections in optical rotatory power of quartz and selenium,” Phys. Rev. Lett. **76**, 1372–1375 (1996).

[56] W. Flygare, “Magnetic interactions in molecules and an analysis of molecular electronic charge distribution from magnetic parameters,” Chem. Rev. **74**, 653–687 (1974).

[57] S. M. Cybulski and D. M. Bishop, “Calculation of magnetic properties. VI. Electron correlated nuclear shielding constants and magnetizabilities for thirteen small molecules,” J. Chem. Phys **106**, 4082–4090 (1997).

[58] D. Ceresoli and E. Tosatti, “Berry-phase calculation of magnetic screening and rotational g factor in molecules and solids,” Phys. Rev. Lett. **89**, 116402 (2002).

[59] D. Ceresoli, “Berry phase calculations of the rotational and pseudorotational g factor in molecules and solids,” PhD thesis (Scuola Internazionale Superiore di Studi Avanzati, 2002).

[60] M. V. Berry, “Quantal phase factors accompanying adiabatic changes,” Proc. R. Soc. A: Math. Phys. Eng. **392**, 45–57 (1984).

[61] D. Ceresoli, T. Thonhauser, D. Vanderbilt, and R. Resta, “Orbital magnetization in crystalline solids: Multi-band insulators, Chern insulators, and metals,” Phys. Rev. B **74**, 024408 (2006).

[62] J. Shi, G. Vignale, D. Xiao, and Q. Niu, “Quantum theory of orbital magnetization and its generalization to interacting systems,” Phys. Rev. Lett. **99**, 197202 (2007).

[63] R. Resta, “Electrical polarization and orbital magnetization: the modern theories,” J. Condens. Matter Phys. **22**, 123201 (2010).

[64] W. Cai and G. Galli, “*Ab Initio* calculations in a uniform magnetic field using periodic supercells,” Phys. Rev. Lett. **92**, 186402 (2004).

[65] E. Lee, W. Cai, and G. A. Galli, “Electronic structure calculations in a uniform magnetic field using periodic supercells,” J. Comput. Phys. **226**, 1310–1331 (2007).

[66] S. G. Balasubramani, G. P. Chen, S. Coriani, M. Diedenhofen, M. S. Frank, Y. J. Franzke, F. Furche, R. Grotjahn, M. E. Harding, C. Hättig, et al., "TURBOMOLE: Modular program suite for *ab initio* quantum-chemical and condensed-matter simulations," J. Chem. Phys. **152**, 184107 (2020).

[67] D. B. Williams-Young, A. Petrone, S. Sun, T. F. Stetina, P. Lestrange, C. E. Hoyer, D. R. Nascimento, L. Koulias, A. Wildman, J. Kasper, et al., "The Chronus quantum software package," Wiley Interdiscip. Rev. Comput. Mol. Sci., e1436 (2019).

[68] R. M. Martin, *Electronic structure: basic theory and practical methods* (Cambridge University Press, 2004).

[69] D. S. Sholl and J. A. Steckel, *Density functional theory: a practical introduction* (John Wiley & Sons, 2022).

[70] E. Engel, *Density functional theory* (Springer, 2011).

[71] M. C. Payne, M. P. Teter, D. C. Allan, T. A. Arias, and J. D. Joannopoulos, "Iterative minimization techniques for ab initio total-energy calculations: molecular dynamics and conjugate gradients," Rev. Mod. Phys. **64**, 1045–1097 (1992).

[72] P. Hohenberg and W. Kohn, "Inhomogeneous electron gas," Phys. Rev. **136**, B864–B871 (1964).

[73] W. Kohn and L. J. Sham, "Self-consistent equations including exchange and correlation effects," Phys. Rev. **140**, A1133–A1138 (1965).

[74] X. Gonze, "First-principles responses of solids to atomic displacements and homogeneous electric fields: implementation of a conjugate-gradient algorithm," Phys. Rev. B **55**, 10337–10354 (1997).

[75] X. Gonze, "Perturbation expansion of variational principles at arbitrary order," Phys. Rev. A **52**, 1086–1095 (1995).

[76] X. Gonze, "Adiabatic density-functional perturbation theory," Phys. Rev. A **52**, 1096–1114 (1995).

[77] X. Gonze and C. Lee, "Dynamical matrices, Born effective charges, dielectric permittivity tensors, and interatomic force constants from density-functional perturbation theory," Phys. Rev. B **55**, 10355–10368 (1997).

[78] M. Born and R. Oppenheimer, "Zur quantentheorie der molekeln," Ann. Phys. **389**, 457–484 (1927).

[79] L. H. Thomas, "The calculation of atomic fields," Math. Proc. Camb. Philos. Soc. **23**, 542–548 (1927).

[80] D. M. Ceperley and B. J. Alder, "Ground state of the electron gas by a stochastic method," Phys. Rev. Lett. **45**, 566–569 (1980).

[81] J. P. Perdew and Y. Wang, "Accurate and simple analytic representation of the electron-gas correlation energy," Phys. Rev. B **45**, 13244–13249 (1992).

[82] J. P. Perdew, K. Burke, and M. Ernzerhof, "Generalized gradient approximation made simple," Phys. Rev. Lett. **77**, 3865–3868 (1996).

[83] M. Methfessel and A. T. Paxton, "High-precision sampling for Brillouin-zone integration in metals," Phys. Rev. B **40**, 3616–3621 (1989).

[84] N. Marzari, D. Vanderbilt, A. De Vita, and M. C. Payne, "Thermal contraction and disordering of the Al(110) surface," Phys. Rev. Lett. **82**, 3296–3299 (1999).

[85] D. J. Singh and L. Nordstrom, *Planewaves, pseudopotentials, and the LAPW method* (Springer Science & Business Media, 2006).

[86] D. R. Hamann, M. Schlüter, and C. Chiang, "Norm-conserving pseudopotentials," Phys. Rev. Lett. **43**, 1494–1497 (1979).

[87] L. Kleinman and D. M. Bylander, "Efficacious form for model pseudopotentials," Phys. Rev. Lett. **48**, 1425–1428 (1982).

[88] D. R. Hamann, "Optimized norm-conserving Vanderbilt pseudopotentials," Phys. Rev. B **88**, 085117 (2013).

[89] S. Wei and M. Y. Chou, "Phonon dispersions of silicon and germanium from first-principles calculations," Phys. Rev. B **50**, 2221–2226 (1994).

[90] J. J. Sakurai and E. D. Commins, *Modern quantum mechanics* (Cambridge University Press, 2020).

[91] X. Gonze and J.-P. Vigneron, "Density-functional approach to nonlinear-response coefficients of solids," Phys. Rev. B **39**, 13120–13128 (1989).

[92] R. P. Feynman, "Forces in molecules," Phys. Rev. **56**, 340–343 (1939).

[93] R. M. Sternheimer, "Electronic polarizabilities of ions from the Hartree-Fock wave functions," Phys. Rev. **96**, 951–968 (1954).

[94] A. A. Quong and B. M. Klein, "Self-consistent-screening calculation of interatomic force constants and phonon dispersion curves from first principles," Phys. Rev. B **46**, 10734–10737 (1992).

[95] S. de Gironcoli, "Lattice dynamics of metals from density-functional perturbation theory," Phys. Rev. B **51**, 6773–6776 (1995).

[96] D. R. Hamann, X. Wu, K. M. Rabe, and D. Vanderbilt, "Metric tensor formulation of strain in density-functional perturbation theory," Phys. Rev. B **71**, 035117 (2005).

[97] R. M. Martin, "Piezoelectricity," Phys. Rev. B **5**, 1607–1613 (1972).

[98] C. E. Dreyer, M. Stengel, and D. Vanderbilt, "Current-density implementation for calculating flexoelectric coefficients," Phys. Rev. B **98**, 075153 (2018).

[99] A. Schiaffino, C. E. Dreyer, D. Vanderbilt, and M. Stengel, "Metric wave approach to flexoelectricity within density functional perturbation theory," Phys. Rev. B **99**, 085107 (2019).

[100] M. Stengel and D. Vanderbilt, "Quantum theory of mechanical deformations," Phys. Rev. B **98**, 125133 (2018).

[101] S. Ismail-Beigi, E. K. Chang, and S. G. Louie, "Coupling of nonlocal potentials to electromagnetic fields," Phys. Rev. Lett. **87**, 087402 (2001).

[102] A. M. Essin, A. M. Turner, J. E. Moore, and D. Vanderbilt, "Orbital magnetoelectric coupling in band insulators," Phys. Rev. B **81**, 205104 (2010).

[103] M. Stengel, "Flexoelectricity from density-functional perturbation theory," Phys. Rev. B **88**, 174106 (2013).

[104] S. Baroni, S. de Gironcoli, A. Dal Corso, and P. Giannozzi, "Phonons and related crystal properties from density-functional perturbation theory," Rev. Mod. Phys. **73**, 515–562 (2001).

[105] M. Stengel, "From flexoelectricity to absolute deformation potentials: The case of $SrTiO_3$," Phys. Rev. B **92**, 205115 (2015).

[106] M. Stengel, "Unified ab initio formulation of flexoelectricity and strain-gradient elasticity," Phys. Rev. B **93**, 245107 (2016).

[107] N. Marzari, D. Vanderbilt, and M. C. Payne, "Ensemble density-functional theory for *ab nitio* molecular dynamics of metals and finite-temperature insulators," Phys. Rev. Lett. **79**, 1337–1340 (1997).

[108] X. Gonze, S. Rostami, and C. Tantardini, "Variational density functional perturbation theory for metals," Phys. Rev. B **109**, 014317 (2024).

[109] N. D. Mermin, "Thermal properties of the inhomogeneous electron gas," Phys. Rev. **137**, A1441–A1443 (1965).

[110] M. J. Gillan, "Calculation of the vacancy formation energy in aluminium," J. Phys.: Condens. Matter **1**, 689 (1989).

[111] M. P. Grumbach, D Hohl, R. M. Martin, and R. Car, "Ab initio molecular dynamics with a finite-temperature density functional," J. Phys.: Condens. Matter **6**, 1999 (1994).

[112] R. M. Wentzcovitch, J. L. Martins, and P. B. Allen, "Energy versus free-energy conservation in first-principles molecular dynamics," Phys. Rev. B **45**, 11372–11374 (1992).

[113] J. VandeVondele and A. De Vita, "First-principles molecular dynamics of metallic systems," Phys. Rev. B **60**, 13241–13244 (1999).

[114] M. Stengel and A. De Vita, "First-principles molecular dynamics of metals: A Lagrangian formulation," Phys. Rev. B **62**, 15283–15286 (2000).

[115] X. Liu, S. S. Tsirkin, and I. Souza, "Covariant derivatives of Berry-type quantities: Application to nonlinear transport in solids," arXiv preprint arXiv:2303.10129 (2023).

[116] R. Kubo, "Statistical-mechanical theory of irreversible processes. I. General theory and simple applications to magnetic and conduction problems," J. Phys. Soc. Jpn. **12**, 570–586 (1957).

[117] M. Born and K. Huang, *Dynamical theory of crystal lattices* (Clarendon Press, 1954).

[118] M. Stengel, "Macroscopic polarization from nonlinear gradient couplings," Phys. Rev. Lett. **132**, 146801 (2024).

[119] K. Ishito, H. Mao, Y. Kousaka, Y. Togawa, S. Iwasaki, T. Zhang, S. Murakami, J.-i. Kishine, and T. Satoh, "Truly chiral phonons in α-HgS," Nat. Phys. **19**, 35–39 (2023).

[120] M. van Setten, M. Giantomassi, E. Bousquet, M. Verstraete, D. Hamann, X. Gonze, and G.-M. Rignanese, "The PseudoDojo: training and grading a 85 element optimized norm-conserving pseudopotential table," Comput. Phys. Commun. **226**, 39–54 (2018).

[121] G. Marchese, F. Macheda, L. Binci, M. Calandra, P. Barone, and F. Mauri, "Born effective charges and vibrational spectra in superconducting and bad conducting metals," Nat. Phys. **20**, 88–94 (2024).

[122] F. Macheda, P. Barone, and F. Mauri, "Electron-phonon interaction and longitudinal-transverse phonon splitting in doped semiconductors," Phys. Rev. Lett. **129**, 185902 (2022).

[123] X. Gonze and J. W. Zwanziger, "Density-operator theory of orbital magnetic susceptibility in periodic insulators," Phys. Rev. B **84**, 064445 (2011).

[124] B. Wang, Y. Gu, S. Zhang, and L.-Q. Chen, "Flexoelectricity in solids: progress, challenges, and perspectives," Prog. Mater. Sci. **106**, 100570 (2019).

[125] A. K. Tagantsev, "Piezoelectricity and flexoelectricity in crystalline dielectrics," Phys. Rev. B **34**, 5883–5889 (1986).

[126] R. Resta, "Towards a bulk theory of flexoelectricity," Phys. Rev. Lett. **105**, 127601 (2010).

[127] J. Hong and D. Vanderbilt, "First-principles theory of frozen-ion flexoelectricity," Phys. Rev. B **84**, 180101 (2011).

[128] J. Hong and D. Vanderbilt, "First-principles theory and calculation of flexoelectricity," Phys. Rev. B **88**, 174107 (2013).

[129] X. Wu, D. Vanderbilt, and D. R. Hamann, "Systematic treatment of displacements, strains, and electric fields in density-functional perturbation theory," Phys. Rev. B **72**, 035105 (2005).

[130] O. Diéguez and M. Stengel, "Translational covariance of flexoelectricity at ferroelectric domain walls," Phys. Rev. X **12**, 031002 (2022).

[131] D. Hickox-Young, D. Puggioni, and J. M. Rondinelli, "Polar metals taxonomy for materials classification and discovery," Phys. Rev. Mater. **7**, 010301 (2023).

[132] S. Bhowal and N. A. Spaldin, "Polar metals: principles and prospects," Annual Review of Materials Research **53**, 53–79 (2023).

[133] S. Tinte, J. Íñiguez, K. M. Rabe, and D. Vanderbilt, "Quantitative analysis of the first-principles effective Hamiltonian approach to ferroelectric perovskites," Phys. Rev. B **67**, 064106 (2003).

[134] U. V. Waghmare and K. M. Rabe, "Ab initio statistical mechanics of the ferroelectric phase transition in $PbTiO_3$," Phys. Rev. B **55**, 6161–6173 (1997).

[135] J. Narvaez, S. Saremi, J. Hong, M. Stengel, and G. Catalan, "Large flexoelectric anisotropy in paraelectric barium titanate," Phys. Rev. Lett. **115**, 037601 (2015).

[136] H. Sim and B. G. Kim, "First-principles study of octahedral tilting and ferroelectric-like transition in metallic $LiOsO_3$," Phys. Rev. B **89**, 201107 (2014).

[137] G. Li, X. Huang, J. Hu, and W. Zhang, "Shear-strain gradient induced polarization reversal in ferroelectric $BaTiO_3$ thin films: A first-principles total-energy study," Phys. Rev. B **95**, 144111 (2017).

[138] V. Shelke, D. Mazumdar, G. Srinivasan, A. Kumar, S. Jesse, S. Kalinin, A. Baddorf, and A. Gupta, "Reduced coercive field in $BiFeO_3$ thin films through domain engineering," Advanced Materials **23**, 669–672 (2011).

[139] S. Rahimi, S Jalali-Asadabadi, P. Blaha, and F. Jalali-Asadabadi, "Nonzero spontaneous electric polarization in metals: novel predictive methods and applications," Sci. Rep. **14**, 672 (2024).

[140] P. Ghosez, J.-P. Michenaud, and X. Gonze, "Dynamical atomic charges: the case of ABO_3 compounds," Phys. Rev. B **58**, 6224–6240 (1998).

[141] X. Li, B. Fauqué, Z. Zhu, and K. Behnia, "Phonon thermal Hall effect in strontium titanate," Phys. Rev. Lett. **124**, 105901 (2020).

[142] C. Mead and D. Truhlar, "On the determination of Born-Oppenheimer nuclear motion wave functions including complications due to conical intersections and identical nuclei," J. Chem. Phys. **70**, 2284–2296 (1979).

[143] J. R. Eshbach and M. W. P. Strandberg, "Rotational magnetic moments of $^1\Sigma$ molecules," Phys. Rev. **85**, 24–34 (1952).

[144] J. M. Brown, R. J. Buenker, A. Carrington, C. D. Lauro, R. N. Dixon, R. W. Field, J. T. Hougen, W. Hüttner, K. Kuchitsu, M. Mehring, et al., "Remarks on the signs of g factors in atomic and molecular zeeman spectroscopy," Mol. Phys. **98**, 1597–1601 (2000).

[145] S. M. Cybulski and D. M. Bishop, "Calculations of magnetic properties. IV. Electron-correlated magnetizabilities and rotational g factors for nine small molecules," J. Chem. Phys. **100**, 2019–2026 (1994).

[146] E. Roman, J. R. Yates, M. Veithen, D. Vanderbilt, and I. Souza, "*Ab initio* study of the nonlinear optics of III-V semiconductors in the terahertz regime," Phys. Rev. B **74**, 245204 (2006).

[147] R. A. Cowley, "Lattice dynamics and phase transitions of strontium titanate," Phys. Rev. **134**, A981–A997 (1964).

[148] W. Flygare and R. Benson, "The molecular Zeeman effect in diamagnetic molecules and the determination of molecular magnetic moments (g values), magnetic susceptibilities, and molecular quadrupole moments," Mol. Phys. **20**, 225–250 (1971).

[149] D. Ceresoli and E. Tosatti, Private Communication.

[150] A. Buckingham and M. Dunn, "Optical activity of oriented molecules," J. Chem. Soc. A, 1988–1991 (1971).

[151] S. Grimme, "Calculation of frequency dependent optical rotation using density functional response theory," Chem. Phys. Lett. **339**, 380–388 (2001).

[152] J. Autschbach, S. Patchkovskii, T. Ziegler, S. J. A. van Gisbergen, and E. Jan Baerends, "Chiroptical properties from time-dependent density functional theory. II. Optical rotations of small to medium sized organic molecules," J. Chem. Phys. **117**, 581–592 (2002).

[153] M. Krykunov and J. Autschbach, "Calculation of origin-independent optical rotation tensor components in approximate time-dependent density functional theory," J. Chem. Phys. **125** (2006).

[154] R. Resta, "Molecular Berry curvatures and the adiabatic response tensors," J. Chem. Phys. **158**, 024105 (2023).

[155] R. H. Asendorf, "Space group of tellurium and selenium," J. Chem. Phys. **27**, 11–16 (1957).

[156] J. K. Desmarais, B. Kirtman, and M. Rérat, "First-principles calculation of the optical rotatory power of periodic systems: Modern theory with modern functionals," Phys. Rev. B **107**, 224430 (2023).

[157] J. P. Perdew, A. Ruzsinszky, G. I. Csonka, O. A. Vydrov, G. E. Scuseria, L. A. Constantin, X. Zhou, and K. Burke, "Restoring the density-gradient expansion for exchange in solids and surfaces," Phys. Rev. Lett. **100**, 136406 (2008).

[158] G. I. Pagola, M. B. Ferraro, P. F. Provasi, S. Pelloni, and P. Lazzeretti, "Theoretical estimates of the anapole magnetizabilities of $C_4H_4X_2$ cyclic molecules for X=O, S, Se, and Te," J. Chem. Phys. **141**, 094305 (2014).

[159] S. Pelloni and P. Lazzeretti, "On the determination of the diagonal components of the optical activity tensor in chiral molecules," J. Chem. Phys. **140**, 074105 (2014).

[160] J. Ma and D. A. Pesin, "Chiral magnetic effect and natural optical activity in metals with or without Weyl points," Phys. Rev. B **92**, 235205 (2015).

[161] K. Shinada, A. Kofuji, and R. Peters, "Quantum theory of the intrinsic orbital magnetoelectric effect in itinerant electron systems at finite temperatures," Phys. Rev. B **107**, 094106 (2023).

[162] W. Peng, S. Y. Park, C. J. Roh, J. Mun, H. Ju, J. Kim, E. K. Ko, Z. Liang, S. Hahn, J. Zhang, et al., "Flexoelectric polarizing and control of a ferromagnetic metal," Nature Physics **20**, 450–455 (2024).

[163] J. Bardeen and W. Shockley, "Deformation potentials and mobilities in non-polar crystals," Phys. Rev. **80**, 72–80 (1950).

[164] R. Resta, L. Colombo, and S. Baroni, "Absolute deformation potentials in semiconductors," Phys. Rev. B **41**, 12358–12361 (1990).

[165] A. Antons, J. B. Neaton, K. M. Rabe, and D. Vanderbilt, "Tunability of the dielectric response of epitaxially strained $SrTiO_3$ from first principles," Phys. Rev. B **71**, 024102 (2005).

[166] D. Bennett, D. Tanner, P. Ghosez, P.-E. Janolin, and E. Bousquet, "Generalized relation between electromechanical responses at fixed voltage and fixed electric field," Phys. Rev. B **106**, 174105 (2022).

[167] D Vanderbilt, "Berry-phase theory of proper piezoelectric response," J. Phys. Chem. Solids **61**, 147–151 (2000).